

Nanomaterials from Natural Products for Industrial Applications

Lead Guest Editor: Sohel Rana

Guest Editors: Raul Fanguero, Vijay K. Thakur, Mangala Joshi, Sabu Thomas,
and Bodo Fiedler





Nanomaterials from Natural Products for Industrial Applications

Journal of Nanomaterials

Nanomaterials from Natural Products for Industrial Applications

Lead Guest Editor: Sohel Rana

Guest Editors: Raul Figueiro, Vijay K. Thakur, Mangala Joshi,
and Bodo Fiedler



Copyright © 2017 Hindawi. All rights reserved.

This is a special issue published in "Journal of Nanomaterials." All articles are open access articles distributed under the Creative Commons Attribution License, which permits unrestricted use, distribution, and reproduction in any medium, provided the original work is properly cited.

Editorial Board

Domenico Acierno, Italy
Katerina Aifantis, USA
Nageh K. Allam, USA
Margarida Amaral, Portugal
Martin Andersson, Sweden
Raul Arenal, Spain
Ilaria Armentano, Italy
Vincenzo Baglio, Italy
Lavinia Balan, France
Thierry Baron, France
Andrew R. Barron, USA
Hongbin Bei, USA
Stefano Bellucci, Italy
Enrico Bergamaschi, Italy
Debes Bhattacharyya, New Zealand
Sergio Bietti, Italy
Giovanni Bongiovanni, Italy
Mohamed Bououdina, Bahrain
Victor M. Castaño, Mexico
Albano Cavaleiro, Portugal
Bhanu P. S. Chauhan, USA
Shafiq Chowdhury, USA
Jin-Ho Choy, Republic of Korea
Yu-Lun Chueh, Taiwan
Elisabetta Comini, Italy
Giuseppe Compagnini, Italy
David Cornu, France
Miguel A. Correa-Duarte, Spain
P. Davide Cozzoli, Italy
Anuja Datta, USA
Loretta L. Del Mercato, Italy
Yong Ding, USA
Zehra Durmus, Turkey
Joydeep Dutta, Oman
Ovidiu Ersen, France
Claude Estournès, France
Andrea Falqui, Saudi Arabia
Matteo Ferroni, Italy
Ilaria Fratoddi, Italy
Miguel A. Garcia, Spain
Siddhartha Ghosh, Singapore
Filippo Giubileo, Italy
Fabien Grasset, France
Jean M. Greneche, France
Kimberly Hamad-Schifferli, USA
Simo-Pekka Hannula, Finland
Michael Harris, USA
Yasuhiko Hayashi, Japan
Michael Z. Hu, USA
Nay Ming Huang, Malaysia
Zafar Iqbal, USA
Balachandran Jeyadevan, Japan
Jeong-won Kang, Republic of Korea
Hassan Karimi-Maleh, Iran
Antonios Kelarakis, UK
Alireza Khataee, Iran
Ali Khorsand Zak, Iran
Philippe Knauth, France
Prashant Kumar, UK
Eric Le Bourhis, France
Jun Li, Singapore
Meiyong Liao, Japan
Shijun Liao, China
Silvia Licoccia, Italy
Nathan C. Lindquist, USA
Zainovia Lockman, Malaysia
Jim Low, Australia
Laura M. Maestro, Spain
Gaurav Mago, USA
Muhamamd A. Malik, UK
Francesco Marotti de Sciarra, Italy
Sanjay R. Mathur, Germany
Tony McNally, UK
Yogendra Mishra, Germany
Paulo Cesar Morais, Brazil
Paul Munroe, Australia
Jae-Min Myoung, Republic of Korea
Rajesh R. Naik, USA
Albert Nasibulin, Russia
Toshiaki Natsuki, Japan
Natalia Noginova, USA
Sherine Obare, USA
Won-Chun Oh, Republic of Korea
Abdelwahab Omri, Canada
Ungyu Paik, Republic of Korea
Piersandro Pallavicini, Italy
Edward A. Payzant, USA
Alessandro Pegoretti, Italy
Oscar Perales-Pérez, Puerto Rico
Jorge Pérez-Juste, Spain
Alexey P. Popov, Finland
Thathan Premkumar, Republic of Korea
Helena Prima-García, Spain
Alexander Pyatenko, Japan
Haisheng Qian, China
You Qiang, USA
Philip D. Rack, USA
Peter Reiss, France
Ilker S. Bayer, Italy
Lucien Saviot, France
Sudipta Seal, USA
Shu Seki, Japan
Donglu Shi, USA
Bhanu P. Singh, India
Surinder Singh, USA
Vladimir Sivakov, Germany
Adolfo Speghini, Italy
Marinella Striccoli, Italy
Fengqiang Sun, China
Xuping Sun, Saudi Arabia
Ashok K. Sundramoorthy, India
Angelo Taglietti, Italy
Bo Tan, Canada
Leander Tapfer, Italy
Valeri P. Tolstoy, Russia
Muhammet S. Toprak, Sweden
R. Torrecillas, Spain
Achim Trampert, Germany
Takuya Tsuzuki, Australia
Tamer Uyar, Turkey
Luca Valentini, Italy
Antonio Vassallo, Italy
Ester Vazquez, Spain
Ajayan Vinu, Australia
Ruibing Wang, Macau
Shiren Wang, USA
Yong Wang, USA
Magnus Willander, Sweden
Ping Xiao, UK
Zhi Li Xiao, USA
Yoke K. Yap, USA
Dong Kee Yi, Republic of Korea
Jianbo Yin, China
William Yu, USA
Michele Zappalorto, Italy
Renyun Zhang, Sweden

Contents

Nanomaterials from Natural Products for Industrial Applications

Sohel Rana, Raul Fangueiro, Vijay K. Thakur, Mangala Joshi, Sabu Thomas, and Bodo Fiedler
Volume 2017, Article ID 4817653, 2 pages

Synthesis and Bactericidal Properties of Hyaluronic Acid Doped with Metal Nanoparticles

Galo Cárdenas-Triviño, Macarena Ruiz-Parra, Luis Vergara-González, Javier Ojeda-Oyarzún, and Guillermo Solorzano
Volume 2017, Article ID 9573869, 9 pages

Comparative Study on Properties of Polylactic Acid Nanocomposites with Cellulose and Chitin Nanofibers Extracted from Different Raw Materials

Jingjing Li, Jian Li, Dejun Feng, Jingfeng Zhao, Jingrong Sun, and Dagang Li
Volume 2017, Article ID 7193263, 11 pages

Nanoporosity of MCM-41 Materials and Y-Zeolites Created by Deposition of *Tournefortia hirsutissima* L. Plant Extract

Miguel Angel Hernández, Gabriela Itzel Hernández, Roberto Portillo, Martha Alicia Salgado, Fernando Rojas, and Vitalii Petranovskii
Volume 2017, Article ID 2783143, 10 pages

Nanosized Minicells Generated by Lactic Acid Bacteria for Drug Delivery

Huu Ngoc Nguyen, Santa Romero Jovel, and Tu Hoang Khue Nguyen
Volume 2017, Article ID 6847297, 10 pages

Lignocellulosic Micro- and Nanomaterials as Copper Frames for the Evaluation of the Copper(I)-Catalyzed Azide-Alkyne Cycloaddition

Charles W. Owens, Gloria S. Oporto, Björn C. G. Söderberg, and Katherine E. Lambson
Volume 2017, Article ID 9461615, 6 pages

Nanofibrillated Cellulose from Appalachian Hardwoods Logging Residues as Template for Antimicrobial Copper

Masoumeh Hassanzadeh, Ronald Sabo, Alan Rudie, Richard Reiner, Roland Gleisner, and Gloria S. Oporto
Volume 2017, Article ID 2102987, 14 pages

Modification of Functional Properties of Whey Protein Isolate Nanocomposite Films and Coatings with Nanoclays

Kerstin Müller, Marius Jesdinzski, and Markus Schmid
Volume 2017, Article ID 6039192, 10 pages

Andiroba Oil (*Carapa guianensis* Aublet) Nanoemulsions: Development and Assessment of Cytotoxicity, Genotoxicity, and Hematotoxicity

Susana Suely Rodrigues Milhomem-Paixão, Maria Luiza Fascineli, Luis Alexandre Muehlmann, Karina Motta Melo, Hugo Leonardo Crisóstomo Salgado, Graziella Anselmo Joanitti, Julio Cesar Pieczarka, Ricardo Bentes Azevedo, Alberdan Silva Santos, and Cesar Koppe Grisolia
Volume 2017, Article ID 4362046, 11 pages

An Efficient Method for Cellulose Nanofibrils Length Shearing via Environmentally Friendly Mixed Cellulase Pretreatment

Yuan Chen, Yuchan He, Dongbin Fan, Yanming Han, Gaiyun Li, and Siqun Wang
Volume 2017, Article ID 1591504, 12 pages

Editorial

Nanomaterials from Natural Products for Industrial Applications

Sohel Rana,¹ Raul Fanguero,¹ Vijay K. Thakur,² Mangala Joshi,³ Sabu Thomas,⁴ and Bodo Fiedler⁵

¹Centre for Textile Science and Technology (2C2T), University of Minho, Guimarães, Portugal

²Enhanced Composites & Structures Centre, Cranfield University, Cranfield, UK

³Department of Textile Technology, Indian Institute of Technology, Delhi, India

⁴School of Chemical Science, Mahatma Gandhi University, Kottayam, Kerala, India

⁵Institute of Polymer and Composite, Technical University of Hamburg, Hamburg, Germany

Correspondence should be addressed to Sohel Rana; soheliitd2005@gmail.com

Received 22 November 2017; Accepted 23 November 2017; Published 26 December 2017

Copyright © 2017 Sohel Rana et al. This is an open access article distributed under the Creative Commons Attribution License, which permits unrestricted use, distribution, and reproduction in any medium, provided the original work is properly cited.

This special issue is focused on the nanomaterials derived from natural products and their application in different industrial sectors.

Nanotechnology has emerged as one of the most promising tools for creating high performance and multifunctional materials for various industrial applications. Looking at the growing concern about the environment and sustainability, nanomaterials from natural sources are receiving great attention in the scientific community as well as in industrial sectors. A wide variety of nanomaterials synthesized from natural products possess exceptional strength characteristics, light weight, transparency, and excellent biocompatibility and are, therefore, promising materials for coatings, packaging, medicine, construction, electronics, filtration, transportation, and other areas. Among various techniques, electrospinning has been considered to be a simple and versatile technique for producing continuous nanofibres from natural polymers. Therefore, besides particles, it has been possible to produce continuous fibres and textiles based on these nanomaterials.

Within the range of natural nanomaterials, nanocellulose has attracted a special attention and has been widely used for industrial applications. Nanocellulose has been either synthesized through bottom-up approach using bacteria (known as bacterial cellulose) or produced from plant cellulose through physical (such as ultrasonication, homogenization, and ball milling) or chemical methods (such as acid hydrolysis) or

their combination in the form of nano-fibrillated cellulose (NFC) and nano-crystalline cellulose (NCC). Nanocellulose possesses high mechanical properties (NCC's axial Young's modulus: 120–220 GPa, transverse modulus: 11–57 GPa, tensile strength: 7.5 GPa), high surface area, and interesting barrier and optical properties and is, therefore, considered to be an excellent reinforcement for composite materials. This special issue presented a number of sources for production of nano cellulose and its application in different areas. For example, M. Hassanzadeh et al. produced NFC from two underutilized Appalachian hardwoods, Northern red oak (*Quercus rubra*) and yellow poplar (*Liriodendron tulipifera*) and explored the possibility of using the produced NFC as templates for antimicrobial copper for packaging and medical/pharmaceutical applications. J. Li et al. produced NFC from poplar and cotton sources and used for the reinforcement of Polylactic Acid (PLA) composites. An interesting application of copper immobilized NFC has been reported by C. W. Owens et al. as catalyst for the synthesis of 1-benzyl-4-phenyl-1H-1,2,3-triazole from benzyl azide and phenylacetylene with a yield of over 90%.

A number of attempts have been made to control the size and morphology as well as functionality of produced nanocellulose targeting different applications. These approaches either include pretreatment of cellulosic materials prior to nanocellulose extraction or functionalization of produced nanocellulose using different chemical or physical

methods. In this special issue, Y. Chen et al. presented a green pretreatment approach with exoglucanase and endoglucanase enzymes to produce NFC with controlled length for special applications.

Nanomaterials produced by bacteria are also getting tremendous attention in recent times. Bacterial cellulose is an appropriate example of this type of materials with high purity, crystallinity, and excellent mechanical properties. Minicells generated by lactic acid bacteria are another type of nanosized particles with huge application potential in drug delivery systems for treatment of cancer, microbial infection, and other diseases, as discussed in the review paper by H. N. Nguyen et al. included in the present special issue.

Nanoclays such as montmorillonite (MMT), kaolinite, and saponite are other natural nanomaterials which have been widely used for reinforcement of polymeric as well as cementitious composites. Reinforcement of polymers with nanoclays improves their physical, mechanical, and gas barrier properties. On the other hand, in case of cementitious materials, nanoclays are used to improve the mechanical performance, resistance to chloride penetration, and self-compacting performance and to reduce the permeability and shrinkage properties. Nanoclays find diversified applications in cosmetics, drug delivery systems, pollution control and water treatment, food industry, and so on. An application of nanoclays to improve the mechanical and barrier performance of whey protein isolate nanocomposites films for food packaging applications has been presented in this special issue by K. Müller et al. The use of other inorganic nanomaterials such as MCM-41 silicate and Y-Zeolites, deposited with a bioactive plant extract for medical applications, has been discussed by M. A. Hernández et al. Some other nanomaterials from natural products for medical applications, discussed in this issue, include nanoemulsion produced from the extract of Amazonian andiroba plant oil as reported by S. S. R. Milhomem-Paixão et al. and nanocomposite films of hyaluronic acid containing metal nanoparticles as discussed by G. Cárdenas-Triviño et al.

However, despite promising properties and applications, further research and developments are extremely essential for nanomaterials obtained from various natural products. Production of these nanomaterials at industrial scale needs cost-effective production processes, improved production rate, and consistent quality as well as predictable and consistent performance of nanomaterials based products. This special issue presented some of the recent research approaches to study and optimize the properties of a few natural product based nanomaterials and highlighted their enormous application potential in diversified industrial sectors.

*Sohel Rana
Raul Fanguero
Vijay K. Thakur
Mangala Joshi
Sabu Thomas
Bodo Fiedler*

Research Article

Synthesis and Bactericidal Properties of Hyaluronic Acid Doped with Metal Nanoparticles

Galo Cárdenas-Triviño,¹ Macarena Ruiz-Parra,² Luis Vergara-González,³ Javier Ojeda-Oyarzún,⁴ and Guillermo Solorzano⁵

¹Facultad de Ingeniería, Centro de Biomateriales y Nanotecnología, Universidad del Bío-Bío, Av. Collao 1202, Concepción, Chile

²Facultad de Ciencia, Química y Farmacia, Universidad San Sebastián, Lientur 1457, Concepción, Chile

³Facultad de Ciencia, Departamento de Ciencias Biológicas y Químicas, Universidad San Sebastián, Lientur 1457, Concepción, Chile

⁴Facultad de Medicina Veterinaria, Universidad Austral de Chile, Independencia 641, Valdivia, Chile

⁵Departamento de Engenharia Química e de Materiais, Pontifical Catholic University of Rio de Janeiro, R. Marquês de São Vicente 225, Gávea, Rio de Janeiro, RJ, Brazil

Correspondence should be addressed to Galo Cárdenas-Triviño; gcardenas@ubiobio.cl

Received 23 March 2017; Accepted 9 October 2017; Published 17 December 2017

Academic Editor: Raul Fangueiro

Copyright © 2017 Galo Cárdenas-Triviño et al. This is an open access article distributed under the Creative Commons Attribution License, which permits unrestricted use, distribution, and reproduction in any medium, provided the original work is properly cited.

A study on the nanoparticles size and the antibacterial properties of hyaluronic acid (HA) doped with nanoparticles is reported. Nanoparticles from gold, silver, copper, and silver palladium with HA support were performed. The solvated metal atom dispersion (SMAD) method with 2-propanol and HA was used. High-resolution transmission electron microscopy (HRTEM), infrared spectroscopy (FT-IR), and thermogravimetric analysis (TGA) were conducted. The average sizes of nanoclusters were as follows: HA-Au = 1788 nm; HA-Ag = 50.41 nm; HA-Cu = 13.33 nm; and HA-AgPd = 33.22 nm. The antibacterial activity of solutions and films containing nanoparticles against American Type Culture Collection (ATCC) bacterial strains *Escherichia coli* (EC), *Staphylococcus aureus* (SA), *Staphylococcus epidermidis* (SE), and *Pseudomonas aeruginosa* (PA) was determined. Inhibition was observed for HA-Ag, HA-Cu, and HA-AgPd. Toxicological tests were performed in rats that were injected intraperitoneally with two concentrations of gold, copper, silver, and silver-palladium nanoparticles. No alterations in hepatic parameters, including ALT (alanine aminotransferase), GGT (gamma-glutamyl transpeptidase) bilirubin, and albumin, were observed after 14 days. These films could be used as promoters of skin recovery and Grades I and II cutaneous burns and as scaffolds.

1. Introduction

Nanotechnology is now one of the highest priorities in science and technology research [1]. By controlling the size, shape, and distribution of nanoparticles (NPs), it is possible to determine their properties and the nature and intensity of their interactions with other molecules. One way to modify the final properties of a nanomaterial is to use a polymeric support. The unique properties of supported metallic nanoparticles (MNPs) are directly related to the types of particles (size and shape), the dispersion, concentration, and electronic properties of the metal in the support [2, 3]. MNPs dispersed in solvents have been widely studied over the past few years because their properties have enabled applications

in the areas of electronics, medicine, environmental science, and materials science [4].

Nanomedicine is a field that encompasses applied nanotechnology methods in medicine. Thus, it allows the use of nanotechnology in cutting-edge research that will lead to the creation of better techniques for the treatment of diseases to improve the prognosis of patients [5]. The revolutionary aim of this science is focused primarily on monitoring, repairing tissue, controlling the evolution of disease, and defending and improving human biological systems. The most significant biotechnological advances in this field include biosensors, novel pharmacoselective agents, and the development of materials for grafts, among others [6].

The antimicrobial activity of metal nanoparticles had been reported profusely in the last years [7–10] as a possible alternative treatment for infected wounds, particularly with antimicrobial resistant bacteria, and nanoparticles of various metals have been studied.

There is evidence that demonstrates that gold nanoparticles are inert or have nontoxic effect on human cells [11]. No proinflammatory cytokines secretion, such as necrosis factor tumor alpha (TNF- α), was detected in a study with macrophage cells; these results emphasize that AuNPs are not cytotoxic or immunogenic but are biocompatible, corroborating their excellent potential in the areas of nanoimmunology, nanobiotechnology, and nanomedicine [12]. On the other hand, good antibacterial activity has been demonstrated against various pathogenic bacteria [13, 14].

In contrast to gold nanoparticles, silver nanoparticles (AgNPs) show toxicity associated with their oxidative and inflammatory nature [15], which is related to their genotoxicity and cytotoxicity [16, 17]. Therefore, it is suggested that AgNPs can inhibit the mechanisms of antioxidant defense through the reduction of glutathione, inactivation of the superoxide dismutase, and promotion of lipid peroxidation [18]. Consequently, reactive oxygen species accumulation and oxidative stress can cause many physiological and cellular events, including stress, disruption and destruction of mitochondria, apoptosis, inflammation, and damage to DNA [19]. The mitochondria appear to be the cellular compartment most sensitive to the toxicity of AgNPs [20].

In addition to the damage to DNA and mitochondria, it has also been observed that AgNP exposure, in contrast with AuNPs, induces the release of a series of proinflammatory markers, predominantly TNF- α , pulmonary intravascular macrophages, and granulocyte colony-stimulating factor [21]. However, the toxicity of AgNPs is still a concern matter because AgNPs release Ag⁺ ions in aqueous solution [22], and there is evidence that the silver ion presence enhances significantly the toxicity of AgNPs [23].

On nanoscale, pure copper or copper oxides become even more toxic to pathogenic microorganisms, an effect that is directly related to the size of the particles. As is the case with other metals, the presence of excess copper has also been proven to be toxic, to a certain extent, to cellular organisms in general [24, 25]. This is because, in the presence of water and oxygen, copper releases positive ions and generates hydroxyl radicals, both of which are highly toxic. In addition, the electrons produced by oxidation reactions interact with water molecules, forming other hydroxyl radicals [26, 27].

There are multiple effects that show the toxicity of copper: (1) inhibition or alteration of protein synthesis; (2) alterations to the permeability of the cell membrane, causing the peroxidation of lipids by inducing oxidative damage to them; as a result, an imbalance is created in the entrance and the exit of minerals, including sodium and potassium, that are essential for normal cells to function; and (3) destruction or alteration of nucleic acids (DNA), thus disrupting the ability of cells to multiply [28].

In a study that evaluated the *in vitro* toxicity of CuNPs in fibroblast cells from mouse embryos showed that Cu²⁺ ions

are more cytotoxic than covered NPs (CuNPs) [26] as has been reported also for AgNPs and silver ions.

Palladium has been used in alloy with gold, silver, and tin as a material for dental restoration for years, and health concerns about his use are due it known effect on the immune system [29, 30]. Limited other data about palladium toxicity has been reported [31]. For this reason, AgPd-NPs was included in this study.

Hyaluronic acid (HA) is a fundamental component of the extracellular matrix of the skin, mucosal tissue, joints, eyes, and many other organs and tissues. It is involved in tissue repair processes and is an essential component in the resurfacing of the skin and the prevention of scar formation. Its osmotic capability restores tissue hydration during the inflammatory process, and its viscosity helps to prevent the passage of bacteria and viruses into the pericellular area (around the cell). It is a known stimulator of the inflammatory process because it acts as a barrier to tissue degradation and has antioxidant properties, including the ability to eliminate free radicals [32–34], which are tissue-damaging byproducts derived from the metabolism of oxygen that can cause inflammation and cancer [35].

HA, is a potent water attractant. This property provides hydration, firmness, smoothness, and a defensive barrier to the skin and also offers mechanical stability to joints and slows down skin aging.

The main goal of this work is to obtain films of HA doped with MNPs to improve skin recovery and to control bacterial infections of wounds.

2. Materials and Methods

2.1. Metal Atom Reactor (Chemical Liquid Deposition-Solvated Metal Atom Dispersion Method). The metal atom reactor used has been previously described [36, 37]. In a typical procedure, an alumina-tungsten crucible at the bottom of the reactor was charged with 0.150 g of Au metal and 3.0 g of HA. Dry 2-ethoxyethanol was placed in a ligand inlet tube and degassed by several freeze-pump-thaw cycles. The reactor was pumped down to 0.008 mbar, while the crucible was heated until it was red. A liquid nitrogen-filled Dewar was placed around the vessel, and Au and 2-ethoxyethanol (70 ml) were deposited over a period of 1 h with a current of 35 A. The matrix was a blue/purple color at the end of the deposition. The matrix was then allowed to warm slowly under vacuum for 1 h by removing the liquid nitrogen Dewar. Upon meltdown, a purple colloid was obtained. After returning the matrix to 1 atm by the addition of nitrogen, the colloid was allowed to warm for another 0.5 h at room temperature. The dispersion was stirred for 12 h and was then syphoned out under nitrogen into a flask. Based on the evaporated metal and 2-ethoxyethanol in the inlet, the molarity of the metal could be calculated. Several concentrations were prepared under the same conditions for Ag, Cu, and AgPd (between 50 and 200 mg). No hydrogen evolution during the metal evaporation was observed. The vacuum remained constant during the evaporation process.

2.2. Metallic Solids. Metallic solids were prepared by the direct evaporation of solvent, achieved by connecting the receiver flask to the vacuum line for a period of approximately 10 h. Once the solvent had evaporated, the flask and the solid could be collected, after which it was stored in a dry chamber under atmosphere of nitrogen gas to prevent the oxidation of the material.

2.3. High-Resolution Transmission Electron Microscopy (HRTEM). Micrographs were obtained on a JEOL 2100F high-resolution transmission electron microscope (200 kV) or on a JEOL 2010 TEM (200 KV). It was possible to determine the range of size distribution of NPs in addition to possible distortions and imperfections in the MNPs of Au, Ag, Cu, and the alloy AgPd. Sample preparation included a procedure that separated and dissolved the polymer nanoparticles using only HA and water as solvent. This step allowed us to view the NPs in more detail. In this procedure, solid polymer containing MNPs and weighing approximately 0.002 g to 0.008 g was dissolved in 3 or 6 ml of sterile distilled water and sonicated for 15 minutes; then, 1 drop of the solution obtained was placed in the grid of copper or nickel with a carbon film. The average particle size was obtained from 59 measurements.

2.4. Infrared Spectroscopy with Fourier Transform (FT-IR). The spectrophotometer used to obtain IR spectra was a Nicolet Magna 500 equipped with Nicolet EZ OMNIC software for the collection and analysis of spectra.

The sample preparation method used most often for the analysis of solid samples involved a KBr matrix; specifically, the solid samples were dispersed and supported on a KBr matrix tablet. For the preparation of the tablet, solid fiberglass (1 mg), previously cut with a microtome, was dispersed on an array of KBr (100 mg) by mixing and grinding to homogenize the mixture inside an agate mortar. Then, the mixture was introduced into a mold and compressed to obtain a disc. Subsequently, the disc was stored in a desiccator until FT-IR analysis.

Spectra were recorded in a wavelength range from 400 cm^{-1} (25 micrometers) to 4000 cm^{-1} (2.5 micrometers), which defined the IR electromagnetic radiation spectrum. The analysis included obtaining the far and middle IR spectra of each of the samples.

2.5. Thermogravimetric Analysis (TGA). Thermogravimetry was performed with a Q50 V2010 Build 36 TGA. Samples of the solid were heated at a rate of $10^\circ\text{C}/\text{min}$ in air with a flow rate of 20 ml/min. From the corresponding thermogram, the temperature of decomposition and the mass percent composition of the degradation products were determined.

2.6. Microbiological Tests. For the bacteriological assays, four bacterial strains were used: *Escherichia coli* (ATCC 25922), *Pseudomonas aeruginosa* (ATCC 27853), *Staphylococcus aureus* (ATCC 25923), and *Staphylococcus epidermidis* (ATCC 12228).

The antibacterial properties of the NPs supported in HA were assayed by a qualitative approach. For this, a 1 cm^2 film prepared from HA and the appropriate NPs was deposited in a Petri dish containing a thin layer of Mueller-Hinton (MH) agar. Then, 10 ml of MH agar containing an inoculum of approximately 10^6 CFU/ml was poured onto the film until it was covered. The antibacterial activity was determined by comparing the growth to that of a control film without NPs.

2.7. Toxicological Test: Bioassays in Rats. The experimental method of intraperitoneal injection in mice started with a full physical examination of the rats before beginning the administration of the solutions under study. The average temperature, pulse, and breathing needed to be 38°C , 280 beats/min, and 90 breaths/min, respectively, before proceeding. The animals were supplied with adequate food and water, in addition to controlling the conditions in terms of light and humidity. Ether was used as an anesthetic; before the induction, the rats were fasted for at least 12 h. This procedure employed all possible hygienic measures, such as the use of surgical gloves, apron, cap, and mask. Once the mouse was sedated, it was held during injection of the solution under study using a syringe that conformed to the desired volume level. The solution was injected into the back of the mouse, around the cervical area.

After the solutions were administered, all the rats under study, including the control group, were maintained under conditions with adequate food, light, temperature, and humidity until the day established as the end of the analysis, at which point a number of rats in each group under study were sacrificed. For example, a rat from each group was analyzed in terms of their liver enzymes to determine toxicity in the long and short term.

The studies that were performed in the present work were conducted, without exception, while respecting international standards for the management of laboratory animals according to National Institute of Health Guide for the Care and Use of Laboratory Animals and the Bioethics Committee (Universidad Austral de Chile).

3. Results

3.1. High-Resolution Transmission Electron Microscopy (HRTEM). From the micrographs (Figure 1(a)) obtained, it is possible to observe atomic planes previously reported in the literature for each NP. Using Digital Micrograph software, measurements of interplanar spacing values were performed to identify the type of atomic plane. From these data, it is possible to determine the space between each interplanar layer of the metallic element (0.39 nm) and that the MNPs have a face-centered cubic (fcc) crystal structure. One of the objectives of this TEM analysis was to determine the size distribution of the MNPs under study and to determine the presence or absence of any distortions or imperfections in the particles arising from an incomplete synthesis process.

Assuming that its crystalline structure is fcc on both sides, the measurement of the extent of the interplanar distance is

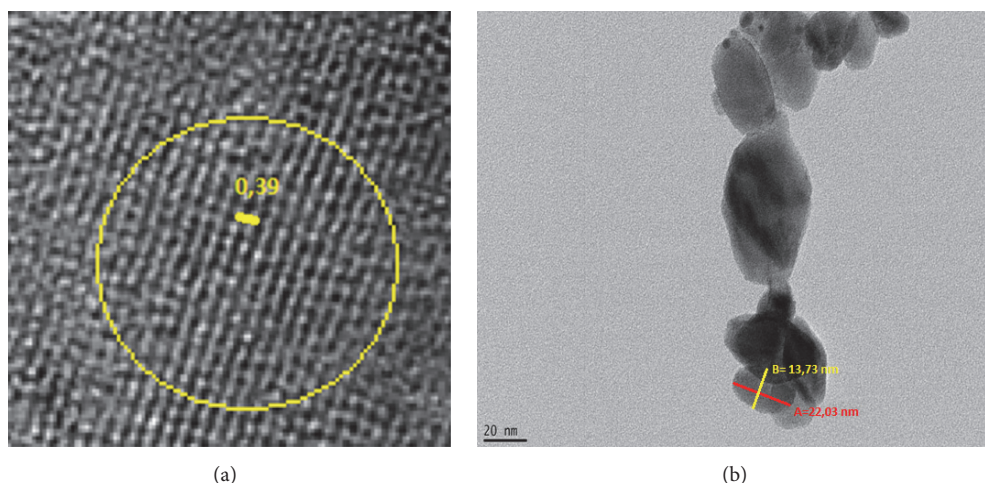


FIGURE 1: (a) High-resolution micrograph of HA-Au-2. Interplanar distance = 0.39 nm. (b) Micrograph exhibiting Au NP supported in HA with an average particle size of 17.88 nm.

TABLE 1: Frequency bands of the major functional groups present in the HA and HA + metal NPs.

Number	Bond	Frequency (cm^{-1}) pure HA	Frequency (cm^{-1}) HA+Au-2	Frequency (cm^{-1}) HA+Ag-2	Frequency (cm^{-1}) HA+Cu-2	Frequency (cm^{-1}) HA+AgPd-2
(1)	$\nu\text{O-H}$	3428,52	3419,14	3431,03	3430,83	3426,44
(2)	$\nu\text{C-H}$	2928,61	2926,71	2914,37	2925,68	2922,69
(3)	$\nu\text{C=O}$	1624,47	1728,94	1629,23	1630,56	1623,40
(4)	$\nu\text{C-C}$	1414,42	1412,76	1416,64	1417,31	1415,47
(5)	$\nu\text{C-C}$	1326,19	1281,01	1316,18	1319,27	1321,25
(6)	$\nu\text{C-O}$	1154,97	—	—	1155,23	1154,67
(7)	$\nu\text{C-O}$	1041,64	1077,03	1043,18	1042,60	1039,55
(8)	δCH_2	611,40	611,01	604,97	606,98	613,01
(9)	$\nu\text{C=O}$	—	1618,63	—	—	—

equal to 0.362 nm. It can be concluded that the observed plane is the (111) plane.

The quality of the two high-resolution images in Figure 3 of the silver-palladium (alloy) NPs should be noted; it is possible to see at a glance atomic levels, interplanar distances, and facets of the location of the atoms. Clearly, the observation of the spatial arrangement of atoms in the more stable (111) plane was achieved.

The shape of the NPs was generally not a perfect sphere, so, the average size was calculated as the mean of the width and the length of several particles (see Figure 4).

According to measurements made using Digital Micrograph software, the sizes of the gold, silver, copper, and silver-palladium MNPs were within the range of 10–50 nm.

Based on the results obtained and the micrographs shown above, it is possible to determine that the sizes of the different types of NP, for example, Au and Ag NPs, are not homogeneous, which is to be expected because, during the synthesis process, unequal amounts in terms of milligrams of metal not used in the formation reaction lead to different particle sizes at the nanometer scale. However, it was not

expected that there would be a difference in the distribution of sizes between a single type of metal NP, for example, silver, in which case there were no more than two NPs with equal sizes, which may be attributable to the synthesis process. There were several factors that influenced NP growth not being realized in its entirety in all the NPs; therefore, the sizes measured varied within the particles containing the same type of metal.

3.2. FT-IR Spectroscopy. Shown below are IR spectra from which polymer structure characterization can be achieved. HA was analyzed in the middle or intermediate IR range (up to 4000 cm^{-1}) to corroborate the presence of polymer in each of solid samples containing NPs of Au, Ag, Cu, and AgPd. From these spectra, one can check for the presence of the main organic groups present in the molecule. In addition, spectroscopy in the far IR range (up to 400 cm^{-1}) was performed on the samples of MNPs, making it possible to distinguish the main bonds where the MNPs are linked to the polymer and the presence of clusters or atomic groupings of the same metal (see Table 1).

TABLE 2: HA and MNP bonds and their possible frequency bands.

HA-metal	Frequency of metal-oxygen (cm^{-1})	Frequency of metal (clusters) (cm^{-1})
HA-Au	451,39	126,56
HA-Ag	444,72	186,72
HA-Cu	445,25	132,72
HA-AgPd	459,06	122,86

TABLE 3: Summary table of decomposition temperatures and mass losses of solid NPs of Au, Ag, Cu, and AgPd-2 alloy supported by HA.

Solid	Total mass (mg)	Decomposition temperature ($^{\circ}\text{C}$)	Percentage of mass loss (%)	Mass loss (mg)	Residual loss temperature ($^{\circ}\text{C}$, approx.)	Residual mass percentage (%)
HA	12,185	220,98	63,07	7,685	500	36,93
HA-Au-2	11,568	217,94	73,89	8,547	500	26,11
HA-Ag-2	6,269	217,80	76,87	4,819	550	23,16
HA-Cu-2	5,264	218,72	72,01	3,791	550	27,99
HA-AgPd-2	7,563	220,45	76,26	5,768	550	23,74

TABLE 4: Inhibition of bacterial growth by films of metallic NPs supported by HA.

Films of MNPs	HA-Au-2	HA-Au-3	HA-Ag-2	HA-Ag-3	HA-Cu-2	HA-Cu-3	HA-AgPd-2	HA-AgPd-3
<i>S. aureus</i> ATCC (25923)	x	x	xx	xxx	xx	xx	xx	x
<i>S. epidermidis</i> ATCC (122228)	xx	x						
<i>E. coli</i> ATCC (25922)	x	xx	xxx	xx	xx	xx	x	xx
<i>P. aeruginosa</i> ATCC (27853)	xx	xx	xxx	xxx	xx	xxx	xx	xx

(x = no inhibition; xx = decreases growth; xxx = inhibits).

To confirm the presence or absence of the major functional groups of HA as a polymer solid used to support NPs, it is not necessary to obtain an equal value in terms of frequency but rather to confirm that bands move only within similar ranges with a minimal difference. This difference between each solid sample containing a different metal arises from the metal causing the bands to behave similarly but not exhibit the same vibrations. The 3428 cm^{-1} bands correspond to the vibration of $-\text{OH}$ bond stretching. The band at 2928 cm^{-1} is due to $-\text{CH}$ bond stretching. At 1727 cm^{-1} , the band corresponds to the absorption from $\text{C}=\text{O}$ double bond stretching, and the 1624 and 1625 cm^{-1} bands show absorption from the stretching of the $\text{C}=\text{C}$ double bonds or chelated groups in the case of Au-2.

3.3. Far FT-IR. Spectrum allows us to demonstrate the possible bonds between HA and the metal, which are concentrated around the metal-oxygen groups of hyaluronate (a monomer unit that interacts with metals) and the carbonyl of the glucuronic acid group, which displaces the band. Furthermore, the presence of bonds between clusters of atoms of the same metal is observed [38, 39]. Table 2 summarizes the far IR bands of different nanoclusters involved.

3.4. Thermogravimetric Analysis (TGA). The main objective of TGA is to demonstrate the stability of metallic solids in response to temperature changes. From the obtained scans, it is possible to determine the temperature of decomposition of a polymer and a polymer doped with MNPs and to obtain

information on the percentage of mass loss of a sample, which can be used to determine which sample is more stable.

From the results in Table 3, it can be concluded that the average experimental decomposition temperature of the polymer supporting MNPs is 218.73°C . On the other hand, the decomposition temperature of pure HA is around 220°C (shown in Figure 5). Similar result occurs with chitosan; a decrease in decomposition temperature is observed between pure and MNPs-doped polymer [40]. The observed values of percentage of mass loss are, with some degree of similarity, directly related to the loss in mass (in mg) undergone by the solid samples. The residual mass percentage and temperature refer to the peak temperature at which mass is no longer lost as a result of increasing the temperature of the sample. The residual mass is between 23 and 27% for doped HA, while the pure HA exhibit a residual mass of 36,93%.

3.5. Bacteriological Assays. The results of the qualitative analysis are shown in Table 4. In general, the highest activity was found in gels containing NPs of copper and silver, with both displaying activity against the four tested strains of bacteria.

Comparison of the results with the literature is challenging, mainly due to differences in the methodologies used and the polymer used as a support. Most of the work in this field uses chitosan as the polymer support. Chitosan is known to have antibacterial properties significantly different from those of HA, which has weak or no antibacterial activity depending on the tested microorganism [41]. Our results

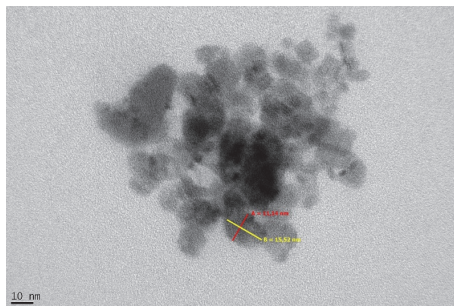


FIGURE 2: Copper cluster supported in HA. It is possible to observe single particles with average particle size of 13.33 nm.

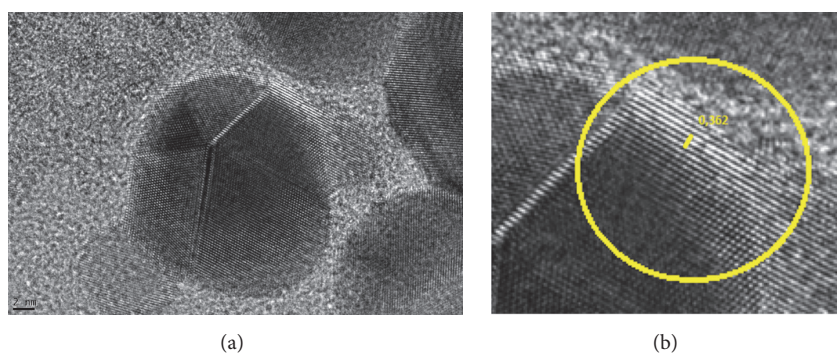


FIGURE 3: Two high-resolution micrographs of HA-AgPd (a). The interplanar distance is observed in (b).

show that strong antibacterial activity is achieved with NPs of copper and silver, while low activity is observed with gold and silver palladium. These results are consistent with the literature, which indicates that metals such as gold and platinum have low antibacterial activity [8]. Anisha et al. (2013) [42] used a matrix of chitosan/hyaluronic acid as support for silver nanoparticles and determined the antibacterial activity of the compound. They demonstrated that the mix was active against all the bacteria tested, including methicillin-resistant *Staphylococcus aureus* strains. These results are comparable with the result of this work. One study reports MIC values comparable to those obtained in this study for silver and copper, with values of >0.395 mg/ml and 0.048 mg/ml, respectively, against *E. coli* and 0.198–0.395 and 0.048 mg/ml, respectively, against *S. aureus*, values that are similar to the inhibition of bacteria growing on the films. This study shows a MIC for copper that is the same (0.048 mg/ml) against all the strains tested, which is less than half the value reported by Ruparelia et al. [8] for this metal; in the case of silver, the values are similar.

3.6. Bioassays in Rats. The toxicity tests were conducted in laboratory rats weighing 100 g that were separated into two groups, one experimental and the other a control, whose evaluation was performed after the solution was injected intraperitoneally at days 1 and 7. A blood sample of 0.5 ml was taken to determine the hepatic biochemical parameters, including ALT, GGT, bilirubin, and albumin. After euthanasia, all hepatic and renal tissue was extracted for histopathologic analysis. This analysis was used to determine if the solutions of the MNPs supported on HA were sufficiently nontoxic to permit their use.

We find that the levels of ALT, GGT, and bilirubin measured at 14 days after intraperitoneal injection were normal in the group of animals injected at days 1 and 7 with 0.5 ml of a 0.5% solution of Au, Ag, and Cu or AgPd-NPs supported by HA (see Figure 6).

There were no changes associated with hepatotoxicity after 14 days in all sampled groups since the liver functionality-specific enzymes and the levels of albumin and bilirubin synthesized were found to be within normal ranges. There were also no signs associated with damage to the hepatic or renal tissue in samples taken 14 days later after the euthanasia of each animal. With regard to the pathology, macroscopic analysis indicated that no mice belonging to the group injected with metals and HA had adhesions in their abdominal cavity. This finding leads to the conclusion that solution of MNPs supported in HA does not present high levels of toxicity; in fact, toxicity levels were within the normal ranges for continuous exposure.

4. Conclusions

Analyses were performed on metallic NPs of gold, silver, copper, and silver palladium (alloy) supported in the biopolymer HA, which, despite not having antibacterial properties, acts as a favorable stabilizer of MNPs, allowing them to exhibit their unique properties, particularly their antibacterial abilities. These properties were evident from the first characterization analyses, such as HRTEM analysis, which showed MNPs located clearly in a spatial arrangement of atoms in the more stable (111) plane, as shown in Figure 2. Furthermore, the analyses allowed us to determine that the size of the MNPs

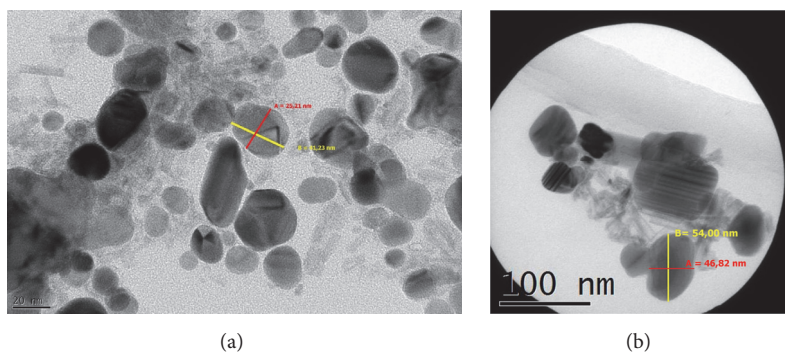


FIGURE 4: (a) Micrograph of HA-AgPd, average particle size of 33.22 nm. (b) Micrograph of HA-Ag, average particle size of 50.41 nm.

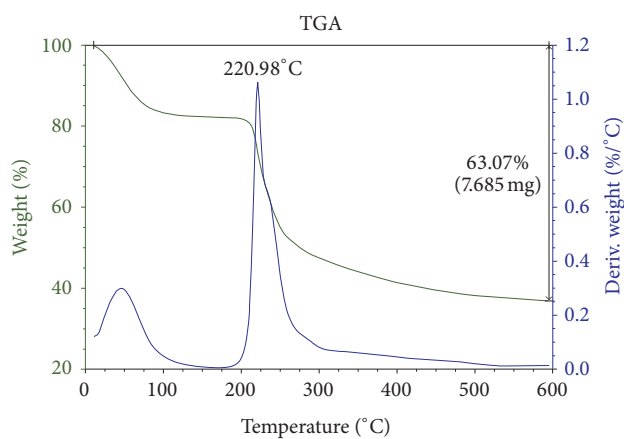


FIGURE 5: Thermogram of pure hyaluronic acid showing a decomposition temperature of 220°C.

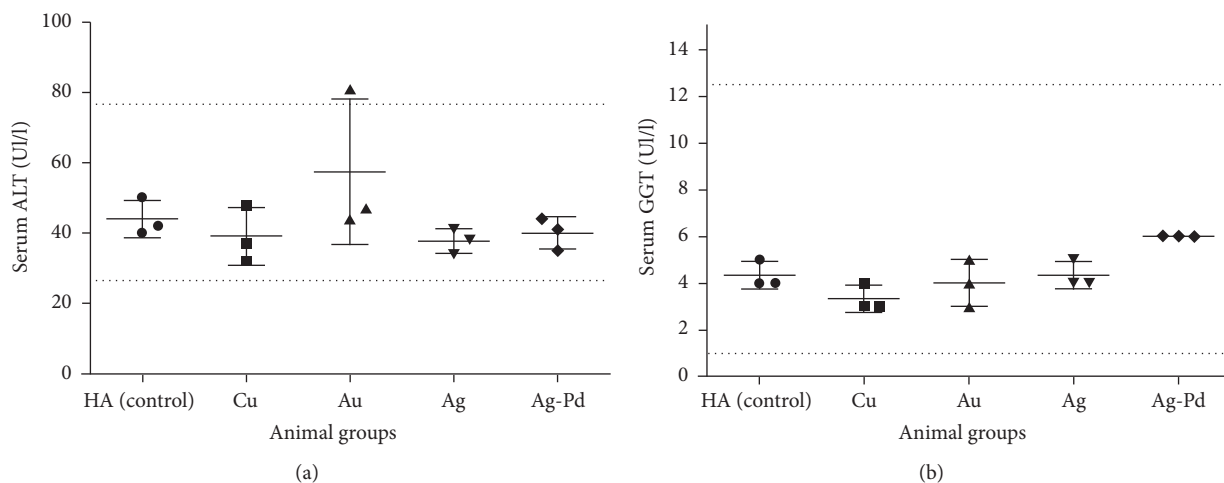


FIGURE 6: (a) Evaluation of ALT after the intraperitoneal injections at days 1 and 7 of 0.5 ml of a 0.5% solution of Au, Ag, Cu, or AgPd-NPs supported on HA. The enzymatic levels are close to the normal reference levels for this species. Dotted lines represent the normal reference range. (b) Evaluation of GGT after the intraperitoneal injection at days 1 and 7 of 0.5 ml of a 0.5% solution of Au, Ag, Cu, or AgPd supported by HA. The enzymatic levels are close to the normal reference level for the species. Dotted lines represent the normal reference range.

was within the range of 10–50 nm and that differences in sizes existed between each of the different types of NPs, with AgNPs being the largest and CuNPs the smallest. We also characterized the presence of deformities and imperfections, such as nanotwins and strips of thickness in the AgNPs,

attributable primarily to incomplete synthesis. Medium and far FT-IR analysis was used to determine that the 3428 cm^{-1} bands correspond to the vibration of the stretching of the $-\text{OH}$ bond. The band at 2928 cm^{-1} is due to the stretching vibration of the $-\text{CH}$ bond. A peak at 1727 cm^{-1} represents

absorption in the C=O double bond stretching band, among others. In the far IR, there were possible bonding interactions between HA and metal, which would be focused in the –Metal-O– groups of hyaluronate (a monomeric unit that interacts with metals) and the carbonyl group of glucuronic acid; these interactions cause the formation of bands. Furthermore, the presence of bonds between clusters of atoms of the same metal with values between 120 and 190 cm^{-1} was observed. TGA analysis determined that the temperature of decomposition for the system exhibits several peaks from 217 to 220°C, values consistent with the literature, which indicates that HA macromolecules decompose at approximately 220°C.

From these analyses, it is concluded that the use of HA as a stabilizing support offers the safety and capacity needed for its use in the preparation of medical dressings with MNPs. Although HA is being compared to other well-known biopolymers (e.g., chitosan) that have significant antibacterial properties, a greater likelihood of allergic reactions is ascribed to these polymers. Neutral HA, however, has no adverse reactions, is fully biocompatible, and is involved in tissue repair process. In addition to this factor, with the proven antibacterial properties of MNPs, we can fully recommend the use of these components for the development of an effective medical dressing. While the course of this work concluded with preclinical trials in animals (mice), it would be appropriate to continue this investigation with clinical trials of patients suffering from skin wounds and diseases.

Conflicts of Interest

The authors declare no competing financial interest.

Acknowledgments

The authors are grateful for the financial support of Conicyt, Fondecyt (Grant no. 1140025), and acknowledge Quitoquímica Ltda. for the use of their laboratory facilities.

References

- [1] N. Scott and H. Chen, "Nanoscale science and engineering for agriculture and food systems," *Industrial Biotechnology*, vol. 9, no. 1, pp. 17–18, 2013.
- [2] C. A. Mirkin, "The beginning of a small revolution," *Small*, vol. 1, no. 1, pp. 14–16, 2005.
- [3] J. M. Campelo, D. Luna, R. Luque, J. M. Marinas, and A. A. Romero, "Sustainable preparation of supported metal nanoparticles and their applications in catalysis," *ChemSusChem*, vol. 2, no. 1, pp. 18–45, 2009.
- [4] DL. Feldheim and CA. Foss, Eds., *Metal Nanoparticles: Synthesis, Characterization, and Applications*, CRC Press, and Applications, 2002.
- [5] R. A. Freitas Jr., "What is nanomedicine?" *Nanomedicine: Nanotechnology, Biology and Medicine*, vol. 1, no. 1, pp. 2–9, 2005.
- [6] E. Sadauskas, H. Wallin, M. Stoltenberg et al., "Kupffer cells are central in the removal of nanoparticles from the organism," *Particle and Fibre Toxicology*, vol. 4, article no. 10, 2007.
- [7] A. Panáček, L. Kvítek, and R. Prucek, "Silver colloid nanoparticles: synthesis, characterization, and their antibacterial activity," *The Journal of Physical Chemistry B*, vol. 110, no. 33, pp. 16248–16253, 2006.
- [8] J. P. Ruparelia, A. K. Chatterjee, S. P. Duttagupta, and S. Mukherji, "Strain specificity in antimicrobial activity of silver and copper nanoparticles," *Acta Biomaterialia*, vol. 4, no. 3, pp. 707–716, 2008.
- [9] W.-R. Li, X.-B. Xie, Q.-S. Shi, H.-Y. Zeng, Y.-S. Ou-Yang, and Y.-B. Chen, "Antibacterial activity and mechanism of silver nanoparticles on *Escherichia coli*," *Applied Microbiology and Biotechnology*, vol. 85, no. 4, pp. 1115–1122, 2010.
- [10] V. Dhanalakshmi, T. R. Nimal, M. Sabitha, R. Biswas, and R. Jayakumar, "Skin and muscle permeating antibacterial nanoparticles for treating *Staphylococcus aureus* infected wounds," *Journal of Biomedical Materials Research Part B: Applied Biomaterials*, vol. 104, no. 4, pp. 797–807, 2016.
- [11] E. E. Connor, J. Mwamuka, A. Gole, C. J. Murphy, and M. D. Wyatt, "Gold nanoparticles are taken up by human cells but do not cause acute cytotoxicity," *Small*, vol. 1, no. 3, pp. 325–327, 2005.
- [12] R. Shukla, V. Bansal, M. Chaudhary, A. Basu, R. R. Bhonde, and M. Sastry, "Biocompatibility of gold nanoparticles and their endocytotic fate inside the cellular compartment: a microscopic overview," *Langmuir*, vol. 21, no. 23, pp. 10644–10654, 2005.
- [13] P. Prema, P. A. Iniya, and G. Immanuel, "Microbial mediated synthesis, characterization, antibacterial and synergistic effect of gold nanoparticles using *Klebsiella pneumoniae* (MTCC-4030)," *RSC Advances*, vol. 6, no. 6, pp. 4601–4607, 2016.
- [14] J. Penders, M. Stolzoff, D. J. Hickey, M. Andersson, and T. J. Webster, "Shape-dependent antibacterial effects of non-cytotoxic gold nanoparticles," *International Journal of Nanomedicine*, vol. 12, pp. 2457–2468, 2017.
- [15] A. Avalos, AI. Haza, P. Morales, and P. Universidad, "Silver nanoparticles: applications and toxic risks to human health and the environment," *Revista Complutense de Ciencias Veterinarias*, vol. 7, p. 23, 2013, <http://revistas.ucm.es/index.php/RCCV/article/viewFile/43408/41203>.
- [16] R. Kohen and A. Nyska, "Oxidation of biological systems: oxidative stress phenomena, antioxidants, redox reactions, and methods for their quantification," *Toxicologic Pathology*, vol. 30, no. 6, pp. 620–650, 2002.
- [17] M. Ahamed and M. K. J. Siddiqui, "Low level lead exposure and oxidative stress: current opinions," *Clinica Chimica Acta*, vol. 383, no. 1–2, pp. 57–64, 2007.
- [18] M. J. Piao, K. A. Kang, I. K. Lee et al., "Silver nanoparticles induce oxidative cell damage in human liver cells through inhibition of reduced glutathione and induction of mitochondria-involved apoptosis," *Toxicology Letters*, vol. 201, no. 1, pp. 92–100, 2011.
- [19] A. Lin, "Activation of the JNK signaling pathway: breaking the brake on apoptosis," *BioEssays*, vol. 25, no. 1, pp. 17–24, 2003.
- [20] C. Carlson, S. M. Hussein, A. M. Schrand et al., "Unique cellular interaction of silver nanoparticles: size-dependent generation of reactive oxygen species," *The Journal of Physical Chemistry B*, vol. 112, no. 43, pp. 13608–13619, 2008.
- [21] N. Miura and Y. Shinohara, "Cytotoxic effect and apoptosis induction by silver nanoparticles in HeLa cells," *Biochemical and Biophysical Research Communications*, vol. 390, no. 3, pp. 733–737, 2009.
- [22] N. Hachicho, P. Hoffmann, K. Ahlert, and H. J. Heipieper, "Effect of silver nanoparticles and silver ions on growth and adaptive response mechanisms of *Pseudomonas putida* mt-2," *FEMS Microbiology Letters*, vol. 355, no. 1, pp. 71–77, 2014.

- [23] C. Beer, R. Foldbjerg, Y. Hayashi, D. S. Sutherland, and H. Autrup, "Toxicity of silver nanoparticles-Nanoparticle or silver ion?" *Toxicology Letters*, vol. 208, no. 3, pp. 286–292, 2012.
- [24] C. Gonnelli, F. Galardi, and R. Gabbrielli, "Nickel and copper tolerance and toxicity in three Tuscan populations of *Silene paradoxa*," *Physiologia Plantarum*, vol. 113, no. 4, pp. 507–514, 2001.
- [25] T. C. Hoang and S. J. Klaine, "Influence of organism age on metal toxicity to *Daphnia magna*," *Environmental Toxicology and Chemistry*, vol. 26, no. 6, pp. 1198–1204, 2007.
- [26] M. Valodkar, P. S. Rathore, R. N. Jadeja, M. Thounaojam, R. V. Devkar, and S. Thakore, "Cytotoxicity evaluation and antimicrobial studies of starch capped water soluble copper nanoparticles," *Journal of Hazardous Materials*, vol. 201–202, pp. 244–249, 2012.
- [27] C. Cruzat Contreras, O. Peña, M. F. Meléndrez, J. Díaz-Visurraga, and G. Cárdenas, "Synthesis, characterization and properties of magnetic colloids supported on chitosan," *Colloid and Polymer Science*, vol. 289, no. 1, pp. 21–31, 2011.
- [28] C. Raymond Rowe, P. J. Sheskey, and M. E. Quinn, *Handbook of Pharmaceutical Excipients*, Pharmaceutical Press and American Pharmacists Association, Washington, USA, 6th edition, 2009.
- [29] K. Imai, T. Shirai, M. Akiyama et al., "Effects on ES cell differentiation on the corroded Surface of four silver alloys for dental use," *Journal of Oral Tissue Engineering*, vol. 14, pp. 34–40, 2016.
- [30] A. Milheiro, J. Muris, C. J. Kleverlaan, and A. J. Feilzer, "Influence of shape and finishing on the corrosion of palladium-based dental alloys," *The Journal of Advanced Prosthodontics*, vol. 7, no. 1, pp. 56–61, 2015.
- [31] J. C. Wataha, "Biocompatibility of dental casting alloys: a review," *Journal of Prosthetic Dentistry*, vol. 83, no. 2, pp. 223–234, 2000.
- [32] W. Y. J. Chen and G. Abatangelo, "Functions of hyaluronan in wound repair," *Wound Repair and Regeneration*, vol. 7, no. 2, pp. 79–89, 1999.
- [33] G. Weindl, M. Schaller, M. Schäfer-Korting, and H. C. Korting, "Hyaluronic acid in the treatment and prevention of skin diseases: molecular biological, pharmaceutical and clinical aspects," *Skin Pharmacology and Physiology*, vol. 17, no. 5, pp. 207–213, 2004.
- [34] M. Rai, A. Yadav, and A. Gade, "Silver nanoparticles as a new generation of antimicrobials," *Biotechnology Advances*, vol. 27, no. 1, pp. 76–83, 2009.
- [35] C. Cruzat, *Synthesis and characterization of Chitosan-supported metal nanoparticles. Thesis submitted to the University of Concepción in partial fulfillment of the requirements to qualify for the degree of Ph.D. in chemistry [Ph.D. thesis]*, Chile, 2010.
- [36] G. Cárdenas-Triviño, "Chemical Reactions at Nanometal Particles," *Journal of the Chilean Chemical Society*, vol. 50, no. 3, 2005.
- [37] G. Cárdenas Triviño, O. Godoy Guzmán, and G. Contreras, "Dysprosium Colloids Prepared in Polar Organic Solvents," *Journal of the Chilean Chemical Society*, vol. 54, no. 1, 2009.
- [38] G. Kliche and Z. V. Popovic, "Far-infrared spectroscopic investigations on CuO," *Physical Review B: Condensed Matter and Materials Physics*, vol. 42, no. 16, pp. 10060–10066, 1990.
- [39] M. R. H. Siddiqui, S. F. Adil, M. E. Assal, R. Ali, and A. Al-Warthan, "Synthesis and characterization of silver oxide and silver chloride nanoparticles with high thermal stability," *Asian Journal of Chemistry*, vol. 25, no. 6, pp. 3405–3409, 2013.
- [40] M. Heuser and G. Cárdenas, "Chitosan-copper paint types as antifouling," *Journal of the Chilean Chemical Society*, vol. 59, no. 2, pp. 2415–2419, 2014.
- [41] M. Bračić, L. Pérez, R. I. Martínez-Pardo et al., "A novel synergistic formulation between a cationic surfactant from lysine and hyaluronic acid as an antimicrobial coating for advanced cellulose materials," *Cellulose*, vol. 21, no. 4, pp. 2647–2663, 2014.
- [42] B. S. Anisha, R. Biswas, K. P. Chennazhi, and R. Jayakumar, "Chitosan-hyaluronic acid/nano silver composite sponges for drug resistant bacteria infected diabetic wounds," *International Journal of Biological Macromolecules*, vol. 62, pp. 310–320, 2013.

Research Article

Comparative Study on Properties of Polylactic Acid Nanocomposites with Cellulose and Chitin Nanofibers Extracted from Different Raw Materials

Jingjing Li,¹ Jian Li,¹ Dejun Feng,¹ Jingfeng Zhao,¹ Jingrong Sun,¹ and Dagang Li²

¹College of Forestry, Northwest A&F University, Yangling, China

²College of Materials Science and Engineering, Nanjing Forestry University, Nanjing, China

Correspondence should be addressed to Dagang Li; 396420748@qq.com

Received 15 May 2017; Revised 17 September 2017; Accepted 16 October 2017; Published 20 November 2017

Academic Editor: Mangala Joshi

Copyright © 2017 Jingjing Li et al. This is an open access article distributed under the Creative Commons Attribution License, which permits unrestricted use, distribution, and reproduction in any medium, provided the original work is properly cited.

Polylactic acid (PLA) was reinforced with ultralong cellulose and chitin nanofibers extracted from four raw materials by extrusion. The mechanical, rheological, thermal, and viscoelastic performances of four nanocomposites were comparatively studied in detail. The results showed that fibrillation of poplar was much easier than that of cotton, and fibrillation of crab shell was relatively hard as compared to prawn shell. The poplar CNFs/PLA composite exhibited the best mechanical properties among four nanocomposites due to the highest aspect ratio of nanofibers, while both the cotton CNFs/PLA composite and the crab shell CHNFs/PLA composite had low mechanical strength due to the relatively low aspect ratio. FE-SEM images showed that the ultralong nanofibers were uniformly dispersed in PLA matrix for all four samples with the water preblending method. The CTE values of the nanocomposites with 40 wt% nanofibers extracted from poplar, cotton, crab shell, and prawn shell were $69.5 \times 10^{-6} \text{ K}^{-1}$, $79.6 \times 10^{-6} \text{ K}^{-1}$, $77.2 \times 10^{-6} \text{ K}^{-1}$, and $75.3 \times 10^{-6} \text{ K}^{-1}$, respectively. All the results indicated that the aspect ratio of the nanofibers has a great influence on the performance of the composites, irrespective of the composites prepared by cellulose or chitin.

1. Introduction

Polylactic acid (PLA) is a renewable, biocompatible, and biodegradable polymer and it is one of the most widely used bioplastics [1]. Due to the excellent modulus and tensile strength and high transparency comparable to petroleum-based polymers, PLA is a good alternative for the conventional synthetic polymers in different applications, especially in packaging [2]. Nevertheless, the properties of PLA such as thermal stability and impact toughness are inferior to those of conventional polymers used for thermoplastic applications [3]. To overcome the mentioned drawbacks and broaden the application areas of PLA, considerable researches have been carried out to develop and study modified PLA, PLA-based copolymers, and PLA-based composites [4].

Cellulose nanofibers (CNFs) and chitin nanofibers (CHNFs) have attracted the attention of researches as additives in the green nanocomposites field because they are

biodegradable and renewable polymers with good mechanical properties. CNFs have highly ordered crystalline regions alternating with disordered amorphous domains [5]. The crystalline regions of CNFs have a high Young's modulus of 138 GPa [6] and a very low thermal expansion coefficient (10^{-7} K^{-1} in the longitudinal direction) [7]. As the second most abundant natural polysaccharide after cellulose, chitin is the major structural component of cell walls in fungi and yeast, the exoskeleton of arthropods, and mollusk shells [8]. It is reported that the longitudinal modulus and the transverse modulus of chitin nanocrystals are 150 GPa and 15 GPa, respectively [9]. Because of these distinctive properties, CNFs/CHNFs have been used in a wide range of applications such as optically transparent materials, reinforced polymer nanocomposites, biomimetic foams, multifunctional fibers, templates for chiral nematic mesoporous materials, and conductive materials [10].

Cellulose nanomaterials have been extensively used as an additive to improve the thermal, mechanical, and barrier properties of PLA [11–17]. However, most of the literature has focused on the NCC or MCC (microcrystal cellulose) reinforced PLA composites. There is a lack of study on the CNFs with high aspect ratio reinforced PLA composites due to the dispersion problem of the ultralong CNFs. In addition, chitin nanofibers are mainly used in other polymers, such as poly (caprolactone), chitosan, PVA, PMMA, and starch [14], while the research on chitin nanofibers reinforced PLA is very rare [18].

Although CNFs and CHNFs have great potential as reinforcements, the uniform dispersion in polymer matrix is the major challenge. It is well known that materials in nanosize have a strong tendency to aggregate. In addition, the strong hydrogen bonds form when cellulose and chitin are dried, leading to the aggregation problem. To overcome the dispersion and compatibility difficulties, cellulose/chitin nanofibers have been subjected to physical treatments and chemical modification [19]. However, the mechanical properties of the prepared nanocomposites are not remarkably improved due to the damaged molecular structure of nanofibers by chemical modification.

Until now, the preparation of CNFs/CHNFs reinforced polymer composites is mainly focused on the methods of solvent casting, freeze-drying, and electrospinning. The development of more flexible and viable processing techniques for industrial applications is needed to promote the commercialization of nanofibers-based composites. Among the processing techniques, the melt-compounding process is the most potential technique, since the final product prepared by this technique can be easily shaped [13]. However, there are only very few studies on the nanocomposite prepared by the melt-compounding technique, especially in the case of chitin nanofibers [20, 21].

In this study, four different CNFs/CHNFs reinforced PLA composites were prepared using the extrusion process. The CNFs/CHNFs were extracted from the raw materials of poplar flour, cotton, crab shell, and prawn shell. All the isolated CNFs/CHNFs showed network structure and high aspect ratio. The effects of fiber morphology on the mechanical, thermal, and viscoelastic properties of the prepared nanocomposites were comparatively investigated to evaluate the reinforcing effect of CNFs and CHNFs. To solve the dispersion problem of ultralong CNFs/CHNFs in PLA matrix, the PLA powders were premixed with the CNFs/CHNFs water slurry followed by freeze-drying before the nanocomposites were extruded. This process is a time-saving and environmentally friendly method due to the absence of chemical reagent.

2. Materials and Methods

2.1. Materials. Polylactic acid (PLA), NatureWorks TM 4032D, was supplied by Nanjing Jufeng Advanced Materials Co., Ltd. (Nanjing, China). The glass transition temperature (T_g) and melting point (T_m) were 55°C and 180°C, respectively. The melt flow index (MFI) was 6 g/10 min (190°C,

2.16 kg). The poplar flour with the size of 60–80 mesh was obtained from Nanjing Jufeng Advanced Materials Co., Ltd. (Nanjing, China). Absorbent cotton, medical grade, was purchased from Beijing Tianheng Bohao Medical Equipment Co., Ltd. (Beijing, China). Dried crab shell powder and prawn shell powder were obtained from Golden Shell Biochemical Co., Ltd. (Zhejiang, China). The other chemicals and distilled water were purchased from Nanjing Chemical Reagent Company and used without further purification in this study (Nanjing, China).

2.2. Preparation of Poplar CNFs. Based on our previously reported methods [22], the preparation procedure of poplar CNFs was mainly divided into chemical pretreatment and grinding nanofibrillation. After chemical treatment, the water slurry with 1 wt% CNFs was passed through a grinder (MKCA6-2, Masuko Sangyo Co., Japan) for 20 times with the grinding stone at 1800 rpm.

2.3. Preparation of Cotton CNFs. The preparation of cotton CNFs was conducted according to our previously reported methods [23]. The extraction process of cotton CNFs was simpler than that of poplar CNFs due to higher cellulose content in cotton.

2.4. Preparation of Crab/Prawn CHNFs. Crab/prawn shells are composed of chitin and some other constituents such as proteins, lipids, calcium carbonate, and pigments. The chemical treatment of crab/prawn shell was conducted according to our previously reported methods [24]. Finally, a water suspension with 1 wt% CHNFs was passed through the grinder for 20 times with the grinding stone at 1800 rpm.

2.5. Preparation of Nanofibers/PLA Composites. Before the extrusion process, different contents of PLA powders (60–80 mesh) were added to the 1 wt% CNFs/CHNFs water slurry and were continuously stirred by a magnetic stirrer at 75°C for 1 h. After the water preblending process, the mixture slurry was dehydrated by vacuum filtration using a Büchner funnel and then was freeze-dried. Subsequently, the nanofibers/PLA mixture was fully broken using a blender and fed into a HAAKE MiniLab (HAAKE MiniLab II, Thermo Fisher Scientific, Germany) for compounding. The HAAKE MiniLab is a small twin screw extruder for laboratory use. The samples were extruded through a rectangular die with the sectional dimension of 3.5 × 1 mm². The samples were crushed into powder by a blender and then hot-pressed at 170°C for 5 min with a press vulcanizer.

2.6. Characterization

Cellulose/Chitin Nanofibers

FE-SEM. The morphologies of four different nanofibers were observed using a field emission scanning electron microscope (HITACHI S-4860, HITACHI, Japan). Prior to FE-SEM observations, the samples were kept in a vacuum oven at 30°C overnight and then coated with gold for 30–60 s to avoid

charging. The acceleration voltage was 3 kV and the coating current was 10 mA. The width of nanofibers was measured using a microscope image analysis system, Image-Pro Plus.

CNFs/CHNFs Reinforced PLA Composites

Rheological Properties. The nanofibers/PLA mixture was fed into the HAAKE MiniLab for capillary rheological test. The extrusion temperature was set at 180°C. The rotating screw speed was set from 10 rpm to 100 rpm. After the rheological measurement, the mixture was extruded through the die. The rotating screw speed was fixed at 40 rpm in the extrusion process.

FE-SEM. The fracture surfaces of four different nanofibers/PLA composites were observed by a FE-SEM. The nanocomposite samples were frozen in liquid nitrogen and then quickly broken.

Mechanical Properties. The tensile and flexural properties of different nanofibers/PLA composites were tested using a universal materials testing machine (AG-10TA, Shimadzu, Japan). The tensile gauge length was fixed at 25 mm at a tensile speed of 1 mm/min. Each sample was prepared with a dumbbell shape and dimensions of 50 mm length, 3 mm width, and 3 mm thickness. The flexural properties were tested in bending mode with the span of 40 mm and the cross head speed of 1 mm/min following ASTM-D 790-2010. The results represent the average value of six specimens for each formulation.

The impact strength of different nanofibers/PLA composites was measured by an Izod impact test machine (QJBCX, Shanghai Qingji Instrumentation Technology Co., China) according to ASTM D256-2010. Moreover, at least four replications were tested for each measurement.

Coefficient of Thermal Expansion (CTE). The CTE values of different nanofibers/PLA composites were measured using a thermal mechanical analyzer (TMA 401F1, NETZSCH, Germany) to investigate the change in length with the increase of temperature. The samples were tested in tension mode with a static load of 1 N and the dimension of 15 mm × 5 mm × 1 mm. The tests were performed over the temperature range from -20 to 110°C at a heating rate of 5°C/min.

Dynamic Mechanical Analysis (DMA). Dynamic mechanical analysis of different nanofibers/PLA composites was performed on a dynamic mechanical analyzer (DMA 242C, NETZSCH, Germany). Prior to the test, the samples were cut into strips with dimension of 32 mm × 3.5 mm × 1 mm. The tests were carried out in a dual cantilever mode at a heating rate of 3°C/min over the temperature range from -20 to 110°C.

3. Results and Discussion

3.1. Cellulose/Chitin Nanofibers

FE-SEM. The SEM images of poplar CNFs, cotton CNFs, crab shell CHNFs, and prawn shell CHNFs after the grinding treatment are shown in Figure 1. A classical web-like network

structure is observed in all the nanofibers. Moreover, a very long entangled cellulosic filament can be found. The fibers of poplar CNFs in Figure 1(a) are highly uniform even over an extensive area, with the average width of approximately 30–80 nm. The SEM observation also reveals that the length of most obtained poplar CNFs is a few microns. Hence the aspect ratio of poplar CNFs is up to 500–2000. Compared to poplar CNFs, the morphology of cotton CNFs is very different (Figure 1(b)). Although long and single-cellulose nanofiber can be clearly observed, many large fiber bundles are still present. Therefore, the grinder treatment is unable to fibrillate the cotton fibers into nanofibers with a uniform width because of the remaining strong hydrogen bonding within the adjacent cotton cellulose after the chemical purification [25]. Figure 1(c) displays the morphology of crab shell CHNFs after removal of the protein and mineral matrix components. It can be noticed that crab shell could not be uniformly nanofibrillated as compared to the poplar CNFs. The widths of the fibers derived from crab shell are in a range from 120 to 200 nm. The thick fibers corresponding to bundles of nanofibers of 10–20 nm in width were not successfully fibrillated by the grinding treatment. Compared to crab shell, the CHNFs extracted from prawn shell using the same treatment are relatively uniform over an extensive area, and the width of the nanofibers is 80–120 nm (Figure 1(d)). Fibrillation of the prawn shell was relatively easy as compared to crab shell due to the differences in the cuticle structure and fiber thickness. Prawn is primarily made up of a fine exocuticle, while crab shell is mainly composed of the endocuticle, which has a much coarser matrix structure with a thicker fiber diameter than exocuticle [26].

Diameter Distribution. Figure 2 presents the diameter distribution of four different nanofibers after the grinding treatment. In Figure 2(a), the percentage of the poplar CNFs with the width of 30–80 nm is about 65%. The percentage of the cotton CNFs with the width of 120–500 nm is approximately 80% (Figure 2(b)). These results show that cotton CNFs have much thicker fiber bundles as compared to the poplar CNFs. It is very difficult for cotton to fibrillate into nanofibers with a uniform width by the only grinding treatment. Other mechanical processes are necessary to break the strong hydrogen bonding and individualize cotton fibers into much finer nanofibers. For the crab shell CHNFs, the percentages of nanofibers with widths of 120–200 nm and 80–120 nm are about 50% and 24%, respectively (Figure 2(c)). In contrast, the percentages of prawn shell CHNFs with the widths of 120–200 nm and 80–120 nm are 23% and 52%, respectively. The data suggests that fibrillation of prawn shell is easier than that of crab shell.

3.2. CNFs/CHNFs Reinforced PLA Composites

Rheological Properties. Figure 3 presents the capillary rheological curves in terms of the viscosity and shear stress of four nanofibers (40 wt%)/PLA composite melts as functions of shear rate. All samples show a shear-thinning behavior without a plateau region and a less frequency-dependency behavior, especially at lower frequencies. The shear-thinning

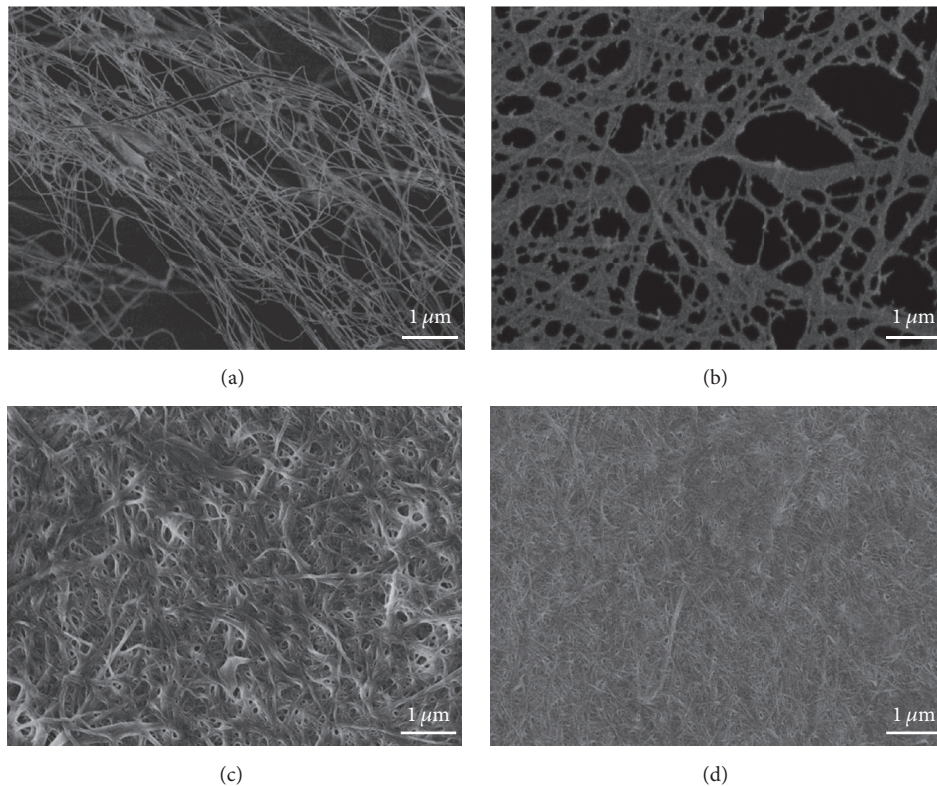


FIGURE 1: FE-SEM micrographs of the nanofibers extracted from original (a) poplar, (b) cotton, (c) crab shell, and (d) prawn shell.

behavior can be attributed to disentanglement and orientation of nanofibers and PLA chains in the flow direction reducing the viscous resistance. In addition, the viscosity and shear stress of four composites are much higher than those of the pure PLA, suggesting a network formation with the addition of cellulose/chitin nanofibers. Nanofibers will disturb the normal flow of the matrix melt and hinder the mobility of chain segments of polymers. It can also be noticed that the viscosity and shear stress of the poplar CNFs/PLA composite are highest among four samples, and the corresponding values of the cotton/PLA composite are the lowest. According to the SEM images in Figure 1, poplar CNFs have higher aspect ratio, more refined structure, and larger specific surface area than other nanofibers extracted from cotton and crab/prawn shell. Consequently, much stronger CNF/PLA interactions and restriction to PLA chain mobility are generated, leading to the relatively high viscosity and shear stress. It was reported that, in addition to the interfacial interactions through molecular entanglement and mechanical interlocking between nanofibers and the polymer matrix [27], CNFs may have electrostatic attractions with PLA as well [28, 29]. The cotton/crab shell nanofibers are more easily aligned and distributed along the direction of flow due to the relatively low aspect ratio. Hence, the probability of fiber/fiber collisions is much less than that of the poplar CNFs composite, leading to the lower viscosity and shear stress of the nanocomposites.

Mechanical Properties. Generally, mechanical properties are the key factors in determining the reinforcing effect of nanofibers for PLA. The effect of nanofiber content on the tensile, flexural, and impact properties of four nanofibers/PLA composites is presented in Figure 4. The tensile strength of PLA is increased slightly with the addition of 10 wt% nanofibers due to the high stiffness of the nanofiber itself. As shown in Figure 4(a), the tensile strength of nanocomposites increases with increasing nanofiber content up to 30 wt%. However, it can be noticed that the tensile strength of the 40 wt% nanofiber/PLA composite is lower than that of the 30 wt% nanofiber/PLA composite. The decrease in the tensile strength indicates that nanofibers' aggregation and poor dispersion will occur in the composite with high content of nanofibers. Different from the tensile strength, Young's modulus, bending strength (MOR), bending modulus (MOE), and impact toughness of four nanocomposites increase rapidly with increasing the loading of nanofibers. The dramatic improvement can be attributed to the excellent dispersion and improved interfacial interaction between nanofibers and PLA chains. Excellent dispersion of nanofibers leads to the formation of a network structure, which leads to significant improvement in mechanical strength. However, when the content of nanofiber is fixed, four composites show different mechanical properties. The poplar CNFs/PLA composite exhibits the best mechanical properties and the prawn shell CHNFs/PLA composite shows the second highest

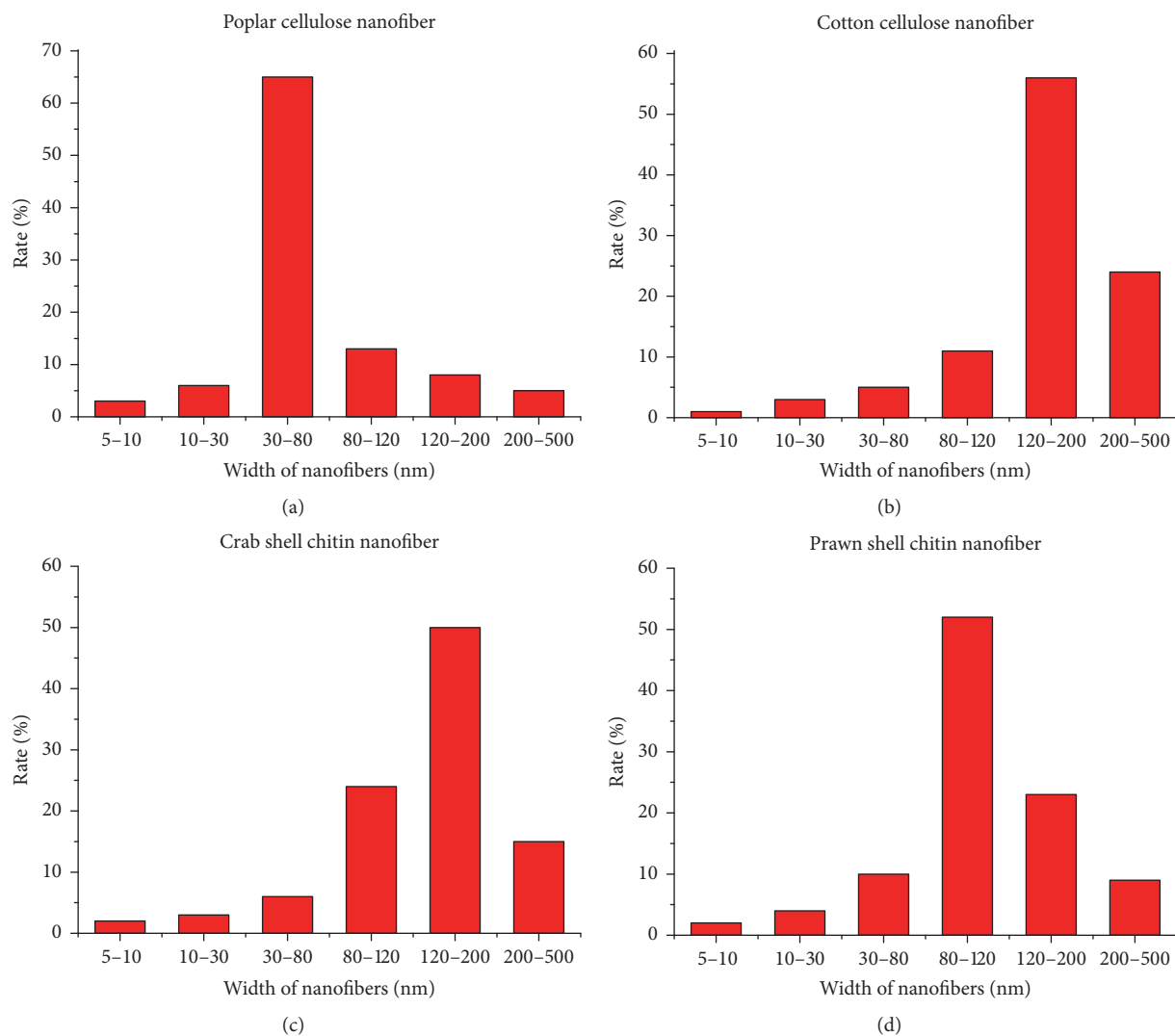


FIGURE 2: Diameter distribution of the nanofibers extracted from original (a) poplar, (b) cotton, (c) crab shell, and (d) prawn shell.

mechanical strength among four nanocomposites. The mechanical properties of cotton CNFs/PLA composite and the crab shell CHNFs/PLA composite are the worst. The excellent mechanical performance of the poplar CNFs/PLA composite is ascribed to the highest aspect ratio of poplar CNFs. So it can be concluded that the aspect ratio of nanofibers is the main reason for different mechanical properties of the nanocomposites, whether raw material is cellulose or chitin. Rowell and coworkers reported that a high aspect ratio is very important in fiber reinforced composites, as it indicates potential strength properties [30]. Stark and Rowlands reported that aspect ratio, rather than particle size, has the greatest effect on strength and stiffness [31]. The mechanical properties of the fiber/polymer composites are determined by several factors, such as nature of the reinforcement fiber, fiber aspect ratio, fiber-matrix interfacial adhesion, and also the fiber orientation in the composites [32]. Except for the factor of fiber aspect ratio, the interfacial adhesion and fiber dispersion are also very important factors

to influence the reinforcing effect of fibers. The improvements of mechanical properties demonstrate that homogeneous dispersion of CNFs/CHNFs could be achieved by using the water preblending method. Furthermore, the excellent impact toughness of the nanocomposites could be obtained due to the ultralong CNFs/CHNFs. If the nanofibers are uniformly dispersed in the matrix, the refined nanofibers network structure can absorb a large amount of energy in the process of fracture, leading to a great improvement in impact strength of the nanocomposite.

FE-SEM. FE-SEM micrographs of fractured surfaces of four different nanofibers reinforced PLA composites are presented in Figure 5. Homogeneous dispersion of nanofibers in PLA matrix could be achieved for all four samples with the water preblending method. It is observed that lots of ultralong and refined nanofibers are distributed uniformly and compactly on the fracture surface of the nanocomposite in the form of a “spider web” without aggregation. The cellulose/chitin

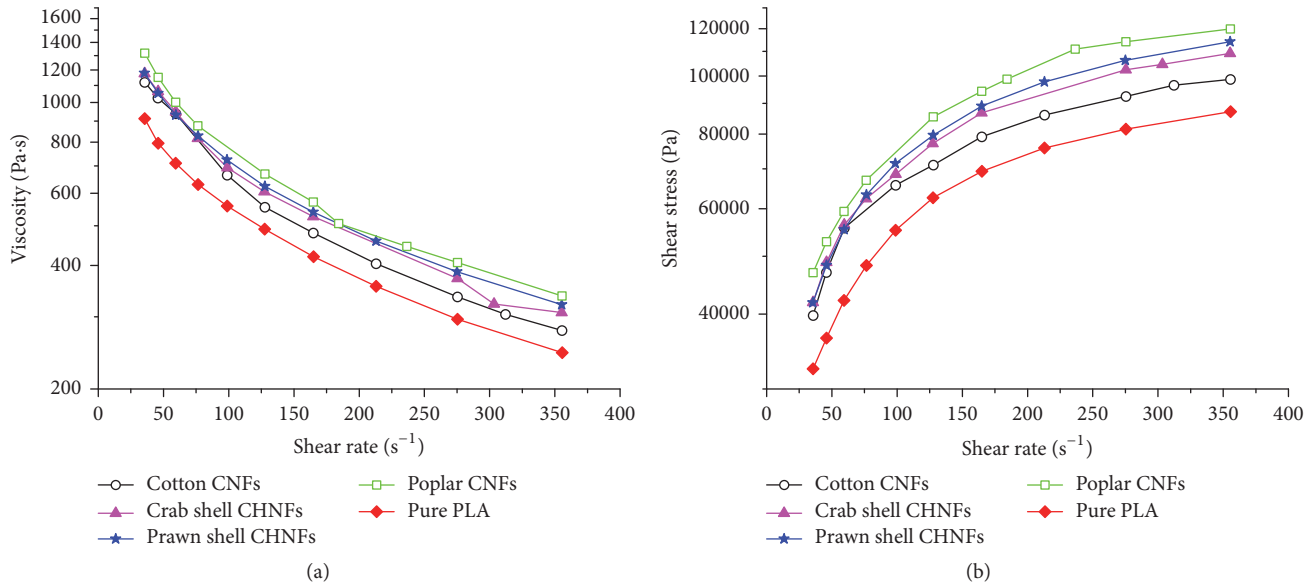


FIGURE 3: The viscosity and shear stress of four nanofibers/PLA composites as functions of shear rate.

nanofibers in the composites have the same entangled structure as the nanofibers, which means that the network structure of the nanofibers is stable and unaltered even after the water preblending and extrusion processes. The rough fracture surface suggests that large plastic deformation has occurred in the process of the fracture instead of the brittle fracture mode for the neat PLA. The fiber bundles disruption and delamination take more energy as compared to fiber fracture, leading to the prolonged crack propagation before failure. This mechanism is responsible for high toughness in the nanofiber/PLA composite. For the water pretreatment method, hydrophilic nanofiber and hydrophobic PLA fibers can be uniformly dispersed in aqueous suspension [33]. During the preblending process, nanofibers are adsorbed on PLA fiber and entangled to form a net shape. Therefore, the formed electrostatic repulsion and steric hindrance between nanofibers and PLA result in the uniform dispersion of cellulose/chitin nanofibers.

From the SEM images, it can be found that there are distinct differences in the fiber diameter and length for four samples. The poplar CNFs in the PLA matrix are the most homogeneous, having the lowest fiber diameter and highest length. These finer and longer fibers have higher resistance to deformation under the vacuum applied and develop greater network strength. The prawn shell CHNFs/PLA sample is intermediate between the poplar sample and the crab shell/cotton samples, as it contains some thicker fibers compared to poplar CNFs but finer fibers compared to crab shell/cotton nanofibers. For the crab shell/cotton nanofibers, both samples have some large fiber bundles; thus the samples are highly heterogeneous. This is because the strong hydrogen bonding between the nanofiber bundles makes it difficult to obtain thin and uniform nanofibers from crab shell/cotton. The fiber bundles with low aspect ratio lead to relatively low mechanical properties of the nanocomposites.

Coefficient of Thermal Expansion (CTE). The reinforcement effect of fibers can also be characterized to analyze the thermal expansion of plastics examined using the TMA. As reported, thermal expansion has an inverse relationship with Young's modulus [33]. The CTE values of four different nanocomposites and sheets prepared by different raw materials are presented in Figure 6. The CTE value of neat PLA is up to $180 \times 10^{-6} \text{ K}^{-1}$ due to its amorphous flexible molecular chains (Figure 6(a)). The thermal expansion of PLA was remarkably suppressed by the introduction of CHNFs/CNFs. The CTE values of the composites with 40 wt% nanofibers extracted from poplar, cotton, crab shell, and prawn shell are $69.5 \times 10^{-6} \text{ K}^{-1}$, $79.6 \times 10^{-6} \text{ K}^{-1}$, $77.2 \times 10^{-6} \text{ K}^{-1}$, and $75.3 \times 10^{-6} \text{ K}^{-1}$, respectively. CNFs/CHNFs with low CTE and high Young's modulus can effectively decrease the thermal expansion of PLA matrix due to the reinforcement effect, resulting from the suppression of the expansion for PLA matrix by the rigid three-dimensional nanostructural networks of nanofibers at high temperature [34]. On the other hand, the reinforcement effect can be attributed to the homogeneous dispersion of nanofibers in PLA matrix with the water preblending method. It can also be found that the poplar CNFs/PLA composite shows the lowest thermal expansion and the cotton CNFs/PLA composite shows the highest thermal expansion. In addition, it can be noticed that the CTE value of the crab shell CHNFs/PLA composite is slightly lower than that of cotton CNFs/PLA composite, which is different from the result of mechanical properties. This phenomenon can be explained by the fact that chitin nanofibers have higher thermal stability and higher crystallinity than cellulose nanofibers [14]. Furthermore, the CTE values of nanofibers sheets were measured in the same temperature region. From Figure 6(b), it can be seen that CTE values of the sheets made from poplar, cotton, crab shell, and prawn shell are $36.9 \times 10^{-6} \text{ K}^{-1}$, $45.7 \times 10^{-6} \text{ K}^{-1}$, $36.4 \times$

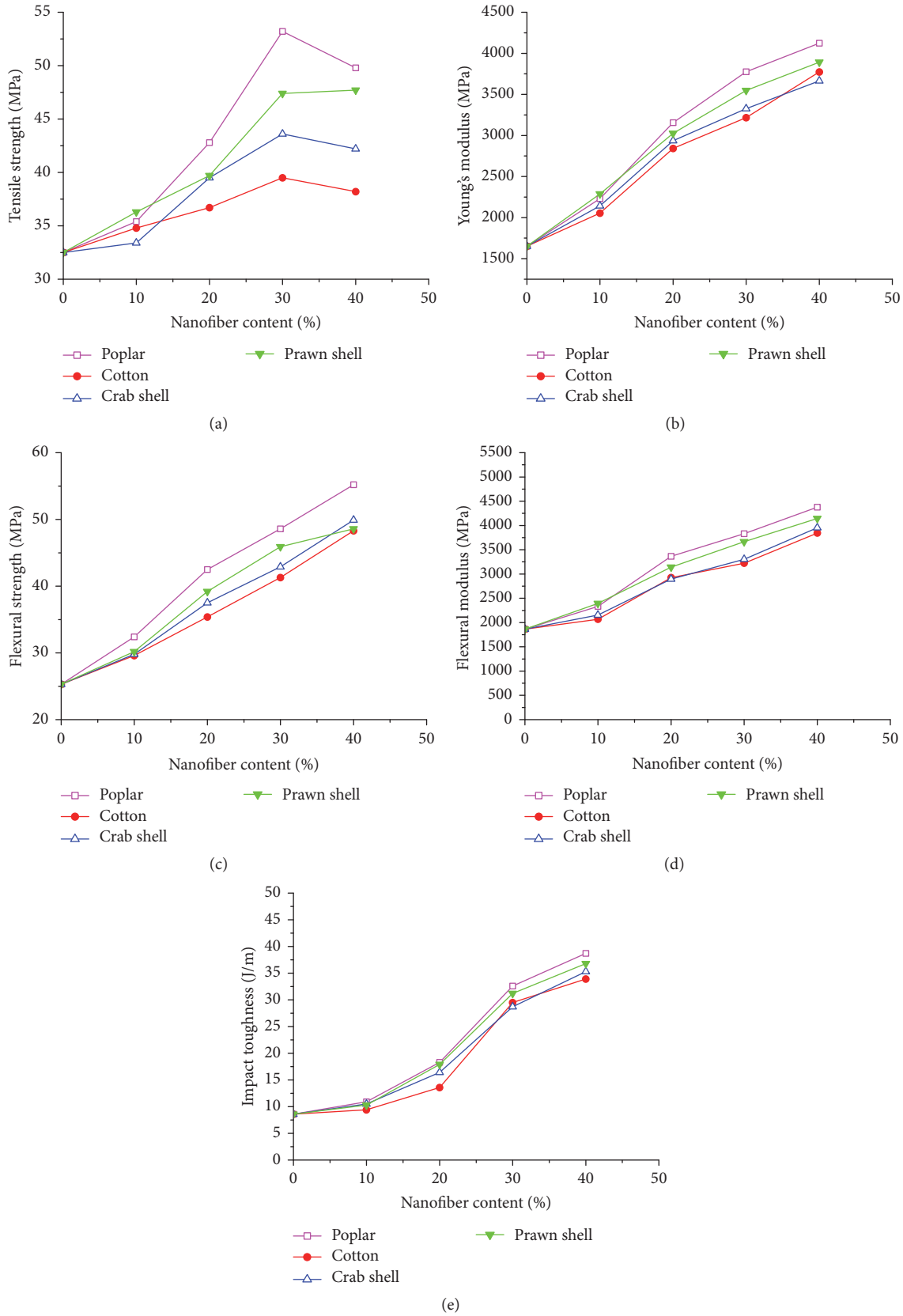


FIGURE 4: The mechanical properties, (a) tensile strength, (b) Young's modulus, (c) flexural strength, (d) flexural modulus, and (e) impact toughness of four nanofibers/PLA composites as functions of nanofiber content.

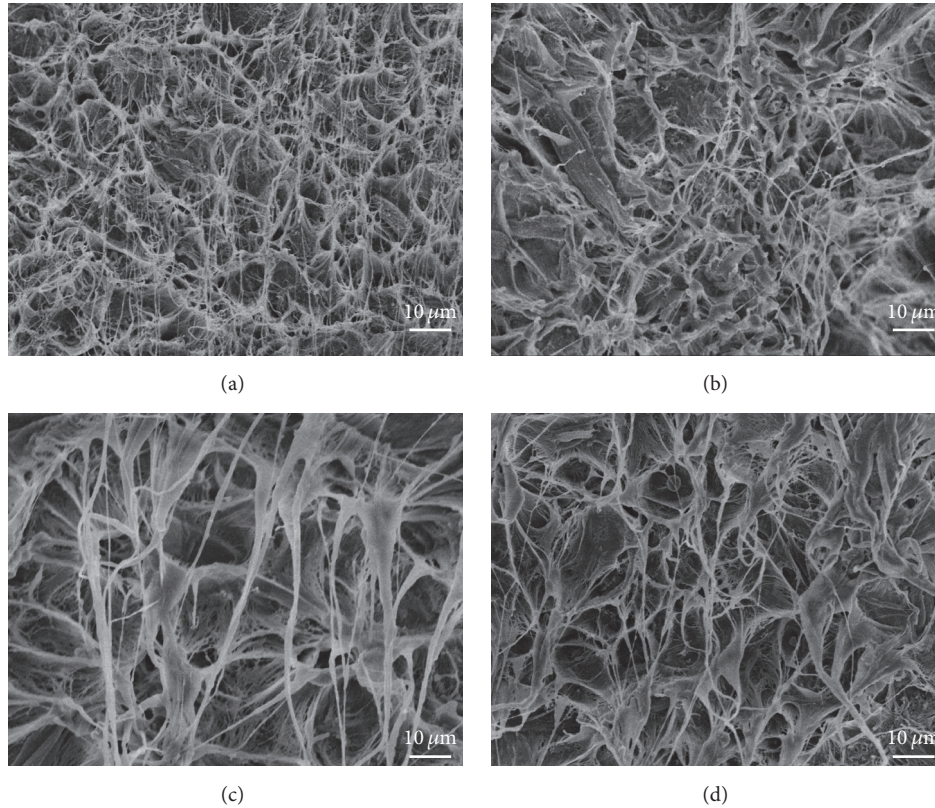


FIGURE 5: The FE-SEM images of fracture surfaces for 40 wt% nanofibers/PLA composites: (a) poplar CNFs, (b) cotton CNFs, (c) crab shell CHNFs, and (d) prawn shell CHNFs.

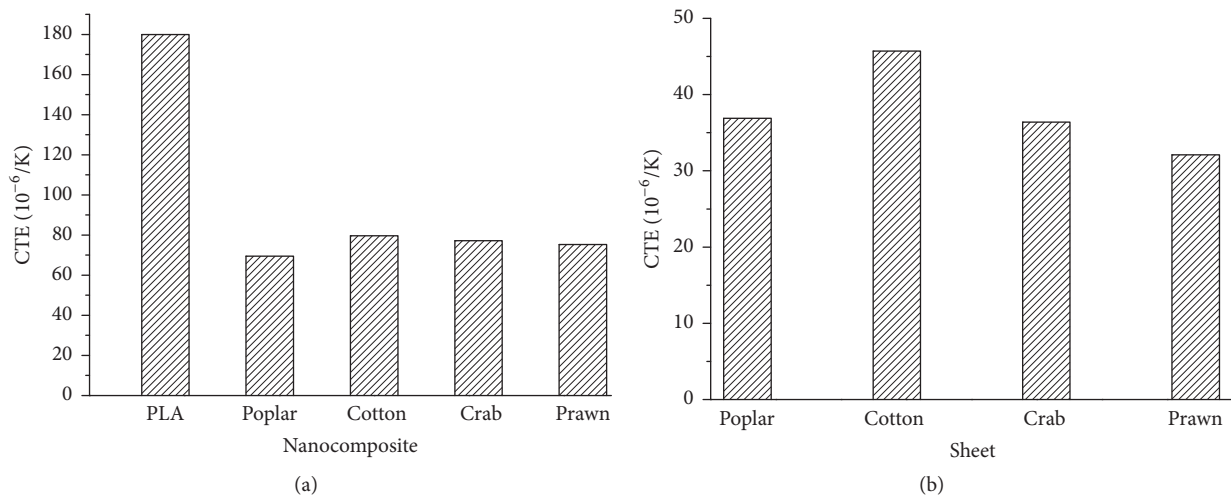


FIGURE 6: CTE values of (a) nanofibers/PLA composites and (b) nanofiber sheets.

$10^{-6} K^{-1}$, and $32.1 \times 10^{-6} K^{-1}$, respectively. CHNFs sheets have lower thermal expansion than that of CNFs sheets. Hence, the crab shell CHNFs/PLA composite presents lower CTE value than the cotton CNFs/PLA composite. In addition, it can be noticed that the CTE value of the crab shell CHNFs sheet is approximately equal to that of the poplar CNFs sheet, but the poplar CNFs/PLA composite shows much lower thermal expansion than that of crab shell CHNFs/PLA composite.

This result can be ascribed to the fact that poplar CNFs have much higher aspect ratio than the crab shell CHNFs, leading to higher mechanical properties. Therefore, it can be concluded that the aspect ratio of fibers has great influence on the thermal expansion of the polymer matrix.

DMA. Dynamic mechanical test methods have been widely employed for investigating the structures and viscoelastic

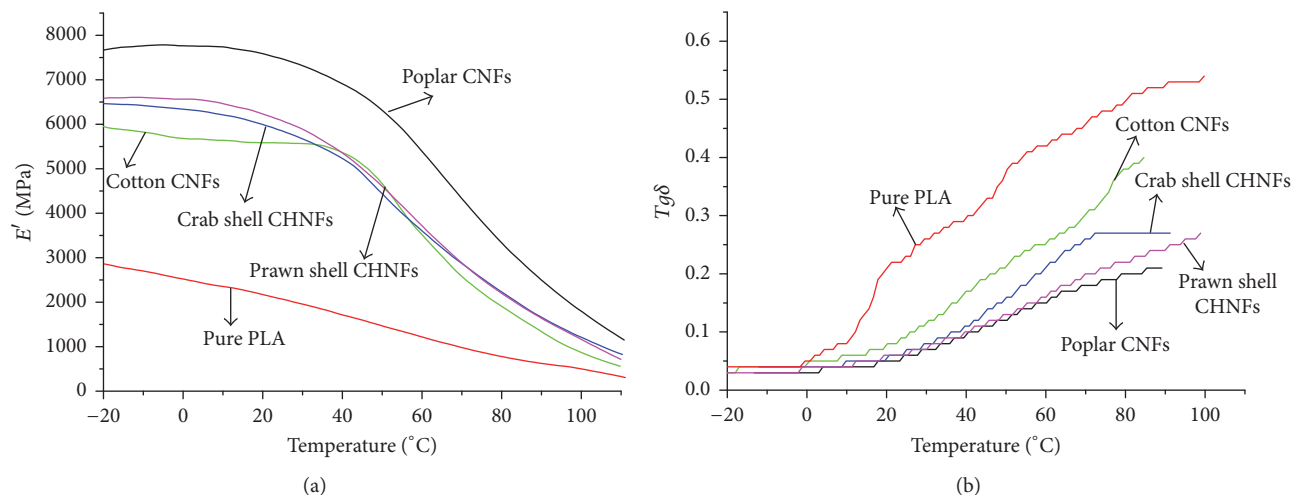


FIGURE 7: Temperature dependence on (a) storage modulus (E') and (b) loss factor ($\tan \delta$) of four nanofibers/PLA composites at fiber content of 40 wt%.

behavior of polymeric materials to determine their stiffness and damping characteristics for various applications. Figure 7 represents the plots of storage modulus (E') and loss factor ($\tan \delta$) with respect to temperature for the four nanofibers/PLA composites. In Figure 7(a), all the nanocomposites exhibit the storage modulus in the following order in the glassy region: poplar CNFs/PLA > prawn shell CHNFs/PLA > crab shell CHNFs/PLA > cotton CNFs/PLA. The storage modulus in the glassy state is primarily determined by the strength of the intermolecular forces and the way of the polymer chains packed by fibers [35]. High E' value can be attributed to the high interfacial adhesion and high aspect ratio of nanofibers, which may be helpful to the stress transfer in the nanofiber-matrix interface [36]. $\tan \delta$ is a dimensionless parameter that measures the ratio of loss modulus to storage modulus. For fibers/polymer composites, the loss of energy mainly occurs on the interface of fibers and polymers; thus high strength of composites indicates the low energy loss and low $\tan \delta$ [37]. In contrast, four nanocomposites exhibit $\tan \delta$ in the following order (Figure 7(b)): cotton CNFs/PLA > crab shell CHNFs/PLA > prawn shell CHNFs/PLA > poplar CNFs. An increase in $\tan \delta$ among different composites indicates that the viscosity of the composite is improved. The DMA results indicate that the aspect ratio of the nanofibers has a great influence on the thermal and mechanical performance of the composites, irrespective of the composites prepared by cellulose or chitin.

4. Conclusions

Polylactic acid (PLA) was reinforced with ultralong cellulose and chitin nanofibers extracted from four raw materials by the extrusion molding. The poplar CNFs/PLA composite exhibited the best mechanical properties among four nanocomposites, while both the cotton CNFs/PLA composite

and the crab shell CHNFs/PLA composite had low mechanical strength. Rheological measurement indicated that the viscosity and shear stress of the poplar CNFs/PLA composite are the highest among four samples, and the corresponding values of the cotton/PLA composite are the lowest. FE-SEM images showed that homogeneous dispersion of nanofibers in PLA matrix can be achieved with the water preblending method. The CTE values of the nanocomposites with 40 wt% nanofibers extracted from poplar, cotton, crab shell, and prawn shell were $69.5 \times 10^{-6} \text{ K}^{-1}$, $79.6 \times 10^{-6} \text{ K}^{-1}$, $77.2 \times 10^{-6} \text{ K}^{-1}$, and $75.3 \times 10^{-6} \text{ K}^{-1}$, respectively. The storage modulus of four nanocomposites in the glassy region is listed in the following order: poplar CNFs/PLA > prawn shell CHNFs/PLA > crab shell CHNFs/PLA > cotton CNFs/PLA. All the results indicated that the aspect ratio of the nanofibers has a great influence on the performance of the composites, irrespective of the composites prepared by cellulose or chitin.

Disclosure

Jingjing Li and Jian Li are co-first authors.

Conflicts of Interest

The authors declare that there are no conflicts of interest regarding the publication of this manuscript.

Authors' Contributions

Jingjing Li and Jian Li contributed equally to this work.

Acknowledgments

This work is financially supported by Ph.D. Start-up Fund of Northwest A&F University (Z109021613).

References

- [1] I. Armentano, N. Bitinis, E. Fortunati et al., "Multifunctional nanostructured PLA materials for packaging and tissue engineering," *Progress in Polymer Science*, vol. 38, no. 10-11, pp. 1720-1747, 2013.
- [2] M. M. Reddy, S. Vivekanandhan, M. Misra, S. K. Bhatia, and A. K. Mohanty, "Biobased plastics and bionanocomposites: current status and future opportunities," *Progress in Polymer Science*, vol. 38, no. 10-11, pp. 1653-1689, 2013.
- [3] H. Li and M. A. Huneault, "Effect of nucleation and plasticization on the crystallization of poly(lactic acid)," *Polymer Journal*, vol. 48, no. 23, pp. 6855-6866, 2007.
- [4] R. Auras, B. Harte, and S. Selke, "An overview of polylactides as packaging materials," *Macromolecular Bioscience*, vol. 4, no. 9, pp. 835-864, 2004.
- [5] D. Klemm, B. Heublein, H. P. Fink, and A. Bohn, "Cellulose: fascinating biopolymer and sustainable raw material," *Angewandte Chemie*, vol. 44, no. 22, pp. 3358-3393, 2005.
- [6] I. Sakurada, Y. Nukushina, and T. Ito, "Experimental determination of the elastic modulus of crystalline regions in oriented polymers," *Journal of Polymer Science*, vol. 57, no. 165, pp. 651-660, 1962.
- [7] T. Nishino, I. Matsuda, and K. Hirao, "All-cellulose composite," *Macromolecules*, vol. 37, no. 20, pp. 7683-7687, 2004.
- [8] J. Jin, P. Hassanzadeh, G. Perotto et al., "A biomimetic composite from solution self-assembly of chitin nanofibers in a silk fibroin matrix," *Advanced Materials*, vol. 25, no. 32, pp. 4482-4487, 2013.
- [9] J.-B. Zeng, Y.-S. He, S.-L. Li, and Y.-Z. Wang, "Chitin whiskers: An overview," *Biomacromolecules*, vol. 13, no. 1, pp. 1-11, 2012.
- [10] W. Chen, K. Abe, K. Uetani, H. Yu, Y. Liu, and H. Yano, "Individual cotton cellulose nanofibers: pretreatment and fibrillation technique," *Cellulose*, vol. 21, no. 3, pp. 1517-1528, 2014.
- [11] P. Dhar, D. Tarafder, A. Kumar, and V. Katiyar, "Thermally recyclable polylactic acid/cellulose nanocrystal films through reactive extrusion process," *Polymer (United Kingdom)*, vol. 87, pp. 268-282, 2016.
- [12] A. N. Frone, S. Berlioz, J.-F. Chailan, and D. M. Panaitescu, "Morphology and thermal properties of PLA-cellulose nanofibers composites," *Carbohydrate Polymers*, vol. 91, no. 1, pp. 377-384, 2013.
- [13] N. Herrera, A. P. Mathew, and K. Oksman, "Plasticized polylactic acid/cellulose nanocomposites prepared using melt-extrusion and liquid feeding: Mechanical, thermal and optical properties," *Composites Science and Technology*, vol. 106, pp. 149-155, 2015.
- [14] N. Herrera, A. M. Salaberria, A. P. Mathew, and K. Oksman, "Plasticized polylactic acid nanocomposite films with cellulose and chitin nanocrystals prepared using extrusion and compression molding with two cooling rates: Effects on mechanical, thermal and optical properties," *Composites Part A: Applied Science and Manufacturing*, vol. 83, pp. 89-97, 2016.
- [15] M. Jonoobi, J. Harun, A. P. Mathew, and K. Oksman, "Mechanical properties of cellulose nanofiber (CNF) reinforced polylactic acid (PLA) prepared by twin screw extrusion," *Composites Science and Technology*, vol. 70, no. 12, pp. 1742-1747, 2010.
- [16] M. Kowalczyk, E. Piorkowska, P. Kulpinski, and M. Pracella, "Mechanical and thermal properties of PLA composites with cellulose nanofibers and standard size fibers," *Composites Part A: Applied Science and Manufacturing*, vol. 42, no. 10, pp. 1509-1514, 2011.
- [17] L. Suryanegara, A. N. Nakagaito, and H. Yano, "The effect of crystallization of PLA on the thermal and mechanical properties of microfibrillated cellulose-reinforced PLA composites," *Composites Science and Technology*, vol. 69, no. 7-8, pp. 1187-1192, 2009.
- [18] A. N. Nakagaito, K. Yamada, S. Ifuku, M. Morimoto, and H. Saimoto, "Fabrication of chitin nanofiber-reinforced polylactic acid nanocomposites by an environmentally friendly process," *Journal of Biobased Materials and Bioenergy*, vol. 7, no. 1, pp. 152-156, 2013.
- [19] L. Tang, B. Huang, N. Yang et al., "Organic solvent-free and efficient manufacture of functionalized cellulose nanocrystals via one-pot tandem reactions," *Green Chemistry*, vol. 15, no. 9, pp. 2369-2373, 2013.
- [20] A. M. Salaberria, J. Labidi, and S. C. M. Fernandes, "Chitin nanocrystals and nanofibers as nano-sized fillers into thermoplastic starch-based biocomposites processed by melt-mixing," *Chemical Engineering Journal*, vol. 256, pp. 356-364, 2014.
- [21] R. Rizvi, B. Cochrane, H. Naguib, and P. C. Lee, "Fabrication and characterization of melt-blended polylactide-chitin composites and their foams," *Journal of Cellular Plastics*, vol. 47, no. 3, pp. 283-300, 2011.
- [22] J. Li, D. Li, Z. Song, S. Shang, and Y. Guo, "Preparation and properties of wood plastic composite reinforced by ultralong cellulose nanofibers," *Polymer Composites*, vol. 37, no. 4, pp. 1206-1215, 2016.
- [23] J. Li, Z. Song, D. Li, S. Shang, and Y. Guo, "Cotton cellulose nanofiber-reinforced high density polyethylene composites prepared with two different pretreatment methods," *Industrial Crops and Products*, vol. 59, pp. 318-328, 2014.
- [24] J. Li, Y. Gao, J. Zhao, J. Sun, and D. Li, "Homogeneous dispersion of chitin nanofibers in polylactic acid with different pretreatment methods," *Cellulose*, vol. 24, no. 4, pp. 1705-1715, 2017.
- [25] W. Chen, Q. Li, Y. Wang et al., "Comparative study of aerogels obtained from differently prepared nanocellulose fibers," *ChemSusChem*, vol. 7, no. 1, pp. 154-161, 2014.
- [26] S. Ifuku and H. Saimoto, "Chitin nanofibers: Preparations, modifications, and applications," *Nanoscale*, vol. 4, no. 11, pp. 3308-3318, 2012.
- [27] C. Miao and W. Y. Hamad, "Cellulose reinforced polymer composites and nanocomposites: a critical review," *Cellulose*, vol. 20, no. 5, pp. 2221-2262, 2013.
- [28] A. N. Frone, S. Berlioz, J.-F. Chailan, D. M. Panaitescu, and D. Donescu, "Cellulose fiber-reinforced polylactic acid," *Polymer Composites*, vol. 32, no. 6, pp. 976-985, 2011.
- [29] P. Qu, Y. Gao, G.-F. Wu, and L.-P. Zhang, "Nanocomposites of poly(lactic acid) reinforced with cellulose nanofibrils," *Biore-sources*, vol. 5, no. 3, pp. 1811-1823, 2010.
- [30] R. M. Rowell, J. S. Han, and J. S. Rowell, "Characterization and factors effecting fiber properties," in *Natural Polymers and Agrofibers Composites*, pp. 115-134, 2000.
- [31] N. M. Stark and R. E. Rowlands, "Effects of wood fiber characteristics on mechanical properties of wood/polypropylene composites," *Wood and Fiber Science*, vol. 35, no. 2, pp. 167-174, 2003.
- [32] J. K. Sameni, S. H. Ahmad, and S. Zakaria, "Effects of processing parameters and graft-copoly(propylene/maleic anhydride) on mechanical properties of thermoplastic natural rubber composites reinforced with wood fibres," *Plastics, Rubber and Composites*, vol. 31, no. 4, pp. 162-166, 2002.

- [33] A. N. Nakagaito and H. Yano, "The effect of fiber content on the mechanical and thermal expansion properties of biocomposites based on microfibrillated cellulose," *Cellulose*, vol. 15, no. 4, pp. 555–559, 2008.
- [34] H. Yousefi, M. Faezipour, S. Hedjazi, M. M. Mousavi, Y. Azusa, and A. H. Heidari, "Comparative study of paper and nanopaper properties prepared from bacterial cellulose nanofibers and fibers/ground cellulose nanofibers of canola straw," *Industrial Crops and Products*, vol. 43, no. 1, pp. 732–737, 2013.
- [35] L. A. Pothan, Z. Oommen, and S. Thomas, "Dynamic mechanical analysis of banana fiber reinforced polyester composites," *Composites Science and Technology*, vol. 63, no. 2, pp. 283–293, 2003.
- [36] M. M. Andrade-Mahecha, F. M. Pelissari, D. R. Tapia-Blácido, and F. C. Menegalli, "Achira as a source of biodegradable materials: isolation and characterization of nanofibers," *Carbohydrate Polymers*, vol. 123, pp. 406–415, 2015.
- [37] P. Zugenmaier, "Materials of cellulose derivatives and fiber-reinforced cellulose-polypropylene composites: Characterization and application," *Pure and Applied Chemistry*, vol. 78, no. 10, pp. 1843–1855, 2006.

Research Article

Nanoporosity of MCM-41 Materials and Y-Zeolites Created by Deposition of *Tournefortia hirsutissima* L. Plant Extract

Miguel Angel Hernández,¹ Gabriela Itzel Hernández,² Roberto Portillo,³ Martha Alicia Salgado,³ Fernando Rojas,⁴ and Vitalii Petranovskii⁵

¹Departamento de Investigación en Zeolitas, Universidad Autónoma de Puebla, Complejo de Ciencias, Ciudad Universitaria, 72570 Puebla, PUE, Mexico

²Facultad de Ingeniería Química, Universidad Autónoma de Puebla, Puebla, PUE, Mexico

³Facultad de Ciencias Químicas, Universidad Autónoma de Puebla, Puebla, PUE, Mexico

⁴Departamento de Química, Universidad Autónoma Metropolitana-Iztapalapa, Apartado Postal 55-534, 09340 Mexico City, Mexico

⁵Centro de Nanociencias y Nanotecnología, Universidad Nacional Autónoma de México, Carretera Tijuana-Ensenada, Km. 107, Ensenada, BC, Mexico

Correspondence should be addressed to Miguel Angel Hernández; vaga1957@gmail.com

Received 13 May 2017; Revised 2 August 2017; Accepted 8 August 2017; Published 18 September 2017

Academic Editor: Bodo Fiedler

Copyright © 2017 Miguel Angel Hernández et al. This is an open access article distributed under the Creative Commons Attribution License, which permits unrestricted use, distribution, and reproduction in any medium, provided the original work is properly cited.

Hybrid materials based on MCM-41 silica and Y-zeolites with a variable Si/Al ratio and an appropriate countercationic composition were prepared by impregnating inorganic substrates with an organic extract. The organic phase was previously characterized by GC-MS and IRTF, while XRD, SEM, TEM, N₂-physisorption, and TPD of NH₃ were used to analyze the selected inorganic supports. The effect of size- and shape-selectivity was manifested in MCM-41 and Y-zeolites. Texture results confirm that the extract containing relatively large branched organic molecules is deposited in the internal voids of MCM-41 material and on the outer area of Y-zeolites. In the case of Y-zeolites, the results demonstrate the effect of the SiO₂/Al₂O₃ molar ratio and countercations on the textural properties of the samples.

1. Introduction

Nanomaterials such as aluminosilicate zeolites and sponge silicon dioxide are porous substances with well-defined regular pore systems. Zeolites are widely used in the industry for many applications, including catalysis, gas separation, and adsorption [1, 2]. Mesoporous silica nanomaterials are also extensively studied for potential use in various areas [3]. Their proposed applications include medical and biological fields, which attract a great research interest [4, 5]. These nanostructured substrates possess a high porosity and surface area, as well as a large pore volume, together with a uniform and adjustable pore size, which makes them suitable for special applications in biomedical areas [6, 7].

For the deposition of organic plant extracts, the loading capacity of traditional materials, such as inorganic oxides or

polymer matrixes, is usually not high enough; in addition, trapped organic components cannot be selectively released without difficulties. To achieve high loading and controlled release, nanoporous materials possessing large volumes and regular structures are preferred; no doubt, these requirements are met by Y-zeolites and MCM-41 materials [8, 9]. Their impact on living organisms and the likely toxicity were carefully considered [10, 11].

The loading capacity and release of active phases in the nanoporous carrier are determined by a variety of factors, including pore size, shape, connectivity, and host affinity. Microporous and mesoporous materials, such as zeolites and mesoporous silica, become important solids for the delivery of the active phase. The advantages of zeolites and mesoporous silica for biomedical applications include their biocompatibility, a large surface area, and the ability to tune

and control their physicochemical properties. For example, Lehman and Larsen [11] mentioned the use and application of porous nanomaterials in the delivery of drugs for the treatment of various diseases. Datt et al. [12] conducted research related to intelligent nanomaterials for medicine. This review reports on the effect of nanostructured materials on the type of toxicity. Colella [13] published a review taking into account the structure, composition, and ion-exchange properties of nanoporous materials, such as clinoptilolite zeolite, for modern therapeutic applications. Pavelić et al. [14] used Ca-exchanged clinoptilolite as a potential adjuvant for the treatment of various cancers. Due to their versatility, zeolites and MCM-41 have acquired great importance for the development of new nanomaterials. Recently, the Sanchez group reported [15] a large group of organic-inorganic hybrid nanomaterials and their applications.

The faujasite zeolite (a structure code is FAU, according to the database of the International Zeolite Association, IZA) [16] is a zeolite that has nearly spherical cavities with a diameter of 12 Å connected by windows of 7.2 Å. This structure, as well as the inner and outer surfaces, are shown in Figure 1. Independent of their composition, all faujasites are topologically identical, but they have different properties depending on the Al content in their structure, giving two different materials: type X- or type Y-zeolites. The unit cell of faujasite has 192 tetrahedrally coordinated atoms, which can be Al or Si. Materials with the number of Al atoms between 96 and 77 per unit cell belong to the X-type, and materials with a lower Al content belong to the Y-type. This means that the $\text{SiO}_2/\text{Al}_2\text{O}_3$ molar ratio of X-zeolites is lower than 3, and the faujasites with MR above the value of 3 appear as Y-zeolites [17].

The discovery of MCM-41 materials containing the hexagonal arrangement of one-dimensional tubular mesopores with a diameter from 20 to 100 Å [17] and a large surface area has opened up new possibilities for the development of molecular sieves of this type, because their high surface areas are very attractive for the development of new adsorbents and catalysts. MCM varieties are relatively stable (thermally, hydrothermally, mechanically, and chemically) and a suitable choice of organic templates and synthesis conditions can create materials with pore diameters suitable for the adsorption of large organic molecules [18–21].

In the continuation of our earlier work [22], this paper describes the preparation and characterization of nanoporosity in hybrid materials created after the deposition of the extract of the plant *Tournefortia hirsutissima* L. on the outer surface of Y-zeolites and into the inner nanopores of MCM-41 silica, as well as the possible use of obtained materials in the treatment of diabetic foot.

Potential advantages of this study are (i) the development of new hybrid materials by precipitation of the extract of the *Tournefortia hirsutissima* L. on carriers, Y-zeolites and MCM-41 silica materials; (ii) characterizing hybrid materials by various physical chemical methods; and (iii) the study of nanoporosity in these hybrid materials, which have the potential properties of cell regeneration. The experimental study on the preparation of a group of hybrid materials by means of impregnation and the influence of the preparation protocol on the secondary porosity was performed. The

organic part of the hybrid materials was characterized by Gas Chromatography-Mass Spectroscopy (GC-MS), and the inorganic supports were characterized by X-Ray Diffraction (XRD), Scanning Electron Microscopy (SEM), Transmission Electron Microscopy (TEM), High-Resolution Adsorption (HRADS), Energy Dispersive Spectroscopy (EDS), and Temperature Programmed Desorption (TPD). The textural parameters such as surface area, external surface area, micropore volume, total pore volume, and pore size distribution of the microporous were calculated from the adsorption isotherms. The primary interest of this work is to obtain and analyze the morphological characteristics of nanoporous solids with highly developed surface areas, used as carriers of bioactive phases of organic nature, with the aim of getting a vehicle that allows an efficient and controlled desorption of active ingredients, constituting the organic phase deposited on the surface of such materials.

2. Experimental Section

2.1. Materials. MCM-41 materials were prepared in the laboratory by hydrothermal synthesis [18]. Commercial Y-zeolites with faujasite structure (FAU topology of the framework, see the WEB site of International Zeolite Association [16] for detailed description) were supplied by Zeolyst International. The faujasites with the compositions in the range of the so-called Y-zeolite, with the same topology of the structure, but with different $\text{SiO}_2/\text{Al}_2\text{O}_3$ molar ratio (MR) in the range from 5.1 up to 30 and in different cationic form (Na^+ , NH_4^+ , and H^+), were selected for this work. These materials and some of their properties presented by the supplier are listed in Table 1. Labeling of samples through text and figures is listed in the last column of Table 1 and includes the type of cation, the structure of the zeolite (Y), and the molar ratio MR, for example, NaY5.1. For as-prepared substrates and for samples after impregnation, characters S (NaY5.1-S) or I (NaY5.1-I), respectively, are added to the label. It should be emphasized that in nominally hydrogen or ammonium forms of Y-zeolites nonetheless some amount of sodium cations is presented (see Table 1). Thermal activation of the inorganic phase substrates was done before impregnation by plant extracts (see Section 2.2.1).

2.2. Methodology

2.2.1. Dispersion and Stabilization of Organic Phase Nanodeposits on Y-Zeolites and MCM-41 Materials. Both Y-zeolites and MCM-41 (5 g) materials were dried at 373 K for 8 h and, afterward, were cooled below 300 K and mixed under stirring with the ethanol extract of *Tournefortia hirsutissima* L. (2.5 mL). The obtained slurry was stirred for two hours at room temperature. After this, the solvent was evaporated at 393 K.

The initial step consists in the preparation, formation, and stabilization of nanodeposits on the surface of Y-zeolite and MCM-41 materials. These processes were carried out by impregnation and heat treatment; these steps were performed using the previously obtained liquor extract of *Tournefortia hirsutissima* L. in EtOH for 24 h under stirring. Subsequently,

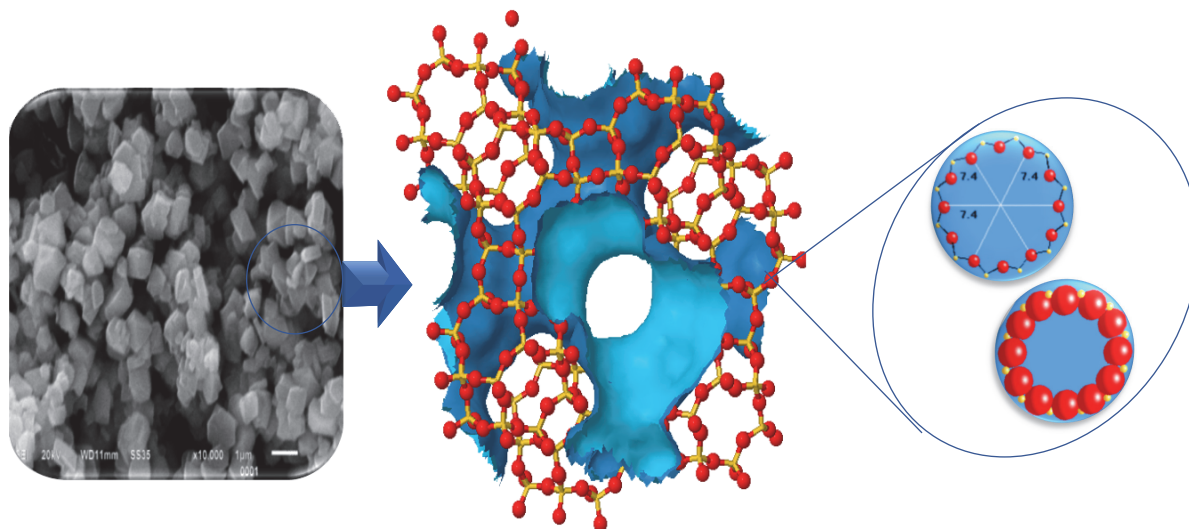


FIGURE 1: Surfaces in Y-zeolites.

TABLE 1: Y-zeolites supplied by Zeolyst International.

Zeolyst products	SiO ₂ /Al ₂ O ₃ molar ratio	Nominal cation form	Na ₂ O weight%	Unit cell size, Å	Labeling of the samples
CBV-100	5.1	Sodium	13.0	24.65	NaY5.1
CBV-300	5.1	Ammonium	2.8	24.68	NH ₄ Y5.1
CBV-400	5.1	Hydrogen	2.8	24.50	HY5.1
CBV-500	5.2	Ammonium	0.2	24.53	NH ₄ Y5.2
CBV-600	5.2	Hydrogen	0.2	24.35	HY5.2
CBV-720	30	Hydrogen	0.03	24.28	HY30

the solvent was removed by evaporation at 363 K. Finally, the resultant hybrid materials were stabilized at 423 K.

2.2.2. Characterization of the Substrates and Impregnated Materials. (i) *Gas chromatography-mass spectrometry (GC-MS)* analysis of the extract was performed by means of a coupled system of an Agilent Model 7890A gas chromatograph and an Agilent Model 5975 mass spectrometer and has been previously reported [23].

(ii) *X-ray diffraction (XDR)* test samples were performed with a Siemens D500 diffractometer using a Cu K_α radiation ($\lambda = 1.54 \text{ \AA}$), operating at 40 kV and 30 mA. The samples were previously ground. Crystalline phases were identified with the help of cards supplied by the Joint Committee on Powder Diffraction Standards (JCPDS) and Collection of XRD Patterns for zeolites edited by IZA [24]. Samples were analyzed over a diffraction angle range $2\theta = 1\text{--}6^\circ$ for MCM-41 materials and $2\theta = 5\text{--}65^\circ$ for Y-zeolites, employing a step size of 0.03° and a time of 6 s.

(iii) *Scanning Electron Microscopy (SEM)* was performed using a JEOL JSM-5300 electron microscope (SEM) employing a tungsten filament operated at 10 kV at 298 K. Photomicrographs of the surface were gotten and the morphology of obtained materials was observed and chemical analyses were performed through energy dispersive spectroscopy (EDS).

(iv) *Transmission Electron Microscopy (TEM)* was performed on TITAN 80 operated at 300 kV.

(v) *Fourier Transform Infrared Spectroscopy (FTIR)* analyses were carried out in a Bruker Vector spectrometer.

(vi) *N₂ adsorption* isotherms were determined at the boiling temperature of liquid nitrogen (77 K at the 2,150-m altitude of Puebla, Mexico) applying fully automated volumetric instrument (Autosorb1LC, Quantachrome Corp.). This system was previously calibrated with reference adsorbents. Adsorption isotherms were determined in the range of relative pressure, p/p^0 from 10^{-6} to 1; p^0 is the saturation N₂ pressure and it was continuously recorded throughout the experiment. Prior to the N₂ sorption runs, each sample was degassed at 200°C for 20 h under a vacuum of 10^{-6} mbar. Textural parameters (surface areas and pore volumes) were obtained from the analysis of sorption isotherms by means of (i) the BET [25] equation, (ii) the Langmuir equation [26], (iii) the method of external area [27], and (iv) the Gurvitsch rule [28]. The pore size distribution of the samples under study was obtained from the data, processing the boundary desorption curves through the BJH method [29].

(vii) *Temperature Programmed Desorption (TPD)* of NH₃ was used to characterize acid sites on the substrates. This process was carried out by chemisorption of a NH₃/He gas mixture at different adsorption temperatures. The instrument

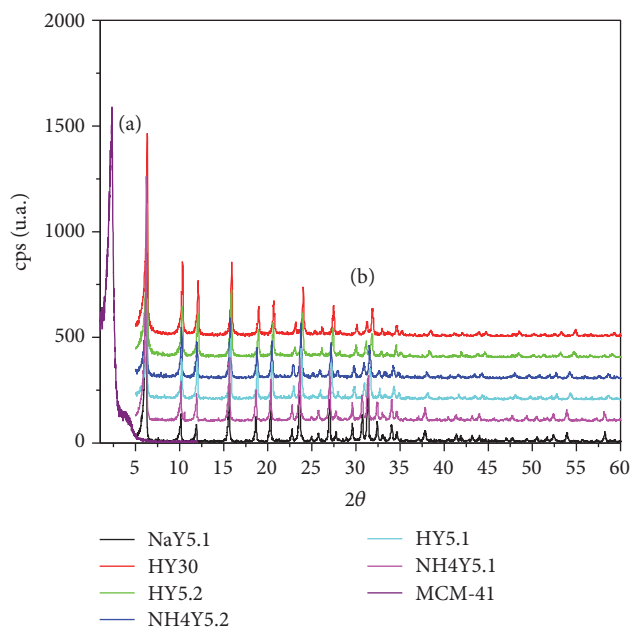


FIGURE 2: XRD patterns of (a) MCM-41 and (b) Y-zeolites.

used was an Autosorb-IC-MS Quantachrome automatic sorption characterization device.

3. Results and Discussion

3.1. GS-MS. The chemical composition and the mass percentage of each of the components presented in the active phase of the *Tournefortia hirsutissima* L. ethanol extract were estimated by GC-MS and have been previously reported [23]. Table 2 summarizes the information of the compounds detected by gas chromatography that exist in higher concentrations, together with their retention times and identification factor for each one of them. This table shows that 1,2-benzenedicarboxylic acid, mono (2-ethylhexyl) ester (21.04%), γ -sitosterol (16.42%), and 3,7,11,15-tetramethyl-2-hexadecen-1-ol (6.34%) are the three main components, followed by hexadecanoic acid, ethyl ester (4.77%), phenol, 2,2'-methylene bis (4.53%), (E)-9-octadecenoic acid ethyl ester (4.11%), and hexadecanoic acid, methyl ester (4.08%).

3.2. X-Ray Diffraction. Diffraction patterns of the materials under study at $2\theta = 2\text{--}6^\circ$ for the MCM-41 materials and at $2\theta = 5\text{--}65^\circ$ for the Y-zeolites are shown in Figure 2. In the diffraction pattern of MCM-41 materials predominant signals were observed at approximately $2\theta = 2^\circ$; however, these signals are relatively wide thus manifesting an amorphous character. It appears that higher 2θ values than the usual ones indicate some contraction of the structure of this material. The diffraction patterns of Y-zeolites (JCPDS card 33-1270.) exhibit typical signals of such materials. The predominant peaks appear at 2θ : 6.19° , 15.61° , 18.64° , 20.3° , 23.6° , 26.97° , 31.32° , and 33.99° .

3.3. Scanning Electron Microscopy. The analysis performed on the same sample by using Scanning Electron Microscopy

shows Y-zeolite aggregates, as well as thin crystals of cubic form and varying sizes of about $1\ \mu\text{m}$ (Figures 3(a) and 3(b)).

3.4. Transmission Electron Microscopy. TEM analysis was performed for the MCM-41-S specimen; the corresponding micrograph unveiled the presence of well-defined and ordered channels (Figures 3(c)-3(d)).

3.5. Energy Dispersive Spectroscopy. Studies of Y-zeolites indicate that MR ratio remains constant after impregnation; with respect to the abundance of Na_2O , the following sequence is set up: $\text{NaY5.1} > \text{NH}_4\text{Y5.1} = \text{HY5.1} > \text{NH}_4\text{Y5.2} = \text{HY5.2} > \text{HY30}$, which coincide with the sequence of the provider values (Table 1). It means that ion content is not changed during the treatment. Meanwhile, the size of the unit cell is similar for all Y-zeolites, Table 1.

3.6. FTIR. The infrared spectra of the *Tournefortia* Ethanolic Extract (TEE) in solution and with impregnated Y-zeolites and MCM-41 nanomaterials have the following features. The most intense absorptions were observed in the range of (a) $400\text{--}1700\ \text{cm}^{-1}$ and (b) $2800\text{--}3800\ \text{cm}^{-1}$, Figures 4(a) and 4(b). The infrared spectrum has the following features (cm^{-1}): $3300\ \text{cm}^{-1}$ typical absorption of C-H stretch in alcohols and phenols; $2900\ \text{cm}^{-1}$ absorption characteristic of C-H stretch of methylene groups; $1720\ \text{cm}^{-1}$ typical of C=O stretching vibrations of carbonyl group; $1450\ \text{cm}^{-1}$ of CH_2 ; and $1400\ \text{cm}^{-1}$ typical of COCH_3 ; other absorption peaks include $1200\ \text{cm}^{-1}$ (OH), $1100\ \text{cm}^{-1}$ (cycloalkane), and $950\ \text{cm}^{-1}$ [23]. The framework vibration bands of Y-zeolite show the spectra below $1200\ \text{cm}^{-1}$ in the regions 750 and $700\ \text{cm}^{-1}$, which are attributed to double ring, symmetric stretching, and asymmetric stretching vibrations, respectively [30].

3.7. Analysis of the Adsorption Isotherms. The N_2 sorption isotherms at 77 K, that is, relative pressure, p/p^0 versus adsorbed volume in cm^3 STP per gram of material are shown in Figure 5.

These isotherms correspond to the samples before and after being impregnated with the alcoholic extract of *Tournefortia hirsutissima* L. plant. These sorption isotherms are of Type IV in the IUPAC classification for the MCM-41 substrates. In turn, the N_2 sorption isotherms of the Y-zeolites are Type Ia in the same classification [31]. The results of the textural studies of the samples, before (S) and after impregnation (I), are reported in Table 3. It can be observed that a greater adsorption capacity of the MCM-41-S material exists, along with the entire p/p^0 range if compared to the case of Y-zeolites. However, when this material has been impregnated with the extract solution, the adsorption capacity for the MCM-41-I material is considerably diminished, since the extract is deposited in the interior of the structure voids, thus blocking the pore cavities of this material. There is a decrease in the available volume by approximately 3.5 times. This behavior may be related to the effect of size selectivity depicted by MCM-41 materials. The textural properties of the samples, before (S) and after impregnation (I), conform to the following order according to their adsorption values.

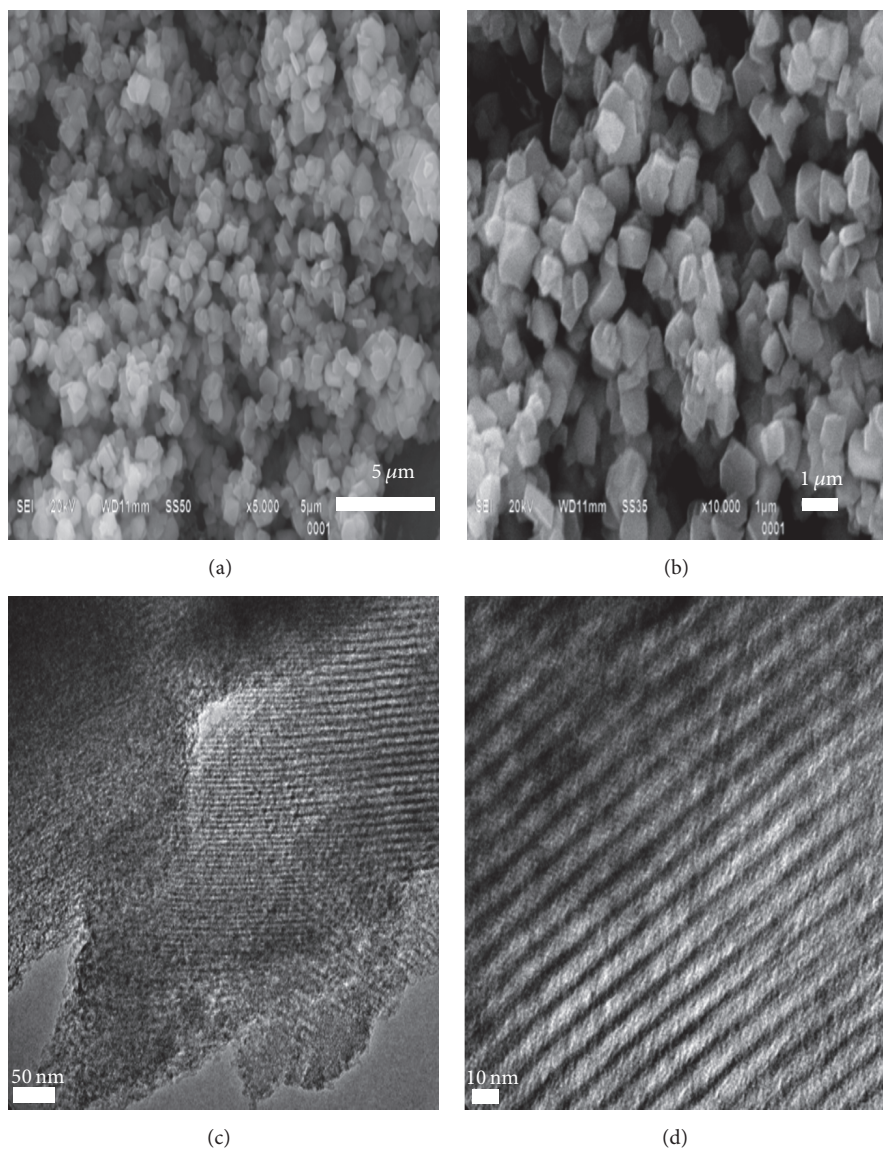


FIGURE 3: SEM images of Y-zeolites (a-b) and TEM images of MCM-41 materials synthetic samples with different crystal sizes (c-d).

TABLE 2: Principal organic molecule composition of the ethanolic extract of *Tournefortia hirsutissima* L. as measured by GC-MS.

RT min	Compound	Formula	M g mol^{-1}	RC %
11.878	3,7,11,15-Tetramethyl-2-hexadecen-1-ol (Phytol)	$\text{C}_{20}\text{H}_{40}\text{O}$	296	6.34
12.732	Hexadecanoic acid, methyl ester	$\text{C}_{25}\text{H}_{42}\text{O}_2$	374	4.08
13.334	Phenol, 2,2'-methylene bis	$\text{C}_{13}\text{H}_{12}\text{O}_2$	200	4.53
13.389	Hexadecanoic acid, ethyl ester	$\text{C}_{18}\text{H}_{36}\text{O}_2$	284	4.77
14.998	(E)-9-Octadecenoic acid ethyl ester	$\text{C}_{20}\text{H}_{38}\text{O}_2$	310	4.11
19.804	1,2-Benzenedicarboxylic acid, mono(2-ethylhexyl) ester	$\text{C}_{16}\text{H}_{22}\text{O}_4$	278	21.04
55.946	γ -Sitosterol	$\text{C}_{29}\text{H}_{50}\text{O}$	414	16.42

RT: retention time, M: molecular mass, and RC: relative concentration (%) of *Tournefortia hirsutissima* L. of ethanolic extract.

TABLE 3: Textural parameters of FAU-CBV zeolites and MCM-41 materials determined from N_2 adsorption before (S) and after being impregnated (I) with *Tournefortia* ethanolic extract.

Materials	A_{SB} $m^2 g^{-1}$	C_B	A_{SL} $m^2 g^{-1}$	A_{st} $m^2 g^{-1}$	V_{Σ} $cm^3 g^{-1}$	W_{of} $cm^3 g^{-1}$	V_{meso} $cm^3 g^{-1}$	Pore diameter BJH, Å
Before								
CBV-100-S	670	-37	1018	38	0.395	0.335	0.06	51, 106
CBV-300-S	601	-55	882	31	0.326	0.291	0.035	
CBV-400-S	604	-61	886	84	0.275	0.265	0.010	
CBV-500-S	678	-61	994	127	0.414	0.284	0.130	72
CBV-600-S	529	-65	772	101	0.378	0.217	0.161	
CBV-720-S	725	-80	1060	121	0.496	0.306	0.190	34
MCM-41-S	1009	52	1185	1009	0.777	0	0.777	24, 34
Impregnated								
CBV-100-I	692	-53	1016	38	0.369	0.335	0.034	
CBV-300-I	462	-56	680	44	0.267	0.214	0.053	
CBV-400-I	604	-61	886	84	0.363	0.265	0.098	36, 103
CBV-500-I	678	-61	994	96	0.414	0.297	0.117	
CBV-600-I	526	-65	772	101	0.378	0.217	0.161	36, 47, 151
CBV-720-I	725	-80	1060	124	0.496	0.304	0.192	36
MCM-41-I	286	78	415	286	0.309	0	0.309	36

A_{SB} is the specific surface area BET; A_{SL} is the specific surface area Langmuir; A_{st} is the external surface area t -method; C_B is the BET constant; V_{Σ} is the volume adsorbed close to saturation ($p/p^0 = 0.95$), calculated as volume of liquid (Gursvitch rule); W_{of} is micropore volume calculated by t -plots; V_{meso} is mesopore volume; and Pore diameter BJH is the pore size estimated by BJH method.

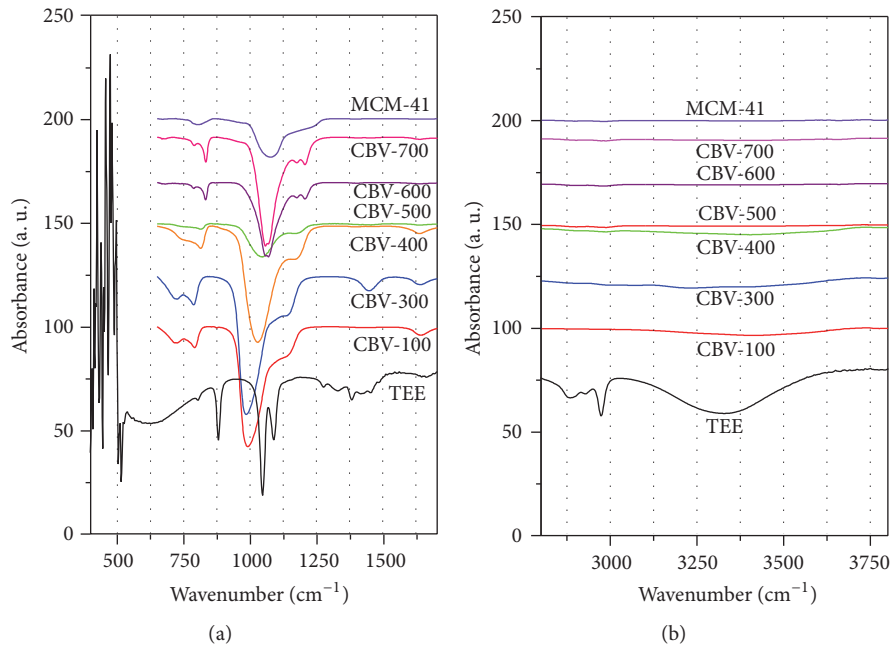


FIGURE 4: FTIR spectra of *Tournefortia* Ethanolic Extract (TEE) in solution and with impregnated materials, (a) 400–1700 cm^{-1} and (b) 2800–3800 cm^{-1} .

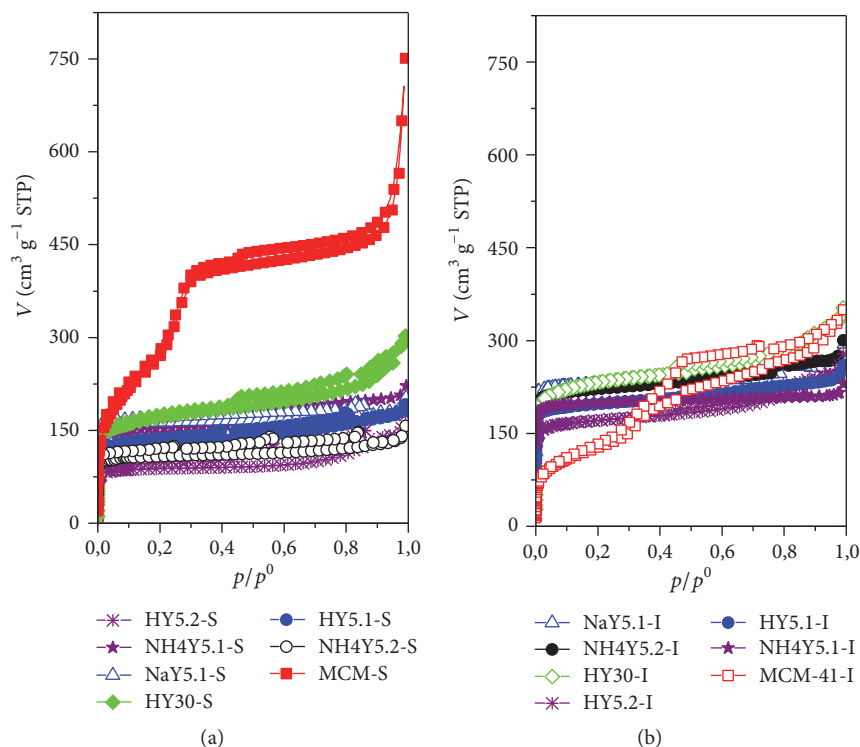


FIGURE 5: N_2 adsorption isotherms at 77 K on Y-zeolites and MCM-41 materials: (a) nonimpregnated and (b) impregnated with ethanolic solution.

Initial Substrates before Impregnation

$$A_{SB} \text{ (m}^2 \text{ g}^{-1}\text{): HY30-S} > \text{NH}_4\text{Y5.2-S} > \text{NaY5.1-S} > \text{HY5.1-S} > \text{NH}_4\text{Y5.1-S} > \text{HY5.2-S}$$

$$V_{\Sigma} \text{ (cm}^3 \text{ g}^{-1}\text{): HY30-S} > \text{NH}_4\text{Y5.2-S} > \text{NaY5.1-S} > \text{HY5.2-S} > \text{NH}_4\text{Y5.1-S} > \text{HY5.1-S}$$

$$W_{0f} \text{ (cm}^3 \text{ g}^{-1}\text{): NaY5.1-S} > \text{HY30-S} > \text{NH}_4\text{Y5.1-S} > \text{NH}_4\text{Y5.2-S} > \text{HY5.1-S} > \text{HY5.2-S}$$

Impregnated Materials

$$A_{SB} \text{ (m}^2 \text{ g}^{-1}\text{): HY30-I} > \text{NaY5.1-I} > \text{NH}_4\text{Y5.2-I} > \text{HY5.1-I} > \text{HY5.2-I} > \text{NH}_4\text{Y5.1-I}$$

$$V_{\Sigma} \text{ (cm}^3 \text{ g}^{-1}\text{): HY30-I} > \text{NH}_4\text{Y5.2-I} > \text{HY5.2-I} > \text{NaY5.1-I} > \text{HY5.1-I} > \text{NH}_4\text{Y5.1-I}$$

$$W_{0f} \text{ (cm}^3 \text{ g}^{-1}\text{): NaY5.1-I} > \text{HY30-I} > \text{NH}_4\text{Y5.2-I} > \text{HY5.1-I} > \text{HY5.2-I} > \text{NH}_4\text{Y5.1-I}$$

Regarding the Y-zeolites, the deposition of the extract is performed on the outer surface area of these materials, and their textural properties do not change noticeably after the impregnation.

3.8. Pore Size Distribution. The pore size distribution (PSD) functions for impregnated samples were obtained by the method of Barrett-Joyner-Halenda, BJH, by using the desorption points of the respective isotherms (Figures 6(a) and 6(b)). It can be seen in Figure 6(a) that PSD curves of Y-zeolites before impregnation produce unimodal distributions

with peaks occurring at specific values of pore diameters for zeolite HY30-S (74 Å) and bimodal (51 and 106 Å) for zeolite NaY5.1-S. It can be noted the MCM-41-S materials possess bimodal distributions arising at 24 and 34 Å. Meanwhile, the PSD distribution curves of the impregnated materials render unimodal distributions for the MCM-41-I specimen centered at 36 Å. The HY5.2-I zeolite sample shows bimodal distributions centered at 26 and 47 Å, Figure 6(b). The results of these PSD estimations are listed in the last column of Table 2.

3.9. Temperature Programmed Desorption (TPD). NH_3 TPD curves associated with the acidity of protonic zeolites, such as HY5.1, HY5.2, and HY30 herein studied, usually, demonstrate peaks in two temperature ranges (see Figure 7). These intervals lie within 150 to 300 K and 350 to 600 K and are referred to as low temperature (LT) and high temperature (HT) intervals, respectively. The peaks in the LT region are attributed to the desorption of weakly bound NH_3 . The peaks in the HT range can be attributed to ammonia desorption from Brønsted acid sites and strong Lewis ones. The maximum temperature desorption peak was used to characterize the strength of acidity according to the classification. The NaY5.1, NH_4 Y5.1, NH_4 Y5.2, HY5.2, and HY30 samples showed NH_3 TPD profiles consistent with those reported in the literature [32]. The NH_4 Y5.1 zeolite has the highest total acidity in the two defined regions. The position of the high-temperatures desorption peak of NH_3 (around 660°C) is the same as the position of dehydroxylation peak. The dehydroxylation and deammoniation occur from the strongest acid sites. The population of these strongest Brønsted sites determined after

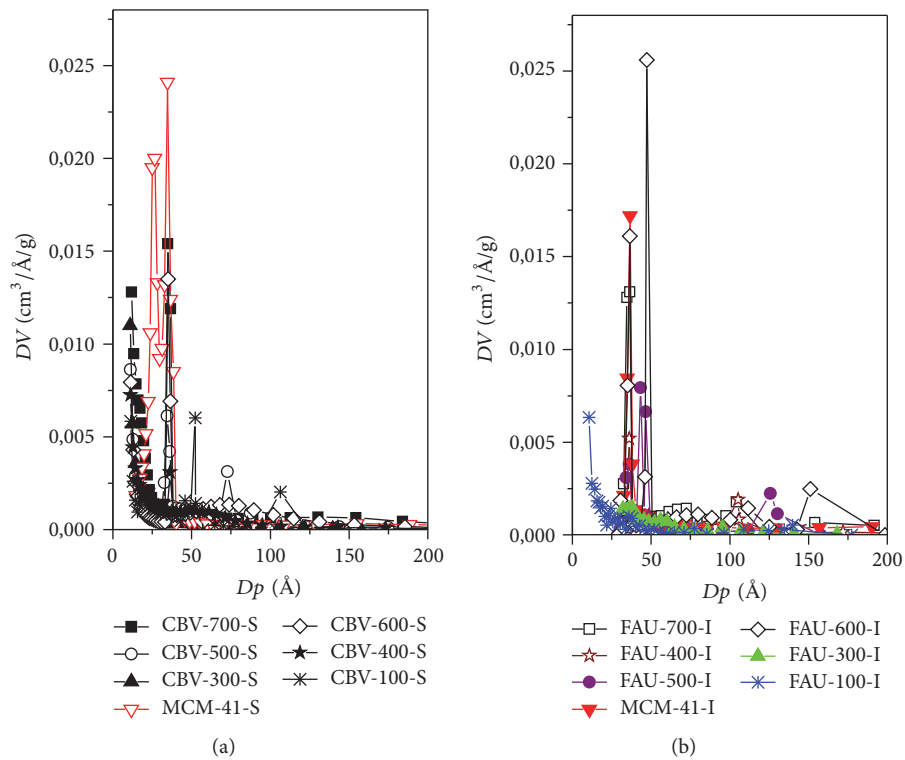


FIGURE 6: PSDs of Y-zeolites and MCM-41 materials calculated from the BJH method: (a) nonimpregnated and (b) impregnated.

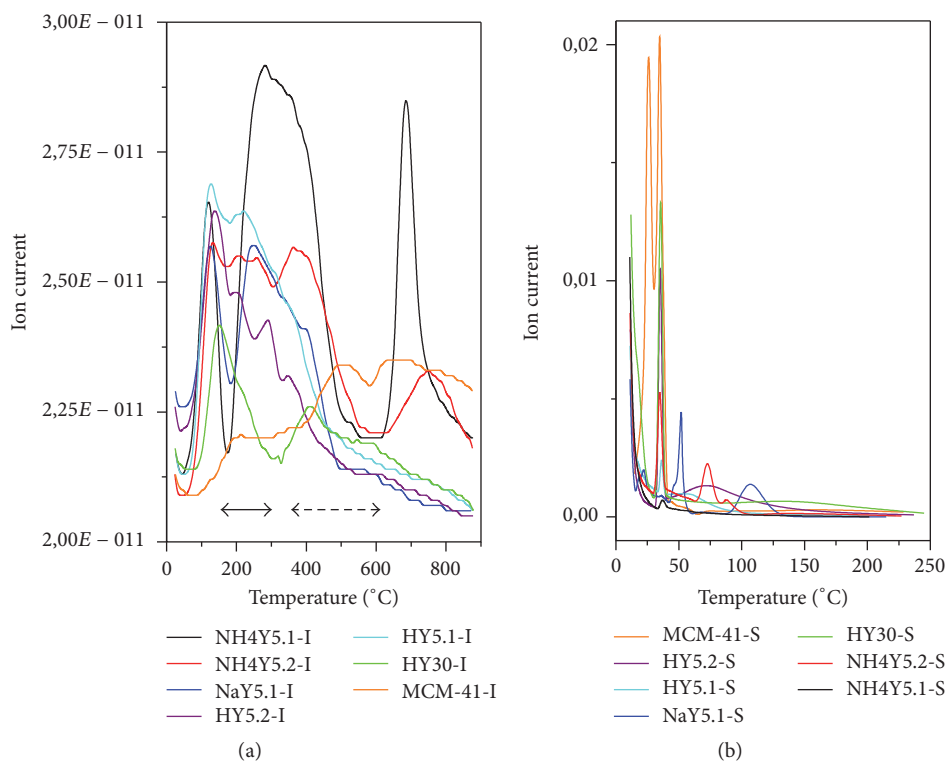


FIGURE 7: TPD of NH_3 in Y-zeolites and MCM-41 materials: (a) impregnated and (b) nonimpregnated.

deconvolution of the TPD spectra is a small fraction of the total number of sites.

4. Conclusions

A group of microporous and mesoporous hybrid materials was obtained; these inorganic substrates were impregnated with a bioactive organic phase. The active phase could be introduced and stabilized inside the internal surface of the voids of MCM-41 materials. Meanwhile, the same extract was deposited on the outer surface of the Y-zeolites. The chemical composition of the ethanol *Tournefortia hirsutissima* L. extract indicates that a group of compounds exists constituting the mixture, in which 1,2-benzenedicarboxylic acid, mono(2-ethylhexyl) ester, and γ -sitosterol prevail as the most abundant compounds. XRD analysis was performed at low and normal angles. N_2 adsorption indicates the adsorption capacity is clearly affected after extract impregnation has been performed in the supporting materials; this appears so since the surface area is covered with the bioactive organic phase and results in a decreasing surface area. The pore size distribution indicates a bimodal pore character for the NaY5.1-S zeolites material while in the case of MCM-41-S the behavior is similar to these materials. On the other hand, HY5.1-I has a bimodal character and renders a multimodal character HY5.2-I, so projecting the HY5.2-I acidity and study shows that there are different acid sites (strengths and weaknesses).

Conflicts of Interest

The authors declare that they have no conflicts of interest.

References

- [1] M. Sun, C. Chen, L. Chen, and B. Su, "Hierarchically porous materials: Synthesis strategies and emerging applications," *Frontiers of Chemical Science and Engineering*, vol. 10, no. 3, pp. 301–347, 2016.
- [2] S. F. Anis, A. Khalil, Saepurahman, G. Singaravel, and R. Hashaikah, "A review on the fabrication of zeolite and mesoporous inorganic nanofibers formation for catalytic applications," *Microporous and Mesoporous Materials*, vol. 236, pp. 176–192, 2016.
- [3] B. Subotić, T. Antičić, and J. J. Bronić, "Theoretical basis of the gel "memory effect" and its implications on the controlling of the particulate properties of zeolites," in *From Zeolites to Porous MOF Materials - The 40th Anniversary of International Zeolite Conference, Proceedings of the 15th International Zeolite Conference*, vol. 170 of *Studies in Surface Science and Catalysis*, pp. 233–241, Elsevier, 2007.
- [4] W. J. Parak, D. Gerion, T. Pellegrino et al., "Biological applications of colloidal nanocrystals," *Nanotechnology*, vol. 14, no. 7, pp. R15–R27, 2003.
- [5] M. Danilczuk, K. Długopolska, T. Ruman, and D. Pogocki, "Molecular sieves in medicine," *Mini reviews in medicinal chemistry*, vol. 8, no. 13, pp. 1407–1417, 2008.
- [6] M. E. Davis, "Ordered porous materials for emerging applications," *Nature*, vol. 417, no. 6891, pp. 813–821, 2002.
- [7] C. Laurino and B. Palmieri, "Zeolite: the magic stone ; main nutritional, environmental, experimental and clinical fields of application," *Nutrición Hospitalaria*, vol. 32, no. 2, pp. 573–581, 2015.
- [8] J. Jiang, R. Babarao, and Z. Hu, "Molecular simulations for energy, environmental and pharmaceutical applications of nanoporous materials: From zeolites, metal-organic frameworks to protein crystals," *Chemical Society Reviews*, vol. 40, no. 7, pp. 3599–3612, 2011.
- [9] L. A. Delouise, "Applications of nanotechnology in dermatology," *Journal of Investigative Dermatology*, vol. 132, no. 3, pp. 964–975, 2012.
- [10] E. Koohsaryan and M. Anbia, "Nanosized and hierarchical zeolites: A short review," *Cuihua Xuebao/Chinese Journal of Catalysis*, vol. 37, no. 4, pp. 447–467, 2016.
- [11] S. E. Lehman and S. C. Larsen, "Zeolite and mesoporous silica nanomaterials: Greener syntheses, environmental applications and biological toxicity," *Environmental Science: Nano*, vol. 1, no. 3, pp. 200–213, 2014.
- [12] A. Datt, N. Ndiege, and S. C. Larsen, "Development of Porous Nanomaterials for Applications in Drug Delivery and Imaging," in *Nanomaterials for Biomedicine*, vol. 1119 of *ACS Symposium Series*, pp. 239–258, American Chemical Society, Washington, DC, 2012.
- [13] C. Colella, "A critical reconsideration of biomedical and veterinary applications of natural zeolites," *Clay Minerals*, vol. 31, no. 2, pp. 295–309, 2011.
- [14] K. Pavelić, M. Hadžija, and L. Bedrica, "Natural zeolite clinoptilolite: new adjuvant in anticancer therapy," *Journal of Molecular Medicine*, vol. 78, no. 12, pp. 708–720, 2001.
- [15] C. Sanchez, P. Belleville, M. Popall, and L. Nicole, "Applications of advanced hybrid organic-inorganic nanomaterials: from laboratory to market," *Chemical Society Reviews*, vol. 40, no. 2, pp. 696–753, 2011.
- [16] The Database of Zeolite Structures, <http://www.iza-structure.org/databases/>.
- [17] S. Calero, "Simulación molecular de la adsorción de hidrocarburos en zeolitas con cationes de intercambio," *Anales de Química*, vol. 102, no. 1, pp. 21–26, 2006.
- [18] L. Zhao, J. G. Yu, X. J. Zhao, B. Cheng, Z. Q. Zhang, and R. Guo, "Research and development of mesoporous nanostructured materials," *Rare Metal Materials Engineering*, vol. 33, no. 1, p. 10, 2004.
- [19] Y. Feng, N. Panwar, D. J. H. Tng, S. C. Tjin, K. Wang, and K.-T. Yong, "The application of mesoporous silica nanoparticle family in cancer theranostics," *Coordination Chemistry Reviews*, vol. 319, pp. 86–109, 2016.
- [20] Y. Wang, Q. Zhao, and N. Han, "Mesoporous silica nanoparticles in drug delivery and biomedical applications," *Nanomedicine: Nanotechnology, Biology and Medicine*, vol. 11, no. 2, pp. 313–327, 2015.
- [21] E. Dündar-Tekkaya and Y. Yürüm, "Mesoporous MCM-41 material for hydrogen storage: A short review," *International Journal of Hydrogen Energy*, vol. 41, no. 23, pp. 9789–9795, 2016.
- [22] M. A. Hernandez, F. Rojas, F. Hernández, and M. A. Salgado, "Nanopore organic-inorganic hybrid materials with properties of cell regeneration: Physicochemical and morphological characterization," in *Proceedings of the 21st International Materials Research Congress, IMRC 2012*, pp. 20–26, Mex, August 2012.
- [23] M. Á. Hernández, F. Rojas, R. Portillo, M. A. Salgado, V. Petranovskii, and K. Quiroz, "Textural Properties of Hybrid Biomedical Materials Made from Extracts of *Tournefortia hirsutissima* L. Imbibed and Deposited on Mesoporous and

- Microporous Materials,” *Journal of Nanomaterials*, vol. 2016, Article ID 1274817, 2016.
- [24] M. M. J. Treacy and J. B. Higgins, *Collection of simulated XRD Powder patterns for zeolites*, Elsevier, Amsterdam, The Netherlands, 4th edition, 2001.
- [25] G. S. Armatas, D. E. Petrakis, and P. J. Pomonis, “A method of distinction between microporosity and mesoporosity using BET-Scatchard plots,” *Microporous and Mesoporous Materials*, vol. 83, no. 1-3, pp. 251–261, 2005.
- [26] F. Rouquerol, J. Rouquerol, K. S. W. Sing, P. Llewellyn, and G. Maurin, *Adsorption by Powders and Porous Solids*, Elsevier, Amsterdam, The Netherlands, 2014.
- [27] M. J. Remy and G. Poncelet, “A new approach to the determination of the external surface and micropore volume of zeolites from the nitrogen adsorption isotherm at 77 K,” *Journal of Physical Chemistry*, vol. 99, no. 2, pp. 773–779, 1995.
- [28] R. A. Roberts, K. S. W. Sing, and V. Tripathi, “Adsorption of nitrogen and neopentane vapor by microporous carbons,” *Langmuir*, vol. 3, no. 3, pp. 331–335, 1987.
- [29] J. C. Groen, L. A. A. Peffer, and J. Pérez-Ramírez, “Pore size determination in modified micro- and mesoporous materials. Pitfalls and limitations in gas adsorption data analysis,” *Microporous and Mesoporous Materials*, vol. 60, no. 1-3, pp. 1–17, 2003.
- [30] C. K. Modi and P. M. Trivedi, “Synthesis, characterization and catalytic behaviour of entrapped transition metal complexes into the zeolite Y,” *Advanced Materials Letters*, vol. 3, no. 2, pp. 149–153, 2012.
- [31] M. Thommes, K. Kaneko, A. V. Neimark et al., “Physisorption of gases, with special reference to the evaluation of surface area and pore size distribution (IUPAC Technical Report),” *Pure and Applied Chemistry*, vol. 87, no. 9-10, pp. 1051–1069, 2015.
- [32] V. Dondur, V. Rakić, L. Damjanović, and A. Auroux, “Comparative study of the active sites in zeolites by different probe molecules,” *Journal of the Serbian Chemical Society*, vol. 70, no. 3, pp. 457–474, 2005.

Review Article

Nanosized Minicells Generated by Lactic Acid Bacteria for Drug Delivery

Huu Ngoc Nguyen,¹ Santa Romero Jovel,² and Tu Hoang Khue Nguyen¹

¹*School of Biotechnology, International University, Vietnam National University, Hochiminh City, Quarter 6, Linh Trung Ward, Thu Duc District, Hochiminh City, Vietnam*

²*National Scientific Research Center of El Salvador, Alameda Juan Pablo II y Calle Guadalupe, Plan Maestro Edif. A4, 3er Nivel DNICTI, San Salvador, El Salvador*

Correspondence should be addressed to Tu Hoang Khue Nguyen; nhktu@hcmiu.edu.vn

Received 4 May 2017; Accepted 25 July 2017; Published 7 September 2017

Academic Editor: Sohel Rana

Copyright © 2017 Huu Ngoc Nguyen et al. This is an open access article distributed under the Creative Commons Attribution License, which permits unrestricted use, distribution, and reproduction in any medium, provided the original work is properly cited.

Nanotechnology has the ability to target specific areas of the body, controlling the drug release and significantly increasing the bioavailability of active compounds. Organic and inorganic nanoparticles have been developed for drug delivery systems. Many delivery systems are through clinical stages for development and market. Minicell, a nanosized cell generated by bacteria, is a potential particle for drug delivery because of its size, safety, and biodegradability. Minicells produced by bacteria could drive therapeutic agents against cancer, microbial infection, and other diseases by targeting. In addition, minicells generated by lactic acid bacteria being probiotics are more interesting than others because of their benefits like safety, immunological improvement, and biodegradation. This review aims to highlight the stages of development of nanoparticle for drug delivery and discuss their advantages and limitations to clarify minicells as a new opportunity for the development of potential nanoparticle for drug delivery.

1. Introduction

There are many researches concentrating on the ways of delivering drugs directly to tumor tissue. Drug delivery undergoes many stages consisting of entering the body, passing through the blood-stream to cancerous cells [1, 2]. Furthermore, drug delivery system is developed to achieve a higher degree of tumor cell specificity and reduce side effects. However, nanoparticle could also accumulate in the liver and the spleen, where they provide no therapeutic benefit and can cause side effects [3, 4]. To minimize unwanted effects, researchers developed biodegradable materials. The first biodegradable nanoparticles to be developed for drug delivery coated the active agent with lipids [5]. The first drug of this type to be approved was Doxil in 1995 [6]. According to the US National Cancer Institute, six nanoparticles are currently approved for use on the market worldwide, while these costs of products were higher ten times than conventional treatment [7, 8].

Recently, using bacterially derived nanosized particles to package a range of different chemotherapeutic drugs is a

new technology that is specifically targeting the minicells to tumor cell surface receptors via bispecific antibodies coating the minicells. Minicells loading drugs could have effect on the apoptosis of tumor cells both in vitro and in vivo. They also targeted cancer cells in vivo with high specificity and effectivity without toxicity [9].

The minicells are generated from mutant bacteria and kept their cell membrane structure. The minicells could load chemicals as anticancer drugs and are coated with antibodies to bind the specific receptors on the surface. The cancer cells recognize the bacterial minicells and then swallow these minicells with cancer killing drug. In previous study for phase I, minicells were loaded with a cytotoxic chemotherapy drug called paclitaxel and coated with an antibody targeting tumors expressing the epidermal growth factor receptor (EGFR) for treating small groups of patients [10, 11].

The purpose of this review was to discuss the positive and negative effects of nanotechnology for drug delivery and propose novel biodegradable nanocells originating from lactic acid bacteria due to their benefits.

2. General Nanoparticle

Nanotechnology was first defined in 1974 by Norio Taniguchi that is the engineering technology for understanding and control of matter at the length scale of approximately 1 to 100 nanometers [1]. Numerous nanomaterials preparations have been potentially applied for drug delivery system to therapeutics. Several nanosized preparations such as liposomes, polymeric micelles, and polymeric-drug conjugates have been developed in vitro, while others undertake preclinical studies [12, 13]. Besides, some successful nanosized preparations have already emerged in today's pharmaceutical market and showed better clinical performance than traditional drugs [14, 15]. The properties including size, surface charge, shape, and density of surface associated ligands can allow nanoparticles to avoid renal clearance but reach the designated cellular destinations in sufficient amounts, eliciting a biological response with minimal nonspecific interactions [16].

Nanoparticles are the best drug delivery systems that can be administered via intravenous injection or other routes based on their sizes [17]. The materials for nanoparticle preparation are not only biological like lactic acid, dextran, phospholipids, lipids, carbon, and chitosan but also chemical like polymers, silica, and metals [18–21]. Each nanoparticle had a special property in drug delivery. Even though solid nanoparticles may be used for drug targeting, the delivered drug must escape after reaching the target. Therefore, nanoparticle should be structured well to let the drug be released effectively.

Currently, there are several products already available on the market, while many others are in the preclinical-to-clinical pipeline. The major interest in cancer therapy is also reflected in an important industry. Some currently marketed nanotherapeutics in cancer therapy are liposomes, nanoparticles, nanocapsules, nanoemulsions, nanocrystals, and micelles [22–26]. However, nanomedicines currently approved for cancer therapy are mostly liposomes. Other products are in advanced clinical trials. Several others are at earlier stages of clinical trials or in preclinical phase.

Over the last years, the importance of bridging together nanotechnology and cancer therapy has been realized. The National Cancer Institute (NCI) in US has created the NCI Alliance for Nanotechnology in Cancer [27, 28] and the European Science Foundation has also issued a report in analyzing the situation of nanomedicine in Europe [29, 30]. They have designated nanotechnology and its applications to biomedicine as one of its major priority research areas.

3. Advantage of Nanomedicine

Targeted drug delivery system is developed to achieve a higher degree of tumor cell specificity but also reduces side effects. Active targeting of nanoparticles is the merging of target sections such as ligands or antibodies on the surface of nanocarriers to specific receptors on the tumor cells and endothelium shown on Figure 1 [31–34]. The active targeting increases the selectivity of the drug delivery. Furthermore,

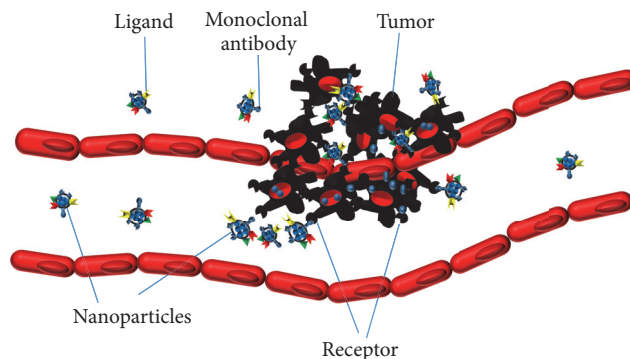


FIGURE 1: Nanoparticles coated with monoclonal antibody for specific activity.

nanocarriers have a high surface area allowing for multiple ligands to combine on their surfaces to direct cells and have some drawbacks [35, 36]. Nanoparticles combined with ligands to reduce toxicity due to avoiding the nonspecific binding and then decrease multidrug resistance in tumor cells as well [37].

Based on the expression of receptors or epitopes on the cell surface, nanoparticles could bind to target cells through ligand receptor interaction. Internalization of targeting conjugates can also occur by receptor-mediated endocytosis after binding to target cells; then drug will be released inside the cells (Figure 2) [38, 39]. The conjugates bind with their receptors, followed by plasma membrane enclosure around the ligand receptor complex to form an endosome based on the receptor-mediated endocytosis mechanism. The newly formed endosome is transferred to specific organelles where drug was released by acidic pH or enzymes [40].

On the other hand, nanoparticle used to improve a drug formulation could be served as an alternative to conventional administration vehicles, which are sometimes toxic; for example, the potent chemotherapeutic paclitaxel is not soluble in water. Under the trade name as Taxol[®], paclitaxel is dissolved in cremophor EL, a polyoxyethylated castor oil, which is toxic. Abraxane[®], an albumin-bound form of paclitaxel, uses the nanotech platform of albumin as an alternative to cremophor EL. Abraxane has been shown to be both more efficacious and less toxic than Taxol [41, 42].

3.1. The Increase of Drug Stability. Many drugs used in anticancer therapy are unstable even under mild conditions. Low molecular weight drugs suffer degradation by diverse mechanisms as photochemical reactions, oxidation, hydrolysis, and so on [43]. Polypeptide drugs can be partially denatured during storage and lose their activities. Nanocarriers can increase the stability of many anticancer drugs by integrating them into their structure. For instance, doxorubicin is quickly degraded upon exposure to light, whereas doxorubicin entrapped into nanoparticles maintains its biological activity under the same conditions [44]. The stability of doxorubicin has also been increased through its incorporation into liposomes [45]. In the same way, paclitaxel

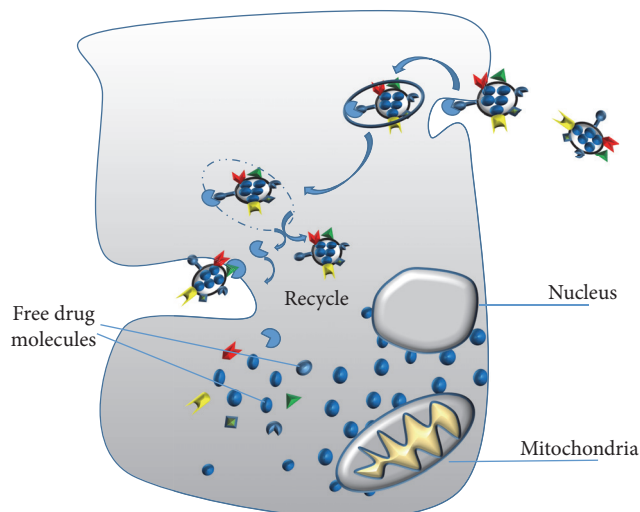


FIGURE 2: Schematic drawing of the drug release and organelle-specific targeting of drug loaded nanoparticles via endocytosis.

used for the antineoplastic treatment was formulated in a surfactant/alcohol mixture and increased the shelf-life to 71 days at 25°C, and its stability is reduced even further upon dilution [46, 47]. Previous study reported a beneficial effect on long-term DNA stability when this molecule was complexed to polymeric micelles [48, 49].

3.2. The Improvement of Drug Administration and Absorption

3.2.1. Oral Administration. In general terms, anticancer drugs have low oral bioavailability. For large macromolecules, this is related to their fast enzymatic degradation and their inefficiency in crossing biological barriers [50, 51]. For hydrophobic drugs, their main limitation is their low solubility at the absorption site, but also their biodegradation. The case of many conventional hydrophobic drugs is finely illustrated by paclitaxel [52, 53]. This molecule has low oral bioavailability in conventional formulations because most of the drug is eliminated through the cytochrome P450-dependent metabolism and excreted by the P-glycoprotein pump present in the intestinal wall [54–56]. Nanosystems may improve drug absorption in oral chemotherapy by protecting the drug, enhancing its residence time at the absorption site or through the inhibition of efflux pumps. Previous studies reported that new d- α -tocopheryl-PEG succinate nanoparticles could be used for oral delivery of paclitaxel [57–59]. On the other hand, liposomes formed by a blend of collagen and carrageenan polymeric core were also found to enhance the permeability of 5-fluorouracil (5-FU) and methotrexate crossing the Caco-2 and TC7 monolayers [23].

3.2.2. Parenteral Administration. Parenteral formulations have the additional advantage of drug absorption. However, the preparation of injectable formulations of many hydrophobic drugs is very low water solubility. Indeed, intravenous injection of these drugs may cause embolization

of blood vessels due to drug aggregation, and ultimately, local toxicity as a result of high drug concentrations at the site of deposition [60, 61]. Cremophor EL (Taxol) has been the standard solvent system for paclitaxel including clinically relevant acute hypersensitivity reactions and peripheral neuropathy [62]. Moreover, paclitaxel-loaded albumin nanoparticles (Abraxane or ABI-007) have recently been approved by FDA for the treatment of metastatic breast cancer [23].

3.3. Increase in Blood Circulation. Changes in drug biodistribution and accumulation in the target tissues can be achieved through the incorporation of these drugs into specific nanocarriers. Classical nonselective nanocarriers are known to be opsonized and rapidly cleared by the mononuclear phagocytic systems (MPS) which is predominantly distributed in liver, lungs, spleen, and bone marrow [23, 63]. This uptake can be very advantageous for the chemotherapeutic treatment of MPS-localized tumors like hepatocarcinoma or hepatic metastasis. This therapeutic benefit has been observed with doxorubicin in a murine hepatic metastases model when this drug was incorporated into biodegradable poly(alkylcyanoacrylate) nanoparticles [64–66]. Polyethylglycol has been applied to enhance the plasmatic half-life of several nanocarriers including liposomes and micelles [67–69].

3.4. Active Targeting to the Cancer Cells. Nanomedicine designed to actively target cancer cells showed high binding affinity to its receptor on cancer cells. Specific monoclonal antibodies were able to bind to corresponding tumor antigens [12, 70, 71]. At present, there are several formulations comprising antibodies approved or undergoing clinical trials. For example, Mylotarg[®] conjugated with CD33 antibody and Zevalin[®] and Bexxar[®] conjugated with two CD20 have already been approved by the FDA [72]. A liposome-plasmid DNA formulation (SGT-53) that uses an antibody fragment for tumor targeting is currently in phase I clinical trial [23, 73]. The other work reported that there were encapsulated antineoplastic drugs in bacterially derived nanosized delivery system linked with antibodies to the target [74]. Actively targeted minicells resulted in antitumor effects enhanced efficacy even compared to other less sophisticated nanomedicines.

4. Challenges of Nanoparticles

However, there are limited reports about the effects of nanoparticles on the body. It is difficult to predict the long-term effects on our health. Nanoparticles have large surface that helps them react very quick [75]. A metal nanoparticle is an example that they might speed up reactions in living things in unpredictable ways causing illness or death [75, 76]. Furthermore, nanoparticles have ability in antimicrobial activities but also they may kill benefit bacterial communities in the intestinal tract. Besides, there are chemicals or physical systems applied to maintain them to retain their nanoscale properties because nanoparticles are easy to aggregate or club together [77, 78].

In addition, drug delivery system in nanoparticles is more expensive to produce when compared with traditional materials due to containing lots of complicated steps [19, 79]. Therefore, it is difficult to scale up nanoparticle production leading to limitation in market production. More importantly, the human immune system may be defenseless against particles on the nanoscale [80–82]. As a result, tiny solid particles can cause irritation in the lungs and potentially cause lung damage and cancer. In summary, nanoparticles are usually reported in a positive way because of their exciting potential applications in drug delivery. However, a nanoparticle is also a risk due to their unknown side effects and bioavailability that have not been reported yet [18, 83–87].

Nanoparticles used as drug delivery are more and more popular with a lot of challenges in pharmaceutical engineering. There are many reports about nanotoxicology, the potential negative impact of the interactions between nanomaterials and biological systems. For example, naked quantum dots show cytotoxicity by induction of reactive oxygen species, resulting in damage to the nucleus, mitochondria, and plasma membranes [18, 88]. Furthermore, cadmium-(Cd-) containing quantum dots have been reported to be toxic due to the release of free Cd²⁺ ions [89, 90]. Gold (Au) solution has not been considered to present a hazard, and gold nanoparticles (Au NPs) have been taken up by cells without cytotoxic effects [91, 92]. By contrast, gold nanorod cytotoxicity could be attributed to the presence of the stabilizer cetyltrimethylammonium bromide [93, 94]. For silica nanoparticles (NPs), only concentrations over 0.1 mg/ml were found to be toxic as shown in a reduction of cell availability and proliferation [18, 94]. The production of carbon nanotubes also causes reactive oxygen species generation, mitochondria dysfunction, lipid peroxidation, and changes in cell morphology, while graphite and fullerene produce no significant adverse effects [18, 95, 96]. In addition, it was reported that most cationic NPs can cause hemolysis and blood clotting, while neutral and anionic NPs are quite nontoxic [40, 97].

Another challenge facing nanosized drug delivery is the large scale production of nanomaterials in terms of scaling up laboratory or pilot technologies for commercialization. A number of nanosized drug delivery technologies may not be compatible with large scale production due to the nature of the preparation method and high cost of materials [98]. The challenges of scaling up include a low concentration of nanomaterials, agglomeration, and the chemistry process [99–101].

Generally, most drugs do not cross the blood brain barrier (BBB). The endothelial barrier is specifically tight at the interface with the brain astrocytes and can be in normal conditions only being passed using endogenous BBB transport or receptor-mediated transport [18, 102, 103]. However, the barrier properties may be compromised intentionally or unintentionally by drug treatment allowing passage of nanoparticles [104–107]. The drugs delivered by nanocarrier to pass through blood brain barrier were recently reviewed [108, 109].

5. Nanosized Delivery Generated by Microorganisms

Minicells are one of nanoparticles generated from bacteria that can deliver active compounds to reduce the side effects and improve bioavailability of the treatment [110]. Minicells are chromosomal cells containing RNA and protein but little or without chromosomal DNA. There are lots of applications of minicells reported as delivery for therapeutics, nucleic acids, and other bioactive compounds to target cells. MacDiarmid introduced minicells generated by *Shigella flexneri*, *Pseudomonas aeruginosa*, *Salmonella typhimurium*, *Escherichia coli*, and *Listeria monocytogenes* with diameter about 400 nm [9]. In addition, *Lactobacillus rhamnosus* and *Lactobacillus acidophilus* could generate minicells with nanosize as well [111–113].

During the cell division cycle, the cells must identify the mid-cell site prepared for cytokinesis and division septum (Figure 3). For example, the mutants in *E. coli* were divided into two groups, fts mutants (temperature sensitive filamentation) and par mutants (partition). There are many important proteins involved in the division cycle. FtsZ is one of proteins that play a significant role in the division process of *E. coli* [114, 115]. In previous report, MacDiarmid and colleagues described bacterial minicells encapsulated chemotherapeutics guided by antibodies to deliver their load to target cells. Minicells have diameter of 400 nm produced from both Gram-positive and Gram-negative bacteria. Furthermore, the minicells were loaded with different chemotherapeutics in hydrophobic and hydrophilic forms. Besides, minicells could lead to the targeted tumor cells with bispecific antibodies of epidermal growth factor receptor (EGFR), HER2/neu (ERBB2), CD33, or CD3 [116–118].

Minicell formation related to cell division inhibitor genes of *ftsZ*, *minBCD* locus causing asymmetrical division at mid-cell leading to cells of different sizes including minicells as well as filaments. The minicells were isolated and showed the stable round shape. Minicells keep the rigid cell wall structure of 20 kinds of lipopolysaccharide like their parental bacteria [119]. The pathogen strains could produce minicells applied to vaccine but not complete safe for patient compared to lactic acid bacteria strains [120]. Therefore, minicells generated by lactic acid bacteria that are probiotic strain should be more interesting than others.

The Gram-positive cell wall of lactic acid bacteria consists mainly of peptidoglycans, (lipo)teichoic acids, proteins, and polysaccharides [121]. The inner layer of the cell wall consists of a peptidoglycan network covered by a variety of substances. The most important of these substances are (lipo)teichoic acids, neutral and acidic polysaccharides, and surface proteins [122]. Teichoic acids are the negative charged polymers constituted with polyol phosphate that linked to the peptidoglycan [122, 123].

The polysaccharides associated with the bacterial cell walls and the extracellular polysaccharides of lactic acid bacteria are either neutral or acidic [120, 121]. There are abundance polysaccharides at the outer surface of the cell wall and extracellular. The most abundant surface proteins in many *Lactobacillus* species are the S-layer proteins [122, 124, 125].

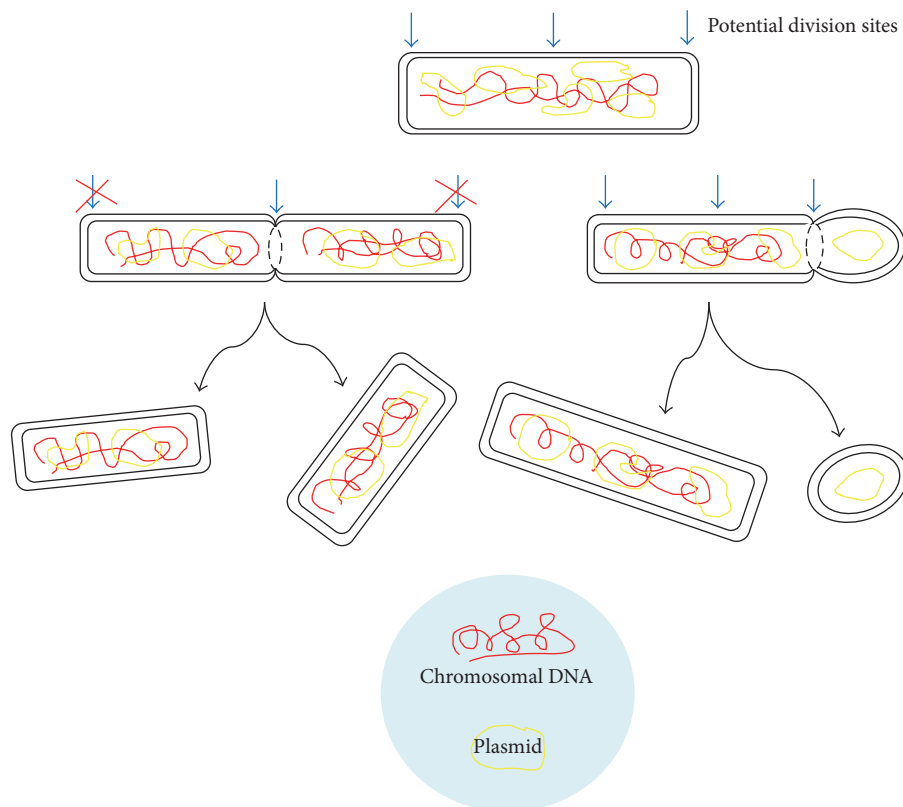


FIGURE 3: Bacterial minicell formation.

To date, S-layers have been found in *L. brevis*, *L. acidophilus*, *L. crispatus*, *L. helveticus*, *L. amylovorus*, and *L. gallinarum*. S-layer proteins are usually small proteins of 40–60 kDa with generally highly stable tertiary structures [126]. *L. rhamnosus* and *L. acidophilus* in combination with glucose and fructose occurred to produce the highest minicells with the size less than 400 nm that could be used as nanocells in delivering cisplatin, paclitaxel, and cephalosporin [111–113].

6. Minicell Loading with Different Drugs

Interestingly, minicells can be packaged with 1–10 million drug molecules [18]. Minicells pass through tumor cells by receptor-mediated endocytosis. In *in vivo* experiments, doxorubicin loading minicells inhibited tumor growth in mice as breast, ovarian, leukemia, or lung [127]. Importantly, comparatively small amounts of doxorubicin could induce tumor regression in liposome encapsulation. The anticancer efficacy of the minicells was further evaluated in dogs having T-cell non-Hodgkin's lymphoma by tumor regression and tumor lysis [116]. Importantly, many researches showed that minicells did not have side effects such as proinflammatory cytokine increase after repeating the doses. Other experiments in animals were also performed and pointed that there were no adverse reactions [128]. Minicells derived from bacteria have been used for the first time in human with the significantly safe, well-tolerated results. Solomon et al. reported that minicells packaged paclitaxel and coated with antibody targeting to tumors expressing EGFR of many

TABLE 1: Functional groups detected in bacteria.

Functional group	Interaction or reaction
Hydroxyl	Carbonyl, aromatic, alkyl groups or a carbon atom
Carboxyl	Acid-base
Phosphoryl	Group transfer
Amide	Acid-base
Phosphate	Acid-base
Carbohydrate	Protein, enzyme

cancer cells. The study was then conducted in phase I with small groups of patients. Minicells loaded with doxorubicin were also continuously tested in phase II in patients with glioblastoma (a type of brain tumor) [128, 129].

However, *Lactobacillus* species being the safe microorganisms with many biological activities in anticancer and immunotherapy, they were used to generate nanosized minicells tested in drug delivery. Due to living cells, *Lactobacillus* minicells are the place of different reactions. Therefore, minicells containing a variety of functional groups mentioned in Table 1 can bind with different compounds easily when they meet together. Minicells from *Lactobacillus* could show their own activities and load with hydrophilic and hydrophobic drugs as well, for example, paclitaxel and cephalosporin (Figure 4) [111]. Hydrogen bond in minicells could help

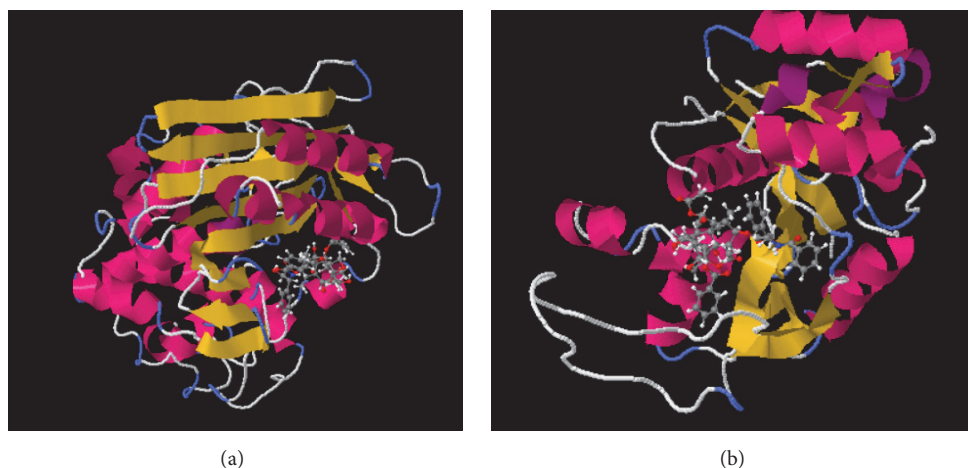


FIGURE 4: The interaction between minicell membrane and molecule. (a) Interaction between teichoic acid and paclitaxel. (b) Interaction between dd-transpeptidase and paclitaxel.

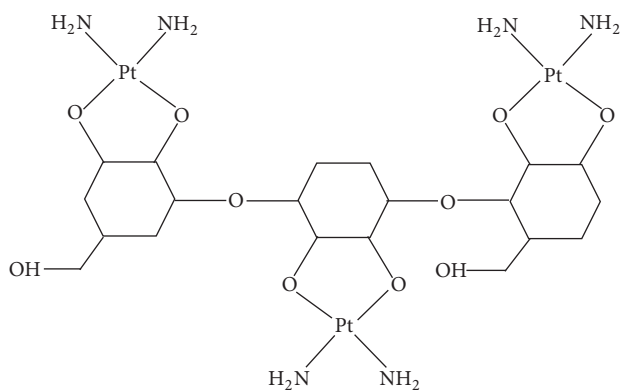


FIGURE 5: Model of exopolysaccharide representative in the interaction with cisplatin.

in loading drug molecules. Using docking to explain the interaction of drug to minicells, paclitaxel binds to dd-transpeptidase and teichoic acid of minicell membrane by the interaction with many residues by hydrogen bonds. The average binding energy is -7 to -10 . In the other illustration for drug loading of minicells, exopolysaccharide could bind to cisplatin as presented in Figure 5. With the interaction, cisplatin could be released out of minicells to show activities. Moreover, minicells have the cell walls that make many drugs pass through by concentration gradient. Generally, the model of drug loading was showed as in Figure 6.

7. Minicells Avoid Phagocytosis

There were many arguments that minicells used in treatment could be phagocytosed. However, by experiments, minicells could go inside and outside the macrophages. They can be stable in about 6 hours. Actually, minicells loaded doxorubicin could be used in trials and treat cancer in the volunteers. Remarkably, minicells can be an ideal drug delivery because of safety, biodegradability, and avoiding

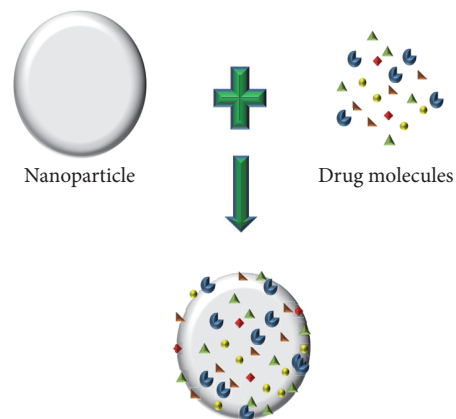


FIGURE 6: The model of drug molecules loaded by minicells.

of phagocytosis. Minicells produced from *L. acidophilus* in sugar stress remained stable in storage at -80°C for long time.

8. Conclusions

The nanoparticle development for drug delivery is interesting in therapy. The majority of properties of minicells generated by lactic acid bacteria are nanosized, round shape which is suitable for drug delivery. Multifunctional nanoparticles delivering multiple drugs are now being developed for enhanced detection and treatment of cancer. Furthermore, lactic acid bacteria are used in pharmaceutical field and food industry. Minicells generated by lactic acid bacteria are a biodegradable system which is excellent vehicle for delivery of drugs and vaccines. The application of minicells to cancer has a great promise for cancer patients in the future.

Abbreviations

EGFR: Epidermal growth factor receptor
MPS: Mononuclear phagocytic systems.

Conflicts of Interest

There are no conflicts of interest in all authors regarding the publication of this paper.

References

- [1] R. E. Serda, B. Godin, E. Blanco, C. Chiappini, and M. Ferrari, "Multi-stage delivery nano-particle systems for therapeutic applications," *Biochimica et Biophysica Acta - General Subjects*, vol. 1810, no. 3, pp. 317–329, 2011.
- [2] J. Wright, "Nanotechnology: Deliver on a promise," *Scientific American*, vol. 311, no. 1, pp. S12–S13, 2014.
- [3] M. E. Davis and D. M. Shin, "Nanoparticle therapeutics: an emerging treatment modality for cancer," *Rev Drug Discov*, vol. 7, pp. 771–782, 2008.
- [4] V. J. Mohanraj and Y. Chen, "Nanoparticles—a review," *Trop J Pharm Res*, vol. 5, pp. 561–573, 2006.
- [5] J. Panyam and V. Labhasetwar, "Biodegradable nanoparticles for drug and gene delivery to cells and tissue," *Advanced Drug Delivery Reviews*, vol. 55, no. 3, pp. 329–347, 2003.
- [6] Y. Barenholz, "Doxil: the first FDA-approved nano-drug: lessons learned," *Journal of Controlled Release*, vol. 160, no. 2, pp. 117–134, 2012.
- [7] G. Pillai, "Nanomedicines for Cancer Therapy: An Update of FDA Approved and Those under Various Stages of Development," *SOJ Pharmacy & Pharmaceutical Sciences*, vol. 1, no. 2, 2014.
- [8] V. Weissig, T. K. Pettinger, and N. Murdock, "Nanopharmaceuticals (part 1): products on the market," *International journal of nanomedicine*, vol. 9, pp. 4357–4373, 2014.
- [9] J. A. MacDiarmid, N. B. Mugridge, J. C. Weiss et al., "Bacterially Derived 400 nm particles for encapsulation and cancer cell targeting of chemotherapeutics," *Cancer Cell*, vol. 11, no. 5, pp. 431–445, 2007.
- [10] D. Gastaldi, D. Zonari, and F. Dosio, "Targeted taxane delivery systems: recent advances," *Deliv Lett*, pp. 105–117, 2011.
- [11] Y. D. Livney and Y. G. Assaraf, "Rationally designed nanovehicles to overcome cancer chemoresistance," *Advanced Drug Delivery Reviews*, vol. 65, no. 13–14, pp. 1716–1730, 2013.
- [12] R. Gaspar and R. Duncan, "Polymeric carriers: preclinical safety and the regulatory implications for design and development of polymer therapeutics," *Drug Deliv Rev*, vol. 61, pp. 1220–1231, 2009.
- [13] R. Duncan and M. J. Vicent, "Do HPMA copolymer conjugates have a future as clinically useful nanomedicines? a critical overview of current status and future opportunities," *Drug Deliv Rev*, vol. 62, pp. 272–282, 2010.
- [14] R. Duncan, "Polymer therapeutics: top 10 selling pharmaceuticals—what next?" *Journal of Controlled Release*, vol. 190, pp. 371–380, 2014.
- [15] J. Miller, "Beyond biotechnology: FDA regulation of nanomedicine," *Sci Technol Law Rev*, 2003.
- [16] S. Biswas and V. P. Torchilin, "Nanopreparations for organelle-specific delivery in cancer," *Advanced Drug Delivery Reviews*, vol. 66, pp. 26–41, 2014.
- [17] L. Brannon-Peppas and J. O. Blanchette, "Nanoparticle and targeted systems for cancer therapy," *Drug Deliv Rev*, vol. 64, 2012.
- [18] W. H. De Jong and P. J. Borm, "Drug delivery and nanoparticles: applications and hazards," *Int J Nanomedicine*, vol. 3, pp. 133–149, 2008.
- [19] R. Singh and J. W. Lillard, "Nanoparticle-based targeted drug delivery," *Exp Mol Pathol*, vol. 86, pp. 215–223, 2009.
- [20] N. T. Thanh and L. A. Green, "Functionalisation of nanoparticles for biomedical applications," *Nano Today*, vol. 5, pp. 213–230, 2010.
- [21] M. Athar and A. J. Das, "Therapeutic nanoparticles: state-of-the-art of nanomedicine," *Ad Mater Rev*, vol. 1, pp. 25–37, 2014.
- [22] A. Hafner, J. Lovrić, G. P. Lakö, and I. Pepić, "Nanotherapeutics in the EU: An overview on current state and future directions," *International Journal of Nanomedicine*, vol. 9, no. 1, article no. 1005, pp. 1005–1023, 2014.
- [23] P. Hervella, V. Lozano, M. Garcia-Fuentes, and M. J. Alonso, "Nanomedicine, new challenges and opportunities in cancer therapy," *J Biomed Nanotechnol*, vol. 4, pp. 276–292, 2008.
- [24] C. M. J. Hu, S. Aryal, and L. Zhang, "Nanoparticle-assisted combination therapies for effective cancer treatment," *Ther Deliv*, vol. 1, pp. 323–334, 2010.
- [25] M. L. Etheridge, S. A. Campbell, A. G. Erdman, C. L. Haynes, S. M. Wolf, and J. McCullough, "The big picture on nanomedicine: the state of investigational and approved nanomedicine products," *Nanomedicine: Nanotechnology, Biology, and Medicine*, vol. 9, no. 1, pp. 1–14, 2013.
- [26] S. Swain, P. K. Sahu, S. Beg, and S. M. Babu, "Nanoparticles for cancer targeting: Current and future directions," *Current Drug Delivery*, vol. 13, no. 8, pp. 1290–1302, 2016.
- [27] E. S. Kawasaki and A. Player, "Nanotechnology, nanomedicine, and the development of new, effective therapies for cancer," *Nanomedicine: Nanotechnology, Biology, and Medicine*, vol. 1, no. 2, pp. 101–109, 2005.
- [28] B. Ehdai, "Application of nanotechnology in cancer research: review of progress in the National Cancer Institute's alliance for nanotechnology," *International Journal of Biological Sciences*, vol. 3, no. 2, pp. 108–110, 2007.
- [29] G. Guerra, "European regulatory issues in nanomedicine," *NanoEthics*, vol. 2, no. 1, pp. 87–97, 2008.
- [30] M. Hofmann-Amttenbrink, H. Hofmann, A. Hool, and F. Roubert, "Nanotechnology in medicine: European research and its implications," *Swiss Med Wkly*, vol. 144, 2014.
- [31] M. Wang and M. Thanou, "Targeting nanoparticles to cancer," *Pharmacol Res*, vol. 62, pp. 90–99, 2010.
- [32] N. Nasongkla, E. Bey, J. Ren et al., "Multifunctional polymeric micelles as cancer-targeted, MRI-ultrasensitive drug delivery systems," *Nano Letters*, vol. 6, pp. 2427–2430, 2006.
- [33] E. Pérez-Herrero and A. Fernández-Medarde, "Advanced targeted therapies in cancer: drug nanocarriers, the future of chemotherapy," *Eur J Pharm Biopharm*, vol. 93, pp. 52–79, 2015.
- [34] R. M. Sawant, J. P. Hurley, S. Salmaso et al., "'SMART' drug delivery systems: double-targeted pH-responsive pharmaceutical nanocarriers," *Bioconjug Chem*, vol. 17, pp. 943–949, 2006.
- [35] N. Kamaly, Z. Xiao, P. M. Valencia, A. F. Radovic-Moreno, and O. C. Farokhzad, "Targeted polymeric therapeutic nanoparticles: design, development and clinical translation," *ChemSoc Rev*, vol. 41, pp. 2971–3010, 2012.
- [36] O. Veiseh, J. W. Gunn, and M. Zhang, "Design and fabrication of magnetic nanoparticles for targeted drug delivery and imaging," *Adv Drug Deliv Rev*, vol. 62, pp. 284–304, 2010.
- [37] J. D. Byrne, T. Betancourt, and L. Brannon-Peppas, "Active targeting schemes for nanoparticle systems in cancer therapeutics," *Advanced Drug Delivery Reviews*, vol. 60, no. 15, pp. 1615–1626, 2008.

- [38] L. M. Bareford and P. W. Swaan, "Endocytic mechanisms for targeted drug delivery," *Advanced Drug Delivery Reviews*, vol. 59, no. 8, pp. 748–758, 2007.
- [39] K. Cho, X. U. Wang, S. Nie, and D. M. Shin, "Therapeutic nanoparticles for drug delivery in cancer," *Clin Cancer Res*, vol. 14, pp. 1310–1316, 2008.
- [40] S. Bamrungsap, Z. Zhao, T. Chen et al., "Nanotechnology in therapeutics: a focus on nanoparticles as a drug delivery system," *Nanomedicine*, vol. 7, no. 8, pp. 1253–1271, 2012.
- [41] S. E. McNeil, *Unique Benefits of Nanotechnology to Drug Delivery and Diagnostics*, Humana Press, 2011.
- [42] M. S. Surapaneni, S. K. Das, and N. G. Das, "Designing Paclitaxel drug delivery systems aimed at improved patient outcomes: current status and challenges," *ISRN pharmacology*, 2012.
- [43] J. H. Park, G. Saravanakumar, K. Kim, and I. C. Kwon, "Targeted delivery of low molecular drugs using chitosan and its derivatives," *Adv Drug Deliv Rev*, vol. 62, pp. 28–41, 2010.
- [44] Y. Li, Qi. XR, Y. Maitani, and T. Nagai, "PEG-PLA di block copolymer micelle-like nanoparticles as all-trans-retinoic acid carrier: in vitro and in vivo characterizations," *Nanotechnology*, vol. 20, 2009, PEGPLA di block copolymer micelle-like nanoparticles as all-trans-retinoic acid carrier: in vitro and in vivo characterizations.
- [45] V. P. Torchilin, "Recent advances with liposomes as pharmaceutical carriers," *Nature Reviews Drug Discovery*, vol. 4, no. 2, pp. 145–160, 2005.
- [46] L. Mu and S. S. Feng, "A novel controlled release formulation for the anticancer drug paclitaxel (Taxol): PLGA nanoparticles containing vitamin E TPGS," *Journal of Controlled Release*, vol. 86, no. 1, pp. 33–48, 2003.
- [47] U. S. Sharma, S. V. Balasubramanian, and R. M. Straubinger, "Pharmaceutical and physical properties of paclitaxel (taxol) complexes with cyclodextrins," *Journal of Pharmaceutical Sciences*, vol. 84, no. 10, pp. 1223–1230, 1995.
- [48] D. J. Gary, N. Puri, and Y.-Y. Won, "Polymer-based siRNA delivery: Perspectives on the fundamental and phenomenological distinctions from polymer-based DNA delivery," *Journal of Controlled Release*, vol. 121, no. 1-2, pp. 64–73, 2007.
- [49] M. Dash, F. Chiellini, R. M. Ottenbrite, and E. Chiellini, "Chitosan—a versatile semi-synthetic polymer in biomedical applications," *Progress in Polymer Science*, vol. 36, no. 8, pp. 981–1014, 2011.
- [50] J. M. Rabanel, V. Aoun, I. Elkin, M. Mokhtar, and P. Hildgen, "Drug-loaded nanocarriers: Passive targeting and crossing of biological barriers," *Current Medicinal Chemistry*, vol. 19, no. 19, pp. 3070–3102, 2012.
- [51] L. N. Patel, J. L. Zaro, and W. C. Shen, "Cell penetrating peptides: intracellular pathways and pharmaceutical perspectives," *Pharm. Res*, vol. 24, pp. 1977–1992, 2007.
- [52] D. D. Lasic, "Novel applications of liposomes," *Trends in Biotechnology*, vol. 16, no. 7, pp. 307–321, 1998.
- [53] B. T. Griffin and C. M. O'Driscoll, "Opportunities and challenges for oral delivery of hydrophobic versus hydrophilic peptide and protein-like drugs using lipid-based technologies," *Therapeutic Delivery*, vol. 2, no. 12, pp. 1633–1653, 2011.
- [54] V. J. Wachter, L. Salphati, and L. Z. Benet, "Active secretion and enterocytic drug metabolism barriers to drug absorption," *Advanced Drug Delivery Reviews*, vol. 46, no. 1-3, pp. 89–102, 2001.
- [55] V. J. Wachter, L. Salphati, and L. Z. Benet, "Active secretion and enterocytic drug metabolism barriers to drug absorption," *Advanced Drug Delivery Reviews*, vol. 20, no. 1, pp. 99–112, 1996.
- [56] J. Rautio, H. Kumpulainen, T. Heimbach et al., "Prodrugs: design and clinical applications," *Nature Reviews Drug Discovery*, vol. 7, no. 3, pp. 255–270, 2008.
- [57] N. Cao and S.-S. Feng, "Doxorubicin conjugated to d- α -tocopheryl polyethylene glycol 1000 succinate (TPGS): Conjugation chemistry, characterization, in vitro and in vivo evaluation," *Biomaterials*, vol. 29, no. 28, pp. 3856–3865, 2008.
- [58] Z. Zhang, L. Mei, and S.-S. Feng, "Paclitaxel drug delivery systems," *Expert Opinion on Drug Delivery*, vol. 10, no. 3, pp. 325–340, 2013.
- [59] J. Gong, M. Chen, Y. Zheng, S. Wang, and Y. Wang, "Polymeric micelles drug delivery system in oncology," *Journal of Controlled Release*, vol. 159, no. 3, pp. 312–323, 2012.
- [60] D. S. Kohane, "Microparticles and nanoparticles for drug delivery," *Biotechnology and Bioengineering*, vol. 96, no. 2, pp. 203–209, 2007.
- [61] A. Chaudhary, U. Nagaich, N. Gulati, V. K. Sharma, R. L. Khosa, and M. U. Partapur, "Enhancement of solubilization and bioavailability of poorly soluble drugs by physical and chemical modifications: a recent review," *J Adv Pharm Educ Res*, vol. 2, pp. 32–67, 2012.
- [62] A. J. Ten Tije, J. Verweij, W. J. Loos, and A. Sparreboom, "Pharmacological effects of formulation vehicles: Implications for cancer chemotherapy," *Clinical Pharmacokinetics*, vol. 42, no. 7, pp. 665–685, 2003.
- [63] D. Dube, M. Gupta, and S. P. Vyas, "Nanocarriers for drug targeting to macrophages: emerging options for a therapeutic need," *P Natl A Sci India B*, vol. 82, pp. 151–165, 2012.
- [64] P. Couvreur and C. Vauthier, "Nanotechnology: Intelligent design to treat complex disease," *Pharmaceutical Research*, vol. 23, no. 7, pp. 1417–1450, 2006.
- [65] P. Couvreur, L. Roblot-Treupel, M. F. Poupon, F. Brasseur, and F. Puisieux, "Nanoparticles as microcarriers for anticancer drugs," *Advanced Drug Delivery Reviews*, vol. 5, no. 3, pp. 209–230, 1990.
- [66] S. Bisht and A. Maitra, "Dextran-doxorubicin/chitosan nanoparticles for solid tumor therapy," *Interdisciplinary Reviews: J Nanomed Nanotechnol*, vol. 1, pp. 415–425, 2009.
- [67] L. Zhang, F. X. Gu, J. M. Chan, A. Z. Wang, R. S. Langer, and O. C. Farokhzad, "Nanoparticles in medicine: therapeutic applications and developments," *Clin Pharmacol Ther*, vol. 83, pp. 761–769, 2008.
- [68] D. Peer, J. M. Karp, S. Hong, O. C. Farokhzad, R. Margalit, and R. Langer, "Nanocarriers as an emerging platform for cancer therapy," *Nature Nanotechnology*, vol. 2, no. 12, pp. 751–760, 2007.
- [69] M. E. Davis and D. M. Shin, "Nanoparticle therapeutics: an emerging treatment modality for cancer," *Nat Rev Drug Discov*, vol. 7, pp. 771–782, 2008.
- [70] T. M. Allen, "Ligand-targeted therapeutics in anticancer therapy," *Nature Reviews Cancer*, vol. 2, no. 10, pp. 750–763, 2002.
- [71] Q. Zhang, G. Chen, X. Liu, and Q. Qian, "Monoclonal antibodies as therapeutic agents in oncology and antibody gene therapy," *Cell Research*, vol. 17, no. 2, pp. 89–99, 2007.
- [72] A. M. Wu and P. D. Senter, "Arming antibodies: prospects and challenges for immunoconjugates," *Nat Biotechnol*, vol. 23, pp. 1137–1146, 2005.
- [73] Heath. J. R and M. E. Davis, "Nanotechnology and cancer," *Annu Rev Med*, vol. 59, pp. 251–265, 2008.

- [74] J. A. MacDiarmid and H. Brahmabhatt, "Minicells: Versatile vectors for targeted drug or si/shRNA cancer therapy," *Current Opinion in Biotechnology*, vol. 22, no. 6, pp. 909–916, 2011.
- [75] S. Singh and H. S. Nalwa, "Nanotechnology and health safety—toxicity and risk assessments of nanostructured materials on human health," *Journal of Nanoscience and Nanotechnology*, vol. 7, no. 9, pp. 3048–3070, 2007.
- [76] E. Casals, S. Vázquez-Campos, N. G. Bastús, and V. Puentes, "Distribution and potential toxicity of engineered inorganic nanoparticles and carbon nanostructures in biological systems," *TrAC - Trends in Analytical Chemistry*, vol. 27, no. 8, pp. 672–683, 2008.
- [77] N. R. Panyala, E. M. Peña-Méndez, and J. Havel, "Silver or silver nanoparticles: a hazardous threat to the environment and human health?" *Journal of Applied Biomedicine*, vol. 6, no. 3, pp. 117–129, 2008.
- [78] J. Ai, E. Biazar, M. Jafarpour et al., "Nanotoxicology and nanoparticle safety in biomedical designs," *International Journal of Nanomedicine*, vol. 6, pp. 1117–1127, 2011.
- [79] D. Moinard-Checot, Y. Chevalier, S. Briançon, H. Fessi, and S. Guinebretière, "Nanoparticles for drug delivery: Review of the formulation and process difficulties illustrated by the emulsion-diffusion process," *Journal of Nanoscience and Nanotechnology*, vol. 6, no. 9–10, pp. 2664–2681, 2006.
- [80] B. A. Katsnelson, L. I. Privalova, M. P. Sutunkova et al., "Some inferences from in vivo experiments with metal and metal oxide nanoparticles: The pulmonary phagocytosis response, subchronic systemic toxicity and genotoxicity, regulatory proposals, searching for bioprotectors (a self-overview)," *International Journal of Nanomedicine*, vol. 10, pp. 3013–3029, 2015.
- [81] D. Mukherjee, S. G. Royce, S. Sarkar et al., "Modeling in vitro cellular responses to silver nanoparticles," *J Toxicol*, vol. 2014, Article ID 852890, 13 pages, 2014.
- [82] R. Sequeira, A. Genaidy, R. Shell, W. Karwowski, G. Weckman, and S. Salem, "The nano enterprise: A survey of health and safety concerns, considerations, and proposed improvement strategies to reduce potential adverse effects," *Human Factors and Ergonomics In Manufacturing*, vol. 16, no. 4, pp. 343–368, 2006.
- [83] PH. Hoet, I. Brüske-Hohlfeld, and O. V. Salata, "Nanoparticles—known and unknown health risks," *J Nanobiotechnology*, vol. 2, no. 1, 2004.
- [84] A. Nel, T. Xia, and L. Mädler, "Toxic potential of materials at the nano level," *Science*, vol. 311, pp. 622–627, 2006.
- [85] P. J. Borm, D. Robbins, S. Haubold et al., "The potential risks of nanomaterials: a review carried out for ECETOC," *Part Fibre Toxicol*, vol. 3, no. 11, 2006.
- [86] B. A. Rzigalinski and J. S. Strobl, "Cadmium-containing nanoparticles: perspectives on pharmacology and toxicology of quantum dots," *Toxicol Appl Pharmacol*, vol. 238, pp. 280–288, 2009.
- [87] G. Oberdörster, E. Oberdörster, and J. Oberdörster, "Nanotoxicology: an emerging discipline evolving from studies of ultrafine particles," *Environmental Health Perspectives*, vol. 113, no. 7, pp. 823–839, 2005.
- [88] J. Lovrić, S. J. Cho, F. M. Winnik, and D. Maysinger, "Unmodified cadmium telluride quantum dots induce reactive oxygen species formation leading to multiple organelle damage and cell death," *Chemistry and Biology*, vol. 12, no. 11, pp. 1227–1234, 2005.
- [89] N. Chen, Y. He, Y. Su et al., "The cytotoxicity of cadmium-based quantum dots," *Biomaterials*, vol. 33, pp. 1238–1244, 2012.
- [90] Y. Su, M. Hu, C. Fan et al., "The cytotoxicity of CdTe quantum dots and the relative contributions from released cadmium ions and nanoparticle properties," *Biomaterials*, vol. 31, no. 18, pp. 4829–4834, 2010.
- [91] F. R. Khan, G. M. Kennaway, M.-N. Croteau et al., "In vivo retention of ingested au NPs by daphnia magna: No evidence for trans-epithelial alimentary uptake," *Chemosphere*, vol. 100, pp. 97–104, 2014.
- [92] C. S. Yah, "The toxicity of gold nanoparticles in relation to their physicochemical properties," *Biomedical Research*, vol. 24, no. 3, pp. 400–413, 2013.
- [93] S. Kundu, S. Lau, and H. Liang, "Shape-controlled catalysis by cetyltrimethylammonium bromide terminated gold nanospheres, nanorods, and nanoprisms," *Journal of Physical Chemistry C*, vol. 113, no. 13, pp. 5150–5156, 2009.
- [94] W. H. Suh, K. S. Suslick, G. D. Stucky, and Y. H. Suh, "Nanotechnology, nanotoxicology, and neuroscience," *Prog Neurobiol*, vol. 87, pp. 133–170, 2009.
- [95] A. A. Shvedova, V. Castranova, E. R. Kisin et al., "Exposure to carbon nanotube material: assessment of nanotube cytotoxicity using human keratinocyte cells," *Journal of Toxicology and Environmental Health. Part A*, vol. 66, no. 20, pp. 1909–1926, 2003.
- [96] Y. Zhang, S. F. Ali, E. Dervishi et al., "Cytotoxicity effects of graphene and single-wall carbon nanotubes in neural pheochromocytoma-derived pc12 cells," *ACS Nano*, vol. 4, no. 6, pp. 3181–3186, 2010.
- [97] M. A. Dobrovolskaia, P. Aggarwal, J. B. Hall, and S. E. McNeil, "Preclinical studies to understand nanoparticle interaction with the immune system and its potential effects on nanoparticle biodistribution," *Molecular Pharmaceutics*, vol. 5, no. 4, pp. 487–495, 2008.
- [98] S. Mazumder, D. Sarkar, and I. K. Puri, "Nanotechnology commercialization: prospects in India," *J Mater Sci Nanotechnol*, vol. 2, no. 2, 2014.
- [99] G. Oberdörster, A. Maynard, K. Donaldson et al., "Principles for characterizing the potential human health effects from exposure to nanomaterials: elements of a screening strategy," *Part Fibre Toxicol*, vol. 2, no. 8, 2005.
- [100] D. Thassu, Y. Pathak, and M. Deleers, "Nanoparticulate Drug-Delivery Systems," in *Nanoparticulate Drug Delivery Systems*, pp. 1–131, CRC Press, 2007.
- [101] N. A. Ocheke, P. O. Olorunfemi, and N. C. Ngwuluka, "Nanotechnology and drug delivery part 2: nanostructures for drug delivery," *Tropical Journal of Pharmaceutical Research*, vol. 8, no. 3, pp. 275–287, 2009.
- [102] W. M. Pardridge, "Blood-brain barrier delivery," *Drug Discovery Today*, vol. 12, no. 1–2, pp. 54–61, 2007.
- [103] Y. Chen and L. Liu, "Modern methods for delivery of drugs across the blood-brain barrier," *Adv Drug Deliv Rev*, vol. 64, pp. 640–665, 2012.
- [104] R. L. Oliver, "Whence consumer loyalty?" *Journal of Marketing*, vol. 63, pp. 33–44, 1999.
- [105] M. W. Kreuter, S. N. Lukwago, D. C. Bucholtz, E. M. Clark, and V. Sanders-Thompson, "Achieving cultural appropriateness in health promotion programs: targeted and tailored approaches," *Health Education & Behavior*, vol. 30, no. 2, pp. 133–146, 2003.
- [106] P. R. Lockman, M. O. Oyewumi, J. M. Koziara, K. E. Roder, R. J. Mumper, and D. D. Allen, "Brain uptake of thiamine-coated nanoparticles," *Journal of Controlled Release*, vol. 93, no. 3, pp. 271–282, 2003.

- [107] J. M. Koziara, T. R. Whisman, M. T. Tseng, and R. J. Mumper, "In-vivo efficacy of novel paclitaxel nanoparticles in paclitaxel-resistant human colorectal tumors," *Journal of Controlled Release*, vol. 112, no. 3, pp. 312–319, 2006.
- [108] J. M. Koziara, P. R. Lockman, D. D. Allen, and R. J. Mumper, "The blood-brain barrier and brain drug delivery," *Journal of Nanoscience and Nanotechnology*, vol. 6, no. 9-10, pp. 2712–2735, 2006.
- [109] S. B. Tiwari and M. M. Amiji, "A review of nanocarrier-based CNS delivery systems," *Curr Drug Deliv*, vol. 3, pp. 219–232, 2006.
- [110] A. P. Nikalje, "Nanotechnology and its Applications in Medicine," *Medicinal Chemistry*, vol. 5, no. 2, pp. 81–89, 2015.
- [111] T. T. V. Doan and H. K. T. Nguyen, "Study on Minicell Generation of *Lactobacillus acidophilus* VTCC-B-871 for Drug Delivery," *J Appl Pharm Sci*, vol. 3, pp. 33–36, 2013.
- [112] H. K. T. Nguyen and T. T. V. Doan, "Effects of Carbon Sources on cell differentiation of *Lactobacillus rhamnosus*PN04 and applications," *Biochem Pharmacol*, vol. 6, pp. 197–203, 2013.
- [113] T. H. K. Nguyen, V. T. T. Doan, L. D. Ha, and H. N. Nguyen, "Molecular cloning, Expression of *minD* Gene from *Lactobacillus acidophilus* VTCC-B-871 and Analyses to Identify *Lactobacillus rhamnosus*PN04 from Vietnam *Hottuyenia cordata* Thunb," *Ind J Microbiol*, vol. 53, no. 4, pp. 385–390, 2013.
- [114] P. A. J. Boer, W. R. Cook, and L. I. Rothfield, "Bacterial cell division," *Annu Rev Genet*, vol. 24, pp. 249–274, 1990.
- [115] J. Lutkenhaus and S. G. Addinall, "Bacterial cell division and the Z ring," *Annu Rev Biochem*, vol. 66, 1997.
- [116] A. Flemming, "Minicells deliver lethal load to tumours," *Nature Reviews Drug Discovery*, vol. 6, no. 7, pp. 519–519, 2007.
- [117] H. Brahmabhatt and J. MacDiarmid, *U.S. Patent Application No. 13/711*, p. 848, 2012.
- [118] V. Gujrati, S. Kim, S.-H. Kim et al., "Bioengineered bacterial outer membrane vesicles as cell-specific drug-delivery vehicles for cancer therapy," *ACS Nano*, vol. 8, no. 2, pp. 1525–1537, 2014.
- [119] M. Slater and M. Schaechter, "Control of cell division in bacteria," *Bacteriol Rev*, vol. 38, 1974.
- [120] M. J. Giacalone, J. C. Zapata, N. L. Berkley et al., "Immunization with non-replicating *E. coli* minicells delivering both protein antigen and DNA protects mice from lethal challenge with lymphocytic choriomeningitis virus," *Vaccine*, vol. 25, no. 12, pp. 2279–2287, 2007.
- [121] J. Delcour, T. Ferain, M. Deghorain, E. Palumbo, and P. Hols, "The biosynthesis and functionality of the cell-wall of lactic acid bacteria," *Antonie van Leeuwenhoek, International Journal of General and Molecular Microbiology*, vol. 76, no. 1-4, pp. 159–184, 1999.
- [122] P. Schär-Zammaretti and J. Ubbink, "The Cell Wall of Lactic Acid Bacteria: Surface Constituents and Macromolecular Conformations," *Biophysical Journal*, vol. 85, no. 6, pp. 4076–4092, 2003.
- [123] S. J. Tonn and J. E. Gander, "Biosynthesis of polysaccharides by prokaryotes," *Annu Rev Microbiol*, vol. 33, pp. 169–199, 1979.
- [124] N. Mozes and S. Lortal, "X-ray photoelectron spectroscopy and biochemical analysis of the surface of *Lactobacillus helveticus* ATCC 12046," *Microbiology*, vol. 141, no. 1, pp. 11–19, 1995.
- [125] D. Frenkel and B. Smit, *Understanding Molecular Simulation: From Algorithms to Applications*, vol. 1, Academic Press, 2001.
- [126] H. Engelhardt and J. Peters, "Structural research on surface layers: A focus on stability, surface layer homology domains, and surface layer-cell wall interactions," *Journal of Structural Biology*, vol. 124, no. 2-3, pp. 276–302, 1998.
- [127] J. A. MacDiarmid, N. B. Amaro-Mugridge, J. Madrid-Weiss et al., "Sequential treatment of drug-resistant tumors with targeted minicells containing siRNA or a cytotoxic drug," *Nature Biotechnology*, vol. 27, no. 7, pp. 643–651, 2009.
- [128] B. J. Solomon, J. Desai, M. Rosenthal et al., "A first-time-in-human phase I clinical trial of bispecific antibody-targeted, paclitaxel-packaged bacterial minicells," *PLoS ONE*, vol. 10, no. 12, Article ID e0144559, 2015.
- [129] J. R. Whittle, J. D. Lickliter, H. K. Gan et al., "First in human nanotechnology doxorubicin delivery system to target epidermal growth factor receptors in recurrent glioblastoma," *Journal of Clinical Neuroscience*, vol. 22, no. 12, pp. 1889–1894, 2015.

Research Article

Lignocellulosic Micro- and Nanomaterials as Copper Frames for the Evaluation of the Copper(I)-Catalyzed Azide-Alkyne Cycloaddition

Charles W. Owens,¹ Gloria S. Oporto,¹ Björn C. G. Söderberg,² and Katherine E. Lambson²

¹School of Natural Resources, West Virginia University, Morgantown, WV 26506, USA

²C. Eugene Bennett Department of Chemistry, West Virginia University, Morgantown, WV 26506, USA

Correspondence should be addressed to Gloria S. Oporto; gloria.oporto@mail.wvu.edu

Received 22 February 2017; Accepted 15 June 2017; Published 18 July 2017

Academic Editor: Sohel Rana

Copyright © 2017 Charles W. Owens et al. This is an open access article distributed under the Creative Commons Attribution License, which permits unrestricted use, distribution, and reproduction in any medium, provided the original work is properly cited.

Copper was immobilized onto carboxymethyl cellulose, nanofibrillated cellulose, TEMPO-nanofibrillated cellulose, and lignin. The lignocellulosic frames were used with the aim of providing an effective support for catalyst copper and allowing its further reutilization. Each organic support was successful and effective in the coupling of copper with the exception of lignin. These complexes were used as heterogeneous catalysts to produce 1-benzyl-4-phenyl-1H-[1,2,3]-triazole from the copper(I)-catalyzed azide-alkyne cycloaddition (CuAAC) between benzyl azide and phenylacetylene. Each reaction was carried out in water and acetonitrile. Those performed in water were completed in 15 minutes while those done in acetonitrile were allowed to react overnight, reaching completion in less than 20 hours. The yields for Cu-CMC resulted in over 90% for those reactions performed in acetonitrile. All catalysts were easy to recover except Cu-lignin which could not be filtered or extracted from the reaction effluent.

1. Introduction

The “Huisgen click” reaction refers to an azide-alkyne 1,3-dipolar cycloaddition. This reaction has many useful applications for drug discovery [1], polymer synthesis [2], and material science [3], among other biological applications [4, 5]. However, this reaction often requires high temperatures, has a low reaction rate, and typically produces a mixture of 1,5-substituted and 1,4-substituted triazoles [6].

Copper (Cu) based catalyst for the “Huisgen click” reaction has received significant attention during the last decade due to its versatile reactivity and much lower cost compared with noble metals, such as Pd and Rh. The rate of this copper(I)-catalyzed azide-alkyne cycloaddition (CuAAC) is increased by a factor of 10^7 relative to the purely thermal process [6]. Most CuAAC procedures involve in situ reducing agents to reduce Cu(II) salts in the generation of Cu(I) catalysts [7]. This reaction is quite insensitive to its environment and is also unaffected by most functional groups, so it may be performed in an aqueous or organic solution. However,

it is most commonly performed in a water/alcohol mixture [6, 8, 9], though, without somehow immobilizing the copper on a homogeneous support, this CuAAC reaction is still very limited due to the low recoverability of copper from the product [10].

In general catalytic metal particles have been immobilized on solid supports that include the following: silica, alumina, zirconia, ceria, zeolites, glass fibers, and synthetic polymers [11–14]. The concept of sustainable chemistry is opening incredible opportunities for supporting materials coming from renewable natural polymers. Cellulose-based materials were studied as a support material for metal catalysts some years ago [15]. In recent years, the utilization of cellulose nanomaterials, such as cellulose nanofibers and cellulose nanocrystals, has demonstrated excellent performance to be used as scaffold for metal nanoparticles in catalysis [16–18]. Shen et al. in 2010 used CuSO_4 reduced by sodium ascorbate to catalyze *O*-acetyl- α -L-arabinopyranosyl azide and phenyl acetylene and found yields unsatisfactory at 54% [19]. The group then immobilized Cu onto microcrystalline

cellulose as a catalyst, and the reaction (performed in water at 60°C) produced a 93% yield, showing that a cellulose-supported copper catalyst is favorable. The group also reused the catalyst and, after five cycles, the yield was still favorable at 84%, displaying excellent recoverability of the Cu(0)-cellulose catalyst [20].

Reddy et al. used the same procedure and materials as Yu et al. to create the Cu(0)-cellulose catalyst and had similar results in their catalyst formations, with Cu 2P X-ray photoelectron spectroscopy (XPS) spectra peaks around 932.7 eV. However, inductively coupled plasma atomic emission spectroscopy (ICP-AES) analysis in both studies show that Yu et al.'s Cu(0)-cellulose had almost double the amount of copper compared to Reddy et al.'s at 0.730 mmol/g and 0.368 mmol/g, respectively [20, 21]. This could be due to the type of wood the cellulose was drawn from and, correspondingly, the amount of carboxylate groups on the cellulose fibers.

Koga et al. created a cellulose-supported Cu(I) catalyst using 2,2,6,6-tetramethylpiperidine-1-oxyl (TEMPO) nanofibrillated cellulose (TNFC). The azide-alkyne pair of benzyl azide and phenyl acetylene reacted in an aqueous solution of sodium ascorbate containing the Cu(I)-TNFC catalyst; the copper content of the catalyst used in the reaction was 10 μ mol. Through NMR analysis, the product was found to be entirely 1-benzyl-4-phenyl-1*H*-[1,2,3]-triazole, the desired product [17]. This indicates both the procedure and catalyst were very effective for this azide-alkyne cycloaddition.

Zhong et al. in 2013 used carboxymethyl cellulose (CMC) to immobilize copper that displayed excellent antimicrobial properties against *Escherichia coli*. Then, in 2015, Zhong et al. developed an efficient drying process for Cu-TNFC and Cu-CMC complexes—which was developed using the same procedure from Zhong et al. in 2013. The results of this procedure, through XPS analysis, showed that the oxidative state of copper in the final product was Cu⁺, which was the oxidative state of copper in the research previously discussed by Koga et al. in 2012. In this study, copper nanoparticles were supported on lignin and three different kinds of cellulose (CMC, NFC, and TNFC) for the cycloaddition of benzyl azide and phenyl acetylene. Similar processes to the production of Cu-CMC [22], drying of the Cu-TNFC and Cu-CMC [23], and catalyst performance test of CuAAC [17] were used in this research.

2. Materials and Methods

2.1. Materials. Sodium carboxymethyl cellulose (Na-CMC) with average molecular weight of 90,000 g/mol was purchased from Sigma-Aldrich, USA; nanofibrillated cellulose (NFC), 2.8 wt%, from the University of Maine, USA; TEMPO-nanofibrillated cellulose (TNFC) gel, 0.96 wt%, from Forest Products Laboratory, USA; lignin, alkali from Sigma-Aldrich, USA; copper sulfate pentahydrate (CuSO₄·5H₂O) from Fisher Scientific, USA; sodium borohydride (NaBH₄), 0.5 M, from Acros, USA; ethanol (reagent alcohol, 95%) from Sigma-Aldrich, USA; tert-butanol (99.5%) from Acros, USA; benzyl azide (94%) from Alfa Aesar, England; phenyl acetylene (98%) from Alfa Aesar, England; sodium cyanoborohydride (NaBH₃CN) from Sigma-Aldrich, USA.

2.2. Preparation of Copper Catalysts

2.2.1. Preparation of Copper-Carboxymethyl Cellulose. Sodium carboxymethyl cellulose (Na-CMC) (1 g) was suspended in deionized water (49 mL). After that, CuSO₄ (aqueous, 15 mL, 0.1 M) was added dropwise to the solution under constant stirring. Once all the CuSO₄ had been added, mixing immediately ceased, and the solution rested for 14 h. Sodium borohydride (aqueous, 10 mL, 0.5 M) was added slowly under constant stirring over 30 min in order to reduce the oxidation state of copper [22].

2.2.2. Preparation of Copper-Nanofibrillated Cellulose. Nanofibrillated cellulose (NFC) gel (1 g, 2.8 wt%) was suspended in deionized water (10 mL). After that, CuSO₄ (aqueous, 4 mL, 0.1 M) was then added dropwise to the solution under constant stirring for 1 h. Sodium borohydride (aqueous, 3 mL, 0.5 M) was added as a reducer. Once added, the suspension underwent constant stirring for 30 min.

2.2.3. Preparation of Copper-TEMPO-Nanofibrillated Cellulose. TEMPO-nanofibrillated cellulose gel (5 mL, 0.96 wt%) was suspended in deionized water (10 mL). After that, CuSO₄ (aqueous, 4 mL, 0.1 M) was then added dropwise to the solution under constant stirring for 1 h. Next, to reduce the oxidation state of copper, sodium borohydride (aqueous, 3 mL, 0.5 M) was added and stirred for another 30 min.

2.2.4. Preparation of Copper-Lignin. Lignin (1 g) was suspended in deionized water (10 mL). After that, CuSO₄ (aqueous, 4 mL, 0.1 M) was then added dropwise to the solution under constant stirring for 1 h. Lastly, sodium borohydride (aqueous, 3 mL, 0.5 M) was added slowly and then stirred with the suspension for 30 min to ensure all the copper had been reduced.

2.3. Drying and Purifying the Copper Catalysts. Each suspension was then centrifuged and the upper liquid layer was removed. The solids that remained were then redispersed in water (50 mL) and centrifuged again at 8000 rpm for 5 min. The upper clear solution was removed, and ethanol (25 mL) was mixed with the solid in the bottom of the vial. The vial was centrifuged again at 8000 rpm for 5 min, and the upper clear solution was subsequently removed. Ethanol was again mixed, and, after waiting for two hours upon mixing, the solution was centrifuged at 8000 rpm for 5 min. The upper liquid was then removed. This process was repeated using tert-butanol. The solid that remained from each suspension was then stored in a vacuum for 2 days to prevent oxidation and to allow the tert-butanol to dry. After the solids were dried under vacuum, they were placed in a freeze-dryer for 3 days [23]. Note that this process was only used to dry Cu-CMC, Cu-NFC, and Cu-TNFC. The Cu-lignin suspensions were not able to be separated from the solvent after centrifugation; therefore, the lignin suspension was placed directly in the freeze-dryer.

2.4. Catalyst Performance Test. Sodium cyanoborohydride (aqueous, 3.3 mM, 30 mL) was used to pretreat Cu-CMC

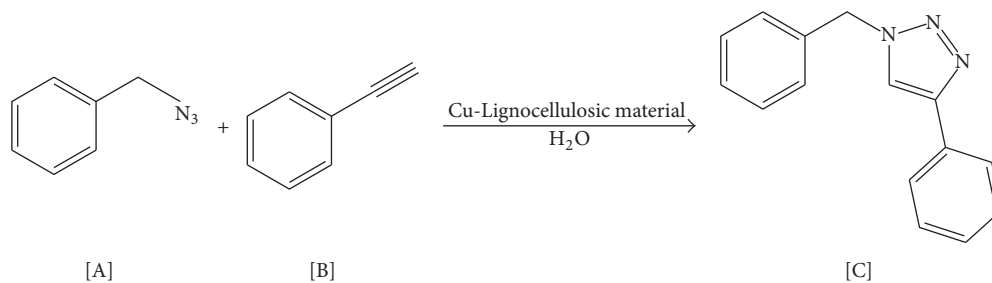


FIGURE 1: Illustration of the CuAAC of benzyl azide and phenylacetylene to produce 1,4-BPT, where [A]: benzyl azide, [B]: phenylacetylene, and [C]: 1-benzyl-4-phenyl-1H-[1,2,3]-triazole (1,4-BPT).

(6 mg), Cu-NFC (11 mg), Cu-TNFC (14 mg), and Cu-lignin (200 mg)—all separately—at 70°C for 20 min prior to performing the CuAAC reaction. For the CuAAC reaction, benzyl azide (125 μ L, 1.00 mmol) and phenylacetylene (110 μ L, 1.00 mmol) were added to each solution under constant stirring at 70°C [17]. The CuAAC reaction is represented in Figure 1. The progress of the reaction was monitored by thin layer chromatography (TLC, hexane/EtOAc, 19 : 1). After the complete disappearance of benzyl azide, the catalyst was recovered from the mixture by filtration and washed with water (2 \times 10 mL) and acetone (2 \times 10 mL) and then allowed to dry in a vacuum. The filtrate was extracted with ethyl acetate (3 \times 30 mL). The combined organic phases were dried (MgSO_4) and filtered and filtrate was concentrated in vacuum [20]. The crude product was purified by filtration through a short plug of silica gel eluting with EtOAc to yield 1-benzyl-4-phenyl-1H-[1,2,3]-triazole (1,4-BPT).

This process was then repeated using Cu-CMC and scaled up by a factor of 5 in order to reduce human error. In addition to scale-up, the recovered catalyst was reused twice for the same reaction to analyze catalytic decay.

This scaled-up process was also repeated using Cu-CMC in 30 mL of acetonitrile, a common solvent medium for CuAAC, instead of 30 mL of water. This was done to compare with other literature, as water is not typically used as the solvent in this CuAAC since copper easily dissolves in water. However, water is a very desirable reaction medium due to its abundance and environmental sustainability.

2.5. Characterization. The copper loading on each catalyst support was determined using Varian Vista-PRO CCD simultaneous inductively coupled plasma-optical emission spectroscopy (ICP-OES) (Palo Alto, USA). In order to prepare these samples for ICP-OES, 30 mg of each catalyst was dissolved in 1 mL of nitric acid (71 wt%). When the solid complexes were completely dissolved, the solution was diluted with 99 mL of deionized water and 15 mL of this solution was then used for ICP-OES analysis.

The oxidation state of copper on each catalyst was determined using Physical Electronics VersaProbe 5000 X-ray Photoelectron Spectroscopy (XPS) system with a monochromatic Aluminum $K\alpha$ X-ray source (Chanhassen, MI, USA). The base pressure in the high vacuum analysis chamber was around 2×10^{-6} Pa. An Aluminum X-ray source of 1486.6 eV

was used for photoelectron excitation with X-ray power of 25 W. Pass energies of 117.4 eV for survey scan and 23.5 eV for detailed scan were used for the data acquisition with energy steps of 0.5 eV for survey scan and 0.05 eV for detailed scan, respectively. PHI MultiPak software was used for element identification and peak fitting. The C1s peak at a binding energy of 284.8 eV was used as the internal reference. A Shirley-type background was subtracted from the spectra and Gauss-Lorentz curves were used to fit the spectra.

The solid product from the CuAAC reaction was dissolved in deuteriochloroform and nuclear magnetic resonance (^1H NMR) measurements were taken using a 400 MHz Agilent Technologies NMR, Model Number 400/54/ASP. Data analysis was performed using Agilent Technologies Software VNMRJ, Version 2.4, Revision A.

2.6. Yield Determination. The yield of each reaction was determined in the following equation:

$$\frac{\text{Theoretical Yield} - \text{Actual Yield}}{\text{Theoretical Yield}} \times 100. \quad (1)$$

3. Results and Discussion

3.1. Production of Copper Catalysts. ICP-OES analysis calculated the amount of copper on each catalyst. Three samples of each complex were used in order to gain an accurate knowledge of the loading of copper onto each organic support. Figure 2 displays the results from ICP-OES. The number above each bar indicates the average mmol of Cu per gram of catalyst. The error bars indicate the standard deviation for all the trials for each sample. These error bars represent the amount of variation of copper throughout the catalyst. The results are excellent when compared to literature.

Yu et al. used microcrystalline cellulose as the platform to attach copper, and the copper loading onto the microcrystalline cellulose only resulted in 0.730 mmol Cu/g catalyst [20]. All of our compounds except Cu-lignin (due to the procedure in which it was created) have higher copper loadings than this, and CMC has over 2.5 times the copper loading of the microcrystalline cellulose. From these results, it can be concluded that CMC is the best organic compound on which to immobilize copper nanoparticles. This is likely due to the presence of high number of Na-carboxyl groups

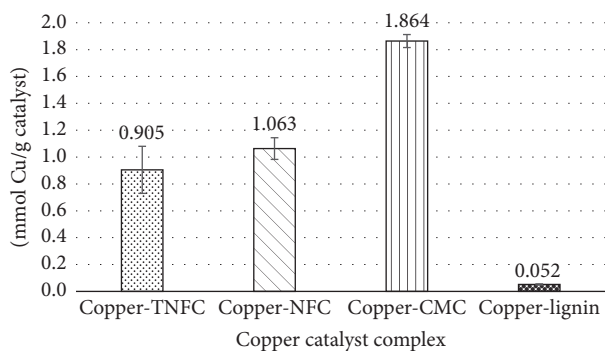


FIGURE 2: Amount of copper per gram of catalyst on each hybrid material.

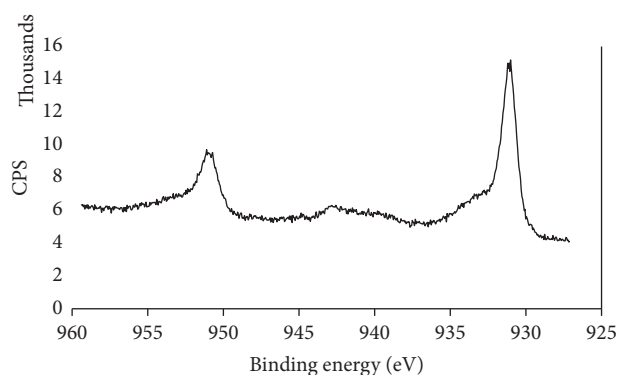


FIGURE 3: XPS spectra of Cu-CMC.

that can facilitate the copper reduction and therefore its further availability.

As determined from XPS the state of oxidation was Cu(I) for all complexes. There were strong peaks around 931-932 and 950-951 with a weak satellite peak between the two around 943. This weak satellite peak was the determining factor for the oxidation state because it is unique to the Cu(I) oxidation state only. Figure 3 displays the XPS data graphically for Cu-CMC. All data for the remaining complexes are very similar and therefore will not be displayed along with the Cu-CMC.

3.2. Catalyst Performance Test

3.2.1. Using Water as Media for the Reaction. The reaction time was outstanding for each catalyst, with each reaction reaching completion in 15 minutes. Compared to Koga et al., who used softwood-derived TNFC as a catalyst support for the same reaction, our copper-cellulose complexes catalyzed the reaction 5 min faster [17]. However, the yields for 1,4-BPT were not satisfactory. Table 1 presents information regarding the yields pertaining to each catalyst.

One thing to note as well is that the Cu-lignin was irrecoverable from the reaction. It appears to have dissolved in the aqueous layer.

Table 2 shows the results of the scaled-up reaction using Cu-CMC and the same reaction reusing the catalyst.

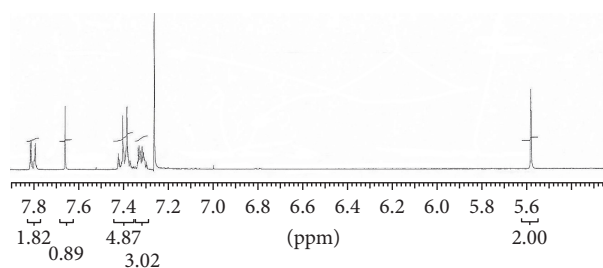


FIGURE 4: NMR results for material produced from procedure used in this research.

TABLE 1: Yield information of each CuAAC using different catalysts.

Catalyst proposed	1,4-BPT yield (mg)	Yield percentage
Cu-CMC	131	56%
Cu-NFC	85	36%
Cu-TNFC	136	58%
Cu-lignin	90	39%

TABLE 2: Results of CuAAC using and reusing Cu-CMC.

Catalyst use	Reaction time	Yield percentage
1	10 min	45%
2	20 min	43%
3	150 min	38%

These results show that the first reuse of the catalyst is still very effective as the reaction time was still very fast, only increasing by 10 minutes. However, after reusing the catalyst once again, the reaction time increased greatly to 150 min suggesting the catalyst is not be reused more than once.

The low yields could be due to the extraction and purification process of the product, as there is much room for human error in this procedure. When using an internal standard of 1,4-dimethoxy benzene, NMR analysis showed yields of over 80% 1,4-BPT. This indicates that improvements can be made to purification in order to isolate the entire desired product that is formed.

The results of the ^1H NMR analysis from Cu-CMC as catalyst were as follows: δ_{H} ppm: 7.80 (d, 2H), 7.66 (s, 1H), 7.36–7.42 (m, 5H), 7.34–7.29 (m, 3H), and 5.58 (s, 2H). The data are shown graphically in Figure 4; the numbers below the x-axis are the areas under each spike (or group of spikes) and represent the number of hydrogen atoms on each carbon. The most indicative datum on Figure 4 is the spike around 5.6 ppm. This is the carbon with two single bonds connecting the phenyl group to the azide group. Since it is known that there are two hydrogen atoms at this point and therefore the area under the spike will be exactly 2, this data was implemented into the analysis and all other areas under each spike were determined using this data as the standard. The large spike around 7.25 ppm is from the solvent, deuteriochloroform, used to dissolve the product for analysis. Since every single area under each spike or group of spikes concurred with literature [17, 24], the results indicate the product was entirely 1,4-BPT using each copper complex as the catalyst.

TABLE 3: Yield information using acetonitrile as reaction medium.

Catalyst proposed	1,4-BPT yield (mg)	Yield percentage
Cu-CMC	1070	91%
Cu-TNFC	872	74%

The reaction completely favors the formation of 1,4-substituted triazoles as well, differing from the thermal reaction which often results in a mixture of 1,4-substituted and 1,5-substituted triazoles [6].

3.2.2. Acetonitrile as Media for the Reaction. Considering that the highest yields in water as media were for Cu-CMC and Cu-TNFC, they were tested in acetonitrile to evaluate differences. The results in this regard are presented in Table 3. When using acetonitrile as the solvent for the reaction and CMC-Cu as catalyst, 5 mmol of reactant yielded 1.07 g (91% yield) of 1,4-BPT. These results are very comparable to other researches [24, 25] concluding that CMC is an effective support for copper to be used as a catalyst. In terms of Cu-TNFC, yields were less satisfactory at 74%, though much improved from the reaction in a water medium.

4. Conclusions

Cu-cellulose was easily prepared using CMC, NFC, TNFC, and lignin. These complexes were then used as catalysts in the CuAAC between benzyl azide and phenylacetylene to produce 1,4-BPT. Water and acetonitrile as media for the reaction were used. In water media, the catalysts, with the exception of lignin, were easy to recover, displaying the low hazardous impact the reaction has on the environment. The reaction was complete in 15 minutes for each copper complex, showing the excellent catalytic ability of each heterogeneous catalyst. Cu-CMC and Cu-TNFC displayed the highest yields and were subsequently used as catalysts when acetonitrile was utilized as media for the reaction. The reaction in this case needed longer time to be completed and the yield resulted higher for Cu-CMC. Based on the process used to fabricate the hybrid Cu-cellulose materials, CMC appears to be the best support for copper of the four organic compounds used as it held the most copper due to its higher number of Na-carboxyl groups and yielded one of the highest amounts of 1,4-BPT. Further investigation will be directed on the improvement of copper attachment on the lignocellulosic raw material for the specific application in the catalysis field.

Abbreviations

1,4-BPT: 1-Benzyl-4-phenyl-1H-1,2,3-triazole
 CMC: Carboxymethyl cellulose
 CuAAC: Copper azide-alkyne cycloaddition
 TEMPO: 2,2,6,6-Tetramethylpiperidine-1-oxyl radical
 NFC: Nanofibrillated cellulose
 TNFC: TEMPO-nanofibrillated cellulose
 ICP-AES: Inductively coupled plasma atomic emission spectroscopy

ICP-OES: Inductively coupled plasma-optical emission spectrometry

NMR: Nuclear magnetic resonance

TLC: Thin layer chromatography

XPS: X-ray photoelectron spectroscopy.

Conflicts of Interest

The authors declare that they have no conflicts of interest.

Acknowledgments

This work was supported by the USDA National Institute of Food and Agriculture, McIntire-Stennis, 1007636-WVA00119, "Advanced Applications for Nanomaterials from Lignocellulosic Sources."

References

- [1] H. C. Kolb and K. B. Sharpless, "The growing impact of click chemistry on drug discovery," *Drug Discovery Today*, vol. 8, no. 24, pp. 1128–1137, 2003.
- [2] J. F. Lutz, "1,3-dipolar cycloadditions of azides and alkynes: a universal ligation tool in polymer and materials science," *Angewandte Chemie International Edition*, vol. 46, no. 7, pp. 1018–1025, 2007.
- [3] G. Delaittre, N. K. Guimard, and C. Barner-Kowollik, "Cycloadditions in modern polymer chemistry," *Accounts of Chemical Research*, vol. 48, no. 5, pp. 1296–1307, 2015.
- [4] A. Martinez, C. O. Mellet, and J. M. G. Fernández, "Cyclodextrin-based multivalent glycodisplays: covalent and supramolecular conjugates to assess carbohydrate-protein interactions," *Chemical Society Reviews*, vol. 42, no. 11, pp. 4746–4773, 2013.
- [5] V. Aragão-Leoneti, V. L. Campo, A. S. Gomes, R. A. Field, and I. Carvalho, "Application of copper(I)-catalysed azide/alkyne cycloaddition (CuAAC) 'click chemistry' in carbohydrate drug and neoglycopolymer synthesis," *Tetrahedron*, vol. 66, no. 49, pp. 9475–9492, 2010.
- [6] J. E. Hein and V. V. Fokin, "Copper-catalyzed azide-alkyne cycloaddition (CuAAC) and beyond: new reactivity of copper(I) acetylides," *Chemical Society Reviews*, vol. 39, no. 4, pp. 1302–1315, 2010.
- [7] V. Hong, S. I. Presolski, C. Ma, and M. G. Finn, "Analysis and optimization of copper-catalyzed azide-alkyne cycloaddition for bioconjugation," *Angewandte Chemie International Edition*, vol. 48, no. 52, pp. 9879–9883, 2009.
- [8] M. Meldal and C. W. Tomøe, "Cu-catalyzed azide-alkyne cycloaddition," *Chemical Reviews*, vol. 108, no. 8, pp. 2952–3015, 2008.
- [9] V. D. Bock, H. Hiemstra, and J. H. Van Maarseveen, "Cu^I-catalyzed alkyne-azide 'click' cycloadditions from a mechanistic and synthetic perspective," *European Journal of Organic Chemistry*, no. 1, pp. 51–68, 2006.
- [10] B. Dervaux and F. E. Du Prez, "Heterogeneous azide-alkyne click chemistry: towards metal-free end products," *Chemical Science*, vol. 3, no. 4, pp. 959–966, 2012.
- [11] J. D. Aiken III and R. G. Finke, "Polyoxoanion- and tetrabutylammonium-stabilized Rh(0)_n nanoclusters: Unprecedented nanocluster catalytic lifetime in solution," *Journal of the American Chemical Society*, vol. 121, no. 38, pp. 8803–8810, 1999.

- [12] M. P. Campello, M. Balbina, I. Santos, P. Lubal, R. Ševčík, and R. Ševčíková, "Lanthanide(III) complexes of 2-[4,7,10-tris (phosphonomethyl)-1,4,7,10-tetraazacyclododecan-1-yl]acetic acid (H₇DOA3P): multinuclear-NMR and kinetic studies," *Helvetica Chimica Acta*, vol. 92, no. 11, pp. 2398–2413, 2009.
- [13] M. L. Kantam, G. T. Venkanna, C. Sridhar, B. Sreedhar, and B. M. Choudary, "An efficient base-free *N*-arylation of imidazoles and amines with arylboronic acids using copper-exchanged fluorapatite," *Journal of Organic Chemistry*, vol. 71, no. 25, pp. 9522–9524, 2006.
- [14] T. Veerakumar, S. Esakkirajan, and I. Vennila, "Salt and pepper noise removal in video using adaptive decision based median filter," in *Proceedings of the International Conference on Multimedia, Signal Processing and Communication Technologies (IMPACT '11)*, pp. 87–90, Aligarh, India, December 2011.
- [15] B. Azambre, O. Heintz, A. Krzton, J. Zawadzki, and J. V. Weber, "Cellulose as a precursor of catalyst support: new aspects of thermolysis and oxidation—IR, XPS and TGA studies," *Journal of Analytical and Applied Pyrolysis*, vol. 55, no. 1, pp. 105–117, 2000.
- [16] S. Barua, G. Das, L. Aidew, A. K. Buragohain, and N. Karak, "Copper-copper oxide coated nanofibrillar cellulose: a promising biomaterial," *RSC Advances*, vol. 3, no. 35, pp. 14997–15004, 2013.
- [17] H. Koga, A. Azetsu, E. Tokunaga, T. Saito, A. Isogai, and T. Kitaoka, "Topological loading of Cu(I) catalysts onto crystalline cellulose nanofibrils for the Huisgen click reaction," *Journal of Materials Chemistry*, vol. 22, no. 12, pp. 5538–5542, 2012.
- [18] Z. Zhou, C. Lu, X. Wu, and X. Zhang, "Cellulose nanocrystals as a novel support for CuO nanoparticles catalysts: facile synthesis and their application to 4-nitrophenol reduction," *RSC Advances*, vol. 3, no. 48, pp. 26066–26073, 2013.
- [19] C. Shen, H. Zheng, P. Zhang, and X. Chen, "Synthesis of some novel glucosyl triazoles from 2,3,4,6-Tetra-*O*-pivaloyl-D-glucopyranosyl azide," *Journal of Carbohydrate Chemistry*, vol. 29, no. 4, pp. 155–163, 2010.
- [20] W. Yu, L. Jiang, C. Shen, W. Xu, and P. Zhang, "A highly efficient synthesis of *N*-glycosyl-1,2,3-triazoles using a recyclable cellulose-copper(0) catalyst in water," *Catalysis Communications*, vol. 79, pp. 11–16, 2016.
- [21] K. R. Reddy, N. S. Kumar, B. Sreedhar, and M. L. Kantam, "*N*-Arylation of nitrogen heterocycles with aryl halides and arylboronic acids catalyzed by cellulose supported copper(0)," *Journal of Molecular Catalysis A: Chemical*, vol. 252, no. 1–2, pp. 136–141, 2006.
- [22] T. Zhong, G. S. Oporto, J. Jaczynski, A. T. Tesfai, and J. Armstrong, "Antimicrobial properties of the hybrid copper nanoparticles-carboxymethyl cellulose," *Wood and Fiber Science*, vol. 45, no. 2, pp. 215–222, 2013.
- [23] T. Zhong, G. S. Oporto, Y. Peng, X. Xie, and D. J. Gardner, "Drying cellulose-based materials containing copper nanoparticles," *Cellulose*, vol. 22, no. 4, pp. 2665–2681, 2015.
- [24] B. R. Buckley, S. E. Dann, D. P. Harris, H. Heaney, and E. C. Stubbs, "Alkynylcopper(I) polymers and their use in a mechanistic study of alkyne-azide click reactions," *Chemical Communications*, vol. 46, no. 13, pp. 2274–2276, 2010.
- [25] K. Kamata, Y. Nakagawa, K. Yamaguchi, and N. Mizuno, "1,3-Dipolar cycloaddition of organic azides to alkynes by a dicopper-substituted silicotungstate," *Journal of the American Chemical Society*, vol. 130, no. 46, pp. 15304–15310, 2008.

Research Article

Nanofibrillated Cellulose from Appalachian Hardwoods Logging Residues as Template for Antimicrobial Copper

Masoumeh Hassanzadeh,¹ Ronald Sabo,² Alan Rudie,² Richard Reiner,²
Roland Gleisner,² and Gloria S. Oporto¹

¹School of Natural Resources, West Virginia University, Morgantown, WV 26506, USA

²USDA Forest Service, Forest Products Laboratory, Madison, WI 53726-2398, USA

Correspondence should be addressed to Gloria S. Oporto; gloria.oporto@mail.wvu.edu

Received 1 March 2017; Accepted 21 May 2017; Published 19 June 2017

Academic Editor: Raul Fanguero

Copyright © 2017 Masoumeh Hassanzadeh et al. This is an open access article distributed under the Creative Commons Attribution License, which permits unrestricted use, distribution, and reproduction in any medium, provided the original work is properly cited.

TEMPO nanofibrillated cellulose (TNFC) from two underutilized Appalachian hardwoods, Northern red oak (*Quercus rubra*) and yellow poplar (*Liriodendron tulipifera*), was prepared to determine its feasibility to be used as template for antimicrobial metallic copper particles. In addition, a comparison of the TNFC from the two species in terms of their morphological, chemical, thermal, and mechanical properties was also performed. The woody biomass was provided in the form of logging residue from Preston County, West Virginia. A traditional kraft process was used to produce the pulp followed by a five-stage bleaching. Bleached pulps were then subjected to a TEMPO oxidation process using the TEMPO/NaBr/NaClO system to facilitate the final mechanical fibrillation process and surface incorporation of metallic copper. The final TNFC diameters for red oak and yellow poplar presented similar dimensions, 3.8 ± 0.74 nm and 3.6 ± 0.85 nm, respectively. The TNFC films fabricated from both species exhibited no statistical differences in both Young's modulus and the final strength properties. Likely, after the TEMPO oxidation process both species exhibited similar carboxyl group content, of approximately 0.8 mmol/g, and both species demonstrated excellent capability to incorporate antimicrobial copper on their surfaces.

1. Introduction

The production of nanofibrillated cellulose (NFC) from woody biomass has been the subject of intensive investigation in recent years, primarily, due to their unique properties including nontoxicity, biodegradability, renewability, biocompatibility, high specific surface area, high mechanical performance, and feasibility to be chemically modified [1]. These properties are opening new opportunities for NFC applications in areas that include the food industry, papermaking, pharmaceutical/medical, and composites/nanocomposites among others [2, 3].

NFC is nanosized cellulosic chains with dimensions less than 50 nm wide and lengths in the order of several micrometers [4, 5]. NFC can be produced by applying a mechanical treatment such as high-pressure homogenization, microfluidization, grinding, and ultrasonication, to bleached pulps [3]. One important disadvantage of any mechanical treatment

is its high energy consumption which has been addressed applying a preliminary pretreatment. Enzymatic and/or chemical pretreatment were demonstrated to decrease the energy demand because they will weaken the bonds that hold the cellulosic chains together making it easier to break them into nanocellulose or nanofibrillated cellulose [6]. The chemical pretreatment TEMPO-mediated oxidation process will facilitate the breakup of the fiber network and release the nanofibrils through electrostatic repulsion and osmotic effects.

TEMPO or 2,2,6,6-tetramethylpiperidine-1-oxyl is a highly stable nitroxyl radical which is used extensively in the selective oxidation of primary alcohols to corresponding aldehydes and carboxylic acids. In aqueous environments, TEMPO catalyzes the conversion of carbohydrate primary alcohols to carboxylate (COO⁻) functional groups in the presence of a primary oxidizing agent, for example, sodium hypochlorite (NaOCl). In particular, wood fibers can be

converted to individual nanofibers 3-4 nm wide with several microns length by TEMPO-mediated oxidation and successive mild disintegration in water [7, 8]. During this reaction significant amounts of C6 carboxylate groups are selectively formed on each cellulose microfibril surface with minimum changes of the original crystallinity of the cellulosic material. The negative charged carboxylate groups introduced by a TEMPO-mediated oxidation will facilitate the subsequent fibrillation process due to the electrostatic forces created among microfibrils [4].

To date, some studies have compared NFC characteristics from softwood and hardwood biomass sources [5, 9–13]. Part of the available information has been focused on the evaluation of the final NFC morphology using only a mechanical fibrillation treatment [12, 13]; the other part has been focused not only on the final NFC morphology but also on its carboxylic acid availability when a preliminary TEMPO-mediated oxidation process is applied to facilitate the mechanical fibrillation [5, 9–11]. To the authors' knowledge there is no previous or ongoing research regarding the use of the modified nanofibrillated surfaces to attach antimicrobial metal particles in addition to the research performed so far at West Virginia University, where we demonstrated that copper nanoparticles can be effectively synthesized on softwoods TEMPO nanofibrillated cellulose (TNFC) [14]. Likewise, the effectiveness of this TNFC-supported copper in terms of antimicrobial performance and controlled release from thermoplastic films has been also demonstrated previously [14, 15].

Currently, in the Appalachian region, there is a vast amount of low-value, low quality hardwood that can be used as feedstock for novel bioproducts. West Virginia is the third most heavily forested state in the nation. The harvesting process yields approximately 2.41 million dry tons of wood residues annually, including 1.34 million dry tones logging residue of which red oak is the predominant species, followed by yellow poplar and maple species [16]. Even though these species constitute a potential source for NFC production, to the extent of the authors' knowledge, no study in NFC preparation from any of the mentioned hardwood species has been performed to date. Only one study has been reported in West Virginia regarding the use of Appalachian underutilized hardwoods as raw material for nanocrystalline cellulose (NCC) production [17]. Consequently, the two hardwood species, red oak (*Quercus rubra*) and yellow poplar (*Liriodendron tulipifera*) which possess similar chemical composition [2], but different anatomical properties, are of interest to evaluate their properties at a nanoscale. Red oak is a ring porous hardwood with prominent and conspicuous rays and thick-walled latewood vessels. Yellow poplar is a diffuse porous hardwood, with small and solitary pores and fine rays.

The goals of this study therefore include (i) evaluating the feasibility of obtaining cellulose nanofibers from highly available underutilized logging residues from red oak and yellow poplar; (ii) comparing their changes in chemical composition, morphology, carboxyl content, and thermal and mechanical properties after TEMPO-mediated oxidation; and (iii) evaluating TNFCs feasibility to synthesize metallic copper for further antimicrobial applications.

TABLE 1: Conditions of pulping process, kappa number, and screen yield after pulping.

Kraft pulping	
Active alkali, % Na ₂ O	24
Maximum temperature	165°C
Rise to maximum temperature	1°/min
Time at maximum temperature	50 min
Liquor to solid ratio	4
Sulfidity	25
H-factor	750
Kappa number (after pulping)	RO: 13.25; YP: 20
Screen yield pulping	RO: 51%; YP: 52.4%

2. Materials and Methods

2.1. Materials. Northern red oak (*Quercus rubra*) (RO) and yellow poplar (*Liriodendron tulipifera*) (YP) samples were collected in 2014 at WVU Research Forest, Preston County, West Virginia, in the form of logging residue. The samples were chipped and screened. The fractions retained between 1/2 inches and 3/8 inches were used for pulping.

2.2. Methods

2.2.1. Pulping Procedure. Small screened samples of RO and YP were oven-dried to determine the moisture content as 12%. Kraft pulp from the oven-dried material was produced using a M/K System 6-L laboratory digester. The conditions for the pulping process are presented in Table 1. All pulping chemical reagents, including effective alkali, EA, (NaOH + (1/2)Na₂S), were expressed in terms of Na₂O. Sulfidity was expressed as a percentage of the EA, and the expected H-factor was 750. The samples were subjected to the maximum temperature of 165°C for 50 min, after which the temperature was reduced rapidly. The final pulp was disintegrated by vigorous agitation, screened on a Valley flat screen (0.008-inch slot), washed, and then collected in a 200 mesh screen box. The screened wet samples were used for the next step (bleaching) while some small samples were oven- and air-dried for different analysis. The oven-dried pulps were characterized in terms of their lignin content via Kappa number determination. The Kappa numbers of the two species were determined by measuring the consumption of potassium permanganate according to T236 cm-85 standard method. The percentage of lignin was estimated using the following equation:

$$\text{Lignin (\%)} = \text{Kappa number} \times 0.15. \quad (1)$$

2.2.2. Bleaching. A five-stage bleaching sequence DEpDEpD was performed, where D denotes chlorine dioxide and Ep represents peroxide reinforced alkaline extraction. The pulps were thoroughly washed between stages. After the completion of all stages, the fibers were washed and oven-dried. Table 2 shows the conditions of the bleaching processes.

TABLE 2: Conditions of bleaching process.

Stage	D	Ep (alkaline extraction stage 1)	D (second chlorine dioxide)	Ep	D
Chemical charge	ClO ₂ (1.7%) H ₂ SO ₄ (0.2%)	NaOH (2%) H ₂ O ₂ (0.38%)	ClO ₂ (0.8%)	H ₂ O ₂ (0.197%) NaOH (1%)	ClO ₂ (0.3%)
Pulp consistency	10%	10%	10%	10%	10%
End pH	2.5	11	3.5	11	
Temperature	70°C	70°C	70°C	70°C	70°C
Time	45 min	60 min	80 min	130 min	60 min

D: chlorine dioxide; E: peroxide reinforced alkaline extraction.

TABLE 3: Chemical characterization of untreated wood (raw) and bleached pulps (B).

Sample	Cellulose%	Hemicellulose%	Klason lignin (%)	ASL* (%)
Raw _{RO}	53.8 ± 0.6	19.34 ± 0.8	22.5 ± 0.2	4.41
Raw _{YP}	56.8 ± 0.7	17.7 ± 1.1	22.3 ± 0.5	3.30
B _{RO}	78.4 ± 1.6	20.5 ± 2.4	1.1 ± 0.7	0.16
B _{YP}	81.5 ± 1.7	17.6 ± 2.1	1.1 ± 0.6	0.15

* ASL: acid soluble lignin was measured just one time.

2.2.3. TEMPO-Mediated Oxidation. Approximately 30 g of oven-dry basis bleached pulp was added to 3 L of water that contained TEMPO (0.016 g per g pulp) and sodium bromide (0.1 g/g pulp). The reaction was started by adding NaClO solution (5.0 mmol NaClO per g of pulp) with stirring at 500 rpm at room temperature. The pH was maintained at 10 by adding 0.5 M NaOH using a pH stat until no NaOH consumption was observed. Additional NaClO was added to each sample as long as no changes in pH were observed. The TEMPO-oxidized cellulose was thoroughly washed with water by filtration and stored at 4°C before homogenization [1]. The yield has been measured based on weight of dried final material and weight of diluted samples which results in approximately 90% for both TOWP samples.

Samples of each species were air-dried and then used to characterize the degree of polymerization (DP) and carboxylic acid group determination. The rest of the TEMPO-oxidized sample was diluted to 1% solid content, before homogenization. Mechanical fibrillation was performed by passing the samples twice through an M-110EH-30 Microfluidizer (Microfluidics, Newton, MA). In the first step, the material passed through a 200 μm chamber and in the second step the suspension passed through 200- and 87-μm chambers in series.

2.2.4. Chemical Analysis. Samples from kraft and bleached pulps were dried and ground in a Willey mill to pass a 20 mesh screen (model number 2, Arthur H. Thomas co). These samples along with untreated samples were used for the chemical composition analyses that included Klason lignin, acid soluble lignin, and hemicellulose and cellulose determination. High performance anion exchange chromatography (Dionex ICS-3000 system) and the procedure developed by Davis (1998) [18] were used for the carbohydrate determination. Lignin was determined based on the amount of sulfuric acid-insoluble Klason lignin, in accordance with

TABLE 4: Viscosity and degree of polymerization of bleached samples and samples after TEMPO oxidation process (TOWP). Note. TOWP: TEMPO-oxidized wood pulp.

Sample(s)	Viscosity (mPa s)	DP
Bleached _(RO)	19.4 ± 0.4	3152–3300
Bleached _(YP)	10.9 ± 0.2	1666–1736
TOWP _(RO)	2.9 ± 0.2	361–421
TOWP _(YP)	2.4 ± 0.1	302–332

the standard of the Technical association of pulp and paper industry (TAPPI) TAPPI standards-T222 om 88. The results are presented in Table 3. All the analyses, with the exception of acid soluble lignin, were performed in duplicate.

2.2.5. Determination of Intrinsic Viscosity and Degree of Polymerization. Viscosity of the resulting nanofibrillated cellulose was measured according to TAPPI Standard Method T230 om-99. Oven-dried cellulosic solids of 0.1 g were dispersed in 10 mL distilled water and then added to 10 mL of 1 M cupriethylenediamine solution (0.5% solid concentration). The viscosity of the resultant solution was determined with a capillary viscometer. The degree of polymerization (DP) was estimated by the following equation:

$$DP = 120 \times [\eta]^{1.11}, \quad (2)$$

where η is the measured viscosity; the results are presented in Table 4.

2.2.6. Carboxyl Content of the Pulp. Determination of carboxyl content of the samples before and after the TEMPO-mediated oxidation process was performed according to T237 om-88, modified as indicated below to account for the high acid content of the fiber with some reagent concentration

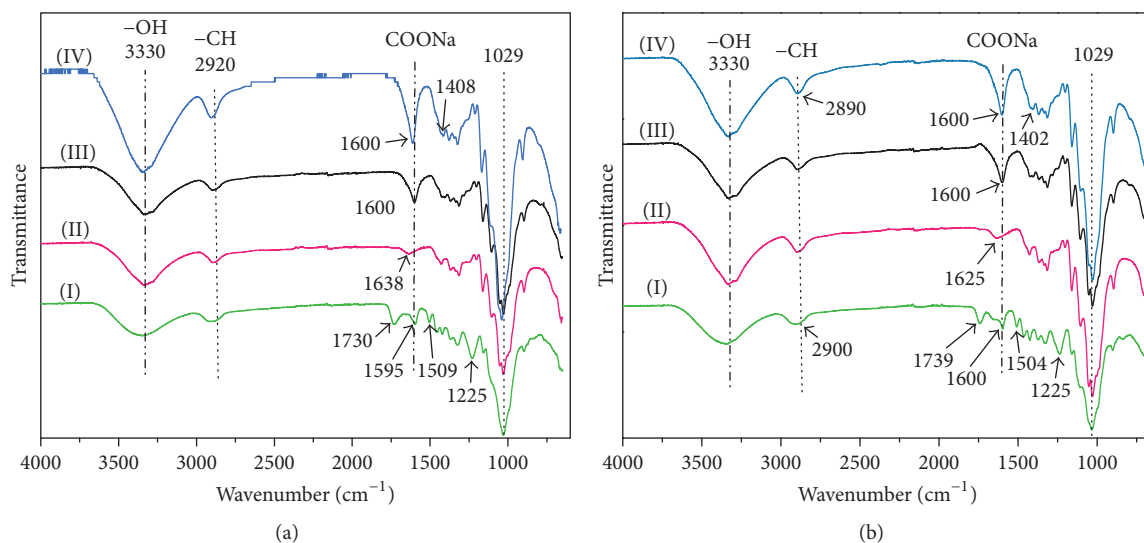


FIGURE 1: (a) FTIR spectra of red oak: (I) raw material, (II) bleached, (III) tempo-oxidized wood pulp (TOWP), and (IV) TEMPO-oxidized cellulose nanofibers (TNFC). (b) FTIR spectra of yellow poplar: (I) raw material, (II) bleached, (III) tempo-oxidized wood pulp (TOWP), and (IV) TEMPO-oxidized cellulose nanofibers (TNFC).

TABLE 5: Carboxylic contents of Red oak and Yellow poplar species for bleached and TEMPO-oxidized samples (TOWP).

Samples	COOH (mmol/g)
Bleached _{RO}	0.05
Bleached _{YP}	0.07
TOWP _{RO}	0.82
TOWP _{YP}	0.80

modifications. The pulps were converted to the acid form by soaking them in 0.01 M HCl and then washing with deionized water. This acidified pulp was reacted with a standardized 0.1 M NaHCO₃ with 0.25 M NaCl solution. The amount of residual NaHCO₃ was determined by titration with 0.1 M HCl, to a methyl red endpoint. The carboxyl content was calculated in milliequivalents (meq) per 100 g of oven-dry pulp and then converted to mmol/g and the results are presented in Table 5.

2.2.7. Fourier Transform Infrared Spectroscopy (FTIR). Fourier transform infrared spectra were recorded for the raw material, bleached pulps, TEMPO-oxidized pulps, and the final TEMPO nanofibrillated cellulose (TNFC) samples using a Perkin-Elmer Spectrum 2000 FTIR spectrometer. The samples were analyzed from 600 to 4,000 cm⁻¹. The spectrum was obtained from dry samples using 16 scans at a 4 cm⁻¹ resolution and a 1 cm⁻¹ interval at room temperature. The results are presented in Figure 1.

2.2.8. X-Ray Diffraction (XRD) Characterization. X-ray diffraction (XRD) analysis was performed on the raw material, TEMPO-oxidized pulps, and the final TEMPO nanofibrillated cellulose (TNFC) samples. The analysis was performed

TABLE 6: Crystallinities of raw material, TEMPO-oxidized wood pulp (TOWP), and TEMPO-oxidized cellulose nanofibers (TNFC).

Sample	Degree of crystallinity (%)
Raw _{RO}	37.0 ± 3.26
Raw _{YP}	34.4 ± 2.5
TOWP _{RO}	61.7 ± 1.66
TOWP _{YP}	59.85 ± 2.2
TNFC _{RO}	39.3 ± 0.9
TNFC _{YP}	39.4 ± 0.5

on a X-ray diffractometer (PANalytical X'Pert Pro XRD) in the range of 10° to 40° 2θ. Cu- α 1 8047.2 eV source and a maximum X-ray power of 45 kV and 40 mA were used. The crystallinity index (CI) after the different treatments was determined using the peak height method and calculated by the Segal empirical method [19] after subtraction of the background signal:

$$CI (\%) = \frac{I_{200} - I_{am}}{I_{200}} \times 100\%, \quad (3)$$

where I_{200} is the peak intensity corresponding to crystalline cellulose I at $2\theta = 22.6^\circ$ and I_{am} is the intensity minimum between the 200 and 110 peaks ($2\theta = 18^\circ$).

The results are presented in Table 6 and Figure 2.

2.2.9. Thermogravimetric Analysis (TGA). Thermogravimetric analysis was performed for the raw material and the final TEMPO nanofibrillated cellulose (TNFC) using 4–6 mg sample. The data was obtained using a TA Q50 thermogravimetric analyzer (Delaware, USA). The temperature was set from 25°C to 600°C at a heating rate of 10°C/min under a nitrogen atmosphere at a flow rate of 20 mL/min. The results of this analysis are presented in Table 7 and Figure 3.

TABLE 7: Onset degradation temperature (T_{onset}), maximum thermal degradation temperature (T_{max}), maximum weight loss (WL_{max}), and CY (char yield) (%) (char residue after 575°C).

Samples	T_{onset} (°C)	Stage I		Stage II		CY (%)
		T_{max} (°C)	WL_{max} (%/°C)	T_{max} (°C)	WL_{max} (%/°C)	
Raw _{RO}	304.5	285	0.45	358	1.12	14.0
Raw _{YP}	312	—	—	366	1.17	13.4
TNFC _{RO}	224	234	0.58	288	0.68	20.0
TNFC _{YP}	225	232	0.6	290	0.7	19.5

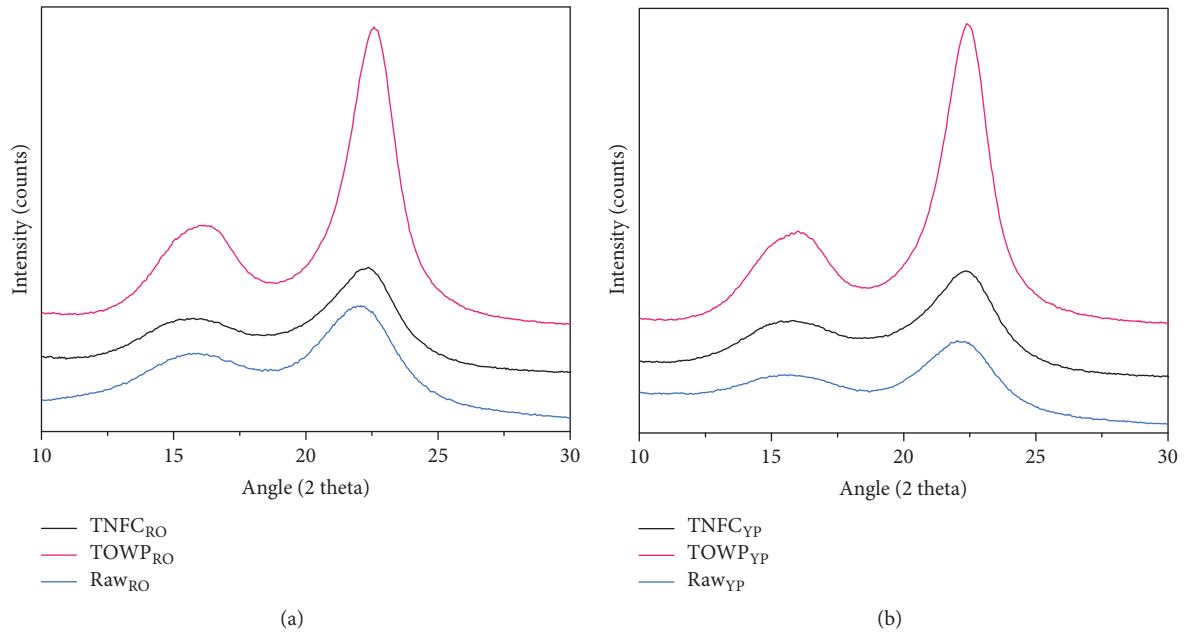


FIGURE 2: X-ray diffraction patterns of (a) Raw_{RO}, TOWP_{RO}, and TNFC_{RO}; (b) Raw_{YP}, TOWP_{YP}, and TNFC_{YP}.

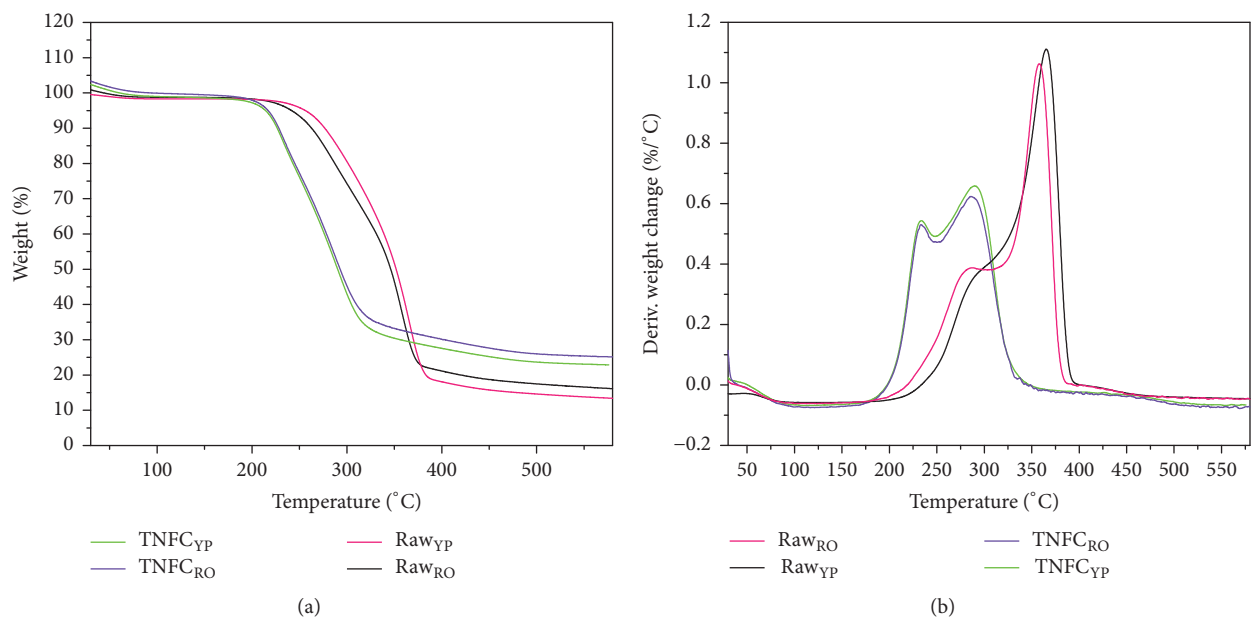


FIGURE 3: Thermogravimetric (TGA (a)) and the corresponding derivative thermogravimetric (DTG) (DTG (b)) curves of the raw material and TEMPO-oxidized cellulose nanofibers (TNFC).

2.2.10. Scanning Electron Microscopy (SEM). Scanning electron microscopy (SEM) was used to evaluate the effect of mechanical fibrillation on the samples morphology. TEMPO-oxidized wood pulp (TOWP) and TEMPO nanofibrillated cellulose (TNFC) were freeze-dried after a preliminary solvent exchange process using ethanol and tert-butanol [20]. Freeze drying was conducted on a VirTis Genesis Freeze Dryer (Warminster, PA, USA) at -40°C for 1 week. The morphological analyses of the samples were performed using a Hitachi S-4700 FESEM-EDX. Before the FESEM-EDX analyses, all the samples were coated with gold-palladium using a sputtering process to provide adequate conductivity. The diameter of different samples after bleaching and TEMPO oxidation was measured and calculated using the ImageJ Manipulation Program [21] for at least 30 fibers for each sample. Results are presented in Figure 4.

2.2.11. Transmission Electron Microscope (TEM). For TEM analysis TNFC samples of RO and YP were used as their original undiluted suspension form. Undiluted TNFC suspensions were deposited on a glow-discharged copper grid with formvar and carbon film (400 mesh) for 5 min and then rinsed thoroughly using a 1% aqueous uranyl acetate stain followed by blotting dry. Samples were imaged using Philips CM-100 TEM (Philips/FEI Corporation, Eindhoven, Holland) operated at 100 kV, spot 3,200 μm condenser aperture, and 70 μm objective aperture. The images were captured in digital form directly on the microscope using Gatan Orius SC200-1 2 Mpixel CCD camera (Gatan, Inc., Pleasanton, CA) with 19k, 46k, and 92k magnification. The diameter of different NFCs was measured and calculated from TEM images using the ImageJ Manipulation Program [21] for at least 50 nanofibers in each sample. The results are presented in Figure 5.

2.2.12. Preparation and Characterization of TNFC Films. TNFC hydrogel films were prepared by filtering TNFC suspensions which were dried afterwards. The filtration was performed by first diluting the TNFC suspension to 0.2% solid by weight with reverse-osmosis-treated water. Following the dilution, the suspensions were filtered using a 142-mm Millipore ultrafiltration system (Millipore Corporation, Billerica, MA, USA) under 0.55 MPa of air pressure. Omnipore TM filter membranes with a pore size of 0.1 μm (JVWPI4225, JV, Millipore Corporation, USA) were supported on filter paper in the ultrafiltration system. The wet films (hydrogels) were peeled from the membrane, processed, stacked, and placed between an assembly of waxy coated papers, absorbent blotter paper, and two metal caul plates. The assembly was air-dried at room temperature for 24 h and then oven-dried at 60°C for 8 h under a load of approximately 250 N. The blotter and filter papers were replaced several times over the first 24 h to minimize wrinkling of the films [22].

The tensile strength of different NFC films was tested using an Instron 5865 universal material testing apparatus (Instron Engineering Corporation, MA, USA) with a 500 N load cell, according to ASTM D638-10. The specimens were cut according to ASTM D638-10 type V dog bone shape using a special die (Qualitest, FL, USA) and were subsequently

conditioned at 50% RH and 23°C for at least 1 week prior to testing, also at 50% RH and 23°C . The specimens were preloaded with a 5 N force to remove slack and the tests were performed with a crosshead speed of 1 mm/min. At least 6 specimens were tested for each sample. A LX 500 laser extensometer (MTS Systems Corporation, MN, USA) was used to determine the displacement with sampling frequency of 10 Hz. The laser recorded the displacement between two strips of reflective tape initially placed 8 mm apart on the necked-down region of the dog bone specimens. Strain was calculated from the displacement and initial gage length [23]. The stress-strain curves were fit to a hyperbolic tangent and the tensile modulus was taken as the slope of the fit curve at zero strain. The statistical significance was determined using a two-tailed unpaired Student's *t*-test and *p* value < 0.05 was considered statistically significant. The maximum tensile strength and the corresponding tensile modulus are presented in Figure 6.

2.2.13. Preparation of Hybrid TNFC and Copper Nanoparticles. The hybrid TNFC-metallic copper particles were prepared according to Jiang et al., 2016 [14], and Zhong et al., 2015 [15]. Upon dispersing the hybrid materials into deionized water, they were dried using a preliminary solvent exchange process with ethanol/tert-butanol and then freeze-dried as described by Zhong et al., 2015 [20].

2.2.14. Copper Determination on TNFC from Red Oak and Yellow Poplar. Copper determination of TNFC-metallic copper particles was conducted using Energy-Dispersive X-ray (EDX) analysis and the results are presented in Table 9. The morphological analysis of the TNFC-metallic copper particles from red oak and yellow poplar was performed using a Hitachi S-4700 FE-SEM; the samples were previously coated with gold-palladium using a sputtering process to provide adequate conductivity. An example of the final morphology of these samples with the presence of copper crystals is presented in Figure 7.

3. Results and Discussion

3.1. Chemical Analysis. The contents of the primary constituents (cellulose, hemicellulose, and lignin) of the untreated woody samples and bleached pulps are presented in Table 3. According to these results, bleached samples of YP contained slightly more cellulose content and less hemicellulose than RO. For RO and YP, carboxylic contents were nearly identical (Table 5) and might be one reason indicating that the difference in hemicellulose content between two samples is negligible to have an effect on carboxyl content. It has also been reported that high content of hemicelluloses facilitates the release of nanofibrils during the mechanical treatment of the pulp [24]; however, as mentioned above, the difference in hemicellulose content in RO and YP does not look significant based on results of carboxyl contents.

In terms of lignin, no differences between RO and YP were determined for both untreated and bleached pulps. The kappa number (KN) of the kraft pulp was 13.25 and 20 giving the lignin percentage of 1.72 and 2.6 for RO and YP

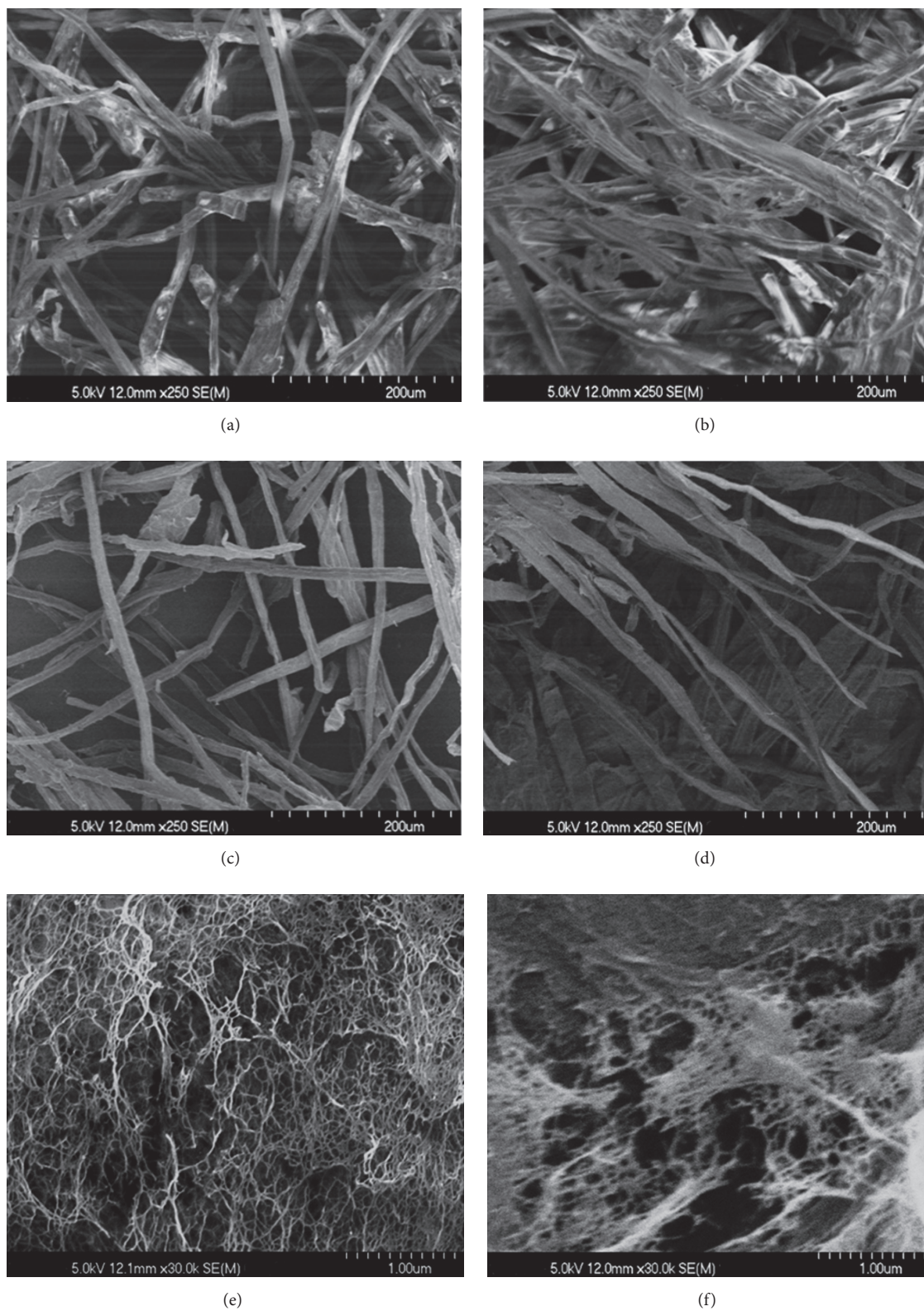


FIGURE 4: FE-SEM micrographs of the bleached RO (a) and YP (b); TEMPO-oxidized wood pulp (TOWP) of RO (c) and YP (d); TEMPO nanofibrillated cellulose (TNFC) of RO (e) and YP (f) samples after a solvent exchange (E/tert-B-FD treatment) followed by freeze drying.

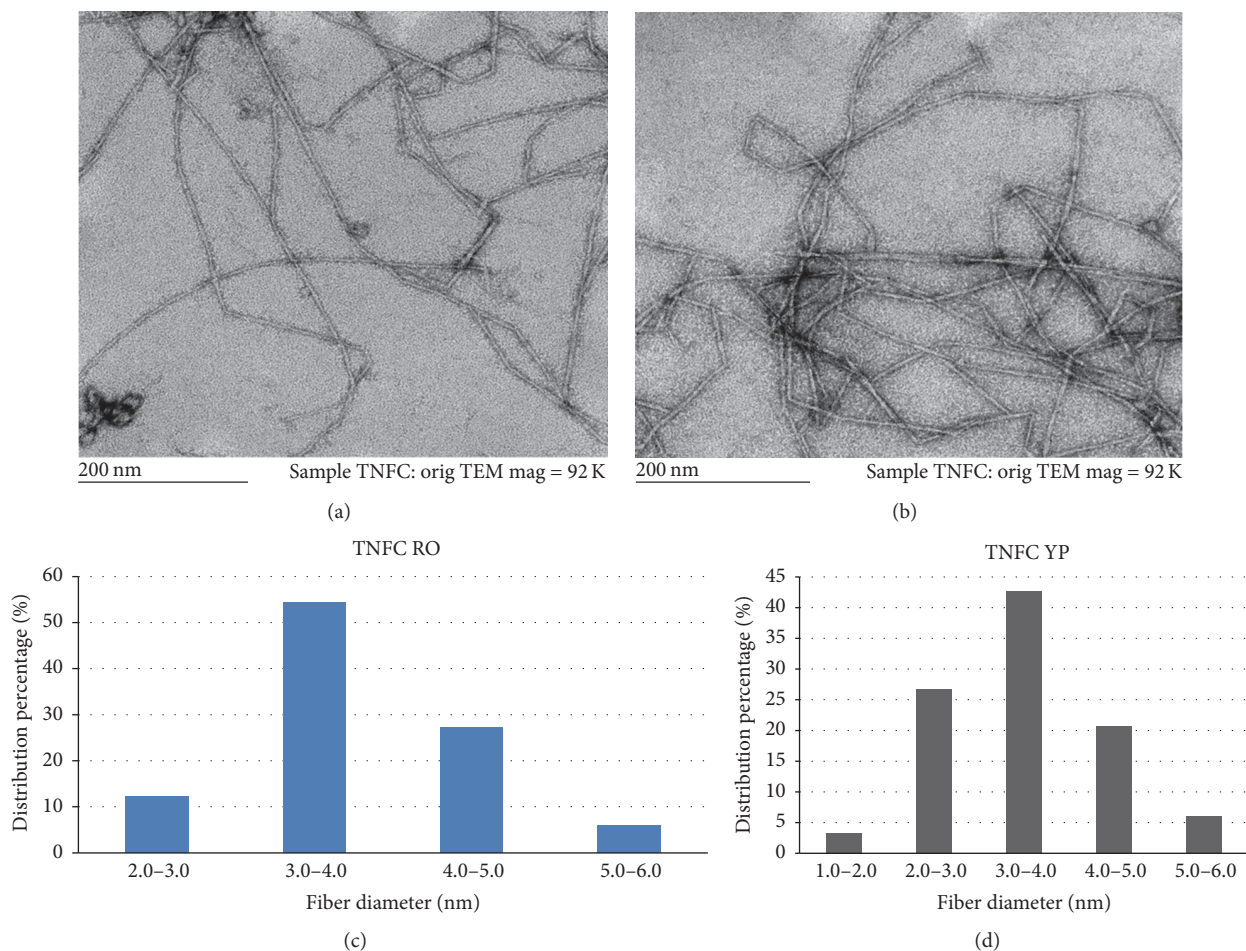


FIGURE 5: TEM images of TNFC_{RO} (a) and TNFC_{YP} (b) and their size distribution properties: (c) RO; (d) YP.

after the kraft pulping, respectively. The kappa number varies according to the wood species and delignification procedure during pulping [25].

3.2. Degree of Polymerization (DP). The degree of polymerization as a function of the viscosity of bleached and TEMPO-oxidized wood pulp (TOWP) from RO and YP is presented in Table 4. The viscosity is an indirect measurement of the cellulose polymer chain length and can be used to indicate chemical degradation of the pulps due to chemical or mechanical treatments.

The viscosity and correspondent DP result are higher for RO bleached and TOWP samples. This result might be related to the previous difference in terms of the hemicellulose content. The TEMPO-mediated oxidation and especially the use of NaClO inevitably lead to depolymerization of the starting material in both samples of RO and YP but showed a slight reduction in YP samples.

3.3. Carboxyl Content. The carboxylic group content was determined for RO and YP bleached pulps and for the RO and YP TEMPO-oxidized samples. As presented in Table 5 the carboxylic group increased from 0.05–0.07 mmol/g for the

bleached pulps to 0.80–0.82 mmol/g after the oxidation process. The increase in the carboxylic content after the TEMPO-mediated oxidation process was similar for both hardwood species.

3.4. FTIR Spectroscopy Analysis. The analysis of functional groups through FTIR is presented in Figure 1(a) for RO and Figure 1(b) for YP, where (I) corresponds to the initial woody raw material; (II) is the bleached samples; (III) is the TEMPO-oxidized samples (TOWP); and (IV) corresponds to the TEMPO nanofibrillated material (TNFC).

The absorption peaks at 3300 cm^{-1} and $2920\text{--}2800\text{ cm}^{-1}$ were attributed to hydrogen bonded hydroxyl (OH) groups of cellulose and absorbed water and aliphatic saturated C–H stretching vibration, respectively [26–30]. These peaks increased in intensity after bleaching and TEMPO oxidation.

The bands present at 1730 and 1739 cm^{-1} which are possible to observe only for the untreated raw material for both RO and YP can be attributed to C=O stretching of the acetyl and uronic ester groups of hemicellulose or the ester linkage of carboxylic groups of ferulic and p-coumaric acids of lignin and/or hemicellulose [31, 32]. This band was no longer present in the FTIR spectra of RO and YP after bleaching

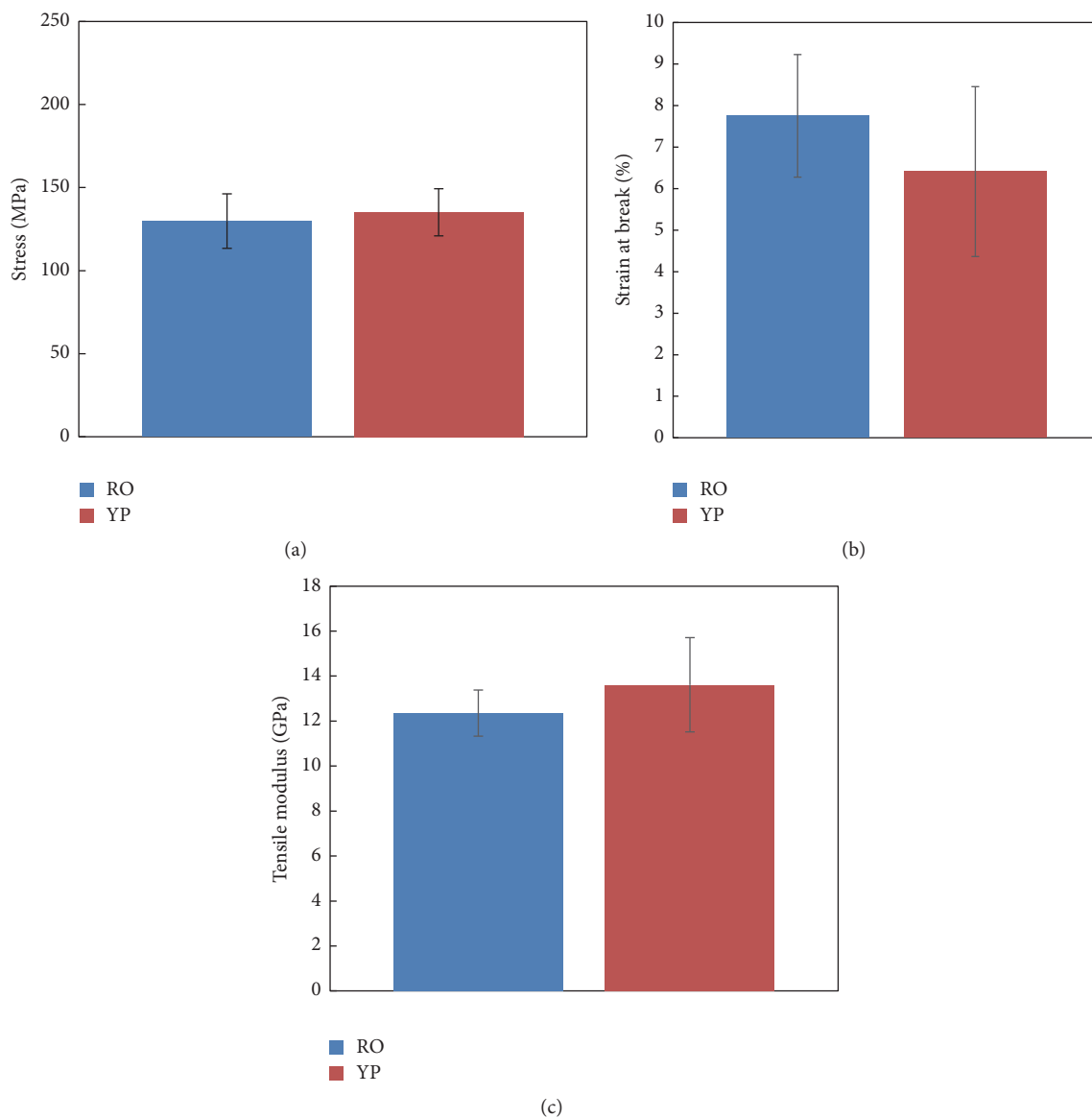


FIGURE 6: Main tensile properties of NFC films prepared from cellulose nanofibrils of RO (RO) and YP (YP). (a) Stress; (b) strain at break; (c) tensile modulus.

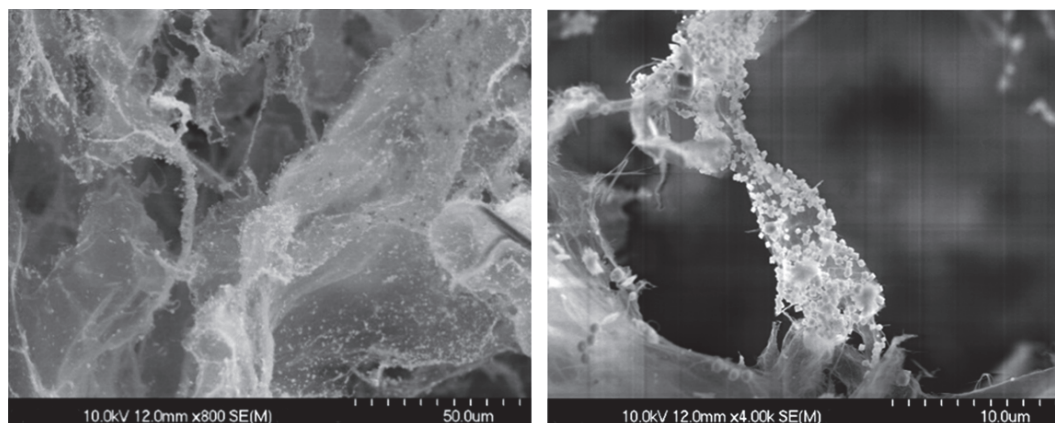


FIGURE 7: SEM images of dried TNFC_{RO} after the treatment with copper sulphate and reducing agent sodium borohydride (TNFC_{RO}-Cu).

and subsequent TEMPO oxidation treatments. The disappearance of this band is largely due to the removal of hemicellulose and lignin from RO and YP fibers during the chemical extraction [31, 33]. The peaks at $1,509\text{--}1,504\text{ cm}^{-1}$ in the spectra of raw samples of RO and YP represent the --C=C-- stretch of the aromatic rings of lignin [32, 34]. The lower amount of this peak in the treated samples is attributed to the removal of lignin during chemical procedures.

Two strong absorption bands at around $1638\text{--}1600$ and $1412\text{--}1402\text{ cm}^{-1}$, which correspond to carbonyl groups --C=O , are present in both spectra in response to the TEMPO-mediated oxidation process. As expected after the TEMPO oxidation process hydroxyl groups at the C6 position of cellulose molecules were converted to sodium carboxylate. The intensity of --C=O peaks for both hardwood species presents the following trend: TNFC = TOWP > bleached > raw material individually, whereas, comparing RO and YP graphs, these areas have shown same intensity.

The peaks observed in the spectra of the fibers around 1225 cm^{-1} are due to the C–O stretching of the aryl group in lignin [35]. Disappearance of this peak from the spectra of the bleached pulp fibers as well as from those of the nanofibers is explained by the removal of lignin due to chemical treatments.

The stretching of C–O and O–H and bending vibration of the C–O–C pyranose ring in cellulose molecules [36, 37] can be observed as peaks around $1070\text{--}1010\text{ cm}^{-1}$ for all samples. The peak at 1029 cm^{-1} for both hardwood species seems to be much higher for TNFC in following the trend TNFC > TOWP > bleached > raw material in RO and YP meaning more carbohydrate content after treatment.

To summarize, the typical absorption band that appears in RO and YP was similar, and there were no significant differences between them after different treatments.

3.5. Crystallinity Determination. The XRD patterns of the raw material, oxidized samples by TEMPO (TOWP), and nanofibrillated cellulose (TNFC) from red oak and yellow poplar are presented in Figures 2(a) and 2(b), respectively. The resultant Crystallinity index for those samples is displayed in Table 6.

All samples had diffraction peaks at $2\theta = 16.5^\circ$ and 22.5° , which is considered to represent the typical cellulose I pattern [38]. The crystallinity index (CI) of the original samples was 37 and 34.4% for RO and YP, respectively. After oxidation, the apparent crystallinity of samples increased to 61.7 and 59.8% in RO and YP, respectively, owing to the removal of hemicellulose and lignin. This increase was expected, but not that significant. Some artifacts in the measurement of CI might be affecting the results, but since the increase was similar for both species, the values were accepted. The crystallinity went through significant reduction upon the homogenization process to a degree of 39% in TNFC species of RO and YP, respectively. Mechanical fibrillation appears to affect importantly the final crystallinity of TNFC samples, but, once again, caution must be considered here because of possible artifacts associated with the measurements of crystallinity of TEMPO-oxidized pulps. Some researchers determined a reduction in

crystallinity after a high level homogenization of TEMPO-oxidized pulps due to either breakage or peeling-off of the cellulose [9, 13, 39]. Even though differences in the crystallinity index after the TEMPO oxidation stage and after the fibrillation process were observed, the differences were similar between the two hardwood species in study.

3.6. Thermal Gravimetric Analysis. Thermogravimetric (TGA) and derivative thermogravimetric (DTG) analyses were performed to compare the thermal degradation characteristics of the untreated and chemomechanical treated RO and YP. Details of the major decomposition temperatures and the corresponding percentage of weight losses are summarized in Table 7. The thermal behaviour of lignocellulosic materials depends on their chemical composition, structure, degree of crystallinity, and the molecular interactions between the different macromolecules [40]. Between the temperatures of 150 and 500°C , the degradation process begins in the cellulose, hemicellulose, and the associated linked water.

In the TGA curve represented by weight (%) (Figure 3(a)), thermal degradation of untreated raw samples begins at temperatures 304.5 and 312°C (T_{onset}), whereas in TEMPO-oxidized NFCs the T_{onset} began at 224 and 225°C for RO and YP, respectively. In the DTG curve represented by deriv. weight ($\%/^\circ\text{C}$) (Figure 3(b)), both TEMPO-oxidized and untreated samples showed a prominent pyrolysis process, with a clear double step degradation for TNFC samples (stages I and II). The maximum weight loss was observed in the temperature ranges $230\text{--}290^\circ\text{C}$ and $285\text{--}366^\circ\text{C}$, respectively.

As shown in the DTG curves in Figure 3(b) the untreated RO showed a small broadening or shoulder at 285°C on the left side of the main peak (366°C), which may have been due to the decomposition of hemicellulose as hemicelluloses has lower thermal stability than lignin and cellulose [41]. In the case of the untreated YP, the DTG curve showed a less sharp peak on the left side of the main peak, which may be explained by the lower content of hemicellulose. This probably resulted in better thermal properties for the untreated YP than RO (304.5 versus 312 in Table 7 for raw RO and raw YP, resp.) since the decomposition of hemicellulose begins at much lower temperatures, compared to cellulose [42]. The final major decomposition peak observed at the high temperature range ($300\text{--}400^\circ\text{C}$) is accounted for in the pyrolysis of cellulose. This peak was higher in YP compared to RO in both raw fibers and TNFC samples (stage II of Table 7) and might be explained by the fact that YP showed a higher cellulose content than RO by carbohydrate measurement (Table 3). As expected, the degradation temperatures of TEMPO-oxidized NFCs for both RO and YP were lower than those of untreated samples, because the carboxylic acid groups initiate thermal decomposition at lower temperatures [43]. These results are consistent with the results obtained from FTIR and XRD measurements. As presented in Table 7, the char residues (CY%) from TNFC samples were higher than those of raw samples. The large amount of char residue from TEMPO-oxidized NFCs is due to the high sodium ion which will hold carbonate, so the high sodium content after neutralization

TABLE 8: Mechanical properties of transparent films of the oxidized cellulose fibrils.

Samples	Tensile modulus (Gpa)	Max tensile stress (Mpa)	Strain at break (%)
TNFC _{RO}	12.35 ± 1.02	129.8 ± 16.36	7.75 ± 1.4
TNFC _{YP}	13.6 ± 2.09	135.15 ± 14.2	6.41 ± 2.04

TABLE 9: Copper determination using EDX of hybrid material TNFC-CuNPs based on TNFC from Red oak and Yellow poplar (three repetitions).

Samples	Cu (wt%)
TNFC _{RO}	18.9 ± 2.8
TNFC _{YP}	20.2 ± 4.1

results in a high ash (char) content in of TEMPO treated pulps (TOWP). In summary, based on TGA analysis, TNFCs from YP and RO have similar thermal stability.

3.7. Morphology of the Treated and Untreated Samples. Figures 4(a) and 4(b) are SEM images of bleached samples of RO and YP, respectively. Before the analysis the samples were dried in a conventional laboratory oven at $103^{\circ}\text{C} \pm 2^{\circ}\text{C}$ overnight. The average in diameter for RO fiber was $9.16 \pm 1.06 \mu\text{m}$ and $15.5 \pm 1.04 \mu\text{m}$ for YP, according to the SEM images.

Figures 4(c) and 4(d) represent SEM images of TEMPO-oxidized fibers (TOWP) of RO and YP, respectively. Before the analysis the samples were dried in a conventional laboratory oven at $103^{\circ}\text{C} \pm 2^{\circ}\text{C}$ overnight. The resultant average in diameter for TOWP of RO is of $7.99 \pm 1.75 \mu\text{m}$ and $17.69 \pm 2.12 \mu\text{m}$ for TOWP of YP. The TEMPO oxidation process has not affected the dry fiber diameters.

Figures 4(e) and 4(f) are SEM images of TEMPO nanofibrillated cellulose (TNFC) from RO and YP, respectively. Before the analysis the samples were dried using a solvent exchange process previously to a freeze drying stage [20]. The preparation method aims to produce a material with high specific surface area. As presented in both images a fibrillar and porous network structure resulted for both red oak and yellow poplar species. The magnification for these samples was different compared to the previous ones, to highlight the high porous structure resultant for both species after their mechanical fibrillation and drying processes.

In Figures 5(a) and 5(b) TEM images of TEMPO nanofibrillated cellulose (TNFC) from RO and YP, respectively, are presented. As mentioned earlier, the diameters of these TNFCs were measured from TEM images using the ImageJ Manipulation Program [21]. The average diameter for TNFC from RO resulted as $3.8 \pm 0.74 \text{ nm}$ and as $3.6 \pm 0.85 \text{ nm}$ for TNFC from YP. The maximum diameter was 5–6 nm with 6% distribution in both species.

The distribution of diameter percentages of nanofibrils is presented in Figures 5(c) and 5(d) for TNFC RO and TNFC YP, respectively. This information indicates that there are 10% more nanofibrils with diameters in the range of 3.0–4.0 nm for RO compared with YP, and also 10% more nanofibrils

with diameters in the range of 5.0–6.0 nm for RO compared to YP. No nanofibrils with diameters in the range 1.0–2.0 nm were found for RO. In the nanofibril diameter range between 2.0 and 3.0 nm YP resulted 14.5% higher than RO. The introduction of negative carboxyl groups on nanofibril surface generated strong repulsive forces, which resulted in separated individual nanofibrils with narrow diameter distribution [44].

3.8. Mechanical Properties of NFC Films. TNFC films of RO and YP were produced and their mechanical properties were measured. Ten randomly chosen films were used for these measurements. The average film thickness was 127 micrometers for both NFC samples.

The tensile modulus (modulus of elasticity or MOE) of the various NFC films was calculated based on the initial linear region of the stress-strain curve and is shown in Figure 6(a). YP and RO were shown to be very close in MOE ($12.35 \pm 1.02 \text{ GPa}$ versus 13.6 ± 2.09) with no significant p value. Previous studies by other groups showed that tensile modulus strongly depends on the crystallinity of nanofibrils as [23, 45, 46]. The results of MOE in both species were in accordance with XRD analysis by which both TNFC samples showed close range of crystallinity after homogenization (Table 6). The strain at break for the various NFC films also demonstrated no significant difference between films of RO ($7.75\% \pm 1.4$) compared to YP ($6.41\% \pm 2.04$) (Figure 6(b) and Table 8).

The maximum tensile stress (strength) of films prepared from different NFCs is shown in Figure 6(c) and Table 8. It can be seen the TEMPO films from YP had almost the same mechanical strength with a small increase of approximately $135.15 \pm 14.2 \text{ MPa}$ compared to RO ($129.8 \pm 16.36 \text{ MPa}$). This difference is not significant according to the t -test (p value > 0.05).

Henriksson et al. (2008) [47] pointed out that the tensile strength, toughness, and strain to failure of nanofiber films correlate with the average molar mass of the nanofibers. Qing et al. (2013) [23] reported similar results from Eucalyptus TNFC samples, showing higher tensile strength of approximately 220 MPa caused mainly because of the higher DP of the oxidized cellulose, while the crystallinity of their TNFC samples was in the range of our samples. Saito et al. (2009) [44] also reported that TEMPO/NaClO/NaClO₂ system provides CNF with up to approximately 1.5 times higher tensile strength (312 MPa) compared to those CNF from TEMPO/NaBr/NaClO, which was again attributed to the higher DP of the final CNF. Moreover, Rodionova et al. (2012) [8] reported that the final refining and homogenization process results in significantly higher defects and shorter lengths for hardwood nanofibers compared to softwood nanofibers;

so, the correspondent tensile strengths of the softwood nanofiber films were significantly higher than the strengths of the hardwood nanofiber films.

3.9. Copper Determination. As mentioned earlier, samples of TNFC from red oak and yellow poplar after the copper synthesis step (TNFC-Cu) were characterized by Energy-Dispersive X-ray Analysis (EDX). The results show that both nanofibrillated hybrid materials (from red oak and yellow poplar) have similar copper weight percentage present after the synthesis process. This result can be attributed to the similar carboxylate content for both TNFC species and sites where copper is reduced from salts to the correspondent metallic state. This result is confirmed through the SEM analysis, presented in Figure 7, where the presence of copper is represented as crystals on the surface of TNFC-Cu from red oak. Similar pictures were found for yellow poplar. The presence of copper in the nanofibrillated hybrid material makes it possible to assume that the final hybrid material will possess antimicrobial properties as demonstrated in a previous research [48].

4. Conclusions

Underutilized woody biomass composed by red oak (*Quercus rubra*) and yellow poplar (*Liriodendron tulipifera*) was used for producing TEMPO nanofibrillated cellulose (TNFC) using a chemimechanical treatment. The morphological analysis performed by TEM on TNFC indicated a final average fibril width between 3 and 4 nm for both species. The carboxylate content after the TEMPO oxidation process resulted in approximately 0.8 mmol/g for both species. No difference in the lignin composition trend was observed after the pulping and bleaching process for both woody species; hemicellulose content was higher for red oak in all treated and untreated samples but showed no impact on the final morphology, carboxylate content, or mechanical properties of the final TNFC. Model films prepared from red oak and yellow poplar evidenced similar thermomechanical properties; however, the strength of the two species seemed to be lower than the values published elsewhere. The low strength of films achieved in this research is probably due to the reduced DP after the mechanical treatment. Overall, both TNFCs from red oak and yellow poplar presented the same capability to support metallic copper to be used as hybrid materials in thermoplastic films for applications in the packaging and medical/pharmacy fields.

Abbreviations

NFC:	Nanofibrillated cellulose
TNFC:	TEMPO nanofibrillated cellulose
TEMPO:	2,2,6,6-Tetramethylpiperidine-1-oxyl radical
XRD:	X-ray diffraction
RO:	Red oak
YP:	Yellow poplar
TOWP:	TEMPO-oxidized (bleached) wood pulp
TEM:	Transmission electron microscopy
SEM:	Scanning electron microscopy
DP:	Degree of polymerization.

Conflicts of Interest

The authors declare that there are no conflicts of interest regarding the publication of this paper.

Acknowledgments

Funding for this work has been provided by NIFA McStennis WVA00098 “Efficient Utilization of Biomass for Biopolymers in Central Appalachia” and USDA NIFA Grant no. 2013-34638-21481 “Development of Novel Hybrid Cellulose Nanocomposite Film with Potent Biocide Properties Utilizing Low Quality Appalachian Hardwoods.” Special thanks are due to Changle Jiang, Ph.D. student in forest resources science, for performing the copper determination analysis on TNFCs (EDX-SEM).

References

- [1] T. Saito, S. Kimura, Y. Nishiyama, and A. Isogai, “Cellulose nanofibers prepared by TEMPO-mediated oxidation of native cellulose,” *Biomacromolecules*, vol. 8, no. 8, pp. 2485–2491, 2007.
- [2] W. Jin, K. Singh, and J. Zondlo, “Pyrolysis kinetics of physical components of wood and wood-polymers using isoconversion method,” *Agriculture*, vol. 3, no. 1, pp. 12–32, 2013.
- [3] T. Pääkkönen, K. Dimic-Misic, H. Orelma, R. Pönni, T. Vuorinen, and T. Maloney, “Effect of xylan in hardwood pulp on the reaction rate of TEMPO-mediated oxidation and the rheology of the final nanofibrillated cellulose gel,” *Cellulose*, vol. 23, no. 1, pp. 277–293, 2016.
- [4] Q. Meng, H. Li, S. Fu, and L. A. Lucia, “The non-trivial role of native xylans on the preparation of TEMPO-oxidized cellulose nanofibrils,” *Reactive and Functional Polymers*, vol. 85, pp. 142–150, 2014.
- [5] K. Syverud, G. Chinga-Carrasco, J. Toledo, and P. G. Toledo, “A comparative study of *Eucalyptus* and *Pinus radiata* pulp fibres as raw materials for production of cellulose nanofibrils,” *Carbohydrate Polymers*, vol. 84, no. 3, pp. 1033–1038, 2011.
- [6] I. Siró and D. Plackett, “Microfibrillated cellulose and new nanocomposite materials: a review,” *Cellulose*, vol. 17, no. 3, pp. 459–494, 2010.
- [7] A. Isogai, T. Saito, and H. Fukuzumi, “TEMPO-oxidized cellulose nanofibers,” *Nanoscale*, vol. 3, no. 1, pp. 71–85, 2011.
- [8] G. Rodionova, Ø. Eriksen, and Ø. Gregersen, “TEMPO-oxidized cellulose nanofiber films: effect of surface morphology on water resistance,” *Cellulose*, vol. 19, no. 4, pp. 1115–1123, 2012.
- [9] I. Besbes, M. R. Vilar, and S. Boufi, “Nanofibrillated cellulose from Alfa, Eucalyptus and Pine fibres: preparation, characteristics and reinforcing potential,” *Carbohydrate Polymers*, vol. 86, no. 3, pp. 1198–1206, 2011.
- [10] F. W. Brodin and H. Theliander, “A comparison of softwood and birch kraft pulp fibers as raw materials for production of TEMPO-oxidized pulp, MFC and superabsorbent foam,” *Cellulose*, vol. 20, no. 6, pp. 2825–2838, 2013.
- [11] G. Rodionova, T. Saito, M. Lenés et al., “TEMPO-Mediated Oxidation of Norway Spruce and Eucalyptus Pulps: Preparation and Characterization of Nanofibers and Nanofiber Dispersions,” *Journal of Polymers and the Environment*, vol. 21, no. 1, pp. 207–214, 2013.

- [12] W. Stelte and A. R. Sanadi, "Preparation and characterization of cellulose nanofibers from two commercial hardwood and softwood pulps," *Industrial & Engineering Chemistry Research*, vol. 48, no. 24, pp. 11211–11219, 2009.
- [13] T. Zimmermann, N. Bordeanu, and E. Strub, "Properties of nanofibrillated cellulose from different raw materials and its reinforcement potential," *Carbohydrate Polymers*, vol. 79, no. 4, pp. 1086–1093, 2010.
- [14] C. Jiang, G. S. Oporto, T. Zhong, and J. Jaczynski, "TEMPO nanofibrillated cellulose as template for controlled release of antimicrobial copper from PVA films," *Cellulose*, vol. 23, no. 1, pp. 713–722, 2016.
- [15] T. Zhong, G. S. Oporto, J. Jaczynski, and C. Jiang, "Nanofibrillated cellulose and copper nanoparticles embedded in polyvinyl alcohol films for antimicrobial applications," *BioMed Research International*, vol. 2015, Article ID 456834, 2015.
- [16] J. Wu, M. Sperow, and J. Wang, "Economic feasibility of a woody biomass-based ethanol plant in central Appalachia," *Journal of Agricultural and Resource Economics*, vol. 35, no. 3, pp. 522–544, 2010.
- [17] P. M. Jacobson, *Properties of Polyvinyl Alcohol Nanocomposites Reinforced with Cellulose Nanocrystals of Red Oak Residues*, West Virginia University, 2011.
- [18] M. W. Davis, "A rapid modified method for compositional carbohydrate analysis of lignocellulosics by high pH anion-exchange chromatography with pulsed amperometric detection (HPAEC/PAD)," *Journal of Wood Chemistry and Technology*, vol. 18, no. 2, pp. 235–352, 1998.
- [19] L. Segal, J. Creely, A. Martin, and C. Conrad, "An empirical method for estimating the degree of crystallinity of native cellulose using the x-ray diffractometer," *Textile Research Journal*, vol. 29, no. 10, pp. 786–794, 1959.
- [20] T. Zhong, G. S. Oporto, Y. Peng, X. Xie, and D. J. Gardner, "Drying cellulose-based materials containing copper nanoparticles," *Cellulose*, vol. 22, no. 4, pp. 2665–2681, 2015.
- [21] T. Ferreira and W. Rasband, *ImageJ User Guide/IJ 1.46r*, Research Services Branch Web, <http://imagej.nih.gov/ij/docs/guide/user-guide.pdf>.
- [22] Y. Qing, R. Sabo, Y. Wu, J. Zhu, and Z. Cai, "Self-assembled optically transparent cellulose nanofibril films: effect of nanofibril morphology and drying procedure," *Cellulose*, vol. 22, no. 2, pp. 1091–1102, 2015.
- [23] Y. Qing, R. Sabo, J. Y. Zhu, U. Agarwal, Z. Cai, and Y. Wu, "A comparative study of cellulose nanofibrils disintegrated via multiple processing approaches," *Carbohydrate Polymers*, vol. 97, no. 1, pp. 226–234, 2013.
- [24] S. Iwamoto, K. Abe, and H. Yano, "The effect of hemicelluloses on wood pulp nanofibrillation and nanofiber network characteristics," *Biomacromolecules*, vol. 9, no. 3, pp. 1022–1026, 2008.
- [25] J. Li, O. Sevastyanova, and G. Gellerstedt, "The relationship between kappa number and oxidizable structures in bleached kraft pulps," *Journal of Pulp and Paper Science (JPPS)*, vol. 28, pp. 262–266, 2002.
- [26] W. Chen, H. Yu, and Y. Liu, "Preparation of millimeter-long cellulose I nanofibers with diameters of 30–80 nm from bamboo fibers," *Carbohydrate Polymers*, vol. 86, no. 2, pp. 453–461, 2011.
- [27] J. P. S. Morais, M. de Freitas Rosa, M. M. S. De Souza Filho, L. D. Nascimento, D. M. Do Nascimento, and A. R. Cassales, "Extraction and characterization of nanocellulose structures from raw cotton linter," *Carbohydrate Polymers*, vol. 91, no. 1, pp. 229–235, 2013.
- [28] P. K. Poddar, A. Gupta, S. S. Jamari, N. S. Kim, T. A. Khan, S. Sharma et al., "Synthesis of nanocellulose from rubberwood fibers via ultrasonication combined with enzymatic and chemical pretreatments," *Asian Journal of Applied Sciences*, vol. 3, 2015.
- [29] R. Wicaksono, K. Syamsu, I. Yuliasih, and M. Nasir, "Cellulose nanofibers from cassava bagasse: characterization and application on tapioca-film," *Chemistry and Materials Research*, vol. 3, no. 13, pp. 79–87, 2013.
- [30] W. Wulandari, A. Rochliadi, and I. Arcana, "Nanocellulose prepared by acid hydrolysis of isolated cellulose from sugarcane bagasse," in *IOP Conference Series: Materials Science and Engineering*, IOP Publishing, 2016.
- [31] A. Alemdar and M. Sain, "Isolation and characterization of nanofibers from agricultural residues—wheat straw and soy hulls," *Bioresource Technology*, vol. 99, no. 6, pp. 1664–1671, 2008.
- [32] X. F. Sun, F. Xu, R. C. Sun, P. Fowler, and M. S. Baird, "Characteristics of degraded cellulose obtained from steam-exploded wheat straw," *Carbohydrate Research*, vol. 340, no. 1, pp. 97–106, 2005.
- [33] M. Jonoobi, K. O. Niska, J. Harun, and M. Misra, "hemical composition, crystallinity, and thermal degradation of bleached and unbleached kenaf bast (*Hibiscus cannabinus*) pulp and nanofibers," *BioResources*, vol. 4, no. 2, pp. 626–639, 2009.
- [34] M. Sain and S. Panthapulakkal, "Bioprocess preparation of wheat straw fibers and their characterization," *Industrial Crops and Products*, vol. 23, no. 1, pp. 1–8, 2006.
- [35] M. Le Troedec, D. Sedan, C. Peyratout et al., "Influence of various chemical treatments on the composition and structure of hemp fibres," *Composites A: Applied Science and Manufacturing*, vol. 39, no. 3, pp. 514–522, 2008.
- [36] N. S. Lani, Ngadi N., A. Johari, and M. Jusoh, "Isolation, characterization, and application of nanocellulose from oil palm empty fruit bunch fiber as nanocomposites," *Journal of Nanomaterials*, vol. 2014, Article ID 702538, 9 pages, 2014.
- [37] D. Liu, Y. Liu, and G. Sui, "Synthesis and properties of sandwiched films of epoxy resin and graphene/cellulose nanowhiskers paper," *Composites Part A: Applied Science and Manufacturing*, vol. 84, pp. 87–95, 2016.
- [38] Y. Nishiyama, P. Langan, and H. Chanzy, "Crystal structure and hydrogen-bonding system in cellulose I β from synchrotron X-ray and neutron fiber diffraction," *Journal of the American Chemical Society*, vol. 124, no. 31, pp. 9074–9082, 2002.
- [39] Q. Q. Wang, J. Y. Zhu, R. Gleisner, T. A. Kuster, U. Baxa, and S. E. McNeil, "Morphological development of cellulose fibrils of a bleached eucalyptus pulp by mechanical fibrillation," *Cellulose*, vol. 19, no. 5, pp. 1631–1643, 2012.
- [40] S. Maiti, J. Jayaramudu, K. Das et al., "Preparation and characterization of nano-cellulose with new shape from different precursor," *Carbohydrate Polymers*, vol. 98, no. 1, pp. 562–567, 2013.
- [41] C. J. Chirayil, J. Joy, L. Mathew, M. Mozetic, J. Koetz, and S. Thomas, "Isolation and characterization of cellulose nanofibrils from *Helicteres isora* plant," *Industrial Crops and Products*, vol. 59, pp. 27–34, 2014.
- [42] M. M. Kabir, H. Wang, K. T. Lau, and F. Cardona, "Effects of chemical treatments on hemp fibre structure," *Applied Surface Science*, vol. 276, pp. 13–23, 2013.
- [43] B. Deepa, E. Abraham, N. Cordeiro et al., "Utilization of various lignocellulosic biomass for the production of nanocellulose: a comparative study," *Cellulose*, vol. 22, no. 2, pp. 1075–1090, 2015.

- [44] T. Saito, M. Hirota, N. Tamura et al., "Individualization of nano-sized plant cellulose fibrils by direct surface carboxylation using TEMPO catalyst under neutral conditions," *Biomacromolecules*, vol. 10, no. 7, pp. 1992–1996, 2009.
- [45] H. Fukuzumi, T. Saito, and A. Isogai, "Influence of TEMPO-oxidized cellulose nanofibril length on film properties," *Carbohydrate Polymers*, vol. 93, no. 1, pp. 172–177, 2013.
- [46] A. Retegi, N. Gabilondo, C. Peña, R. Zuluaga, C. Castro, P. Gañan et al., "Bacterial cellulose films with controlled microstructure-mechanical property relationships," *Cellulose*, vol. 17, no. 3, pp. 661–669, 2010.
- [47] M. Henriksson, L. A. Berglund, P. Isaksson, T. Lindström, and T. Nishino, "Cellulose nanopaper structures of high toughness," *Biomacromolecules*, vol. 9, no. 6, pp. 1579–1585, 2008.
- [48] T. Zhong, G. S. Oporto, J. Jaczynski, A. Tesfai, and J. Armstrong, "Antimicrobial properties of the hybrid copper nanoparticles-carboxymethyl cellulose," *Wood and Fiber Science*, vol. 45, no. 2, pp. 1–8, 2013.

Research Article

Modification of Functional Properties of Whey Protein Isolate Nanocomposite Films and Coatings with Nanoclays

Kerstin Müller,¹ Marius Jesdinszki,¹ and Markus Schmid^{1,2}

¹Materials Development, Fraunhofer Institute for Process Engineering and Packaging IVV, Freising, Germany

²Chair for Food Packaging Technology, Technische Universität München, Freising, Germany

Correspondence should be addressed to Markus Schmid; markus.schmid@ivv.fraunhofer.de

Received 25 February 2017; Accepted 4 May 2017; Published 31 May 2017

Academic Editor: Vijay K. Thakur

Copyright © 2017 Kerstin Müller et al. This is an open access article distributed under the Creative Commons Attribution License, which permits unrestricted use, distribution, and reproduction in any medium, provided the original work is properly cited.

Whey protein based films have received considerable attention to be used for environment friendly packaging applications. However, such biopolymers are prevented for use in commercial packaging due to their limited mechanical and barrier performance. The addition of nanofillers is a common method to overcome those drawbacks of biopolymers. Whey protein isolate (WPI) based nanocomposite cast films and coatings were produced using montmorillonite and vermiculite clay as nanofiller in different concentrations. Uniform distribution of filler within the polymeric matrix was confirmed by scanning electron microscopy. Mechanical properties such as tensile strength as well as Young's modulus were increased after increasing the filler content, while elongation at break values decreased. All samples showed weak barrier potential against water vapor. Nanoclay incorporation, however, reduced water vapor transmission rates by approximately 50%. The oxygen barrier performance was improved for all nanocomposites. Results also indicated proportionality with the filler ratio according to applied models. The highest barrier improvement factors (BIF) were greater than five for the cast films and even greater than sixteen for the coatings. Developed WPI-based composites depicted nanoenhanced material properties representing a promising alternative to fossil-based packaging films.

1. Introduction

The ability of globular proteins such as whey proteins to form self-supporting films showed great potential for edible coatings or numerous packaging applications and have been widely studied [1–6]. However, applications are limited since without any modification, whey protein films only display a low moisture barrier as well as relatively poor mechanical properties compared to commercial and mainly fossil-based packaging materials [7–10]. Recently, polymer nanocomposites have received considerable attention in research and development [11–13] and are already widely used in areas such as automotive or packaging [12, 14]. Just like conventional microcomposites such as glass fiber enforced polymers, material stiffness can be increased by filler addition [15]. However, the nanosize scale brings several advantages such as a reinforcement in all directions, a less filler content needed (wt%), and a better surface finish [13]. In terms of barrier performance, the introduction of nanoclays or particles significantly influences the permeation behavior of

gases by extending diffusion path and time [13]. This effect can be specifically ascribed to exfoliated clay morphologies [16] based on the good platelets distribution within the matrix. Compared to conventional microcomposites, meaning composites with filler particles of approximately 60% vol in a microscale range, nanocomposites already show enhanced properties at low filler loads (<2% vol) [16]. In terms of nanocoatings, even super gas barrier coatings that match performance of metallized films have been developed [17]. Thus, the usage of nanometre-sized filler particles is also becoming a promising option to overcome the limited mechanical and barrier properties of biopolymer based films and coatings [7, 18]. Likewise, whey protein based nanocomposites have been a field of interest in the last decade [7, 11, 19–26] confirming this topic is of scientific and industrial relevance. In case of whey protein based films, present oxygen barrier properties could even potentially be further improved with nanoparticles. The main goal of this study was the development of exfoliated clay–whey protein nanocomposites with enhanced barrier and mechanical properties to maximize

material suitability for packaging applications in industrial applications. The related scientific issue was the effect of the nanofillers on the processability and functional properties of nanomodified whey protein isolate based cast films and coatings with emphasis on packaging related properties.

2. Material and Methods

2.1. Materials. Whey protein isolate (WPI) was obtained from Davisco Foods International Inc, USA. Glycerol was purchased by Chemsolute, Th. Geyer GmbH & Co KG, Germany. Deionized water was supplied by Fraunhofer IVV. The aqueous montmorillonite nanodispersions were provided by ITENE, Spain using Cloisite Na⁺ and Nanofil 116 (both BYK Additives & Instruments, Wesel, Germany) with a clay concentration of 5% (w/w) for both dispersions. The Sunbar Vermiculite SX009 aqueous nanodispersion with a clay concentration of 7.6% (w/w) was obtained from SunChemical Ltd., UK. The chemically treated polyethylene terephthalate (PET) substrate Sarafil Polyplex Polyester Film with a thickness of 23 μm was supplied by Polyplex, Thailand.

2.2. Preparation of Film Forming Suspensions. Following the standard method by McHugh et al. [27] and Schmid et al. [4] a whey protein standard solution (WPSS) was produced. Therefore, 10% WPI (w/w) and deionized water are homogenized at room temperature in an electric stirrer (Thermomix 31-1, Vorwerk Deutschland Stiftung & Co. KG, Wuppertal, Germany) for 30 minutes at 200 rpm. Afterwards the solution is heated for 30 minutes at 90°C with continuous stirring (200 rpm). Thus, denaturation of the proteins was fully completed [28]. For cooling and degassing the solution is placed in an ultrasonic bath for 15 min (DT 514H, Ultrasonic peak output: 860 W, Bandelin electronic GmbH & Co. KG, Berlin, Germany) at 23°C and 37 kHz-s. After cooling down, glycerol (Glycerol, Merck KGaA, Darmstadt, Germany) is added to solution and stirred for further 30 minutes with the Thermomix at 200 rpm. Finally, the solution is placed in an ultrasonic bath again for degassing for further 15 minutes.

For the nanosuspensions, WPSS and the aqueous nanodispersions were mixed using a magnetic stirrer (Ikamag RCT, IKA-Labortechnik, Staufen, Germany) at 1200 rpm for at least one hour in different ratios to achieve the desired nanofiller ratios of 1%, 3%, 6%, and 9% (w/w) with reference to the protein content. To prevent agglomeration, it is highly important to gradually add the nanodispersion under continuous stirring. Additionally, the nanodispersions were redispersed for 30 minutes at 500 rpm electric stirrer (Thermomix 31-1, Vorwerk Deutschland Stiftung & Co. KG, Wuppertal, Germany) at room temperature and ultrasound treated with a sonotrode (Labsonic 1510, B. Braun, Melsungen, Germany) at 400 W for 45 minutes before mixing with WPSS.

2.3. Preparation of WPI/Clay Composite Cast Films and Coatings. All suspensions were coated on a chemically treated 23 μm PET film A4 sheets using the coating unit CUF 5 (Sumet Messtechnik, Denklingen, Germany) with 40 mm/s speed of application, a drying temperature of 105°C and a drying time of 5.5 minutes. For the target dry film thickness of

10 μm , a wired rod with 100 μm wet film thickness was used. Dried coatings were stored at ambient conditions of 23°C and 50% RH. Nanocomposite cast films were produced by solvent casting. Film forming suspensions were casted into square shaped Petri dishes with a target film thickness of 200 μm . Cast films were dried at ambient conditions of 23°C and 50% RH until they reach constant mass (approx. 8 days). All samples were stored at least 3 weeks prior to characterization in order to allow potential postcrosslinking to be completed [29].

2.4. Composite Film and Coating Characterization

2.4.1. Film Thickness. Thickness measurements were performed with a precision thickness gauge FT3 with 0.1 μm resolution (Rhopoint Instruments, Beyhill on Sea, United Kingdom) at five random positions around the film testing area and averaged for determination. For barrier and mechanical measurements, thicknesses were determined for each sample.

2.4.2. Mechanical Properties. Young's modulus (E), tensile strength (TS), and elongation at break (EB) of the cast films were tested using a tensile testing machine Z005 (Allround Line) of the Zwick GmbH & Co.KG, Ulm, Germany, at 23°C and 50% RH according to the DIN EN ISO 527-1. Tensile tests were performed with five strips of 15 mm width with a clamping length of 50 mm. The test speed was 50 mm/min with a load shut-off at 95% and a preload of 0.3 N.

2.4.3. Barrier Properties

Water Vapor Transmission Rate. The water vapor transmission rate was measured with a gravimetric method according to DIN 53122-1. The initial weight was measured by an analytical balance Mettler H315 of the Mettler-Toledo GmbH and the cups were then stored in a climate chamber of the Binder GmbH at 23°C and 85% RH. The samples were weighed four times in 48 hours until the weight gain stagnated. For each specimen, four replicates were tested. The water vapor transmission rate was calculated using the following formula [30]:

$$\text{WVTR} = \frac{24}{t} * \frac{\Delta m}{A} * 10^4 \left[\text{g m}^{-2} \text{d}^{-1} \right], \quad (1)$$

where t is time between two weight measurements of which Δm is calculated [h], Δm is weight difference of two successive weight measurements [g], and A is sample area [cm^2].

Oxygen Permeability. The oxygen permeability (OP) was measured with the oxygen-specific carrier gas method according to DIN 53380-3. The measurements were performed with a Mocon Ox-Tran Twin Oxygen Permeation Measuring Machine at a temperature of 23°C and 50% RH. The measurement stopped when a value was constant for at least ten hours. Two replicates of all coating and cast film specimens were determined.

For a better comparison of different polymers the permeability Q can be standardized to the Q_{100} -value relating to a

thickness of 100 μm [31]:

$$Q_{100} = Q * \frac{d}{100}. \quad (2)$$

To adapt permeability properties of a packaging material, multilayers can be used instead of raising the thickness of a monolayer. The total permeation of a multilayer system Q_{total} can be calculated as follows:

$$\frac{1}{Q_{\text{total}}} = \sum_{i=1}^{i=n} \frac{d_i}{P_i}. \quad (3)$$

2.4.4. Scanning Electron Microscopy (SEM). The scanning electron microscopy was performed with an ISI scanning electron microscope ABT 55 (ISI Akashi Beam Technology Corporation, Tokyo, Japan). Images were taken at 10 kV at different magnification and evaluated with a digital image scanning system DISS 5 by Point electronic GmbH, Halle (Saale), Germany. The measurements were performed in a high vacuum environment of 2×10^{-3} bar at room temperature. For sample preparation, cryofractures of selected samples were performed. The cross sections of the samples were fixed to the specimen holder with carbon tape and sputtered with a metal coating for improved conductivity.

2.5. Statistical Analysis. Statistical evaluations were performed using the computer programme Visual-XSel 12.0 Multivar (CRGRAPH, Munich, Germany). All measured data were tested on normal distribution. Depending on sample size, Kolmogorov-Smirnov test (sample size 3 or 4) or Anderson-Darling normality test (sample size ≥ 5) was used with a significance value α at 0.05. The Hampel test for outliers was used to detect and eliminate outliers of nonnormal distributed data with a significance value α at 0.05. Condition for elimination is that all other values are part of the same population, proved by normality tests. Comparison of sample sets was conducted with a multi- t -test using a significance value of 0.05.

2.6. Descriptive Statistics

2.6.1. Curve Fitting of the Modulus. According to literature, the models widely applied to describe the Young's moduli of composites filled with various types of filler are the Halpin-Tsai model and modified equations from it [12, 32]. According to this model, longitudinal elastic modulus can be expressed as follows:

$$\frac{E_c}{E_m} = \frac{1 + \xi\delta\phi}{1 - \delta\phi} [-], \quad (4)$$

where E_c is Young's modulus of the composite [MPa], E_m is Young's modulus of the matrix [MPa], and ϕ_f is volume fraction of the filler [-] with the constants ξ and δ given by

$$\delta = \frac{(E_f/E_m) - 1}{(E_f/E_m) + \xi} [-], \quad (5)$$

where E_f is Young's modulus of the filler [MPa] and E_m is Young's modulus of the matrix [MPa]

$$\xi = 2 \left(\frac{l}{d} \right) = 2\alpha [-], \quad (6)$$

where l/d is the aspect ratio α of the reinforcing filler [12].

Since this model overestimated the experimental data, a Modulus Correction Factor (MCF) was introduced, adapting an approach by Wu and others [33]. Equation (7) describes the modified model used for calculations.

$$\frac{E_c}{E_m} = \frac{1 + (\text{MCF}) \xi\delta\phi}{1 - \delta\phi}. \quad (7)$$

The parameter MCF was determined for each type of used clay by minimizing the residual sum of squares RSS with Excel Solver (Microsoft Office Professional Plus, Version 14.0.7166.5000).

2.6.2. Predicting Barrier Properties. Table 1 shows different models that have been suggested to predict barrier properties of nanocomposites. The used models differ according to the particle geometry and calculations are based on aspect ratio α and the filler degree ϕ . Since only single particles are considered, those models assume fully exfoliated clays.

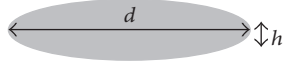
Considering the relatively simple model by Nielsen and making realistic assumptions with an aspect ratio of $\alpha = 500$ and a volume fraction of $\phi = 0.07$ for nanocomposites, a barrier improvement of a factor of 20 is generally possible and was also already achieved in lab-scale experiments [39].

However, interactions between filler and matrix, state of exfoliation, and particle orientation also have to be taken into account. Therefore further important factors for the diffusion path extension are the state of dispersion, eventual aggregation or flocculation, and the orientation within the matrix [40]. The highest possible aspect ratio can be achieved by individual nanolayers requiring complete exfoliation [12]. Although best enhancement of barrier properties can be achieved with aligned platelets, the processing of exfoliated nanoclays mainly shows misaligned structures as well as nonexfoliated areas within the composites [12]. For those reasons, practical permeability data given by suppliers provide much lower barrier improvements compared to the theoretical values, normally with a factor of two [41].

3. Results and Discussion

3.1. Microstructure. The cross-sectional SEM images of selected WPI nanocomposite cast films and coatings can be seen in Figure 1. Nanoparticles are given in lighter color, while dark spots display small holes which are the traces of nanoparticles that remained on the opposite side of the cast films during hand fractioning. All composites show a homogeneous distribution of the nanofiller with maintaining WPI matrix structure. Even at the high nanoparticles concentrations only little agglomeration could be detected. The uniform distribution and dispersion of Cloisite Na⁺ in the WPI matrix contributed to the mechanical and barrier

TABLE 1: Models for predicting barrier properties of platelet filled nanocomposites [13].

Model	Filler type	Particle geometry	Formulas	Reference
Nielsen	Ribbon ^a		$(P_0/P)(1 - \phi) = 1 + \alpha\phi/2$	[34]
Cussler (Random array)	Ribbon ^a		$(P_0/P)(1 - \phi) = (1 + \alpha\phi/3)^2$	[35]
Gusev and Lusti	Disk ^b		$(P_0/P)(1 - \phi) = \exp[(\alpha\phi/3.47)^{0.71}]$	[36]
Fredrickson and Bicerano	Disk ^b		$(P_0/P)(1 - \phi) = 4((1 + x + 0.1245x^2)/(2 + x))^2$ where $x = \alpha\phi/2 \ln(\alpha/2)$	[37]
Bharadwaj	Disk ^b		$(P_0/P)(1 - \phi) = 1 + 0.667\alpha\phi(S + 1/2)$ where $S =$ orientation factor (from $-1/2$ to 1)	[38]

^aFor ribbons, length is infinite, width, w ; thickness, h ; aspect ratio, $\alpha = w/h$; ^bfor disks, circular shape of diameter d and thickness h ; aspect ratio, $\alpha = d/h$.

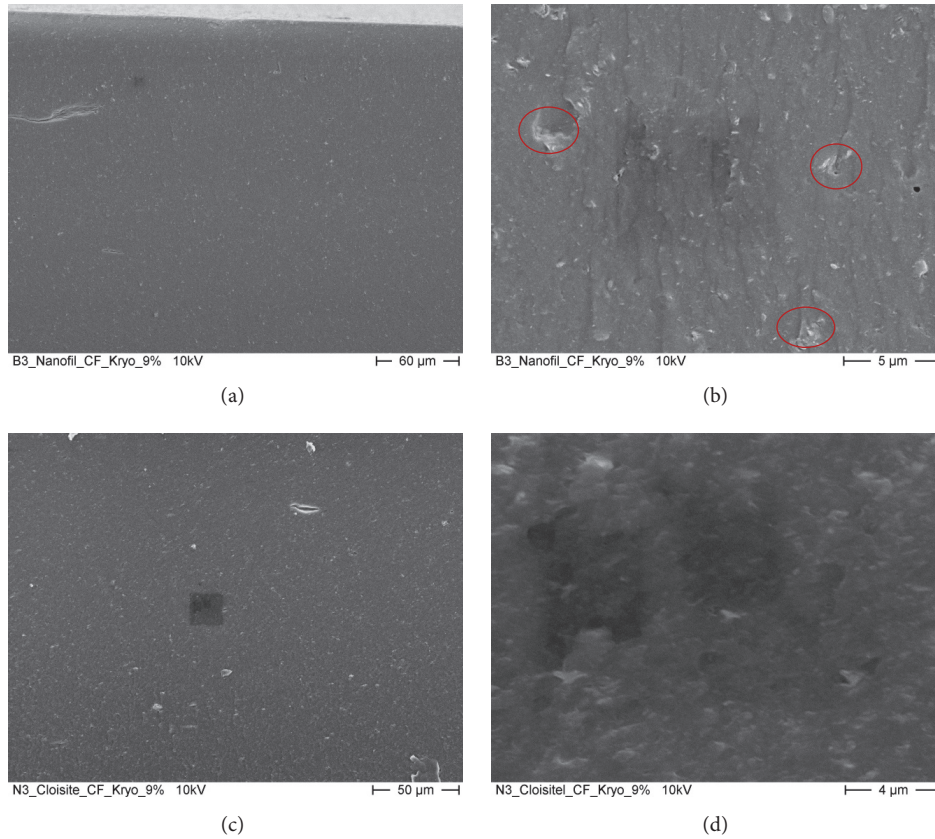


FIGURE 1: SEM images of selected nanomodified WPI-based cast films and coatings. Cryofractionated cross sections of 9% Nanofil cast films (a, b), 9% Cloisite Na⁺ cast films (c, d) at different magnifications (scaling bottom right).

improvement of the nanocomposites. The poor improvements detected at the Nanofil composites could be due to the occurrence of comparably bigger agglomerates marked exemplarily in Figure 1(b). Depending on the sample spot chosen for determination, distribution can of course differ.

3.2. Mechanical Properties. Measured data for mechanical properties of all casted nanocomposites can be seen in Table 2. All nanofillers used showed significant enhancement of Young's modulus and tensile strength at high nanoparticles concentrations. The increase of material stiffness and strength

TABLE 2: Mechanical data of WPI-based nanocomposites with different nanofillers. Columns with different letters are significantly different ($p \leq 0.05$) for each dataset compared to the zero sample.

Filler type	Filler ratio [wt%]	E [MPa]	TS [MPa]	EB [%]
—	0	58.54 ± 3.45^a	3.69 ± 0.24^a	135.48 ± 19.74^{ab}
Cloisite Na ⁺	1	71.70 ± 3.85^b	4.18 ± 0.23^b	129.08 ± 17.48^{ac}
	3	97.50 ± 4.44^c	4.39 ± 0.14^b	111.28 ± 1.54^{cd}
	6	142.80 ± 3.11^d	4.87 ± 0.09^c	90.70 ± 26.69^{de}
	9	208.40 ± 18.64^e	5.67 ± 0.16^d	64.26 ± 14.39^e
	1	57.12 ± 12.27^a	4.07 ± 0.13^b	136.78 ± 13.07^a
Nanofil 116	3	78.36 ± 4.28^b	4.37 ± 0.17^c	141.04 ± 15.13^a
	6	80.32 ± 16.48^b	4.90 ± 0.15^d	144.30 ± 5.07^a
	9	123.00 ± 6.52^c	5.28 ± 0.26^e	116.90 ± 12.96^b
	1	77.78 ± 15.27^b	3.95 ± 0.40^a	125.54 ± 20.13^a
Sunbar	3	121.46 ± 21.90^c	4.10 ± 0.19^b	69.50 ± 10.79^c
	6	218.25 ± 5.12^d	4.76 ± 0.58^b	29.72 ± 3.15^d
	9	283.40 ± 35.98^e	6.19 ± 0.10^c	21.96 ± 1.53^e

by the incorporation of nanofillers into whey protein based matrices was also confirmed by several studies [7, 21, 24–26]. Similar to the modulus, the material reinforcement and therewith higher strength levels depend on composite morphology, since better exfoliation leads to higher improvements. However, tensile strength as well as elongation at break are nonlinear mechanical properties and decrease beyond a critical filler ratio [12]. Here, the transfer of load between filler and matrix is decisive and depends on their compatibility. Results indicate efficient interfacial interaction between matrix and filler at all nanoclays used. In terms of tensile strength, measured improvements are comparable to other studies using nanoclay in whey protein based matrices [21, 24–26]. Furthermore, the continuous increase in tensile strength values is another evidence for a good distribution of the nanofiller at all concentrations as well as good interface adhesion.

Since the addition of filler into a polymeric matrix decreases material ductility, elongation levels of nanocomposites are typically lower than those of the polymer itself [13]. As discussed before, the incorporation of nanofiller contributes to a reinforcement of the cast films and reduces their flexibility at the same time [42], which explains a general decrease of elongation at break with increasing nanofiller ratio at the measured samples. Except for the highest concentration, elongations at break of the Nanofil composites were not statistically different to pure WPSS cast films ($p > 0.05$) and also did not contribute to mechanical strength as good as the other fillers used. The diverse results of the different clays used can be attributed to different matrix-filler interactions, inhomogeneous spots at the measured samples, or the differences in sample thicknesses. Comparable studies using nanofillers in protein based matrices also showed diverse results. Wakai and others also incorporated 5% ((w/w), relative to the protein content) MMT clay into WPI matrix leading to a comparable decrease in elongation at break by 34% [43], while Sothornvit and others reported no significant differences at 5% Nanofiller (Cloisite Na⁺)

in MMT/WPI cast films [20] which was explained by the assumption of incomplete nanoclay dispersion.

As expected by composite theory, the modulus was increased when a filler was incorporated into the polymeric matrix. Young's modulus is a linear mechanical property which is measured at low strains and reflects material stiffness [44]. In the case of polymer nanocomposites, stiffness generally increases with the volume fraction of the nanofiller, as long as sufficient dispersion and exfoliation are ensured [12].

To be able to predict the Young's modulus of such nanocomposites, the data was also fitted to the described modified Halpin-Tsai model. Therefore, the Young's modulus of the Cloisite Na⁺ and Nanofil 116 fillers was assumed to be at 178 GPa, following an estimation by Fornes and Paul for MMT clay [45]. There was no explicit modulus data found for vermiculite clays. Since the range for Young's moduli of layered silica lies between 178 and 265 GPa [45–47], a realistic assumption of 200 GPa was made for the Sunbar vermiculite filler. The modification of the Halpin-Tsai model was needed due to overestimation of the experimental data. This is because the Halpin-Tsai model is based on assumptions that are only partly fulfilled by the examined nanocomposites. The model presumes linear elastic and isotropic matrix and filler as well as completely oriented particles of similar size and shape. Additionally, the properties of matrix and filler do not change in the presence of each other [48]. Also, occurring agglomeration and the state of exfoliation are not considered. The MCF takes deviations into account and gives a better model fit. Table 3 shows the used and calculated constants and parameters for the curve fitting.

The determined Young's modulus values ranged from approximately 60 to 180 MPa. Therefore, the RSS values also lie in a three-digit range. As described before, Sunbar and Cloisite Na⁺ samples showed proportionality between filler ratio and Young's modulus according to the Halpin-Tsai model. RSS as well as R^2 indicates a good model fit; therefore it is possible to describe this proportionality with the adapted Halpin-Tsai model. The correction factors of

TABLE 3: Modified Halpin-Tsai Parameters for different fillers used in whey protein nanocomposites.

Filler type	ξ	δ	MCF	RSS [MPa ²]	R^2
Cloisite Na ⁺	140	0.9557	0.2461	103.727	0.9432
Nanofil 116	140	0.9557	0.0893	315.128	0.5275
Sunbar	200	0.9444	0.2334	271.132	0.7058

Cloisite Na⁺ and Sunbar filler lie in the same range. As can be seen in Figure 2, for the Nanofil filler, the initial Halpin-Tsai theory highly overestimated Young's modulus leading to a lower MCF. This is also in line with the varying results at other tested mechanical properties indicating a heterogeneous filler distribution and occurring agglomeration. Furthermore, inherent moisture of the Nanofil clay is lower compared to the Cloisite clay, resulting in an actual lower net volume of the silicate filler. Therefore also lower R^2 and higher RSS values were determined.

3.3. Barrier Properties Oxygen Permeability

3.3.1. Coatings. To evaluate oxygen barrier properties of the coatings, permeabilities for the coated monolayer without the PET substrate were calculated by converting (3) with the values measured for the bilayer-system and the pure substrate. Coating thicknesses varied from approximately 7 to 9 μm ; therefore resulting values were additionally normalized to 100 μm thickness following formula (2). Cloisite Na⁺ as well as the Sunbar filler both showed decreases at each concentration step, indicating proportionality between filler ratio and permeability (see Figure 3). The lowest permeability of 2.097 [(cm³ 100 μm)/(m² d bar)] was determined for a monolayer with 9% ((w/w), relative to protein) Sunbar filler. The corresponding BIF, defined as the ratio of the permeability through the pure whey protein film and the permeability through the respective composite, was higher than 16. Weizman et al. [49] also used MMT clay for whey protein isolate based coatings with comparable OP for the zero sample. However, compared to Cloisite Na⁺, barrier improvements at measured 1% and 5% clay were lower (appr. 30 and 25 (cm³ 100 μm)/(m² d bar), resp.) compared to this study.

3.3.2. Cast Films. To get comparable results and since cast film thicknesses of the samples varied, measured values were normalized to 100 μm thickness (2).

All samples showed improved barrier performance with the addition of nanofiller, which can be seen in Figure 4. The WPSS sample gave an OP of approx. 80 cm³/(m² d bar) for 100 μm film thickness. By adding Cloisite Na⁺, oxygen permeabilities were reduced up to a factor two at the highest filler ratio of 9% (w/w). The Sunbar Vermiculite filler gave even better results with barrier improvements of 20, 50, 75, and even 80% for the respective ratios compared to the zero sample. Measured values for the Nanofil sample set varied widely and showed no expected decrease of OP with increasing filler ratio. Explanation could be given by filler agglomeration at the measured sample spots generating no

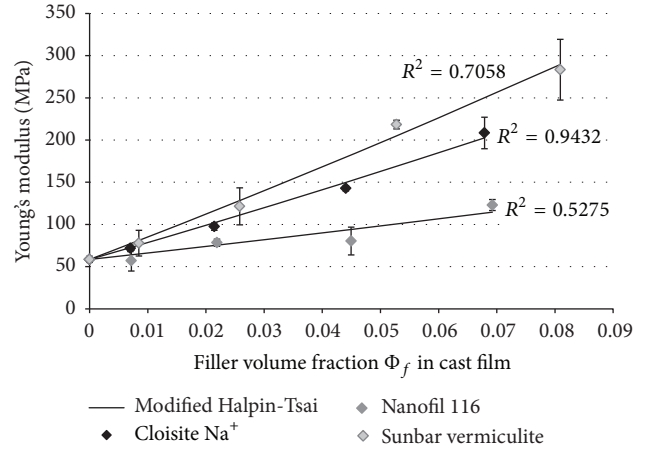


FIGURE 2: Experimental and theoretical Young's modulus of whey protein nanocomposite cast films reinforced with different fillers plotted as a function of their volume fraction with theoretical data given by a modified Halpin-Tsai model.

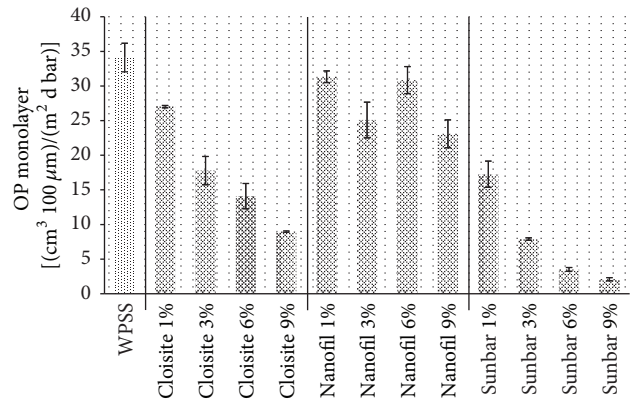


FIGURE 3: Influence of filler ratio on OP of whey protein nanocomposite coated monolayer with different nanofillers. Values were normalized to 100 μm thickness. Error bars show minimum and maximum value (twofold determination).

tortuous pathway for the permeating oxygen molecules. Furthermore, Nanofil 116 clays depict higher inherent moisture (8–13%) compared to the similar MMT clay Cloisite Na⁺ (4–9%). Therefore, the net volume of silicate layers in the composite is lower which could explain lower effects that also were observed at mechanical measurements. In terms of barrier properties and especially oxygen permeability, inherent moisture of the Nanofil clay could have had a negative effect on the barrier performance, since oxygen permeability of whey protein based films is a moisture-related property with decreasing barrier performance at increasing moisture [50]. Similar observations were also made for water vapor measurements, confirming this declaration.

Since both the Cloisite Na⁺ and the Sunbar Vermiculite sample sets showed expected decreases with increasing filler content, measured data was compared to the usual applied models for predicting the barrier performance of polymer

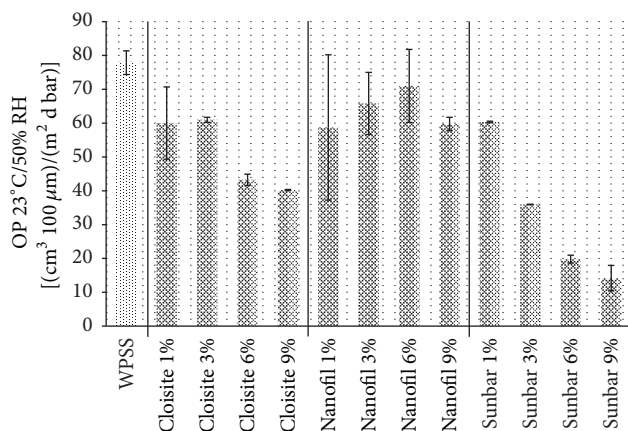


FIGURE 4: Influence of filler ratio on OP of whey protein nanocomposite cast films with different nanofillers. Error bars show minimum and maximum value (twofold determination).

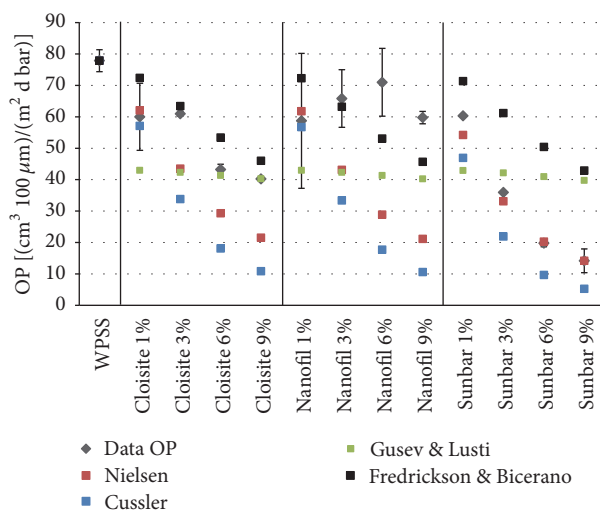


FIGURE 5: Comparison of OP original data with results from various models for predicting barrier properties of platelet filled nanocomposites.

nanocomposites. The following figure shows the measured data and the corresponding theoretical values for four different models. The aspect ratio for Cloisite Na⁺ of 70 was already applied in a former study [43], for both other fillers realistic values were assumed with 70 for Nanofil 116 (also MMT clay) and 100 for Sunbar Vermiculite based on found results, since there was no information available.

For the Cloisite Na⁺ filler, the model by Fredrickson and Bicerano seemed most appropriate to predict barrier properties based on visual assessment (see Figure 5). Unlike Nielsen or Cussler, Fredrickson and Bicerano assumed disk-shaped platelets that are aligned, but positionally disordered [37], which is presumed to be present in here produced nanocomposites. Sunbar Vermiculite showed higher decreases and lowest deviations to the simple model by Nielsen. Due to a higher basal spacing and inherent water

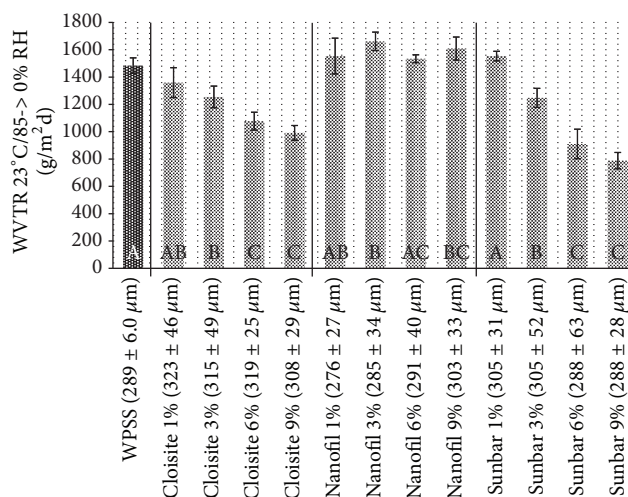


FIGURE 6: Influence of filler ratio on water vapor transmission rates of nano whey protein composite cast films with different nanofillers. Average thicknesses of each sample set after measurement are given in parentheses after the sample labeling. Columns with different letters are significantly different ($p \leq 0.05$) for each dataset compared to the zero sample (WPSS).

compared to MMT, exfoliation processes are favoured in vermiculite clay. Additionally, due to different densities, the net volume ratio of platelets is higher with vermiculite clay. In terms of oxygen permeability, especially a higher state of exfoliation could have caused higher decreases and an approximation to the simple expression by Nielsen. All other models showed higher variations and mainly overestimated the measured data and are therefore not applicable for the used matrix-filler combination. However, for a suitable prediction of oxygen barrier properties for such WPI-based nanocomposites, the type of clay as well as the state of exfoliation and dispersion should be considered. Therefore, further parameters should be included to modify existing models if a barrier performance prediction is desired.

3.4. Water Vapor Permeability. Figure 6 shows water vapor transmission rates of all denatured specimen (cast films). All samples only showed weak barrier potential against water vapor. However, using Cloisite Na⁺ and Sunbar Vermiculite as filler, WVTR could be significantly reduced ($p \leq 0.05$) by approximately 30 and 50% at the highest filler ratio.

The slight increase in WVTR when adding nanofillers (Nanofil and Sunbar) to the cast films could be explained by a decreased post-cross-linking of the WPI matrix due to the presence of the nanoplatelets/clays. At higher concentrations, the influence of an extended tortuous pathway for water vapor molecules takes more account and WVTR is decreased with increasing filler ratio at both the Cloisite and Sunbar filler. Nanofil specimen did not contribute to water vapor barrier capacities of WPI cast films. Possible reasons could be agglomeration of the nanofiller, so that no tortuous pathway was generated. Additionally, sample swelling could have caused free volume and easy water vapor solubility within the

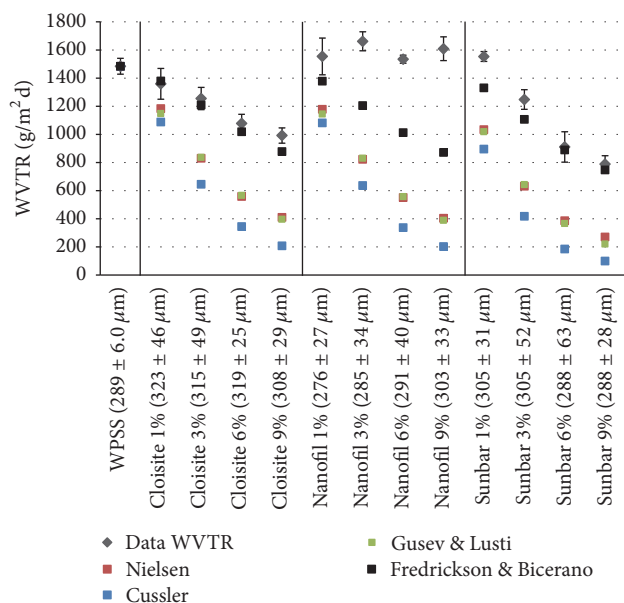


FIGURE 7: Comparison of WVTR original data with results from various models for predicting barrier properties of platelet filled nanocomposites. Average thicknesses of each sample set after measurement are given in parentheses after the sample labeling.

matrix so that even higher transmission rates were detected. Permeation tests performed at large relative humidity steps unluckily lead to swelling of WPI films. Theoretical constant diffusivity and constant thickness cannot not be assumed anymore, resulting in inaccurate measurement values [22]. Compared to a study by Sothornvit et al. [20] also using Cloisite Na⁺ clay (5% w/w relative to protein) in whey protein isolate/clay nanocomposites, measured WVTR values were much higher. However, the improvement by clay incorporation is of the same order of magnitude. Similar to the OP data, WVTR values were compared to common models for barrier predictions (see Figure 7).

Cloisite Na⁺ and Sunbar Vermiculite filler showed good model adjustment for barrier prediction. At WVTR measurements, the Fredrickson and Bicerano gave the best model fit by visual assessment for both sample sets. All other models displayed high differences between measured data and theoretic calculated values.

Compared to the oxygen permeation values, much lower barrier improvements were achieved with the same nanocomposite system. On the one hand, these results can clearly be attributed to the sample swelling which appeared at water vapor transmission measurements. On the other hand, however, other studies using nanoclay fillers in nonswelling PET matrix also revealed oxygen barrier improvements but no significant improvements concerning the water vapor transmission [51]. This different behavior of oxygen and water vapor transmission within the same system can be ascribed to occurring interactions between the permeating molecules with each other, the polymer matrix or the filler. Water vapor molecules generally have a greater tendency to those interactions by forming hydrogen bonds, making

barrier improvements rather a function of hydrophobicity of the filler surface [12]. Since the used nanofillers rather display hydrophilic properties, stronger interactions between water vapor molecules and the filler platelets can occur resulting in lower barrier performances compared to oxygen. Existing models do not take interaction between filler and matrix into account. Thus, at least for water vapor permeability in protein based nanocomposites, interaction parameters should be established and used to adapt models for barrier predictions.

4. Conclusions

The homogeneous distribution proved by microscopy techniques indicated good compatibility and strong interactions between filler and matrix and confirmed a suitable method for the described processing of WPI-based nanocomposites. This was also reflected by the results of the mechanical and barrier properties characterizations. The incorporation of nanofillers gave improved stiffness and strength to the composite materials. Since no decline was visible at elongation and tensile strength measurements, the limit for nonlinear mechanical properties, meaning a critical filler ratio, is not reached yet; therefore further material reinforcement can be expected with higher filler ratios. Just like other protein based films, samples only showed weak barrier potential against water vapor. However, a significant WVTR reduction of approximately 50% was achieved using 9% (w/w) Sunbar Vermiculite as filler in cast films. For all prepared nanocomposites, oxygen barrier improvements were achieved. The highest BIF above 16 was achieved for the 9% (w/w) Sunbar Vermiculite nanocomposite coating with a permeability comparable to conventionally used oxygen barrier materials. Therefore, the development of WPI-based nanocomposites could expand the potential of whey proteins coating to be used in sustainable and biodegradable packaging solutions. Due to shown mechanical and barrier improvements, such nanocomposites could present an alternative to fossil-based packaging materials.

Conflicts of Interest

The authors declare that there are no conflicts of interest regarding the publication of this paper.

Acknowledgments

Part of the research presented in this study received funding from the European Union's Horizon 2020 research and innovation programme under Grant Agreement no. 686116. For more information, refer to <http://www.optinanopro.eu/>. The works on the Sunbar-formulations have been funded by internal means of Fraunhofer IVV. The authors wish to acknowledge their respective colleague M. Pummer for his assistance with material processing and process optimization. Thanks are also extended to Z. Scheuerer and all colleagues responsible for the material characterization. Furthermore the authors want to thank Mr. Safraz Khan for the outstanding support with the Sunbar-formulation and the material supply as well as ITENE for providing the Cloisite and

Nanofil dispersions. The authors thank E. Bugnicourt for the revision of the manuscript. This work was supported by the German Research Foundation (DFG) and the Technische Universität München within the funding programme Open Access Publishing.

References

- [1] T. Lefèvre, M. Subirade, and M. Pézolet, "Molecular description of the formation and structure of plasticized globular protein films," *Biomacromolecules*, vol. 6, no. 6, pp. 3209–3219, 2005.
- [2] D. Plackett, "Biopolymers - New Materials for Sustainable Films and Coatings," *Biopolymers - New Materials for Sustainable Films and Coatings*, 2011.
- [3] P. S. P. De Herrmann, C. M. Pedrosa Yoshida, A. J. Antunes, and J. A. Marcondes, "Surface evaluation of whey protein films by atomic force microscopy and water vapour permeability analysis," *Packaging Technology and Science*, vol. 17, no. 5, pp. 267–273, 2004.
- [4] M. Schmid, K. Dallmann, and E. Bugnicourt, "Properties of whey-protein-coated films and laminates as novel recyclable food packaging materials with excellent barrier properties," *International Journal of Polymer Science*, vol. 2012, Article ID 562381, 7 pages, 2012.
- [5] F. Hammann and M. Schmid, "Determination and quantification of molecular interactions in protein films: a review," *Materials*, vol. 7, no. 12, pp. 7975–7996, 2014.
- [6] J. Zink, T. Wyrobnik, T. Prinz, and M. Schmid, "Physical, chemical and biochemical modifications of protein-based films and coatings: an extensive review," *International Journal of Molecular Sciences*, vol. 17, no. 9, p. 1376, 2016.
- [7] J. J. Zhou, S. Y. Wang, and S. Gunasekaran, "Preparation and characterization of whey protein film incorporated with TiO₂ nanoparticles," *Journal of Food Science*, vol. 74, no. 7, pp. N50–N56, 2009.
- [8] M. B. Pérez-Gago, P. Nadaud, and J. M. Krochta, "Water vapor permeability, solubility, and tensile properties of heat-denatured versus native whey protein films," *Journal of Food Science*, vol. 64, no. 6, pp. 1034–1037, 1999.
- [9] L. Cisneros-Zevallos and J. M. Krochta, "Whey protein coatings for fresh fruits and relative humidity effects," *Journal of Food Science*, vol. 68, no. 1, pp. 176–181, 2003.
- [10] B. Ouattara, L. T. Canh, C. Vachon, M. A. Mateescu, and M. Lacroix, "Use of γ -irradiation cross-linking to improve the water vapor permeability and the chemical stability of milk protein films," *Radiation Physics and Chemistry*, vol. 63, no. 3–6, pp. 821–825, 2002.
- [11] M. S. Hedenqvist, A. Backman, M. Gällstedt, R. H. Boyd, and U. W. Gedde, "Morphology and diffusion properties of whey/montmorillonite nanocomposites," *Composites Science and Technology*, vol. 66, no. 13, pp. 2350–2359, 2006.
- [12] V. Mittal, *Optimization of polymer nanocomposite properties*, John Wiley and Sons, 2009.
- [13] D. R. Paul and L. M. Robeson, "Polymer nanotechnology: nanocomposites," *Polymer*, vol. 49, no. 15, pp. 3187–3204, 2008.
- [14] K. Müller, E. Bugnicourt, M. Latorre et al. et al., "Review on the processing and properties of polymer nanocomposites and nanocoatings and their applications in the packaging, automotive and solar energy fields," *Nanomaterials*, vol. 7, p. 74, 2017.
- [15] T. G. Gopakumar, J. A. Lee, M. Kontopoulou, and J. S. Parent, "Influence of clay exfoliation on the physical properties of montmorillonite/polyethylene composites," *Polymer*, vol. 43, no. 20, pp. 5483–5491, 2002.
- [16] A. Arora and G. W. Padua, "Review: nanocomposites in food packaging," *Journal of Food Science*, vol. 75, no. 1, pp. R43–R49, 2010.
- [17] K. M. Holder, B. R. Spears, M. E. Huff, M. A. Priolo, E. Harth, and J. C. Grunlan, "Stretchable gas barrier achieved with partially hydrogen-bonded multilayer nanocoating," *Macromolecular Rapid Communications*, vol. 35, no. 10, pp. 960–964, 2014.
- [18] M. Avella, J. J. De Vlieger, M. E. Errico, S. Fischer, P. Vacca, and M. G. Volpe, "Biodegradable starch/clay nanocomposite films for food packaging applications," *Food Chemistry*, vol. 93, no. 3, pp. 467–474, 2005.
- [19] R. Sothornvit, S.-I. Hong, D. J. An, and J.-W. Rhim, "Effect of clay content on the physical and antimicrobial properties of whey protein isolate/organo-clay composite films," *LWT - Food Science and Technology*, vol. 43, no. 2, pp. 279–284, 2010.
- [20] R. Sothornvit, J.-W. Rhim, and S.-I. Hong, "Effect of nano-clay type on the physical and antimicrobial properties of whey protein isolate/clay composite films," *Journal of Food Engineering*, vol. 91, no. 3, pp. 468–473, 2009.
- [21] M. Hassannia-Kolae, F. Khodaiyan, R. Pourahmad, and I. Shahabi-Ghahfarrokhi, "Development of ecofriendly bio-nanocomposite: Whey protein isolate/pullulan films with nano-SiO₂," *International Journal of Biological Macromolecules*, vol. 86, pp. 139–144, 2016.
- [22] P. Oymaci and S. A. Altinkaya, "Improvement of barrier and mechanical properties of whey protein isolate based food packaging films by incorporation of zein nanoparticles as a novel bionanocomposite," *Food Hydrocolloids*, vol. 54, pp. 1–9, 2016.
- [23] Y. Li, Y. Jiang, F. Liu, F. Ren, G. Zhao, and X. Leng, "Fabrication and characterization of TiO₂/whey protein isolate nanocomposite film," *Food Hydrocolloids*, vol. 25, no. 5, pp. 1098–1104, 2011.
- [24] V. M. Azevedo, M. V. Dias, S. V. Borges et al., "Development of whey protein isolate bio-nanocomposites: Effect of montmorillonite and citric acid on structural, thermal, morphological and mechanical properties," *Food Hydrocolloids*, vol. 48, pp. 179–188, 2015.
- [25] M. Hassannia-Kolae, F. Khodaiyan, and I. Shahabi-Ghahfarrokhi, "Modification of functional properties of pullulan-whey protein bionanocomposite films with nanoclay," *Journal of Food Science and Technology*, vol. 53, no. 2, pp. 1294–1302, 2016.
- [26] M. Zolfi, F. Khodaiyan, M. Mousavi, and M. Hashemi, "The improvement of characteristics of biodegradable films made from kefiran-whey protein by nanoparticle incorporation," *Carbohydrate Polymers*, vol. 109, pp. 118–125, 2014.
- [27] T. H. McHugh, J. F. Aujard, and J. M. Krochta, "Plasticized whey-protein edible films: water-vapor permeability properties," *Journal of Food Science*, vol. 59, no. 2, pp. 416–419, 1994.
- [28] M. Schmid, B. Krimmel, U. Grupa, and K. Noller, "Effects of thermally induced denaturation on technological-functional properties of whey protein isolate based films," *Journal of Dairy Science*, vol. 97, no. 9, pp. 5315–5327, 2014.
- [29] M. Schmid, K. Reichert, F. Hammann, and A. Stäbler, "Storage time-dependent alteration of molecular interaction-property

- relationships of whey protein isolate-based films and coatings,” *Journal of Materials Science*, vol. 50, no. 12, pp. 4396–4404, 2015.
- [30] DIN, “Bestimmung der wasserdampfdurchlässigkeit. Teil 1: Gravimetrisches verfahren,” in *DIN 53122-1, e.V., D.I.f.N., Ed. Deutsches Institut für Normung*, 2001.
- [31] G. Menges, *Werkstoffkunde kunststoffe*, Hanser Fachbuchverlag, 2002.
- [32] E. Esmizadeh, G. Naderi, and M. H. R. Ghoreishy, “Modification of Theoretical models to predict mechanical behavior of PVC/NBR/organoclay nanocomposites,” *Journal of Applied Polymer Science*, vol. 130, no. 5, pp. 3229–3239, 2013.
- [33] Y.-P. Wu, Q.-X. Jia, D.-S. Yu, and L.-Q. Zhang, “Modeling Young’s modulus of rubber-clay nanocomposites using composite theories,” *Polymer Testing*, vol. 23, no. 8, pp. 903–909, 2004.
- [34] L. E. Nielsen, “Models for the Permeability of Filled Polymer Systems,” *Journal of Macromolecular Science: Part A - Chemistry*, vol. 1, no. 5, pp. 929–942, 1967.
- [35] N. K. Lape, E. E. Nuxoll, and E. L. Cussler, “Polydisperse flakes in barrier films,” *Journal of Membrane Science*, vol. 236, no. 1-2, pp. 29–37, 2004.
- [36] A. A. Gusev and H. R. Lusti, “Rational design of nanocomposites for barrier applications,” *Advanced Materials*, vol. 13, no. 21, pp. 1641–1643, 2001.
- [37] G. H. Fredrickson and J. Bicerano, “Barrier properties of oriented disk composites,” *The Journal of chemical physics*, vol. 110, pp. 2181–2188, 1999.
- [38] R. K. Bharadwaj, “Modeling the barrier properties of polymer-layered silicate nanocomposites,” *Macromolecules*, vol. 34, no. 26, pp. 9189–9192, 2001.
- [39] K. Müller, “Multilayer films for bag-in-container systems used in disposable kegs: Basic principles of possible barrier concepts,” *Brewing Science*, vol. 66, pp. 31–36, 2013.
- [40] V. Rastogi and P. Samyn, “Bio-based coatings for paper applications,” *Coatings*, vol. 5, p. 887, 2015.
- [41] H.-C. Langowski, “Permeation of gases and condensable substances through monolayer and multilayer structures,” in *Plastic Packaging*, pp. 297–347, Wiley-VCH Verlag GmbH & Co, 2008.
- [42] J.-W. Rhim, “Effect of clay contents on mechanical and water vapor barrier properties of agar-based nanocomposite films,” *Carbohydrate Polymers*, vol. 86, no. 2, pp. 691–699, 2011.
- [43] M. Wakai and E. Almenar, “Effect of the presence of montmorillonite on the solubility of whey protein isolate films in food model systems with different compositions and pH,” *Food Hydrocolloids*, vol. 43, pp. 612–621, 2015.
- [44] J. Pelleg, *Mechanical Properties of Materials*, Springer, 2012.
- [45] T. D. Fornes and D. R. Paul, “Modeling properties of nylon 6/clay nanocomposites using composite theories,” *Polymer*, vol. 44, no. 17, pp. 4993–5013, 2003.
- [46] B. Chen and J. R. G. Evans, “Elastic moduli of clay platelets,” *Scripta Materialia*, vol. 54, no. 9, pp. 1581–1585, 2006.
- [47] A. B. Morgan, “Flame retarded polymer layered silicate nanocomposites: a review of commercial and open literature systems,” *Polymers for Advanced Technologies*, vol. 17, no. 4, pp. 206–217, 2006.
- [48] V. Molajavadi and H. Garmabi, “Predicting the young’s modulus of intercalated and exfoliated polymer/clay nanocomposites,” *e-Polymers*, vol. 11, p. 219, 2011.
- [49] O. Weizman, A. Dotan, Y. Nir, and A. Ophir, “Modified whey protein coatings for improved gas barrier properties of biodegradable films,” *Polymers for Advanced Technologies*, vol. 28, no. 2, pp. 261–270, 2016.
- [50] M. Schmid, W. Zillinger, K. Müller, and S. Sänglerlaub, “Permeation of water vapour, nitrogen, oxygen and carbon dioxide through whey protein isolate based films and coatings-Permselectivity and activation energy,” *Food Packaging and Shelf Life*, vol. 6, pp. 21–29, 2015.
- [51] W. J. Choi, H.-J. Kim, K. H. Yoon, O. H. Kwon, and C. I. Hwang, “Preparation and barrier property of poly(ethylene terephthalate)/clay nanocomposite using clay-supported catalyst,” *Journal of Applied Polymer Science*, vol. 100, no. 6, pp. 4875–4879, 2006.

Research Article

Andiroba Oil (*Carapa guianensis* Aublet) Nanoemulsions: Development and Assessment of Cytotoxicity, Genotoxicity, and Hematotoxicity

Susana Suely Rodrigues Milhomem-Paixão,^{1,2} Maria Luiza Fascineli,³
Luis Alexandre Muehlmann,^{3,4} Karina Motta Melo,⁵ Hugo Leonardo Crisóstomo Salgado,⁶
Graziella Anselmo Joanitti,^{3,4} Julio Cesar Pieczarka,⁵ Ricardo Bentes Azevedo,³
Alberdan Silva Santos,⁶ and Cesar Koppe Grisolia²

¹Núcleo de Ensino e Pesquisa em Ciências Ambientais (NEPCA) do Instituto Federal de Educação, Ciência e Tecnologia de Goiás, Campus Valparaíso de Goiás, Goiás, GO, Brazil

²Laboratório de Genética Toxicológica, Departamento de Genética e Morfologia, Instituto de Ciências Biológicas, Universidade de Brasília, Brasília, DF, Brazil

³Laboratório de Nanobiotecnologia, Departamento de Genética e Morfologia, Instituto de Ciências Biológicas, Universidade de Brasília, Brasília, DF, Brazil

⁴Faculdade de Ceilândia, Universidade de Brasília, Brasília, DF, Brazil

⁵Laboratório de Citogenética, Instituto de Ciências Biológicas, Universidade Federal do Pará, Belém, PA, Brazil

⁶Laboratório de Investigação Sistemática em Biotecnologia e Biodiversidade Molecular (LabISisBio), Instituto de Ciências Exatas e Naturais, Universidade Federal do Pará, Belém, PA, Brazil

Correspondence should be addressed to Susana Suely Rodrigues Milhomem-Paixão; susanamilhomem@yahoo.com.br

Received 10 January 2017; Accepted 20 March 2017; Published 27 April 2017

Academic Editor: Sohail Rana

Copyright © 2017 Susana Suely Rodrigues Milhomem-Paixão et al. This is an open access article distributed under the Creative Commons Attribution License, which permits unrestricted use, distribution, and reproduction in any medium, provided the original work is properly cited.

Andiroba oil (AO) is obtained from an Amazonian plant and is used in traditional medicine. We carried out a comparative study to test the cytotoxicity, genotoxicity, and hematotoxicity of the oil and its nanoemulsion (AN) in vitro (fibroblasts, lineage NIH/3T3) and in vivo (Swiss mice). The AN was characterized by DLS/Zeta, and its stability was investigated for 120 days. The biological activity of AN was assessed in vitro by MTT test and cell morphology analyses and in vivo by micronucleus, comet, and hematotoxicity tests. The AN presented a hydrodynamic diameter (Hd) of 142.5 ± 3.0 and PDI of 0.272 ± 0.007 and good stability at room temperature. The MTT test evidenced the cytotoxicity of AO and of AN only at their highest concentrations, but AN showed lower cytotoxicity than AO. A lower cytotoxicity of AN, when compared to AO, is in fact an interesting data suggesting that during therapeutic application there will be a lower impact in the cell viability of healthy cells. Cytotoxicity, genotoxicity, and hematotoxicity were not observed in vivo. These tests on the biological and toxicological effects of andiroba oil and nanostructured oil are still initial ones but will give a direction to future application in cosmetics and/or the development of new phytotherapies.

1. Introduction

Carapa guianensis Aublet (Meliaceae), popularly known in Brazil as Andiroba, is a tree that has various traditional uses, such as an insect repellent and an anti-inflammatory and for healing wounds. The product of the andiroba tree that is

most used for medicinal purposes is its oil, extracted from its seeds. It is rich in fatty acids, including oleic, palmitic, and linoleic acids [1]. The internal use was mainly recommended to combat flu, fever, asthma, and sore throat and even to lower the glucose level in the blood (diabetes) [2]. According to Ekor [3], it has increased the use of natural products

in recent years; however, although the natural products are beneficial by their pharmacological activities, some products may produce the toxicity and adverse effect to the body and they need to be studied regarding these parameters.

There are few scientific data about the possible adverse effects or the safety of andiroba oil after experimental administration to animals. Among these studies, Costa-Silva et al. [4] carried out tests in Wistar rats for acute toxicity (0.625–5.0 g/kg) and subacute toxicity (0.375, 0.75, and 1.5 g/kg/day, for 30 days), per os. Biochemical, hematological parameters and the weight of animals and organs were evaluated. In the acute test there was no type of symptom or death. In the subacute treatment there was an increase in the activity of plasma alanine amino transferase (ALT) and in the relative and absolute weight of the liver, results which indicate hepatotoxicity. Using Swiss mice, Milhomem-Paixão et al. [1] ran a subacute toxicity test (0.5, 1.0, and 2.0 g/kg/day for 14 days), also per os. Hematological, genotoxic, cytotoxic, and mutagenic parameters were evaluated, as well as the weight of the animals and their organs, and no toxicity was detected.

Worldwide, there is great interest from scientific communities and the pharmaceutical industry in developing drugs derived from plants. This interest has become even more evident with the development of new biotechnologies, such as nanobiotechnology [5]. Among the new tools provided by nanobiotechnology to natural product applications, nanoemulsions have been used to disperse oily extracts and compounds in aqueous media [6, 7]. Nanoemulsions are isotropic nanometric formulations, based on oil, water, and surfactants, which have been used as carriers of bioactive compounds. Their long-term stability, ease of preparation, and high solubility of molecules have made them a promising tool in the development of pharmaceutical, cosmetic, and nutritional innovations [8–10]. Used in the production of cosmetics, they present advantages such as greater power to hydrate and to penetrate the skin with their active compounds [11]. In the food industry, products have been developed with ingredients that are difficult to absorb, due to their low solubility in water [10]. In the pharmaceutical industry, nanoemulsions can be used for controlled and directed release of drugs [12].

In the current scientific literature, to our knowledge, there are only three studies that refer to the development of nanoformulations with andiroba oil [13–15]. Other plant oils with therapeutic properties have been incorporated in nanomaterials, but few have been studied for their biocompatibility and toxicity [9, 14, 16].

The aim of this work was to develop a nanoemulsion containing andiroba oil and to study its biocompatibility in vitro and in vivo. The data were compared with andiroba oil in natura. This report is the first in the literature to evaluate the effect of the nanoemulsification of andiroba oil on its toxicity profile.

2. Material and Methods

2.1. The Plant Material. The sample of andiroba oil (AO) was collected in the county of Uruará in Pará State (SUO3),

with coordinates S 03° 58' 31.7'' W 053° 37' 32.1'' under license number MMA/ICMBIO/SISBIO-33336-1 issued by the Brazilian Environmental Agency. The seeds were collected in the months of March to July of 2012. The exsicates were deposited in the herbarium of the Brazilian Agricultural Research Company (Embrapa) under accession number 191736. The seeds were identified by Dr. Regina Celia Viana Martins da Silva, curator of the IAN Embrapa Amazônia Oriental herbarium. The andiroba oil was extracted for an artisanal extraction process [17]. More information about profile of fatty acids, steroids, triterpenes, and secondary metabolites like squalene, stigmasterol, cholesterol, epoxygedunin, 1,3-dipalmitin, deoxylactone derivative, deacetylgedunin, and epoxydeacetylgedunin can be found in Milhomem-Paixão et al. [1].

2.2. Formulation of the Andiroba Nanoemulsion (AN). The nanoemulsion was prepared by a phase-inversion temperature (PIT) method [18, 19]. Briefly, 10 grams of AO and 20 grams of surfactant Kolliphor®ELP SIGMA were mixed under shaking. Next, 10 grams of Milli-Q water was added and the temperature was raised to 90°C. It was confirmed that the solution had been clarified and another 10 grams of ice-cold Milli-Q water was added under shaking. As a control for the tests, a mineral oil nanoemulsion (liquid Nujol Petrolatum) was also developed, using the same methodology and the same quantity of oil, surfactant, and water.

2.3. Characterization of the Nanoemulsion (DLS/Zeta). The mean size of the particles was obtained using the Zetasizer Nano S, Malvern Instruments, based on the dynamic light scattering technique. The readings were carried out after 1:100 (m:v) dilution of the nanoemulsion in distilled water.

To analyze the stability of the nanoemulsion, three freshly prepared samples were separated and maintained at three different temperatures (4°C, 37°C, and at room temperature RT). For each sample, six readings with three replicates were done on the Zetasizer (7, 15, 30, 60, 90, and 120 days), and the parameters of the polydispersity index (PDI), zeta potential, and hydrodynamic diameter (Hd) were obtained.

2.4. Cytotoxicity In Vitro Using the MTT Assay in Mouse Fibroblasts. The fibroblast cell lineage used was NIH/3T3 (ATCC). The cells were cultivated in Dulbecco's Minimum Essential Medium (DMEM) (Gibco) supplemented with 10% of de Fetal Bovine Serum (FBS) and 1% of antibiotic and then incubated with an atmosphere of 5% of CO₂ at 37°C, in plastic bottles of 25 cm³ volume.

To evaluate cytotoxicity, the MTT technique was used, a quantitative assay related to cell metabolic activity. Mitochondrial activity is quantified in a spectrophotometer, measuring the quantity of formazan crystals, which are formed by the reduction of MTT tetrazolium by live cells [20].

The fibroblasts of NIH/3T3 were obtained from cultures with 90–95% of confluence, and 3,000 cells/well were seeded in a 96-well plate. The whole experiment was carried out in triplicate. The cells were seeded with 100 µL of DMEM supplemented with 10% of Fetal Bovine Serum (FBS) and 1%

of antibiotic for 24 hours, allowing it to adapt to the environment and the cells to adhere. After this period, the medium was removed from the plate, and 200 μL of culture medium containing different concentrations (0.125 to 2.5 mg/mL) of each treatment was added to each well: andiroba oil (AO) in natura; andiroba nanoemulsion (AN); mineral oil (MO); and mineral oil nanoemulsion (MON). The control group received only DMEM medium (10% (FBS) and 1% of antibiotic). AO and MO were diluted in ethanol, and AN and MON were diluted in water, all in 1%. According to Jo et al. [21] ethanol exposures at concentrations lower than 3% do not cause interference in the cell viability in primary glioblastoma cells. In our study ethanol and water were used at 1% as control, which really did not show any evidence of cytotoxicity to NIH/3T3, and showed also similar result with DMEM medium. Then, we used only one control.

The exposure was maintained for 24 and 48 hours. Cell viability was evaluated using a solution of yellow tetrazolium dye 3-(4,5-dimethylthiazolyl-2)-2,5-diphenyltetrazolium bromide (MTT) (15 μL of MTT for 135 μL of DMEM per well for two hours). Next, the solution of DMEM plus MTT was removed and 100 μL of DMSO was added. A Spectra Max Plate Reader was used to read the plates at 595 nm. The percentage of cell viability was calculated by making a comparison in the number of viable cells between the controls and the treatments.

2.5. Test for Alteration of Cell Morphology. The morphological analysis of treated cells was carried out using an AxioVert.A1 inverted microscope from Zeiss; this was also used to photograph the cells with an AxioCam MRC camera, from Carl Zeiss Micro Imaging GmbH. The exposures used for this test were AO, MO, MON, AN, and ANC (the latter being the andiroba nanoemulsion control which consisted of surfactant and water), all at concentrations of 1.25 mg/mL for 24 h. This concentration was chosen because it was the one that demonstrated cell viability just below 50% in the MTT assay. Control group C did not receive a treatment.

2.6. In Vivo Tests. Nulliparous nonpregnant female Swiss mice (*Mus musculus*) were used, aged 12 weeks, bred at the bioterium at the State University of Campinas (UNICAMP-SP-CEMIB). The project was approved by the Commission for Ethics in Animal Use (CEUA) of the Institute of Biological Sciences at the University of Brasília, UnBDoc, 127331/2013. The animals were kept in the conditions described in Milhomem-Paixão et al. [1].

2.7. Experimental Design. The animals were divided randomly into five experimental groups ($n = 6$ animals/group), consisting of the negative control, and groups receiving different doses of andiroba nanoemulsion (0.5, 1.0, and 2.0 g/kg/day). The negative control group received only surfactant and water, and the treated animals received the andiroba nanoemulsion via a gastric tube (gavage). The administrations followed a period of 14 consecutive days, and the limit of concentration administered corresponds to what is recommended in guidelines 474 and 475 of the OECD

(Organization for Economic Cooperation and Development) for the evaluation of genotoxicity using micronucleus tests [22] and for chromosome aberrations of the bone marrow [23].

Throughout the whole experimental period, the animals were weighed and their consumption of foodstuffs was monitored every three days. Daily observations were made to check clinical symptoms arising from the treatment. After 14 days, the animals were sedated, and blood was taken for hematological evaluation and to make slides for the comet test. They were necropsied, and bone marrow from the femur was used for the micronucleus test, as described in MacGregor et al. [22, 23].

2.8. Genotoxicity and Mutagenicity Assays. The comet test followed the protocol established by Singh et al. [24] for alkaline comet pH > 13, with some modifications, as described in Milhomem-Paixão et al. [1]. The micronucleus test was carried out using bone marrow from the mice, following the protocols of Schmid [25], with modifications, as described in Milhomem-Paixão et al. [1].

2.9. Hematotoxicity. For the analysis of the hematological parameters, 370 μL of the animals' blood with the anticoagulant EDTA (10%) was submitted to an automatic veterinary hemocytometer (Sysmex pocH 100iV Diff™), calibrated for mice.

2.10. Statistical Analyses. The quantitative data were evaluated by parametric or nonparametric statistical tests, according to the distribution of normality. Parametric data were evaluated by Analysis of Variance (ANOVA) followed by Dunnett test. Nonparametric data were evaluated by Wilcoxon and then Kruskal-Wallis test. For this, the Graphpad InStat 3.02 program was used, considering significance to be of $p \leq 0.05$. The graphics and statistical analyses for MTT and for nanoemulsion characterizations were obtained on Graphpad Prism 5.

3. Results

3.1. Characterization of the Andiroba Nanoemulsion (AN): Mean Hydrodynamic Diameter, PDI, and Zeta Potential. The andiroba nanoemulsion obtained presented homogeneity and stability. The mean hydrodynamic diameter found was 142.5 ± 3.0 nm. The value of the PDI (polydispersity index) was 0.272 ± 0.007 . The mineral oil nanoemulsion presented a hydrodynamic diameter of 610.9 ± 3.0 nm. The PDI was 0.169 ± 0.04 .

Aiming to identify for how long and at what temperature this product remained stable, the characteristics of andiroba nanoemulsion were evaluated for 120 days. In relation to the PDI, there was greatest stability in the sample at room temperature and lowest stability at 4°C. Regarding zeta potential, the sample at room temperature was the most stable and that at 37°C the least stable. For the diameter, the samples at room temperature and at 37°C were the most stable (Figure 1).

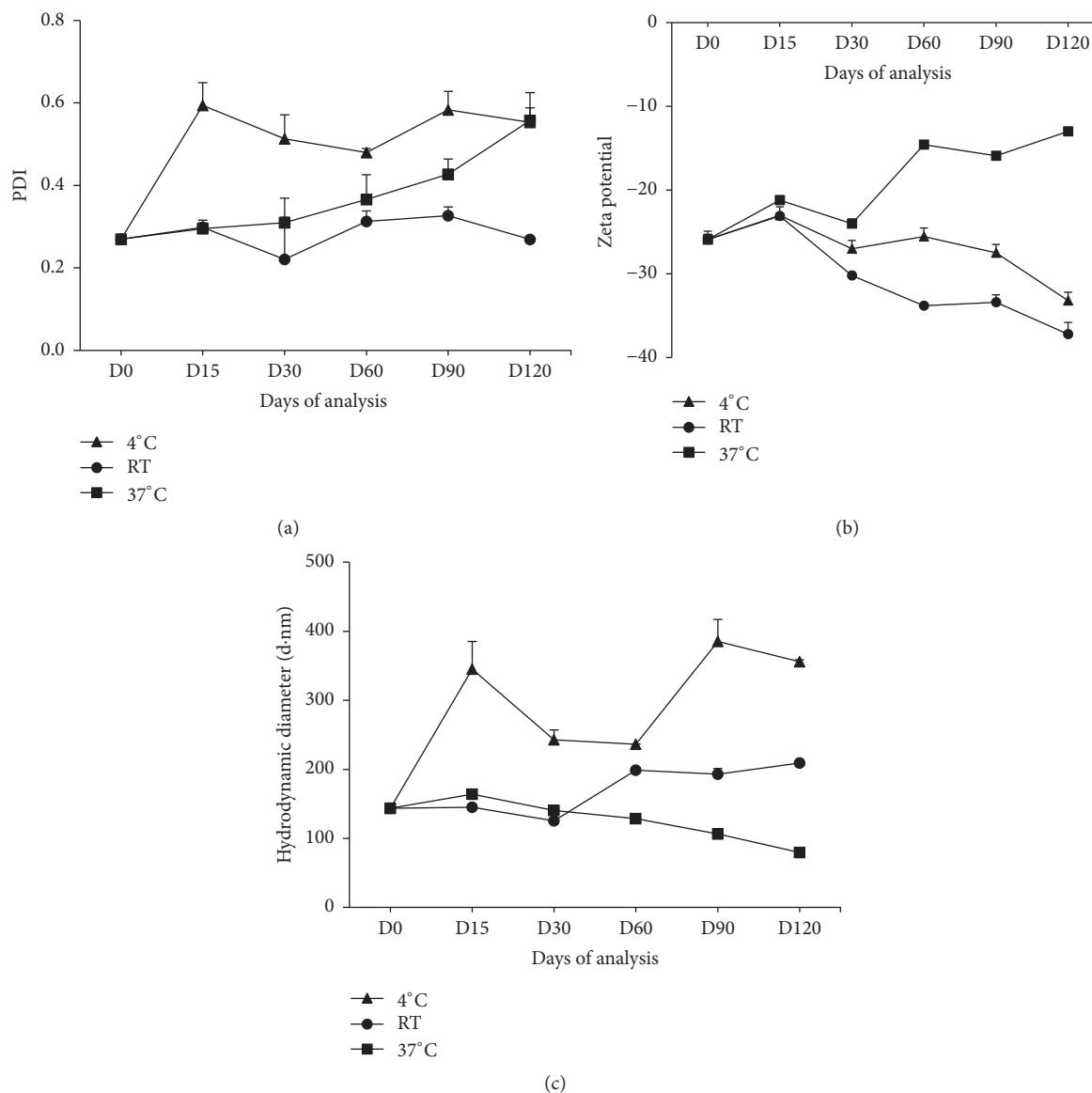


FIGURE 1: Distribution graphs for (a) PDI (polydispersity index), (b) zeta potential, and (c) hydrodynamic diameter of the nanoemulsion at three different temperatures obtained on the Zetasizer Nano S, Malvern Instruments, over a period of 120 days. d-nm: diameter in nanometer, AT: ambient temperature. The data represent the mean and standard deviation ($\bar{X} \pm SD$).

3.2. In Vitro Tests

3.2.1. Cytotoxicity of the Oil In Natura and of the Andiroba Nanoemulsion. The AO and AN samples exhibited a concentration-dependent cytotoxicity profile, meaning that the greater the exposure concentration, the lower the cell viability. This effect was accentuated at 48 hours of exposure (Figure 2). However, the MO sample did not present a significant alteration at 24 and 48 hours of exposure in relation to the control and, in MON, the cell viability remained constant at all concentrations for 24 hours. After 48 hours of exposure, the MON presented small variation at the highest doses, but without a significant difference in relation to the control (0 mg/mL).

The IC₅₀ values (50% reduction in the cell viability) of the samples tested at 24 and 48 hours are also described in Figure 2. The AO showed greater cytotoxicity than the AN. The entrapment of bioactive compounds in nanostructures can potentially alter their route of association or internalization to the targeted cell. Therefore, this is a possible explanation to the difference between the cytotoxicity of AO and AN in vitro. It was not possible to calculate the IC₅₀ in the MO samples (24 and 48 h) and MON (24 h), because the concentrations used in the exposure were not great enough to reduce the cell viability by 50%.

3.2.2. Cell Morphology after Exposure to the Treatments. Figure 3 represents the cell morphology of NIH/3T3 exposed

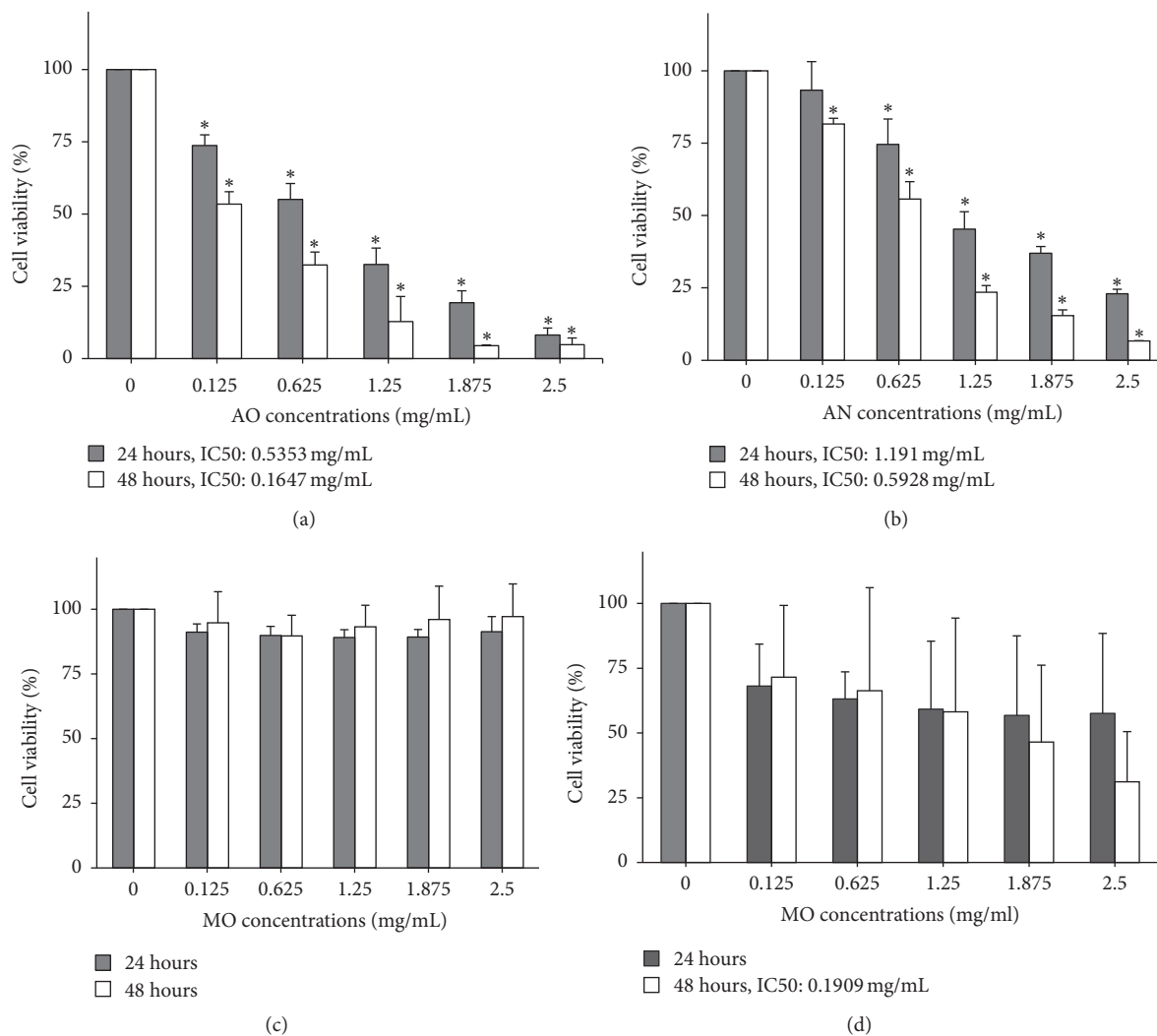


FIGURE 2: Evaluation of the cytotoxicity in NIH/3T3 fibroblasts of samples of (a) andiroba oil (AO) in natura; (b) andiroba nanoemulsion (AN); (c) mineral oil (MO); and (d) mineral oil nanoemulsion (MON), all at different concentrations, after 24 and 48 hours of exposure. The data are expressed by the mean and standard deviation. The statistical test used was ANOVA, in accordance with the distribution of normality. * $p < 0.05$. The IC₅₀ is described in the keys below the graph. The IC₅₀ was obtained using a saturation curve.

at the concentration of 1.25 mg/mL for 24 hours and control group C. This concentration was chosen because it was the one that demonstrated cell viability slightly below 50% by MTT assay.

As can be observed, the morphology of the cells that were exposed to AO, ANC, and AN showed major alterations as those exposed to MO, MON, and the control. The cells that were exposed to AO, ANC, and AN can be seen in the smaller number of cells per field, showing that they were released during exposure. This demonstrates that there is an influence on cell morphology not only by the andiroba oil but also by the andiroba nanoemulsion and by the surfactant used in the production of the andiroba nanoemulsion. Probably AO, ANC, and AN have a profound influence on cell membranes. However, the damaging action of surfactant on the MON is probably attenuated by the presence of the mineral oil and the larger size of oil droplets, because the MON cells are very

similar to those of the control. It was also possible to see that in the AO and AN samples there is a large formation of lipid vacuoles in the cells. In AO there are more of these than in AN.

3.3. In Vivo Tests. To evaluate the possible toxicity arising from the administration of andiroba nanoemulsion, the mice were observed daily for possible alterations. However, no clinical or behavioral alteration was observed and nor were significant differences in body weight. No macroscopic alterations were observed during necropsy nor were alterations seen in the absolute or relative weight of the liver, spleen, or kidneys.

In this study, to characterize the genotoxicity/mutagenicity occasioned by exposure to the nanoemulsion, comet tests (Figure 4) and micronucleus tests (Table 1) were carried out. The results did not show significant alterations in the

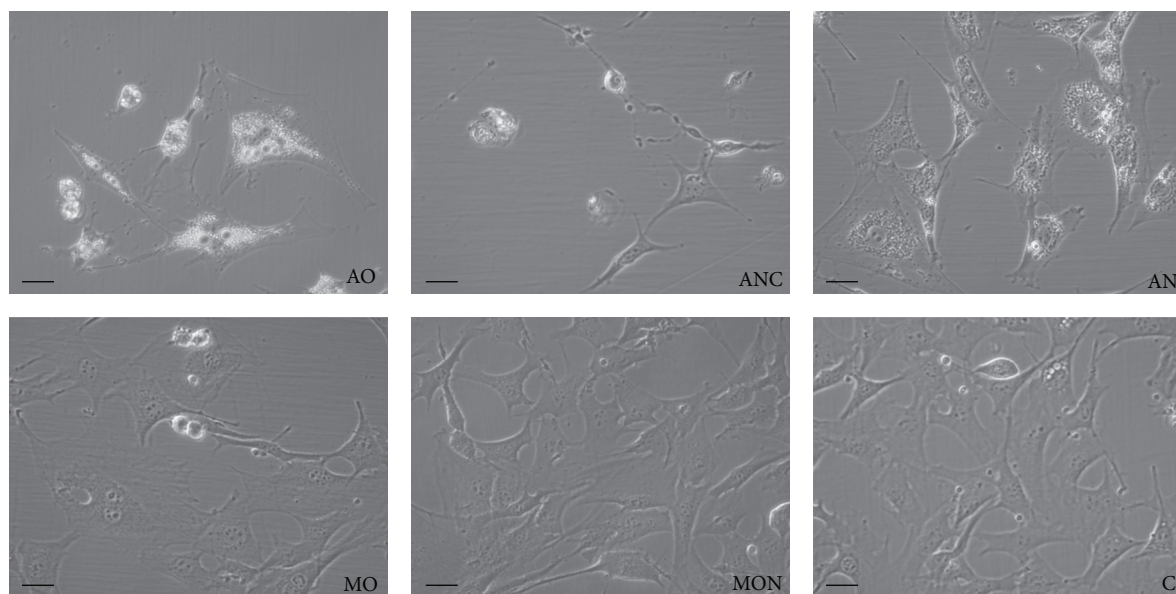


FIGURE 3: Morphology of NIH/3T3 cells after cultivation for 24 hours with the treatments at the third concentration (1.25 mg/mL), AO: andiroba oil, ANC: andiroba nanoemulsion control, AN: andiroba nanoemulsion, MO: mineral oil, MON: mineral oil nanoemulsion, and C: control. The scale bar corresponds to 10 μm .

TABLE 1: Frequency of micronuclei of Swiss mice after oral treatment for 14 days with andiroba oil nanoemulsion.

Treatments	Negative control	0.5 g/kg	1 g/kg	2 g/kg
N° MN-PCE	1.33 ± 1.51	1.33 ± 1.03	2.00 ± 1.55	1.67 ± 1.51
% MN-PCE	6.64 ± 7.49	6.61 ± 5.12	10.40 ± 8.70	8.30 ± 7.48
Relation PCE/NCE	1.32 ± 0.15	1.37 ± 0.21	1.40 ± 0.34	1.49 ± 0.23

The data are represented by the mean and standard deviation ($\bar{X} \pm \text{SD}$). MN: micronucleus; PCE: polychromatic erythrocytes; NCE: normochromatic erythrocytes. Data were analyzed by ANOVA, in accordance with the distribution of normality, $p > 0.05$.

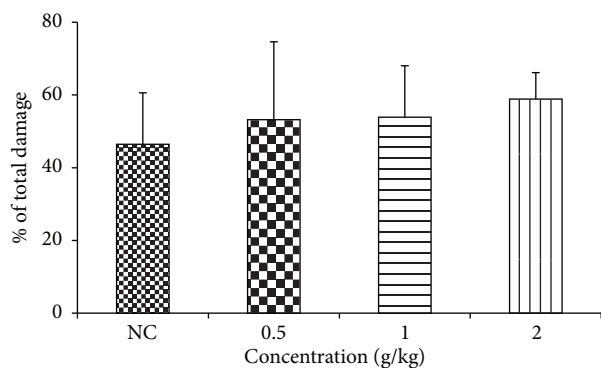


FIGURE 4: Comet test for mice treated orally with andiroba oil nanoemulsion for 14 days. The data represent the mean and standard deviation ($\bar{X} \pm \text{SD}$). Data were analyzed by ANOVA, according to the distribution of normality, $p > 0.05$. NC: negative control.

formation of micronuclei or fragmentation of the DNA molecule.

In the hematological evaluations no significant alteration was seen in the blood parameters (Table 2).

4. Discussion

In the current study, a nanoemulsion was formulated with oil of andiroba plant, which has an enormous cultural value and use in folk medicine in Amazonia. The nanoemulsion and the oil were tested for their biocompatibility, through the assessment of various parameters in vitro and in vivo.

Nanoemulsions are obtained by a number of preparation methods with different components. These methodologies can be divided into high and low-energy methods. Those that use high energy include microfluidization, high-pressure homogenization, and sonication. The low-energy methods involve spontaneous emulsification, solvent diffusion, and phase-inversion temperature. The ideal formulation should consider the safety of its components, as well as incorporating the dose required for the drug's best action and for it to remain stable over time [26].

Oliveira [13] produced a nanoemulsion based on andiroba oil, aiming to combat the mosquito *Aedes aegypti*, using a low-energy method, with Span and Tween as the surfactant. The Hd (hydrodynamic diameter) was less than 300 nm, and the tests in humans showed positive results for insect repellent action. Lorca et al. [14] developed andiroba nanocapsules using the methodology of in situ

TABLE 2: Erythrogram, leukogram, and plateletgram of Swiss mice treated orally with andiroba oil nanoemulsion.

Parameters	Negative control	0.5 g/kg	1 g/kg	2 g/kg
<i>Erythrogram</i>				
RBC $\times 10^6/\mu\text{L}$	8.67 \pm 0.56	9.17 \pm 0.27	9.21 \pm 0.51	9.16 \pm 0.36
HGB g/dL	12.27 \pm 0.81	12.70 \pm 0.25	12.97 \pm 0.82	12.88 \pm 0.45
HCT%	31.58 \pm 2.18	33.10 \pm 0.78	33.58 \pm 2.30	33.57 \pm 1.25
MCV fL	36.4 \pm 0.70	36.1 \pm 0.76	36.4 \pm 0.61	36.7 \pm 0.34
MCH pg	14.2 \pm 0.3	13.8 \pm 0.4	14.1 \pm 0.3	14.1 \pm 0.4
MCHC g/dL	38.8 \pm 0.58	38.4 \pm 0.48	38.6 \pm 0.72	38.4 \pm 0.74
RDW%	13.68 \pm 0.25	13.73 \pm 0.85	14.42 \pm 1.52	13.20 \pm 0.48
<i>Leukogram</i>				
WBC $\times 10^3/\mu\text{L}$	1.83 \pm 0.63	3.07 \pm 0.95	3.10 \pm 0.89	2.23 \pm 0.91
W-SCR%	76.28 \pm 5.25	73.43 \pm 9.40	74.88 \pm 12.44	74.23 \pm 6.55
W-MCR%	19.23 \pm 3.42	22.97 \pm 7.40	23.00 \pm 11.67	24.23 \pm 6.16
W-LCR%	4.48 \pm 2.08	3.60 \pm 3.11	2.12 \pm 2.57	1.53 \pm 1.55
<i>Plateletgram</i>				
PLT $\times 10^3/\text{mL}$	1132 \pm 270	1326 \pm 287	1414 \pm 190	1251 \pm 129
PDW fL	6.88 \pm 0.32	7.02 \pm 0.23	6.80 \pm 0.16	6.74 \pm 0.18
MPV fL	6.63 \pm 0.52	6.48 \pm 0.19	6.58 \pm 0.36	6.26 \pm 0.24
P-LCR%	9.25 \pm 3.72	6.70 \pm 1.95	9.02 \pm 3.02	6.26 \pm 1.30

The data are represented by the mean and standard deviation ($\bar{X} \pm \text{SD}$). The data were analyzed by ANOVA, in accordance with the distribution of normality, $p > 0.05$. RBC: red blood cells; HGB: hemoglobin; HCT: hematocrit; MCV: mean corpuscular volume; MCH: mean corpuscular hemoglobin; MCHC: mean corpuscular hemoglobin concentration; RDW: red cell distribution width; g/dL: grams per deciliter; fL: femtoliters; pg: picogram; WBC: white blood cells; W-SCR: lymphocytes; W-MCR: neutrophils + monocytes; W-LCR: eosinophils; PLT: platelets; PDW: platelet distribution width; MPV: mean platelet volume; P-LCR: platelet large cell ratio.

polymerization of methyl methacrylate with different concentrations of the starter and different temperatures. The Hd varied from 192 nm to 321 nm. The results demonstrated the viability of producing andiroba nanocapsules. Baldissera [15] developed a nanoemulsion based on andiroba oil, aiming to combat the *Trypanosoma evansi*, the etiological agent of the disease known as “Surra” or “Mal das cadeiras” in horses. The nanoemulsion of andiroba was prepared by the spontaneous emulsification method using Span and Tween as the surfactant and organic solvent (acetone). The hydrodynamic diameter (Hd) varied from 129.3 nm to 240.3 nm, and the tests in *Trypanosoma evansi* showed positive results in two concentrations (0.5% and 1.0%). In the present study, we obtained a nanoemulsion with a Hd lower than those described by Oliveira et al. [13, 14] and with Hd intermediate to that described by Baldissera et al. [15]. It is important to analyze the hydrodynamic diameter because it characterizes nanoformulations and allows assessing its stability over time and during dispersion necessary to toxicity experiments. This dispersion of nanoformulation can change Hd and “such changes may alter bioavailability or toxicity in ways that are not entirely understood” [27].

The method used in the present study was suitable for obtaining a nanoemulsion with good homogeneity and an excellent hydrodynamic diameter when compared to literature data [13–15], as well as maintaining its stability for more than four months, when stored at room temperature.

The stability of the material was accompanied by analysis of the PDI, hydrodynamic diameter, and zeta potential for four months. The value of the PDI indicates the distribution

width of the sample size. The closer to zero it is, the lower the variation in the size of the nanoparticles [28]. From these data it was possible to conclude that the best storage temperature for the andiroba nanoemulsion is room temperature (RT). This temperature is also the same as that used by the Amazon population when conserving andiroba oil, as well as being the conservation temperature for other nanoemulsions described by Alam et al. [29–31]. On the other hand, the andiroba oil becomes solid at 4°C, which could explain such variations, once our stock solution was stored at 4°C, due to a possible precipitation in larger particulate compounds.

In the prediction of long-term stability of the nanoemulsion, it is necessary to understand the status of the nanoemulsion surface zeta potential. Nanoparticles with zeta potential values greater than +25 mV or lower than –25 mV typically have showed higher stability. On the other hand, dispersions with a low zeta potential value will eventually aggregate due to Van Der Waal interparticle attractions [28]. In this study, all samples showed stability until 30 days, regarding these parameters. Stability longer than 30 days was observed only in samples stored at 37°C.

As for the analysis of cytotoxicity in vitro, it is very clearly established that lineage NIH/3T3 is a powerful tool for this type of study [32]. In the literature, different effects of the cytotoxic behavior have been described, depending on the type of chemical substance, concentration, system for delivering substances, and type of cell lineage, using the MTT assay, using NIH/3T3 and other kind of cells [33, 34]. The AO and AN samples exhibited a higher concentration-dependent profile after 48 hours of exposure (Figure 2). However, the

MO sample did not induce a significant alteration in cell viability at 24 and 48 hours in relation to the control. For the MON treatment, the cell viability remained constant at all the concentrations for 24 hours, and after 48 hours of exposure the MON presented a concentration-dependent variation in the highest concentrations. These results demonstrate a cytotoxic effect of the AO, at the highest concentrations, and also of the surfactant used in producing the nanoemulsion. In relation to the MON, the toxic action of the surfactant is probably attenuated by the presence of the mineral oil, which was shown not to be cytotoxic. This result was also corroborated by the cell morphology after exposure (Figure 3) when we used the ANC (nanoemulsion control) made only with water and surfactant. The cytotoxicity of Cremophor EL has already been described for endothelial and epithelial cells, using the MTT test, with the endothelial cells being more sensitive than the epithelial cells [35]. Cremophor, similar to other surfactants, has a profound influence on cell membranes. They disturb plasma membranes or remove certain lipids from the membranes [35]. It is important to highlight in this study that the nanostructured oil (AN) showed less cytotoxicity than the andiroba oil (AO) at the 24 h and 48 h exposures. The entrapment of bioactive compounds in nanostructures can potentially alter their route of association or internalization to the targeted cell [36]. Therefore, this is a possible explanation to the difference between the cytotoxicity of AO and AN *in vitro*. According to Chime et al. [37], “an ideal drug delivery system fulfils the objective of maximizing therapeutic effect while minimizing toxicity.” Our results demonstrated the efficacy of andiroba nanoemulsions as a delivery system, which can improve the efficiency of a drug, reducing their concentrations without losing effectiveness and minimizing side-effects [38].

It is important to emphasize that a low cytotoxicity of AN in normal cell does not necessarily implicate a reduced bioavailability of the bioactive compounds in *in vivo* systems. When used for a therapeutic application, nanostructures may accumulate in the desired target by taking advantage of intrinsic characteristics of the pathological process. For instance, it is known that nanoparticles can preferentially accumulate in inflammatory lesions, due the presence of abnormal blood vessels and reduced lymphatic drainage. This passive accumulation is known as EPR effect (enhanced permeation and retention) which contribute in increasing the amount of the bioactive compounds in the desired target [39].

After 24 hours of exposure, the inhibitory concentration 50% (IC₅₀) for the AO was 0.5353 mg/mL and for the AN it was 1.191 mg/mL. Comparing the value of the IC₅₀ of the AO and AN at 24 h with data found in the literature, it can be noted that these values are higher than those described for other plant oils with high antiproliferative power. This is the case of guava (*Psidium guajava*) leaf oil in the KB lineage, of 0.0379 mg/mL, and of basil (*Ocimum basilicum*) oil in the P388 lineage, of 0.0362 mg/mL [40]. AO and AN possess a lower antiproliferative power than guava leaf oil and basil oil. This result is of extreme importance in the development of a nanostructured cosmetic or pharmaceutical product with low cytotoxicity, and our results corroborate the studies that demonstrate that nanoemulsions present a reduction

in toxicity. Moreno et al. [41] reported that lecithin-based microemulsions used for parenteral use showed reduced toxicity. Wang et al. [42] developed aclacinomycin A (E-ACM) emulsion and evaluated its toxicity in M5076 tumor-bearing C57BL/6 mice. E-ACM had lower acute toxicity and greater potential antitumor effects than F-ACM (the free ACM). Bruxel et al. [26] also report that some studies with nanoemulsions describe possibilities in toxicity reduction, increased activity, therapeutic window, bioavailability, and controlled release of drugs.

The nanoemulsions used in the production of cosmetics present the following advantages: greater power to moisturize and for active ingredients to penetrate; uniform distribution of the product over the skin; capacity to penetrate wrinkles; sensorial aspect; transparency and fluidity; ability to carry a fragrance; and perfumes without alcohol, and follicular, and pilosebaceous penetration [43, 44]. In the development of repellent nanoemulsions, they present greater efficacy in the action against insects [45]. In the case of AN, these actions need to be proved with specific tests against insects.

Andiroba oil possesses various uses in traditional medicine, mainly as an anti-inflammatory and a wound healer. Even without scientific studies, the Amazonian population uses this oil indiscriminately *in natura* and even in capsules. Because of this, here in this study the route of administration chosen for andiroba nanoemulsion (AN) was oral. The oral administration of surfactants is relatively safe. Here, this route via a gastric tube (gavage) was tested *in vivo* (Swiss mice). As could be observed in the initial results for cytotoxicity by MTT and cell morphology, the oil presents a concentration-dependent cytotoxic effect. With the data obtained *in vitro* it is not possible to affirm whether the andiroba oil and its nanoemulsion are suitable for use in humans, due to the cell death observed. Additional *in vivo* toxicity tests are needed to establish the concentrations that will allow safe use. In the *in vivo* study model, there is a complex of processes that occur in the gastrointestinal tract, affecting the absorption of the analyte, which does not happen *in vitro*, where the dissolution and absorption of the drug can be immediate [46].

In our studies, administration in the mice was carried out for a period of 14 consecutive days. The analyzed concentration limit is in accordance with the recommendations indicated in guidelines 474 and 475 of the OECD (Organization for Economic Cooperation and Development) for the evaluation of genotoxicity from micronucleus test [22] and of chromosome aberrations in bone marrow [23], as also described in Milhomem-Paixão et al. [1].

Oxidative species, as well as various natural compounds or medicines, can interact with DNA, causing damage. The damage can be reverted by the DNA repair system or may persist, inducing genotoxicity and even mutagenesis. To evaluate the mutagenic and genotoxic effects of numerous compounds, comet and micronucleus tests are well established in the indication of the extent and severity of the interaction between the compounds studied and DNA [47, 48]. Furthermore, these tests are validated by international agencies that evaluate the safety of chemical agents.

The PCE/NCE (polychromatic erythrocyte/normochromatic erythrocyte) relationship is another parameter that can be evaluated by the micronucleus test. The progression of erythroblasts from the PCE to the NCE stage is an indicator of the acceleration or inhibition of erythropoiesis, and thus a reduction in this relationship (PCE/NCE) indicates cytotoxicity [49]. The results of the experiment by Milhomem-Paixão et al. [1] showed that andiroba oil did not induce a significant increase in the MN-PCE frequency and did not reduce the PCE/NCE relationship at any of the tested concentrations. All the tested samples of andiroba oil in natura and of the nanoemulsion indicate a negative result for the micronucleus test, which means that these samples did not induce structural or numerical chromosome damage in the erythroblasts of Swiss mice treated with andiroba and nor did they present cytotoxicity in the bone marrow. The comet assay for the experiments of Milhomem-Paixão et al. [1] and those described here in this study also demonstrated that the substances tested did not produce DNA breakages in blood cells of mice during administration at the maximum dose of 2 g/kg for 14 days. The results show that andiroba oil and nanoemulsion are not genotoxic, cytotoxic, or mutagenic. These results are similar to those found for other plant oils such as Copaíba oil of the genus *Copaifera* [50] and the oil extracted from fruit of the species *Litsea cubeba* [51]. Similar results were observed in Swiss mice treated with a nanoemulsion made from the oil of the Sucupira tree *Pterodon emarginatus* Vogel [52].

In this study, as well as in our previous work, both andiroba nanoemulsion and andiroba oil in natura presented no hematotoxicity in mice [1].

Even with the detection of the high antioxidant potential of AO described by Milhomem-Paixão et al. [1] it could be noted that the cytotoxicity test in vitro showed that andiroba oil and nanoemulsion have a cytotoxic effect only at high concentrations, which was not seen in in vivo tests. This difference may have occurred because of the forms of absorption in the samples tested here. In vitro, there is no barrier to the absorption of the compounds by the cells, while in vivo the absorption is a complex process, involving the interaction of the compounds with the gastrointestinal tract, their transport to organs, hepatic first pass effect, and other events. This process may have prevented or obstructed the delivery of the andiroba compounds to the blood cells, in the case of comet and hematotoxicity analysis, in the bone marrow cells, and in the case of the micronucleus test.

5. Conclusion

In conclusion, this work reports the development of a stable nanoemulsion produced with andiroba oil. In the experimental biological conditions used in vivo in this work, a nanoemulsion did not present genotoxic, cytotoxic, or mutagenic effects, whereas in the in vitro tests it presented cytotoxicity at the highest concentrations.

These tests on the biological and toxicological effects of andiroba oil and nanostructured oil will give a direction to future application in cosmetics and/or the development of

new phytotherapies. The data presented here are still initial ones, but as studies advance, bringing greater knowledge about the properties and applications of this oil, more value may be given to the andiroba tree.

Conflicts of Interest

The authors declare that they have no conflicts of interest.

Acknowledgments

This research was supported by the National Council for the Improvement of Higher Education (CAPES) from the Pro-Amazonia Project no. 3284/2013 and by the National Council for Scientific and Technological Development (CNPq). Susana Suely Rodrigues Milhomem-Paixão received a Post-doctoral Fellowship from the National Council for Scientific and Technological Development (CNPq).

References

- [1] S. S. R. Milhomem-Paixão, M. L. Fascineli, M. M. Roll et al., "The lipidome, genotoxicity, hematotoxicity and antioxidant properties of andiroba oil from the Brazilian Amazon," *Genetics and Molecular Biology*, vol. 39, no. 2, pp. 248–256, 2016.
- [2] A. P. Mendonça and I. D. K. Ferraz, "Óleo de andiroba: processo tradicional da extração, uso e aspectos sociais no estado do Amazonas, Brasil," *Acta Amazonica*, vol. 37, no. 3, pp. 353–364, 2007.
- [3] M. Ekor, "The growing use of herbal medicines: issues relating to adverse reactions and challenges in monitoring safety," *Frontiers in Neurology*, vol. 4, article 177, 2014.
- [4] J. H. Costa-Silva, C. R. Lima, E. J. R. Silva et al., "Acute and subacute toxicity of the *Carapa guianensis* Aublet (Meliaceae) seed oil," *Journal of Ethnopharmacology*, vol. 116, no. 3, pp. 495–500, 2008.
- [5] P. D. Marcato, "Pharmacokinetics and Pharmacodynamics of Nanomaterials," in *Nanotoxicology: Materials, Methodologies, and Assessments*, pp. 97–110, Springer, New York, NY, USA, 2014.
- [6] L. A. Muehlmann, M. C. Rodrigues, J. P. F. Longo et al., "Aluminium-phthalocyanine chloride nanoemulsions for anti-cancer photodynamic therapy: development and in vitro activity against monolayers and spheroids of human mammary adenocarcinoma MCF-7 cells," *Journal of Nanobiotechnology*, vol. 13, article 36, 2015.
- [7] M. C. Rodrigues, "Photodynamic therapy based on Arrabidaea chica (Crajiuru) extract nanoemulsion: in vitro activity against monolayers and spheroids of human mammary adenocarcinoma MCF-7 cells," *Journal of Nanomedicine & Nanotechnology*, vol. 6, no. 3, article 286, 2015.
- [8] A. Azeem, M. Rizwan, F. J. Ahmad et al., "Nanoemulsion components screening and selection: a technical note," *AAPS PharmSciTech*, vol. 10, no. 1, pp. 69–76, 2009.
- [9] C. E. S. Silva, O. J. Dos Santos, J. M. Ribas-Filho et al., "Effect of *Carapa guianensis* aublet (Andiroba) and orbignya phalerata (babassu) in colonic healing in rats," *Revista do Colégio Brasileiro de Cirurgiões*, vol. 42, no. 6, pp. 399–406, 2015.
- [10] A. Gupta, H. B. Eral, T. A. Hatton, and P. S. Doyle, "Nanoemulsions: formation, properties and applications," *Soft Matter*, vol. 12, no. 11, pp. 2826–2841, 2016.

- [11] O. Sonnevile-Aubrun, J.-T. Simonnet, and F. L'Alloret, "Nano-emulsions: a new vehicle for skincare products," *Advances in Colloid and Interface Science*, vol. 108-109, pp. 145-149, 2004.
- [12] S. Tamilvanan, "Formulation of multifunctional oil-in-water nanosized emulsions for active and passive targeting of drugs to otherwise inaccessible internal organs of the human body," *International Journal of Pharmaceutics*, vol. 381, no. 1, pp. 62-76, 2009.
- [13] B. R. Oliveira, *Desenvolvimento e avaliação de nanoemulsões com óleos de Carapa guianensis e Copaifera sp. e estudo de ação repelente frente a Aedes aegypti [M.S. thesis]*, Faculdade de Ciências Farmacêuticas de Ribeirão Preto, 2008.
- [14] B. S. S. Lorca, C. Sayer, P. H. H. Araújo, M. Nele, and J. C. Pinto, "Nanoencapsulação de óleo de andiroba viapolimerização em miniemulsão," in *Anais do 10 Congresso Brasileiro de Polímeros*, Foz do Iguaçu, Brazil, 2009, <https://www.ipen.br/biblioteca/cd/cbpol/2009/PDF/761.pdf>.
- [15] M. D. Baldissera, A. S. Da Silva, C. B. Oliveira et al., "Trypanocidal activity of the essential oils in their conventional and nanoemulsion forms: in vitro tests," *Experimental Parasitology*, vol. 134, no. 3, pp. 356-361, 2013.
- [16] I. C. Costa, R. F. Rodrigues, F. B. Almeida et al., "Development of jojoba oil (*Simmondsia chinensis* (link) C.K. schneid.) based nanoemulsions," *Latin American Journal of Pharmacy*, vol. 33, no. 3, pp. 459-463, 2014.
- [17] P. Shanley, M. Serra, and G. Medina, *Frutíferas e Plantas Úteis na Vida Amazônica*, Editora Supercores, Belém, Brazil, 2005, <http://www.fca.unesp.br/Home/Extensao/GrupoTimbo/frutiferas.pdf>.
- [18] T. Tadros, P. Izquierdo, J. Esquena, and C. Solans, "Formation and stability of nano-emulsions," *Advances in Colloid and Interface Science*, vol. 108-109, pp. 303-318, 2004.
- [19] P. P. Constantinides, M. V. Chaubal, and R. Shorr, "Advances in lipid nanodispersions for parenteral drug delivery and targeting," *Advanced Drug Delivery Reviews*, vol. 60, no. 6, pp. 757-767, 2008.
- [20] T. Mosmann, "Rapid colorimetric assay for cellular growth and survival: application to proliferation and cytotoxicity assays," *Journal of Immunological Methods*, vol. 65, no. 1-2, pp. 55-63, 1983.
- [21] H. Y. Jo, Y. Kim, H. W. Park et al., "The unreliability of MTT assay in the cytotoxic test of primary cultured glioblastoma cells," *Experimental Neurobiology*, vol. 24, no. 3, pp. 235-245, 2015.
- [22] J. T. MacGregor, J. A. Heddle, M. Hite et al., "Guidelines for the conduct of micronucleus assays in mammalian bone marrow erythrocytes," *Mutation Research/Genetic Toxicology*, vol. 189, no. 2, pp. 103-112, 1987.
- [23] R. Julian Preston, B. J. Dean, S. Galloway, H. Holden, A. F. McFee, and M. Shelby, "Mammalian in vivo cytogenetic assays Analysis of chromosome aberrations in bone marrow cells," *Mutation Research/Genetic Toxicology*, vol. 189, no. 2, pp. 157-165, 1987.
- [24] N. P. Singh, M. T. McCoy, R. R. Tice, and E. L. Schneider, "A simple technique for quantitation of low levels of DNA damage in individual cells," *Experimental Cell Research*, vol. 175, no. 1, pp. 184-191, 1988.
- [25] W. Schmid, "The micronucleus test," *Mutation Research/Environmental Mutagenesis and Related Subjects*, vol. 31, no. 1, pp. 9-15, 1975.
- [26] F. Bruxel, M. Laux, L. B. Wild, M. Fraga, L. S. Koester, and H. F. Teixeira, "Nanoemulsões como sistemas de liberação parenteral de fármacos," *Química Nova*, vol. 35, no. 9, pp. 1827-1840, 2012.
- [27] Y. I. Cong, C. Pang, L. Dai, G. T. Banta, H. Selck, and V. E. Forbesy, "Importance of characterizing nanoparticles before conducting toxicity tests," *Integrated Environmental Assessment and Management*, vol. 7, no. 3, pp. 502-503, 2011.
- [28] Malvern Instruments Ltd, "Zetasizer Nano Series User Manual," MAN0317, no. 2.1, July 2004, http://www.biozentrum.unibas.ch/fileadmin/redaktion/Forschung/Research_Groups/BF/instruments/zetasizer_manual.pdf.
- [29] S. Alam, S. Baboota, M. Sajid Ali et al., "Accelerated stability testing of Betamethasone dipropionate nanoemulsion," *International Journal of Pharmacy and Pharmaceutical Sciences*, vol. 4, no. 4, pp. 371-374, 2012.
- [30] M. S. Alam, M. S. Ali, M. I. Alam, T. Anwer, and M. M. A. Safhi, "Stability testing of beclomethasone dipropionate nanoemulsion," *Tropical Journal of Pharmaceutical Research*, vol. 14, no. 1, pp. 15-20, 2015.
- [31] R. Parveen, S. Baboota, J. Ali, A. Ahuja, and S. Ahmad, "Stability studies of silymarin nanoemulsion containing Tween 80 as a surfactant," *Journal of Pharmacy and Bioallied Sciences*, vol. 7, no. 4, pp. 321-324, 2015.
- [32] M. Theiszova, S. Jantova, J. Draganova, P. Grznarova, and M. Palou, "Comparison the cytotoxicity of hydroxyapatite measured by direct cell counting and MTT test in murine fibroblast NIH-3T3 cells," *Biomedical Papers*, vol. 149, no. 2, pp. 393-396, 2005.
- [33] M. Danihelová, M. Veverka, E. Šturdík, and S. Jantová, "Antioxidant action and cytotoxicity on HeLa and NIH-3T3 cells of new quercetin derivatives," *Interdisciplinary Toxicology*, vol. 6, no. 4, pp. 209-216, 2013.
- [34] Y. Cetin and L. B. Bullerman, "Cytotoxicity of *Fusarium* mycotoxins to mammalian cell cultures as determined by the MTT bioassay," *Food and Chemical Toxicology*, vol. 43, no. 5, pp. 755-764, 2005.
- [35] L. Kiss, F. R. Walter, A. Bocsik et al., "Kinetic analysis of the toxicity of pharmaceutical excipients cremophor EL and RH40 on endothelial and epithelial cells," *Journal of Pharmaceutical Sciences*, vol. 102, no. 4, pp. 1173-1181, 2013.
- [36] H. Ding and Y. Ma, "Theoretical and computational investigations of nanoparticle-biomembrane interactions in cellular delivery," *Small*, vol. 11, no. 9-10, pp. 1055-1071, 2015.
- [37] S. A. Chime, F. C. Kenechukwu, and A. A. Attama, "Nanoemulsions—advances in formulation, characterization and applications in drug delivery," in *Application of Nanotechnology in Drug Delivery*, InTech, Rijeka, Croatia, 2014.
- [38] R. P. Patel and J. R. Joshi, "An overview on nanoemulsion: a novel approach," *International Journal of Pharmaceutical Sciences and Research*, vol. 3, no. 12, pp. 4640-4650, 2012.
- [39] A. Watanabe, H. Tanaka, Y. Sakurai et al., "Effect of particle size on their accumulation in an inflammatory lesion in a dextran sulfate sodium (DSS)-induced colitis model," *International Journal of Pharmaceutics*, vol. 509, no. 1-2, pp. 118-122, 2016.
- [40] J. Manosroi, P. Dhumtanom, and A. Manosroi, "Anti-proliferative activity of essential oil extracted from Thai medicinal plants on KB and P388 cell lines," *Cancer Letters*, vol. 235, no. 1, pp. 114-120, 2006.
- [41] M. A. Moreno, M. P. Ballesteros, and P. Frutos, "Lecithin-based oil-in-water microemulsions for parenteral use: pseudoternary phase diagrams, characterization and toxicity studies," *Journal of Pharmaceutical Sciences*, vol. 92, no. 7, pp. 1428-1437, 2003.

- [42] J. Wang, Y. Maitani, and K. Takayama, "Antitumor effects and pharmacokinetics of aclacinomycin A carried by injectable emulsions composed of vitamin E, cholesterol, and PEG-lipid," *Journal of Pharmaceutical Sciences*, vol. 91, no. 4, pp. 1128–1134, 2002.
- [43] M. S. Bangale, S. S. Mitkare, S. G. Gattani, and D. M. Sakarkar, "Recent nanotechnological aspects in cosmetics and dermatological preparations," *International Journal of Pharmacy and Pharmaceutical Sciences*, vol. 4, no. 2, pp. 88–97, 2012.
- [44] J.-L. Gesztesi, L. M. Santos, P. T. Hennies, and K. A. Macian, "Oil-in-water nanoemulsion, a cosmetic composition and a cosmetic product comprising it, a process for preparing said nanoemulsion," United States Patent. No. US 8,956,597 B2, 2015, <https://www.google.com/patents/US8956597>.
- [45] U. Sakulku, O. Nuchuchua, N. Uawongyart, S. Puttipipatkachorn, A. Soottitantawat, and U. Ruktanonchai, "Characterization and mosquito repellent activity of citronella oil nanoemulsion," *International Journal of Pharmaceutics*, vol. 372, no. 1-2, pp. 105–111, 2009.
- [46] G. L. Amidon, H. Lennernäs, V. P. Shah, and J. R. Crison, "A theoretical basis for a biopharmaceutic drug classification: the correlation of in vitro drug product dissolution and in vivo bioavailability," *Pharmaceutical Research*, vol. 12, no. 3, pp. 413–420, 1995.
- [47] V. W. C. Wong, Y. T. Szeto, A. R. Collins, and I. F. F. Benzie, "The COMET assay: a biomonitoring tool for nutraceutical research," *Current Topics in Nutraceutical Research*, vol. 3, no. 1, pp. 1–14, 2005.
- [48] G. A. Asare, B. Gyan, K. Bugyei et al., "Toxicity potentials of the nutraceutical *Moringa oleifera* at supra-supplementation levels," *Journal of Ethnopharmacology*, vol. 139, no. 1, pp. 265–272, 2012.
- [49] P. Venkatesh, B. Shantala, G. C. Jagetia, K. K. Rao, and M. S. Baliga, "Modulation of doxorubicin-induced genotoxicity by *Aegle marmelos* in mouse bone marrow: a micronucleus study," *Integrative Cancer Therapies*, vol. 6, no. 1, pp. 42–53, 2007.
- [50] L. S. Almeida, J. R. Gama, F. d. Oliveira, J. O. Carvalho, D. C. Gonçalves, and G. C. Araújo, "Fitossociologia e uso múltiplo de espécies arbóreas em floresta manejada, comunidade Santo Antônio, município de Santarém, estado do Pará," *Acta Amazonica*, vol. 42, no. 2, pp. 185–194, 2012.
- [51] M. Luo, L. Jiang, and G. Zou, "Acute and genetic toxicity of essential oil extracted from *Litsea cubeba* (Lour.) Pers.," *Journal of Food Protection*, vol. 68, no. 3, pp. 581–588, 2005.
- [52] A. E. M. F. M. Oliveira, J. L. Duarte, J. R. R. Amado et al., "Development of a larvicidal nanoemulsion with *Pterodon emarginatus* vogel oil," *PLoS ONE*, vol. 11, no. 1, Article ID e0145835, 2016.

Research Article

An Efficient Method for Cellulose Nanofibrils Length Shearing via Environmentally Friendly Mixed Cellulase Pretreatment

Yuan Chen,¹ Yuchan He,¹ Dongbin Fan,¹ Yanming Han,¹ Gaiyun Li,¹ and Siqun Wang^{1,2}

¹Chinese Academy of Forestry, Research Institute of Wood Industry, Beijing 100091, China

²Center for Renewable Carbon, University of Tennessee, Knoxville, TN 37996, USA

Correspondence should be addressed to Gaiyun Li; ligy@caf.ac.cn

Received 4 January 2017; Revised 23 February 2017; Accepted 7 March 2017; Published 23 March 2017

Academic Editor: Sohel Rana

Copyright © 2017 Yuan Chen et al. This is an open access article distributed under the Creative Commons Attribution License, which permits unrestricted use, distribution, and reproduction in any medium, provided the original work is properly cited.

Cellulose nanofibrils (CNFs) have potential applications in the development of innovative materials and enhancement of conventional materials properties. This paper focused on the mixed cellulase hydrolysis with major activity of exoglucanase and endoglucanase on the cellulose length shearing. By the cooperation of two-step production route, including (1) enzymatic pretreatment using cellulase from *Trichoderma viride* and (2) mechanical grinding twice, a shorter cellulose nanofiber was fabricated. The influence of enzymatic charge and hydrolysis time on cellulose fibers was analyzed by using scanning electron microscopy (SEM), Fourier Transform Infrared Spectrometer (FTIR), and X-ray diffractometer (XRD). SEM images revealed that the surface morphology change, effective diameter sharpening, and length shearing of cellulose fibers are as a result of cellulase hydrolysis. The XRD suggested that the cellulase acted on the amorphous regions more strongly than the crystalline domains during layer-by-layer hydrolysis. The enzymatic charge and hydrolysis time significantly affected the yields and hydrolysis products concentration. The enzymatic pretreatment assisted mechanical grinding could improve the uniformity of CNF and helped to obtain CNF with exact length according to the requirement for special applications.

1. Introduction

Cellulose is one of the most important biopolymer materials [1]. The renewable, lightweight, and low-cost natural fibers can be used as the ideal reinforcement material [2] to improve the strength and stiffness of polymer composites [3]. In recent years, cellulose nanofibers have attracted great attention due to the super peculiarity [4, 5] (e.g., biodegradation, small size effect, and extremely large surface area), which results in the wild applications [2, 4], including optically transparent materials, surface coating, drug delivery, biomedical materials [6], and food package [7]. A few methods have been developed to manufacture cellulose nanofibers [8–14], including chemical, mechanical, and biological method. The most common chemical method is strong acid hydrolysis [8, 9]. However, the easy-corrosion and high requirements for reaction equipment, nonrecycling, and comparatively low yields limit this method for large-scale production. TEMPO-oxidized cellulose fibers method can obtain a high yield.

But this method seems unsuccessful to apply to the high crystalline nonwood fibrils [10]. Biological preparation is major to be used in the bacterial cellulose, and it is a high cost, long time, and small-scale preparation process [11–13]. Mechanical method is more widely applied because of the nonchemical reagents, nonenvironmental pollution, and ripe equipment. However, plant fibers have the special multilayer structure of cell walls, and there are a large number of hydrogen bonds between the molecular interaction and intramolecularity, which requires more number of repeated cycles to increase the degree of fibrillation [14]. A higher number of passes also increase the energy consumption [15]. In conclusion, mechanical fabrication is the most potential method to produce CNF on a large scale. The high energy consumption and large variability [15–17] are the major problems during the mechanical fabrication.

Pretreatment methods have been reported [8–10] to solve the issues mentioned above. Compared with acid hydrolysis [18, 19], carboxymethylation [20], and TEMPO-mediated

oxidation [10], enzymatic pretreatment is satisfied with the requirements of green and is ecofriendly. It is one of the most promising, efficient, and energy-saving pretreatments to convert plant cellulose fibrils [21, 22]. So far, a series of studies have been reported about the mechanism of enzymatic hydrolysis [23–25]. There is wide recognition that the enzyme hydrolysis is the result of cooperation of monocomponent [26, 27] enzyme, mainly including endoglucanases, exoglucanases, and cellobiases. Nevertheless, there are no explicit reports about the sharpening and shearing action on cellulose fibers during the mixed cellulase hydrolysis process. The action mechanism of mixed cellulase on hardwood pulp fibers dimension control, especially length shearing, is worth to research.

This paper focused on the ecofriendly approach for CNF production on a large scale by enzymatic pretreatment assisted mechanical grinding from hardwood pulp. It mainly studied the action of one of mixed cellulase pretreatments on the length control of cellulose fibers. Compared with monoendoglucanase hydrolysis previously reported [28, 29], the cost of mixed cellulase is much lower, which significantly declines the total cost of CNF products. Then the hydrolysis mechanism of cellulase on the crystalline and amorphous domains was studied by the XRD and FTIR spectrum with enzymatic charge and hydrolysis time change. The enzyme hydrolysis can effectively shear the fibril length and sharpen the diameter of cellulose fibrils, which will help to manufacture CNFs with special size according to the requirements of applications using a virtually nonenvironmental pollution process. The shorter length CNF and its derivatives are being prospectively explored in extensive application in composite reinforcement and nanomaterial fields.

2. Materials and Methods

2.1. Materials. The commercial eucalyptus pulp was purchased from Guangdong Zhanjiang Chenming Paper Co., Ltd. The fiber dimensions were $\geq 10\ \mu\text{m}$ in diameter and $\geq 200\ \mu\text{m}$ in length. The cellulase ($M_w = 45000\sim 76000$, enzyme activity $\geq 15000\ \text{U/g}$) was from *Trichoderma viride* and purchased from Chinese Medicine Group. The commercial enzyme was a mix of endoglucanase and exoglucanase. The phosphate buffer solution was used during enzymatic pretreatment, including KH_2PO_4 and Na_2HPO_4 , where pH was 4.8.

2.2. Preparation of Enzymatic Pretreatment Cellulose. The enzymatic pretreatment of cellulose fibers was carried out by pulp treating and enzymatic treatment followed by three steps: first, never-dried cellulose hardwood pulp (10 g) was shred into pieces (Micro pulverizer, Tianjin Taisite Instrument Co., Ltd.) and soaked in 1000 mL deionized water. The high speed mixer was used to mix the pulp pieces with 500 rpm for 2 h. Then the pulp suspension was placed for 24 h to fully swell the fibers at the room temperature. The suspension was filtered to remove water after well swelling. Secondly, 250 mL phosphate buffer solution was added to a 500 mL erlenmeyer flask, then adding cellulase charge of 0.1 g, 0.2 g, 0.4 g, and 0.6 g, respectively. The enzymatic

solution is shaken evenly and added to the filtered cellulose pulp. The erlenmeyer flask was put into the constant temperature shaking incubator (HZQ-F160, Taicang Laboratory equipment, China) at 50°C with 180 r/min for 10 h. At the same condition, the sample suspension with charge of 0.4 g cellulase was shaken in full temperature oscillation incubator for 5 h, 10 h, 15 h, and 20 h, respectively, which evaluated the influence of hydrolysis time. Thirdly, after the enzymatic reaction achievement, the cellulose fiber treated by enzymatic hydrolysis was filtered and washed using distilled water until the pH ~ 7.0 . The purpose was to get rid of buffer solution and biomass products during the hydrolysis. Then the pulp fibers was added a certain amount of distilled water and placed in the oscillation incubator for 30 min at 80°C to terminate the cellulase reaction.

2.3. Enzymatic Pretreatment Yields Calculation. Using the cellulase reaction method mentioned above, the suspension was filtered and washed using distilled water after the enzymatic reaction. The filtered fiber was dried in the oven at 105°C for 6 h and the never-dried mass was weighted as M_1 . The enzymatic pretreatment yield Y_{enzy} was calculated by the following equation:

$$Y_{\text{enzy}} = \frac{M_1}{M_0} \times 100\%, \quad (1)$$

where M_0 was the raw eucalyptus pulp mass. The yield result was obtained by the average value of thrice parallel experiments.

2.4. Mechanical Grinding Treatment. The enzymatic pretreatment pulp suspension was prepared by adding distilled water until 1000 mL volume and adding it to the grinder (MKCA6-2, Japan Masuko Company) with the millstone gap of $-200\ \mu\text{m}$ and speed of 1500 rpm twice. Then the CNF suspension was fabricated. A comparative suspension without enzymatic treatment was prepared under the same grinding condition. A small amount of CNF suspension was frozen in liquid nitrogen and dried in a freeze drying machine (Beijing Boyikang Laboratory Instrument Co., Ltd.) for 2 days to form the aerogel. The aerogel was used to be tested by SEM, FTIR, and XRD.

2.5. Characterization

2.5.1. Morphology Analysis. The scanning electron microscopy (SEM, Hitachi S-4800) was performed to characterize the morphology of enzymatic pretreatment fibers. It was prepared by sputter-coating with gold to provide adequate conductivity. The further images of CNF were obtained using the transmission electron microscopy (TEM, JEOL JEM-1230) with an accelerating voltage of 120 kV. The TEM samples were prepared by dropping diluted CNF dispersions ($5\ \mu\text{L}$) onto copper grids coated with carbon-coated support film. 1 wt% phosphotungstic acid solution was used to stain negatively and enhance the contrast of images. The samples were dried at room temperature for 24 hours. The length and diameter of CNF were calculated by Nano Measurer Particle Size Distribution Software.

2.5.2. Chemical Composition Analysis. The chemical composition of the raw eucalyptus pulp was determined by national standards GB/T 462-2008, GB/T 2677.10-1995, GB/T 2677.8-1994, and GB/T 774-1989 and expressed as wt% contents of synthetic cellulose, acid insoluble lignin, α -cellulose, and hemicellulose. Three tests on each sample were performed and the average value was calculated.

2.5.3. Fourier Transform Infrared Spectroscopy (FTIR). FTIR was recorded using the spectrum 400 (PE company, America). Before CNF aerogel samples data collection, background scanning was performed using KBr disc. The KBr disc containing 1% of very fine ground samples and one hundred scans were taken in the range of 4000–500 cm^{-1} at a resolution of 4 cm^{-1} in the absorbance mode.

2.5.4. X-Ray Diffraction (XRD) Analysis. The XRD patterns were measured by an X-ray diffractometer (D8 advance, Bruker Co., Ltd., Germany) with Ni-filtered Cu $K\alpha$ radiation at 45 kV and 40 mA. The diffraction data were collected from $2\theta = 5^\circ \sim 40^\circ$ at a scanning rate of $4^\circ/\text{min}$. The relative crystallinity index CrI was estimated using the Segal method [30] by the following equation:

$$\text{CrI (\%)} = \left(1 - \frac{I_{\text{am}}}{I_{200}} \right) \times 100, \quad (2)$$

where I_{am} was the diffraction intensity of amorphous fraction at $2\theta \approx 18.5^\circ$ and I_{200} was the peak intensity of the 002 lattice diffraction at $2\theta \approx 22.5^\circ$ which represented the crystalline region.

2.5.5. The High-Performance Liquid Chromatography (HPLC) Saccharification Analysis. The centrifuged supernatant of enzymatic pretreatment pulp was filtered through a 0.45 μm organic microporous membrane filter. The sugar quantification was performed using a HPLC system (JACSO, Tokyo, Japan), equipped with an Inertsil NH_2 column at 35°C with a flow rate of 1.0 mL 78% acetonitrile/min, to determine the concentration of the monomeric sugars and disaccharide derived from the cellulose and hemicellulose fractions by comparing with the standard samples. The concentration was estimated by the following equation:

$$C = \frac{S}{S_s} \cdot C_s, \quad (3)$$

where C was the concentration of hydrolysis product, S_s was the peak area of standard sugar sample, S was the peak area of hydrolysis product, and C_s was the concentration of standard sugar sample, including glucose, xylose, and cellobiose.

3. Results and Discussions

3.1. The Enzymatic Pretreatment Procedure. The hardwood resource (e.g., *Eucalyptus*) had more rigid structure compared to softwood counterpart [31]. It required more mechanical treatment than softwood homologue to manufacture equivalent fibrillations [32]. Thus, the pretreatment was a necessary technique to extract nanofibrils

assisted mechanical disintegration. Figure 1 showed the schematic representation of enzymatic pretreatment procedure. The chemical composition analysis of raw eucalyptus pulp revealed that the holocellulose, acid insoluble lignin, α -cellulose, and hemicellulose were 95.71%, 0.09%, 84.64%, and 11.07%, respectively. It revealed that the pulp could be directly used in enzymatic hydrolysis and did not need purification treatment. By the constant temperature shaking incubator, the cellulase evenly adhered to the surface of pulp cellulose fiber and started hydrolysis. The cellulose fibrils were about hundreds of microns in length and dozens in diameter (seen in Supporting Figure 1 in Supplementary Material available online at <https://doi.org/10.1155/2017/1591504>). And the cellulose fibrils were consisting of microfibrils with 3–4 nm in dimension and up to 20 nm for wood cell wall. Cellulose was further consisting of hundreds to over ten thousands of β -1,4 linked glucose units and formed a linear polymer, where the chain length varied between 100 and 14000 residues [31]. Due to numerous hydrogen bonds being intra/intermolecular, cellulose chains tended to be oriented in parallel and aggregate crystalline regions were highly ordered. And more disordered amorphous domains were interspersed [33, 34]. By the cooperation of mixed cellulase and layer-by-layer permeated hydrolysis, mixed enzyme finally caused fibers surface wrinkling and length decreasing. The short cellulose nanofibrils (about 1–3 μm in length) were prepared by enzymatic pretreatment assisted twice grinding passes, as shown in Figure 1.

3.2. Micromorphology Characterization of Enzymatic Cellulose. It was essential to investigate the micromorphology structure change of cellulose fibers at different enzymatic charge and hydrolysis time, as the SEM images shown in Figure 2. Figure 2(a) illustrated the morphology change of cellulose fibers including original pulp (O-Pulp), pretreatment with cellulase charge of 0.1g, 0.2g, 0.4g, and 0.6 g at hydrolysis time 10 h, and hydrolysis time of 5h, 10h, 15h, and 20 h, respectively, at 0.4 g cellulase charge. The surface of O-Pulp fiber was obviously smooth. With the cellulase charge and hydrolysis time increasing, the surface of cellulose fiber appeared rough wrinkled and grooved. It was obvious that the most outer layer was protuberant (see the images of $C_{0.1\text{g},10\text{h}}$ and $C_{0.4\text{g},5\text{h}}$) and the finer fiber appeared (see the images of $C_{0.1\text{g},10\text{h}}$ and $C_{0.4\text{g},10\text{h}}$, especially in the pink insert frame). However, there was still a small quantity of smooth outer layer. Furthermore, the smooth outer layer disappeared and a large amount of micro/nanoporosity appeared on the surface of cellulose, which resulted from the cellulase degradation layer by layer unidirectionally and deeply sharpening the fibers; see the images of $C_{0.2\text{g},10\text{h}}$, $C_{0.4\text{g},15\text{h}}$ and the pink insert frames. It was easy to fracture in the porosity, which resulted in a loss of fiber length and diameter. It was apparent that enzymatic pretreatment could receive the purpose of facilitate microfibrillation during the homogenization procedure. Simultaneously, the most significant action of the porosity was to shear the length of cellulose fibrils. Under $C_{0.6\text{g},10\text{h}}$ condition, the surface of cellulose appeared as obvious nanofibrils with a lot of fracture sites, as seen in the image of $C_{0.6\text{g},10\text{h}}$ and the magnified image

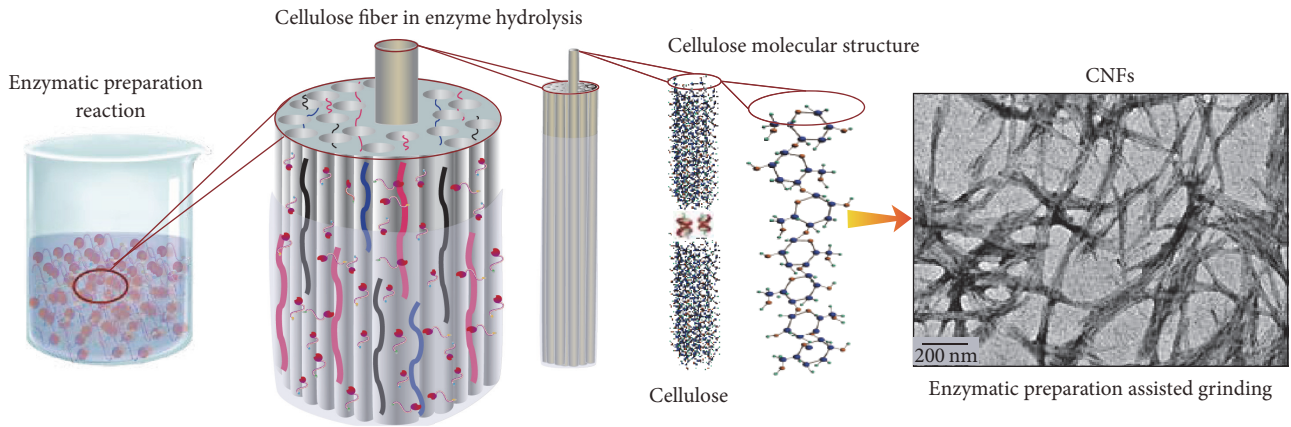


FIGURE 1: The schematic representation of enzymatic pretreatment procedure and the TEM image of CNF by enzymatic pretreatment and grinding. The morphology and structure schemas of the cellulose fibers in the enzymatic hydrolysis solution.

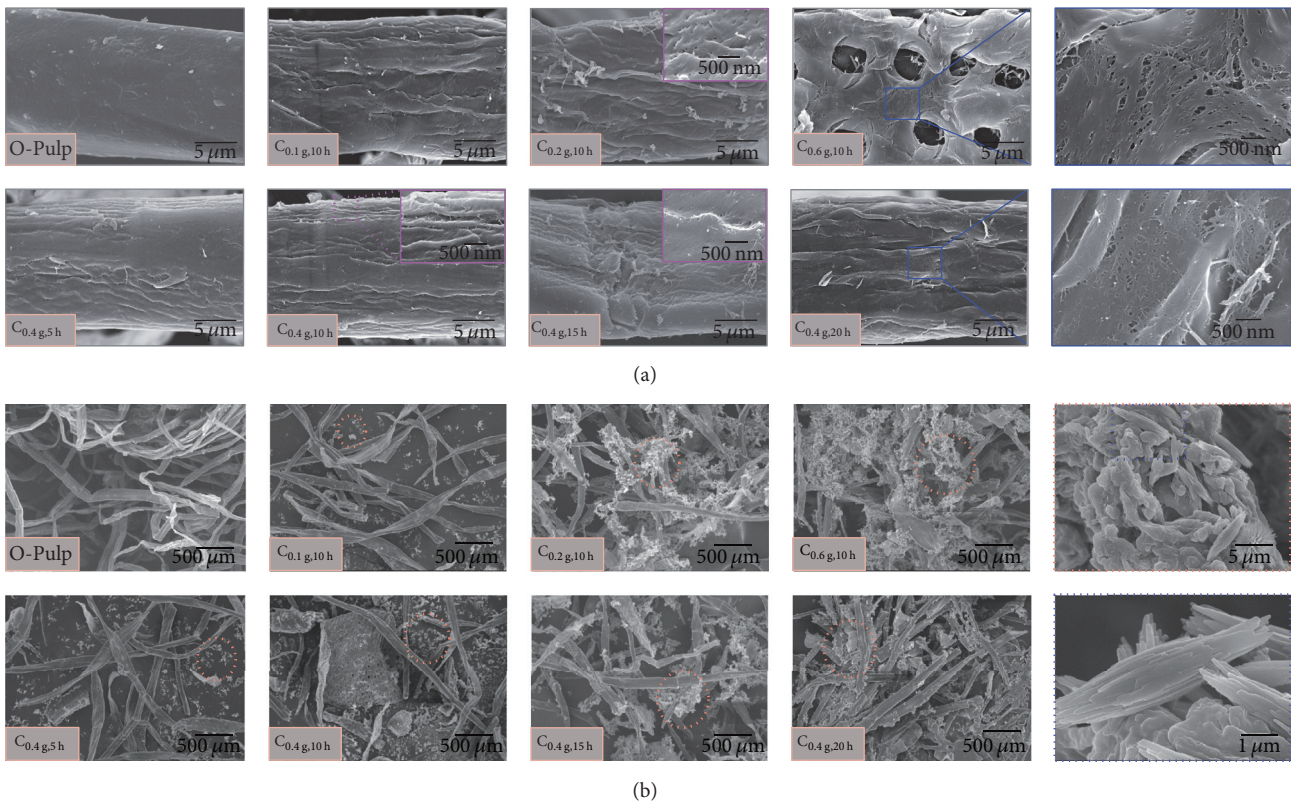


FIGURE 2: The SEM images for micromorphology change of cellulose fibers at different enzymatic charge and hydrolysis time. (a) The surface morphology changing process of single cellulose fiber with different conditions, appearing as rough wrinkle-groove-micro-/nanopores-nanofibrils. (b) The whole morphology of O-Pulp and enzymatic hydrolysis cellulose SEM images. There were numerous white flocculent substances on the surface of enzymatic hydrolysis cellulose fibers, which showed the enzymatic hydrolysis processes layer by layer on the fiber surface. The white flocculent substance was composed of shorter-thicker spindles fiber aggregation, which were cut by the cellulase.

(right blue frame one). However, there were only a handful of nanofibrils appearing on the surface layer with the cellulase time increasing (~20 h, see the image of C_{0.4 g, 20 h} and the magnified one). The next layer was still relatively coarse fiber,

which illustrated that the cellulase hydrolysis process completed layer by layer and the cellulase molecule was gradually permeating inwards. Supporting Figure 2 further showed the diameter of original pulp fiber and enzymatic hydrolysis

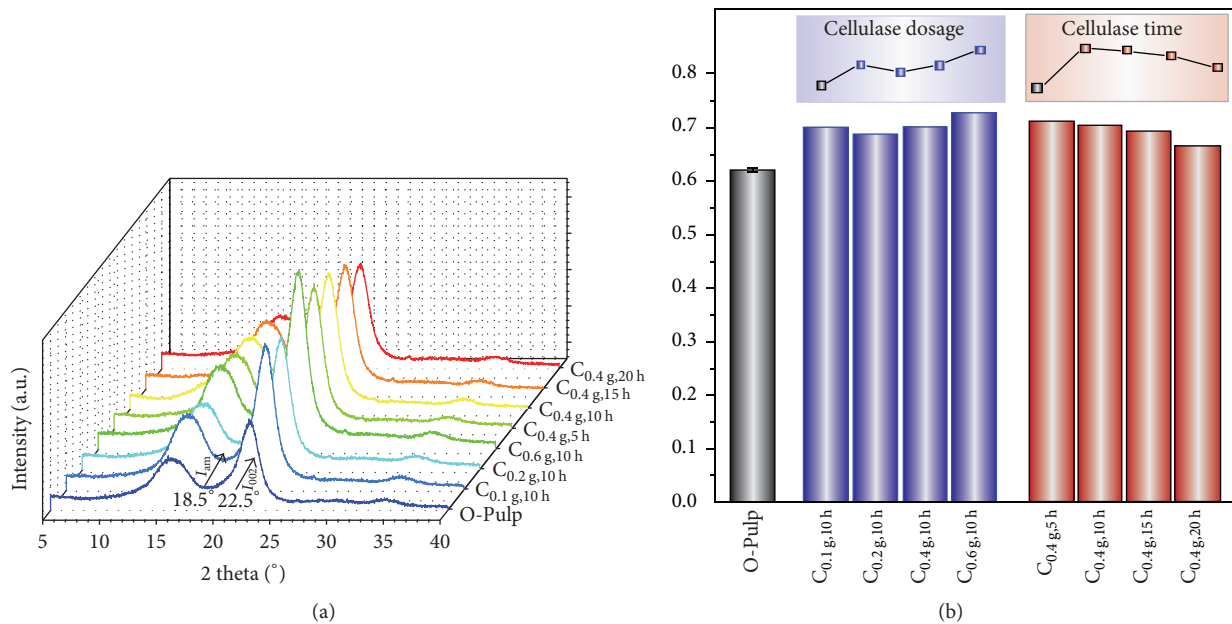


FIGURE 3: The XRD patterns of O-Pulp and enzymatic hydrolysis samples with different enzymatic charge and hydrolysis time. (a) The XRD patterns of the typical diffraction of crystal lattice type I with different conditions. The diffraction peaks were around $2\theta = 16^\circ$ and 22.5° . (b) The crystallinity of cellulose varied under different enzymatic hydrolysis pretreatments. With the cellulase charge increasing, the crystallinity exhibited a ladder increase due to the layer-by-layer hydrolysis. However, the crystallinity tended to evidently decrease with hydrolysis time, which suggested that cellulase hydrolysis rate of amorphous domains reduced gradually and was less than that of crystalline domains.

cellulose fibers with the conditions the same as Figure 2(a). The average diameter had an obvious decreasing after using enzyme hydrolysis due to layer-by-layer action. Due to the synergistic cooperation [35] of enzymatic pretreatment, adding an excess enzymatic charge would make a number of enzyme molecules interaction with the same region and influence on the degradation efficiency. And the enzyme hydrolysis time turned out the effect on the reaction kinetics [25], which was not well as long as possible.

Seen from the minified SEM images, the layer sharpening action of cellulase was more remarkable. Figure 2(b) demonstrated that the surface of original pulp fibers was tidy and clean. There were no flocculent substances in O-Pulp image. With the enzyme addition, the white flocculent substance appeared, seen as the orange dotted circle. And the flocculent substance changed increasing with the cellulase charge and time increasing, especially under C_{0.6 g, 10 h} condition. The magnified images (the orange and blue dotted frame on the right) showed that the white flocculent substance was composed of short-thick spindle fiber aggregation, which were cut by the cellulase. The spindle aggregation obviously consisted of shorter-finer cellulose fibers (seen in the magnified image with blue dotted frame). The formation of spindle fibers might result from the cellulase sharpening action; simultaneously, it led to the length decreasing. The dimension of these spindle fibers was about length of $5 \mu\text{m}$ and diameter of $1.8 \mu\text{m}$, which was greatly less than cellulose fibers. The existence of these white flocculent substances suggested enzymatic hydrolysis processes periodic “skinning” on the fiber surface and shearing the cellulose fiber length.

3.3. XRD in Qualitative Measurements of Enzymatic Cellulose. Regarding the change of crystallinity (CrI) and crystal structure, the enzymatic pretreatment cellulose aerogels were presented in Figure 3(a). Figure 3(a) showed that all the XRD patterns exhibited the typical diffraction of crystal lattice type I, which confirmed the diffraction peaks around $2\theta = 16^\circ$ and 22.5° . The cellulose crystal lattice type was preserved even though it had gone through the cellulase pretreatment. However, Figure 3(b) implied that the crystallinity of cellulose varied under different enzymatic hydrolysis pretreatment. The CrI was calculated as the ratio of the crystalline phase area versus the total area [36, 37]. Origin software was used to accurately select the diffraction intensity of amorphous fraction at $2\theta \approx 18.5^\circ$ and the 002 lattice diffraction at $2\theta \approx 22.5^\circ$ that represented the crystalline region [28]. The CrI of O-Pulp was 62.1%, and that was evidently increasing after different cellulose charge pretreatment, 70.2%, 68.9%, 70.2%, and 72.9%, respectively, for 0.1 g, 0.2 g, 0.4 g, and 0.6 g at 10 h. This suggested that the mixed cellulase mainly affected the amorphous domains of cellulose, which resulted in the crystallinity of all samples increasing 8.1% compared with original pulp. However, with the cellulase charge increasing, part monocomponent cellulase penetrated into the crystalline region interior and allowed a selective hydrolysis of the crystalline sites, which resulted in the CrI reducing in small quantities (1.3%) with 0.2 g charge. With large cellulase increasing, plenty of enzymes were involved in the reaction. The cellulase hydrolysis ability of amorphous domains was much higher than the crystalline ones [38], which resulted in CrI exhibiting a linear increase, 1.3% and 2.7%, respectively,

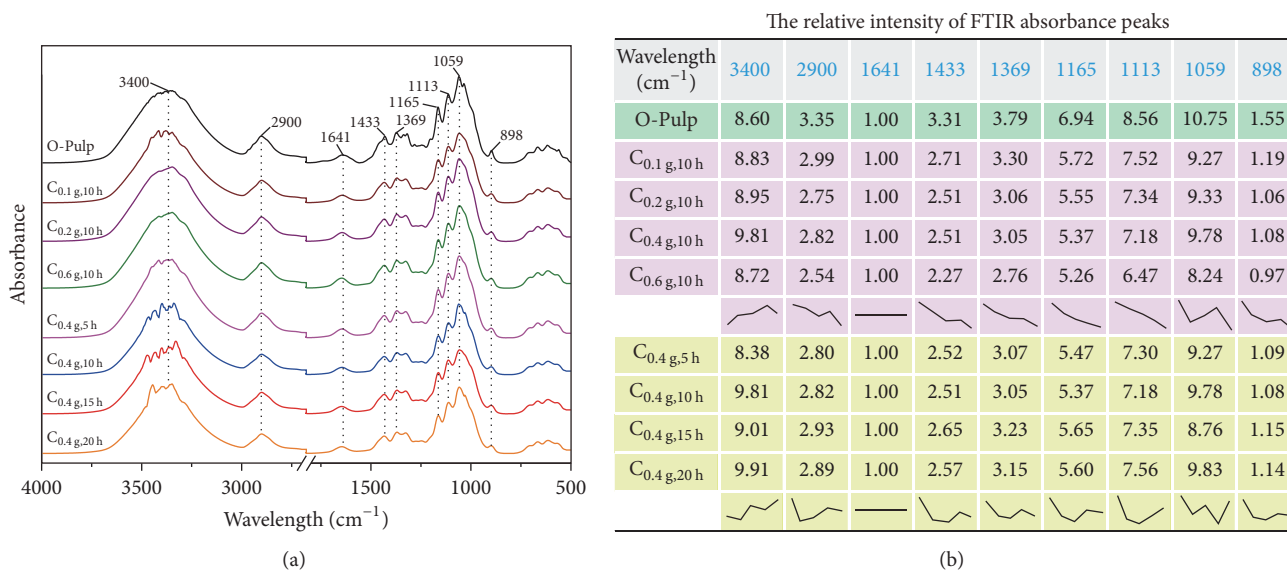


FIGURE 4: The FTIR spectrums and relative absorption peaks intensity of O-Pulp and enzymatic hydrolysis cellulose with different charge and hydrolysis time. (a) The FTIR spectrums of different samples. It is illustrated that enzymatic hydrolysis did not cause the structure transformation change. (b) The relative absorbance peak intensity relative to 1641 cm^{-1} .

for 0.4 g and 0.6 g charge. However, the effect of hydrolysis time presented a different trend. Compared with the O-Pulp crystallinity, it was evidently increasing from 62.1% to 71.0% after hydrolysis for 5 h at 0.4 g charge, which was identical to the change mentioned above. Nevertheless, the CrI tended to evidently decrease with hydrolysis time, 70.2%, 69.1%, and 66.4%, respectively, after hydrolysis for 10 h, 15 h, and 20 h with 0.4 g charge. This suggested that the crystalline domain hydrolysis rate was stronger than the amorphous ones with time extension, which resulted in the CrI decreasing (Figure 3(b)). It further implied that mixed cellulase hydrolysis was not confined to attack the amorphous region but the surfaces of the crystalline and amorphous domains compared to monocomponent endoglucanase [39]. Furthermore, the hydrolysis on these two domains was restrained regarding each other.

3.4. FTIR Spectrums Analysis of Enzymatic Cellulose. FTIR was employed to reveal the absorption peak intensity of O-Pulp, enzymatic hydrolysis cellulose with different charge, and reaction time, as Figure 4 shows. There was no distinction of the absorbance peaks between O-Pulp and enzymatic hydrolysis samples, which illustrated that enzymatic hydrolysis did not cause the structure transformation. The absorbance peaks at 3400 , 2900 , and 1641 cm^{-1} were, respectively, the intramolecular hydroxy O-H stretching vibration, C-H stretching vibration, and oxygen-containing group of absorbed water molecules. The absorbance peaks at 1433 , 1369 , 1165 , 1113 , and 1059 cm^{-1} were, respectively, the $-\text{CH}_2-$ bending vibration and shear vibration (1433 cm^{-1}), the $-\text{CH}$ -bending deformation and vibration (1369 cm^{-1}), C-O-C stretching vibration between cellulose and hemicellulose (1165 cm^{-1}) or between the cellulose (1113 cm^{-1}), and C=O

stretching vibration (1059 cm^{-1}). The absorbance peak at 898 cm^{-1} was β -glycosidic bond vibration [40–42]. Even though there was no structure transformation after enzymatic hydrolysis, the relative absorbance peak intensity changed obviously. Supporting Table 1 provided all absorbance peak intensities of characteristic peaks. Based on the standard deviation, the absorbance peak at 1641 cm^{-1} was the least one and chosen as the relative peak. All the characteristic peaks were related to 1641 cm^{-1} at own samples, as shown in Figure 4(b). Compared with the O-Pulp, the relative absorbance peak intensity at 3400 cm^{-1} presented an obvious increase, which suggested that the intramolecular hydroxyl was heightened due to a large number of hydrogen bonds broken during enzymatic hydrolysis. And the other peaks definitely appeared rectilinear or stepped decreasing with cellulase charge and hydrolysis time, which illustrated that cellulase molecules gradually diffused into the fiber interior with the hydrolysis process and resulted in the chemical bonds changing. For example, the relative absorbance peak intensity at 2900 cm^{-1} had a stepped decreasing compared with original pulp, which stated that the intermolecular hydroxyl had been destroyed. However, cellulase macromolecule structure did not change during enzymatic hydrolysis. The relative absorbance peak intensity at 1433 , 1369 , 1165 , 1113 , and 1059 cm^{-1} presented evident rectilinear decreasing with cellulase charge and wave-like changes with cellulase time, which showed that cellulase hydrolysis presented periodic regularity. It might result from the hydrolysis on fiber crystalline and noncrystalline domains due to the cooperation of mixed cellulase. But the relative absorbance peak intensity at 898 cm^{-1} showed that β -glycosidic bond was broken at the initial stage of enzymatic hydrolysis, and the changes were a little with the hydrolysis continuing.

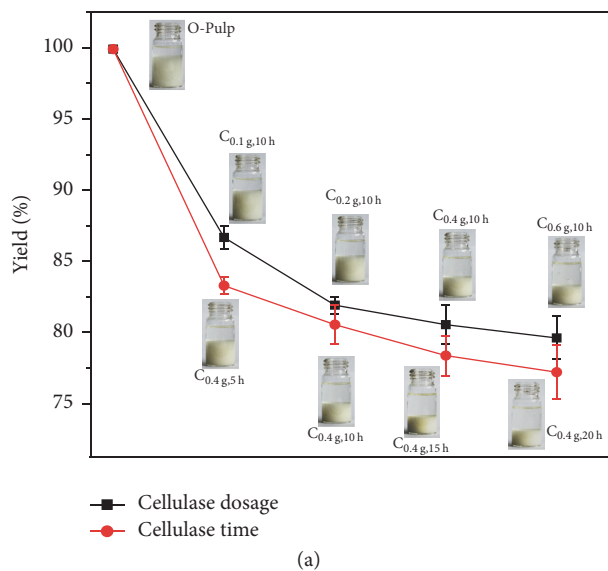


FIGURE 5: The yields of cellulose followed by hydrolysis with different charge and reaction time. (a) The yields of cellulose fibers appeared sharply decreasing at the initial hydrolysis process. (b) The optical images of yields under different conditions.

The FTIR spectra analysis further stated that the enzymatic pretreatment presented periodic effect on the crystalline and amorphous domains of cellulose fiber by layer-by-layer hydrolysis.

3.5. The Cellulose Yields of Fibers Followed by Cellulase Hydrolysis. Figure 5 demonstrated the yields of cellulase hydrolysis with different charge and reaction time. As shown in Figure 5(a), the yields of cellulose fiber appeared sharply decreasing at the initial hydrolysis process, 86.6% and 83.3%, respectively, for $C_{0.1\text{ g},10\text{ h}}$ and $C_{0.4\text{ g},5\text{ h}}$. With the cellulase charge and reaction time increasing, the yields were decreasing accordingly. The yields were respectively 81.9%, 80.5%, and 79.6% with the charge increasing and decreasing to 80.5%, 78.4%, and 77.2% with the cellulase hydrolysis time. It was noteworthy that the yields declined more slowly. It implied that the decreasing rate was restricted that might be affected by reaction kinetics [25]. The final product glucose and intermediate cellobiose could restrain the enzymatic hydrolysis. Therefore, immoderately increasing the charge and hydrolysis time did not help to improve the hydrolysis efficiency. Figure 5(b) showed vividly the optical images under different conditions. The solution volumes were limited with 18 mL and kept for 30 min standing. The hydrolysis products, for example, glucose, were in the supernatant. Therefore, the sediment was proportional to the yields mentioned in Figure 5(a).

3.6. Hydrolysis Products Analysis. The cellulase hydrolysis produced some biomass components, for example, glucose, xylose, and disaccharide. HPLC was performed to estimate the compositions and amounts of cellulase hydrolysis products. Based on the standard samples determination, the main three types of compositions were respectively, glucose, xylose,

and cellobiose. Figure 6 showed the concentration change of hydrolysis products with enzymatic charge and hydrolysis time increasing. The changing of three types of sugar products showed a similar tendency. The highest saccharification yield was glucose, which showed the high-efficiency and full cellulase hydrolysis pretreatment. And higher concentration of glucose was achieved by more charge or hydrolysis time. The glucose concentration sharply increased from 1.408 to 3.630 mg/mL followed by the charge increasing from 0.1 to 0.6 g and from 2.418 to 3.273 mg/mL followed by the hydrolysis time increasing from 5 to 20 h. The other monosaccharide product was xylose. Unlike glucose increasing trend, it slowly increased followed by the enzymatic charge and hydrolysis time increasing. The xylose concentration ranged from 0.372 to 1.543 mg/mL with the enzymatic charge changing and from 0.869 to 1.564 mg/mL with hydrolysis time increasing. The reason might be on account of the xylose derived from hemicellulose hydrolysis. And the hemicellulose content was just 11.07%. In the hydrolysis products, there was little cellobiose (0.570 to 1.258 mg/mL in Figures 6(a) and 6(b)) as the intermediate product of cellulase hydrolysis. Due to the feedback inhibition of reaction kinetics, the abundance of glucose affected the rate of cellobiose hydrolysis by cellobiase (one of monoenzyme in the mixed cellulase). Thus, the increasing rate of cellobiose was slower than glucose and xylose. In general, more enzymatic charge and hydrolysis time resulted in more biomass products, which would result in the reduction of CNF yields.

3.7. CNF Manufactured by Cooperation of Cellulase Pretreatment and Mechanical Grinding. The CNF suspensions were, respectively, manufactured using un-enzyme and cellulase hydrolysis ($C_{0.4\text{ g},10\text{ h}}$) pretreatment followed by grinding twice with the millstone gap $\sim 200\ \mu\text{m}$ and speed 1500 rpm. Figure 7

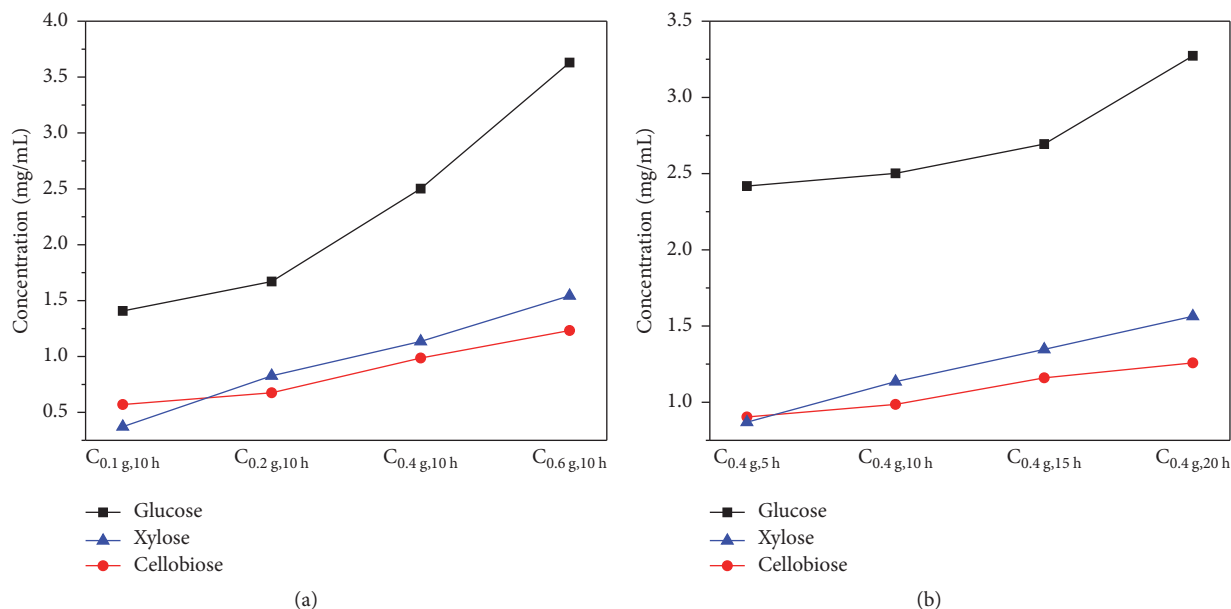


FIGURE 6: The concentration change of hydrolysis products with enzymatic charge (a) and hydrolysis time (b) increasing. All of the glucose, xylose, and cellobiose were increasing with the enzymatic charge and hydrolysis time increasing. The glucose was the highest saccharification yield in all the hydrolysis products.

showed the SEM and TEM images and data statistics of diameter of two types of CNF samples. Figure 7(a) shows the CNF prepared by pure grinding of raw pulp suspension. Nanomeasure software was used to count the diameter of cellulose fibrils, derived from 10 SEM images with 2000 data points. The diameter ranged from 50 nm to 300 nm, as shown in Figure 7(c). The average diameter under that condition was 118.6 ± 62.6 nm, which was highly nonuniform. However, the CNF fabricated by enzymatic pretreatment assisted grinding was more uniform, as shown in Figure 7(b). The average diameter of CNF under C_{0.4 g,10 h} pretreatment was 69.1 ± 15.2 nm (seen in Figure 7(d)). The diameter ranged from 20 to 120 nm. Seen from the data distribution, the diameter of fibrils with enzymatic pretreatment was more centralized than original pulp. It was more interesting that there was obvious fibril breakage as shown the arrows in Figure 7(b), which was inferred from the cellulase hydrolysis. The TEM images further showed the length of CNF. The average length was about $2.4 \pm 0.9 \mu\text{m}$ (seen in the TEM image at Figure 7(e) with red dotted frame), which was much less than that of fibril prepared by original pulp. The TEM image (Figure 7(e) with blue dotted frame) displayed that the shorter fibrils had reached the nanometer level. Compared with two types of cellulose fibrils, it more vividly illustrated the sharpening and shearing action of cellulase pretreatment on fibril dimensions.

3.8. The Mechanism of Enzymatic Hydrolysis and Length Shearing Process. Figure 8 showed the schematic illustration and morphology images of the cellulose fibers from enzymatic hydrolysis to formation CNF. As shown in Figure 8(a), the surface of original pulp fibers was smooth, and no

fibrillation existed. With the enzymatic hydrolysis proceeding, the fiber surface was markedly rough and aggregated microfibrils due to layer-by-layer action. The diameter of fibers declined and the microfibrils vividly displayed many breaking sites (Figure 8(b)). Based on the enzyme action mechanism recognized universally [43] and discussed above, the hydrolysis resulted from the synergistic effect of endoglucanase (EG), exoglucanase (cellobiohydrolases, CBH), and cellobiase (CB). In this research, the cellulase from *Trichoderma viride* was one kind of mixed cellulase. Each of monoenzymes included a globular catalytic domain and one or more carbohydrate binding domains, which were connected by an identifiable link bridge, as shown in Figure 8(b). Based on the previous reports [44–48], CBH included CBH I and CBH II; here, CBH I degraded the crystalline fibrils by layer sharpening [44–46] and CBH II resulted in the crystalline microfibril-end sharpening [47, 48] and reduced the length of fibrils (Figure 8(b)). It suggested the mechanism of mixed cellulase action on fiber length control. The EG mainly caused the degradation of amorphous region [49]. It performed the perfect synergistic degradation effect [50] of CBH and EG (Figure 8). Here, CB further degraded the intermediate product of CBH and EG hydrolysate (cellobiose) and further formed monosaccharide (glucose and xylose), which helped to decrease the feedback inhibition of reaction kinetics. The aim of enzymatic pretreatment was to hydrolyze the cellulose crystalline and noncrystalline domains and destruct the stable hydrogen bonds structure, which further assisted the mechanical grinding to obtain the cellulose nanofibrils with greatly decreasing the length and diameter. The reaction sites of molecular formula of cellulose were shown in Supporting Figure 3. The synergistic

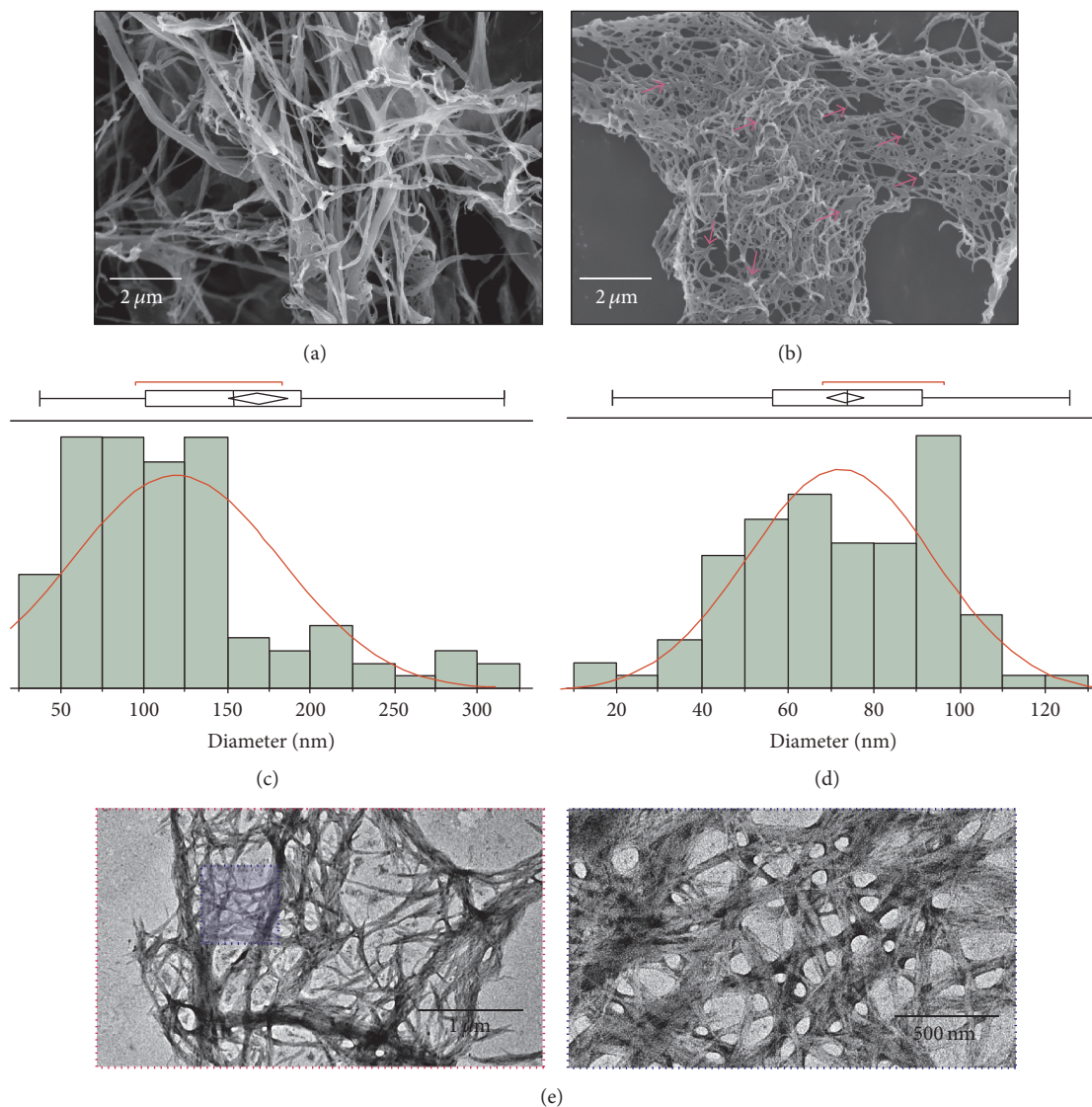


FIGURE 7: The SEM and TEM images and data statistics of diameter of different CNF manufactured by cooperation of original pulp or cellulase hydrolysis pulp with mechanical grinding. (a) The SEM image of CNF prepared by grinding of raw pulp solution. The diameters of these CNFs were highly nonuniform. (b) The SEM image of the CNF prepared by grinding with $C_{0.4g,10h}$ condition pretreatment. There were numerous breaking points. (c-d) The diameter statistics of (a) and (b) samples. The diameter of CNF prepared by original pulp ranged from 50 nm to 300 nm that the average diameter was 118.6 ± 62.6 nm. And the diameter of CNF prepared by $C_{0.4g,10h}$ condition pretreatment ranged from 20 nm to 120 nm that the average diameter was 69.1 ± 15.2 nm. (e) The TEM images of average length CNF prepared by $C_{0.4g,10h}$ condition pretreatment was about 2378 ± 940 nm.

cooperation of mixed enzyme finally caused fibers surface wrinkling and length decreasing. Followed by enzymatic hydrolysis, mechanical grinding further sheared the length of fibers and declined the diameter and ultimately formed the shorter CNF (Figure 8(c)).

4. Conclusions

We reported a kind of green and ecofriendly pretreatment method to manufacture CNF, which was a mixed cellulase from *Trichoderma viride* before hydrolysis. By the

cooperation of enzymatic pretreatment and mechanical grinding twice, the length of fibrils was obviously controlled, in that enzymatic pretreatment led to the key action on cutting the length of fibrils. The as-pretreatment cellulose fibers indicated that cellulase acted on the pulp layer by layer and concurrently hydrolyzed the crystalline and amorphous regions. The shearing action of enzyme hydrolysis resulted in the decreasing of fiber length. This paper further discussed the effect of cellulase charge and hydrolysis time on crystallinity, yields, and hydrolysis products. The result offered an insight into the fabrication method of CNF with length

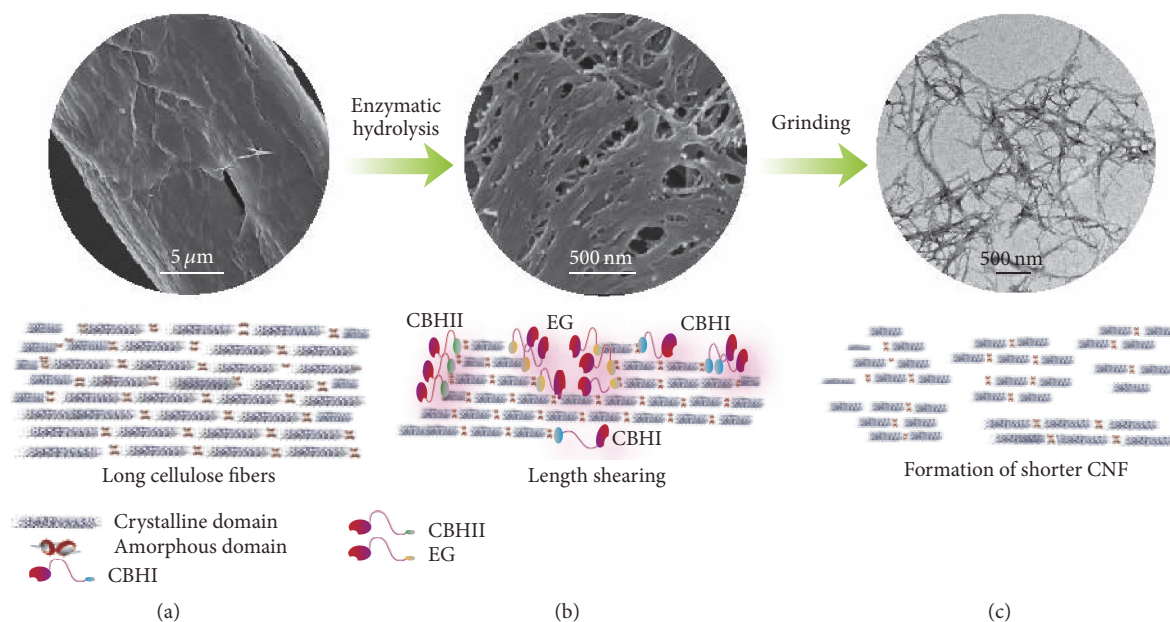


FIGURE 8: The schematic representation of original pulp fiber (a), enzyme hydrolysis fibers (b), and the fibrils followed by grinding, and the corresponding SEM and TEM images.

controlled. It would help to choose the appropriate reaction condition according to the requirements for the specific applications.

Conflicts of Interest

The authors declare that they have no conflicts of interest.

Acknowledgments

This work was supported by Special Fund for Forest Scientific Research in the Public Welfare (201504603) and National Nonprofit Special Fund for Fundamental Research from Research Institute of New Technology of Chinese Academy of Forestry (CAFINT2014K01).

References

- [1] C. Xing, J. Deng, and S. Y. Zhang, "Effect of thermo-mechanical refining on properties of MDF made from black spruce bark," *Wood Science and Technology*, vol. 41, no. 4, pp. 329–338, 2007.
- [2] B. Wang, A. J. Benitez, F. Lossada, R. Merindol, and A. Walther, "Bioinspired mechanical gradients in cellulose nanofibril/polymer nanopapers," *Angewandte Chemie—International Edition*, vol. 55, no. 20, pp. 5966–5970, 2016.
- [3] Y. Wu, S. Wang, D. Zhou, C. Xing, Y. Zhang, and Z. Cai, "Evaluation of elastic modulus and hardness of crop stalks cell walls by nano-indentation," *Bioresource Technology*, vol. 101, no. 8, pp. 2867–2871, 2010.
- [4] W. Chen, Q. Li, Y. Wang et al., "Comparative study of aerogels obtained from differently prepared nanocellulose fibers," *ChemSusChem*, vol. 7, no. 1, pp. 154–161, 2014.
- [5] C. Wan, Y. Lu, Y. Jiao, J. Cao, Q. Sun, and J. Li, "Preparation of mechanically strong and lightweight cellulose aerogels from cellulose-NaOH/PEG solution," *Journal of Sol-Gel Science and Technology*, vol. 74, no. 1, pp. 256–259, 2015.
- [6] H. Mertaniemi, C. Escobedo-Lucea, A. Sanz-Garcia et al., "Human stem cell decorated nanocellulose threads for biomedical applications," *Biomaterials*, vol. 82, pp. 208–220, 2016.
- [7] H. M. C. Azeredo, M. F. Rosa, and L. H. C. Mattoso, "Nanocellulose in bio-based food packaging applications," *Industrial Crops and Products*, vol. 97, pp. 664–671, 2017.
- [8] H. Dong, K. E. Strawhecker, J. F. Snyder, J. A. Orlicki, R. S. Reiner, and A. W. Rudie, "Cellulose nanocrystals as a reinforcing material for electrospun poly(methyl methacrylate) fibers: formation, properties and nanomechanical characterization," *Carbohydrate Polymers*, vol. 87, no. 4, pp. 2488–2495, 2012.
- [9] X. M. Dong, T. Kimura, J.-F. Revol, and D. G. Gray, "Effects of ionic strength on the isotropic-chiral nematic phase transition of suspensions of cellulose crystallites," *Langmuir*, vol. 12, no. 8, pp. 2076–2082, 1996.
- [10] A. Isogai, T. Saito, and H. Fukuzumi, "TEMPO-oxidized cellulose nanofibers," *Nanoscale*, vol. 3, no. 1, pp. 71–85, 2011.
- [11] D. J. Gardner, G. S. Oporto, R. Mills, and M. A. S. A. Samir, "Adhesion and surface issues in cellulose and nanocellulose," *Journal of Adhesion Science & Technology*, vol. 22, no. 5-6, pp. 545–567, 2008.
- [12] S. J. Eichhorn, A. Dufresne, M. Aranguren et al., "Review: current international research into cellulose nanofibres and nanocomposites," *Journal of Materials Science*, vol. 45, no. 1, pp. 1–33, 2010.
- [13] D. Klemm, D. Schumann, F. Kramer et al., "Nanocelluloses as innovative polymers in research and application," *Advances in Polymer Science*, vol. 205, no. 1, pp. 49–96, 2006.
- [14] I. Siró and D. Plackett, "Microfibrillated cellulose and new nanocomposite materials: a review," *Cellulose*, vol. 17, no. 3, pp. 459–494, 2010.

- [15] U. Henniges, S. Veigel, E.-M. Lems et al., "Microfibrillated cellulose and cellulose nanopaper from *Miscanthus* biogas production residue," *Cellulose*, vol. 21, no. 3, pp. 1601–1610, 2014.
- [16] K. Abe and H. Yano, "Comparison of the characteristics of cellulose microfibril aggregates of wood, rice straw and potato tuber," *Cellulose*, vol. 16, no. 6, pp. 1017–1023, 2009.
- [17] Q. Cheng, S. Wang, and Q. Han, "Novel process for isolating fibrils from cellulose fibers by high-intensity ultrasonication. II. fibril characterization," *Journal of Applied Polymer Science*, vol. 115, no. 5, pp. 2756–2762, 2010.
- [18] H. Du, C. Liu, Y. Zhang, G. Yu, C. Si, and B. Li, "Preparation and characterization of functional cellulose nanofibrils via formic acid hydrolysis pretreatment and the followed high-pressure homogenization," *Industrial Crops and Products*, vol. 94, pp. 736–745, 2016.
- [19] C. Tian, J. Yi, Y. Wu, Q. Wu, Y. Qing, and L. Wang, "Preparation of highly charged cellulose nanofibrils using high-pressure homogenization coupled with strong acid hydrolysis pretreatments," *Carbohydrate Polymers*, vol. 136, pp. 485–492, 2016.
- [20] A. Naderi, T. Lindström, and J. Sundström, "Repeated homogenization, a route for decreasing the energy consumption in the manufacturing process of carboxymethylated nanofibrillated cellulose?" *Cellulose*, vol. 22, no. 2, pp. 1147–1157, 2015.
- [21] M. Martelli-Tosi, M. da Silva Torricillas, M. A. Martins, O. B. G. de Assis, and D. R. Tapia-Blácido, "Using commercial enzymes to produce cellulose nanofibers from soybean straw," *Journal of Nanomaterials*, vol. 2016, Article ID 8106814, 10 pages, 2016.
- [22] Y. Qing, R. Sabo, J. Y. Zhu, U. Agarwal, Z. Cai, and Y. Wu, "A comparative study of cellulose nanofibrils disintegrated via multiple processing approaches," *Carbohydrate Polymers*, vol. 97, no. 1, pp. 226–234, 2013.
- [23] B. C. Knott, M. F. Crowley, M. E. Himmel, J. Zimmer, and G. T. Beckham, "Simulations of cellulose translocation in the bacterial cellulose synthase suggest a regulatory mechanism for the dimeric structure of cellulose," *Chemical Science*, vol. 7, no. 5, pp. 3108–3116, 2016.
- [24] G. Ji, C. Gao, W. Xiao, and L. Han, "Mechanical fragmentation of corncob at different plant scales: impact and mechanism on microstructure features and enzymatic hydrolysis," *Bioresource Technology*, vol. 205, pp. 159–165, 2016.
- [25] G. Guerriero, J.-F. Hausman, J. Strauss, H. Ertan, and K. S. Siddiqui, "Lignocellulosic biomass: biosynthesis, degradation, and industrial utilization," *Engineering in Life Sciences*, vol. 16, no. 1, pp. 1–16, 2016.
- [26] P. J. Weimer, J. M. Hackney, and A. D. French, "Effects of chemical treatments and heating on the crystallinity of celluloses and their implications for evaluating the effect of crystallinity on cellulose biodegradation," *Biotechnology and Bioengineering*, vol. 48, no. 2, pp. 169–178, 1995.
- [27] T. Eriksson, J. Börjesson, and F. Tjerneld, "Mechanism of surfactant effect in enzymatic hydrolysis of lignocellulose," *Enzyme and Microbial Technology*, vol. 31, no. 3, pp. 353–364, 2002.
- [28] M. Henriksson, G. Henriksson, L. A. Berglund, and T. Lindström, "An environmentally friendly method for enzyme-assisted preparation of microfibrillated cellulose (MFC) nanofibers," *European Polymer Journal*, vol. 43, no. 8, pp. 3434–3441, 2007.
- [29] M. Pääkko, M. Ankerfors, H. Kosonen et al., "Enzymatic hydrolysis combined with mechanical shearing and high-pressure homogenization for nanoscale cellulose fibrils and strong gels," *Biomacromolecules*, vol. 8, no. 6, pp. 1934–1941, 2007.
- [30] L. Segal, J. J. Creely, A. E. Martin Jr., and C. M. Conrad, "An empirical method for estimating the degree of crystallinity of native cellulose using the X-ray diffractometer," *Textile Research Journal*, vol. 29, no. 10, pp. 786–794, 1959.
- [31] Q. Q. Wang, J. Y. Zhu, R. Gleisner, T. A. Kuster, U. Baxa, and S. E. McNeil, "Morphological development of cellulose fibrils of a bleached eucalyptus pulp by mechanical fibrillation," *Cellulose*, vol. 19, no. 5, pp. 1631–1643, 2012.
- [32] W. Stelte and A. R. Sanadi, "Preparation and characterization of cellulose nanofibers from two commercial hardwood and softwood pulps," *Industrial and Engineering Chemistry Research*, vol. 48, no. 24, pp. 11211–11219, 2009.
- [33] R. Parthasarathi, G. Bellesia, S. P. S. Chundawat, B. E. Dale, P. Langan, and S. Gnanakaran, "Insights into hydrogen bonding and stacking interactions in cellulose," *Journal of Physical Chemistry A*, vol. 115, no. 49, pp. 14191–14202, 2011.
- [34] C. Somerville, S. Bauer, G. Brininstool et al., "Toward a systems approach to understanding plant cell walls," *Science*, vol. 306, no. 5705, pp. 2206–2211, 2004.
- [35] K. Igarashi, T. Uchihashi, A. Koivula et al., "Traffic jams reduce hydrolytic efficiency of cellulase on cellulose surface," *Science*, vol. 333, no. 6047, pp. 1279–1282, 2011.
- [36] E.-L. Hult, T. Iversen, and J. Sugiyama, "Characterization of the supermolecular structure of cellulose in wood pulp fibres," *Cellulose*, vol. 10, no. 2, pp. 103–110, 2003.
- [37] C. J. Garvey, I. H. Parker, and G. P. Simon, "On the interpretation of X-ray diffraction powder patterns in terms of the nanostructure of cellulose I fibres," *Macromolecular Chemistry and Physics*, vol. 206, no. 15, pp. 1568–1575, 2005.
- [38] J. Y. Zhu, R. Sabo, and X. Luo, "Integrated production of nano-fibrillated cellulose and cellulosic biofuel (ethanol) by enzymatic fractionation of wood fibers," *Green Chemistry*, vol. 13, no. 5, pp. 1339–1344, 2011.
- [39] A.-C. Engström, M. Ek, and G. Henriksson, "Improved accessibility and reactivity of dissolving pulp for the viscose process: pretreatment with monocomponent endoglucanase," *Biomacromolecules*, vol. 7, no. 6, pp. 2027–2031, 2006.
- [40] N. Gierlinger, L. Goswami, M. Schmidt et al., "In situ FT-IR microscopic study on enzymatic treatment of poplar wood cross-sections," *Biomacromolecules*, vol. 9, no. 8, pp. 2194–2201, 2008.
- [41] M. Åkerholm and N. L. Salmén, "Interactions between wood polymers studied by dynamic FT-IR spectroscopy," *Polymer*, vol. 42, no. 3, pp. 963–969, 2001.
- [42] J. Guo, K. Song, L. Salmén, and Y. Yin, "Changes of wood cell walls in response to hygro-mechanical steam treatment," *Carbohydrate Polymers*, vol. 115, pp. 207–214, 2015.
- [43] K. Igarashi, M. Wada, and M. Samejima, "Activation of crystalline cellulose to cellulose III results in efficient hydrolysis by cellobiohydrolase," *FEBS Journal*, vol. 274, no. 7, pp. 1785–1792, 2007.
- [44] T. Imai, C. Boisset, M. Samejima, K. Igarashi, and J. Sugiyama, "Unidirectional processive action of cellobiohydrolase Cel7A on *Valonia* cellulose microcrystals," *FEBS Letters*, vol. 432, no. 3, pp. 113–116, 1998.
- [45] Y.-H. P. Zhang and L. R. Lynd, "Toward an aggregated understanding of enzymatic hydrolysis of cellulose: noncomplexed cellulase systems," *Biotechnology and Bioengineering*, vol. 88, no. 7, pp. 797–824, 2004.

- [46] Y.-S. Liu, J. O. Baker, Y. Zeng, M. E. Himmel, T. Haas, and S.-Y. Ding, "Cellobiohydrolase hydrolyzes crystalline cellulose on hydrophobic faces," *The Journal of Biological Chemistry*, vol. 286, no. 13, pp. 11195–11201, 2011.
- [47] J. Jalak, M. Kurašin, H. Teugjas, and P. Väljamäe, "Endo-exo synergism in cellulose hydrolysis revisited," *The Journal of Biological Chemistry*, vol. 287, no. 34, pp. 28802–28815, 2012.
- [48] A. Koivula, T. Kinnari, V. Harjunpää et al., "Tryptophan 272: an essential determinant of crystalline cellulose degradation by *Trichoderma reesei* cellobiohydrolase Cel6A," *FEBS Letters*, vol. 429, no. 3, pp. 341–346, 1998.
- [49] T. M. Wood and S. I. McCrae, "The purification and properties of the C₁ component of *Trichoderma koningii* cellulase," *Biochemical Journal*, vol. 128, no. 5, pp. 1183–1192, 1972.
- [50] T. Ganner, P. Bubner, M. Eibinger, C. Mayrhofer, H. Plank, and B. Nidetzky, "Dissecting and reconstructing synergism in situ visualization of cooperativity among cellulases," *The Journal of Biological Chemistry*, vol. 287, pp. 43215–43222, 2012.